Structural and functional characterization of cytochrome c oxidase, cytochrome bc_1 complex and heme A synthase from *Aquifex aeolicus*

Dissertation

zur Erlangung des Doktorgrades

der Naturwissenschaften

vorgelegt beim Fachbereich 14

Biochemie, Chemie und Pharmazie

der Johann Wolfgang Goethe Universität

in Frankfurt am Main, Deutschland

von

Hui ZENG

aus Hubei, China

Frankfurt am Main (2019)

(D30)

vom Fachbereich Biochemie, Chemie und Pharmazie der Johann Wolfgang Goethe Universität als Dissertation angenommen.

Dekan: Prof. Dr. Clemens Glaubitz

1. Gutachter: Prof. Dr. Klaas Martinus Pos
2. Gutachter: Prof. Dr. Hartmut Michel

Datum der Disputation:

Die Doktorarbeit wurde vom Dezember 2014 bis zum Dezember 2019 unter Leitung von Prof. Dr. Hartmut Michel in der Abteilung für Molekulare Membranbiologie am Max-Planck-Institut für Biophysik in Frankfurt am Main durchgeführt.

Eidesstattliche Erklärung

Hiermit versichere ich, dass ich die vorliegende Arbeit selbstständig angefertigt habe und keine weiteren Hilfsmittel und Quellen als die hier aufgeführten verwendet habe.

Hui ZENG

Frankfurt am Main, den

TO MY BELOVED FAMILY

Publications

1. Guoliang Zhu*, **Hui Zeng***, Shuangbo Zhang*, Jana Juli, Xiaoyun Pang, Jan Hofmann,Yan Zhang, Nina Morgner, Yun Zhu, Guohong Peng, Hartmut Michel, Fei Sun. 3.3 Å structure of hyperthermophilic respiratory complex III from *Aquifex aeolicus* reveals the mechanism of its thermal stability. (*: contributed equally. Angew. Chem. Int. Ed.. doi:10.1002/anie.201911554)
2. **Hui Zeng**, Guoliang Zhu, Shuangbo Zhang, Janosch Martin, Nina Morgner, Fei Sun, Guohong Peng, Hao Xie and Hartmut Michel. The isolated intact heme A synthase from *Aquifex aeolicus* is a trimer. (mbio, in revision)

Table of contents

List of figures

List of tables

Zusammenfassung

Zellen nutzen eine Serie von membranständigen Enzymen in der sogenannten Elektronentransportkette (engl. ETC) um einen elektrochemischen Protonengradienten aufzubauen. Dieser elektrochemische Protongradient treibt die ATP-Synthese der ATP-Synthase an. Die ETC oder auch Atmungskette besteht in Mitochondrien aus vier Enzymkomplexen (Komplex I –IV) und verwendet zwei verschiedene Elektronenüberträger zum Elektronentransfer zwischen den Komplexen, nämlich Cytochrom c und Ubichinon. In der Atmungskette fließen die Elektronen von einem Enzymkomplex zum nächsten. Redoxreaktionen treiben gleichzeitig den Transport von Protonen von der negativen (N) Seite der Membran zur positiven (P) Seite an. Elektronen kommen über Komplex I in die Atmungskette, welcher NADH zu NAD+ oxidiert und gleichzeitig Chinone (Q) zu Chinol (QH2) reduziert. Bei dieser Redoxreaktion werden vier Protonen durch die Membran gepumpt. Komplex II stellt einen alternativen Eintrittspunkt für Elektronen in die Atmungskette dar. Er katalysiert die Oxidation von Succinate zu Fumarat bei gleichzeitiger Reduktion von Q zu QH2. Komplex III, auch bc_1-Komplex genannt, katalysiert dann den Elektronentransfer von QH2 auf Cytochrome c, was auch zu Protonentranslokation führt. Komplex III pumpt zwar keine Protonen aktiv, aber der sogenannte Q-Zyklus führt dazu, das insgesamt vier Protonen von der N- zu der P-Seite wandern. Komplex IV, die Cytochrom c Oxidase, der terminale Komplex der ETC, katalysiert die Reduktion von Sauerstoff zu Wasser und pumpt gleichzeitig vier Protonen durch die Membran. Für alle Komplexe der Atmungskette sind Strukturen aus verschiedensten Organismen verfügbar, jedoch konnten noch nicht alle evolutionären und mechanistischen Fragen restlos aufgeklärt werden. So konnte noch keine Struktur eines Komplexes aus einem hyperthermophilen Organismus aufgeklärt werden. Auch der Oligomerisierungszustand der Cytochcrom c Oxidase wird kontrovers in der Fachliteratur diskutiert. Weitere wichtige Punkte im Aufbau von Atmungkettenkomplexen sind die Synthese und die Eingliederung von

Zusammenfassung

Kofaktoren in die Enzymkomplexe. So enthalten die aktiven Zentren von A- und B-Typ Cytochrom c Oxidasen Häm A, welches durch ein integrales Membranprotein, nämlich die Häm A Synthase (HAS) synthetisiert wird. HAS können Komplexe mit sich selbst bilden und ihr Oligomerisierungszustand ist oftmals kritisch für die Funktion des Enzyms. HAS sind evolutionär zwischen Prokaryoten und Eukaryoten konserviert. Trotz ihrer fundamentalen Bedeutung für die Energiekonservierung ist die Struktur und die Oligomerisierung von HAS nur wenig erforscht. *Aquifex aeolicus* ist einer der hyperthermophilsten Organismen, welcher auch bei extremen Temperaturen von bis zu 95°C noch lebensfähig ist. Aufgrund ihrer fundamentalen Bedeutung im Energiemetabolismus sind Atmungskettenkomplexe Ziel zahlreicher Studien. Jedoch gerade für Atmungskettenkomplexe aus hyperthermophilen oder sehr alten Bakterien, gibt es nur wenig verfügbare Strukturen. Somit ist nur wenig über den Aufbau und den katalytischen Mechanismus von Enzymkomplexen aus hyperthermophilen Organismen bekannt. Ziel dieser Arbeit war die strukturelle Charakterisierung der Cytochrom *c* Oxidase (AaC*c*O), des Cytochrom *bc*$_1$ Komplexes (Aabc1) und der Häm A Synthase (AaHAS) aus *A. aeolicus*. Dabei wurden vier Hauptprojekte bearbeitet: 1) die strukturelle und funktionelle Charakterisierung von AaC*c*O, 2) die Untersuchung der Thermostabilität von Aa*bc*$_1$, 3) das Bestimmen des Oligomerzustandes von AaHAS, 4) die mechanistische Untersuchung des Zusammenhangs der Oligomerisierung mit der Funktion von AaHAS.

1) Strukturelle und funktionelle Charakterisierung von AaC*c*O

Häm-Kupfer-Oxidasen (HCOs) sind terminale Oxidasen welche die Reduktion von Sauerstoff zu Wasser katalysieren. Sie kommen sowohl in der Plasmamembran von Prokaryoten wie auch in der inneren mitochondrialen Membran von Eukaryoten vor. Sie nutzen die Energie der Sauerstoffreduktion um Protonen von der N- auf die P-Seite der Membran zu pumpen und tragen somit zum elektrochemischen Protonengradienten bei. HCOs werden basierend auf einer phylogenetischen Analyse in drei Subfamilien unterteilt; A, B und C. Die gut erforschte *aa*$_3$-Typ Cytochrom c Oxidase repräsentiert die A-Familie. Für die B-Familie gibt es nur eine verfügbare Struktur, nämlich jene der

Zusammenfassung

ba_3-Typ Cytochrom c Oxidase aus *Thermus thermophilus*. Die B-Familie der HCOs beinhaltet eine Vielzahl von bakteriellen und archaealen terminalen Oxidasen. Die C-Familie beherbergt ausschließlich cbb_3-Typ Cytochrom c Oxidasen. AaCcO gehört zu den ba_3-Typ Cytochrom c Oxidasen. Durch genomische Analyse wurde festgestellt, dass in *A. aeolicus* zwei Operone die Cytochrom c Oxidase kodieren (zwei Gene jeweils für Untereinheit I und II, ein Gen für Untereinheit III). Aktuell wurden jedoch nur die Untereinheiten CoxB2 und CoxA2 nachgewiesen. Die zusätzliche IIa-Untereinheit wurde 2012 identifiziert. Studien zeigten, dass AaCcO Cytochrom c aus Pferdeherzen und Decylubichinol als Elektronendonoren verwenden kann. Außerdem wird die AaCcO nicht vollständig durch typische Oxidaseinhibitoren, wie z.B. Cyanide, gehemmt.

In dieser Arbeit wurde die heterologe Expression von AaCcO in *Pseudomonas stutzeri* (*P. stutzeri*) und die Koexpression von AaCcO und AsHAS in *Escherichia coli* etabliert. Der Subkomplex CoxA2/CoxB2 konnte aus *P. stutzeri* aufgereinigt werden, jedoch enthielt dieser nach der Aufreinigung kein Häm A mehr. Zusätzlich wurde ein Protokoll für die heterologe Produktion von Cytochrom c_{555} aus *A. aeolicus* in *Escherichia coli* etabliert. AaCcO wurde auch aus nativen Membranen aufgereinigt. Die Aktivität von AaCcO wurde mit dem nativen Substrat, Cytochrom c_{555}, bestimmt und war im Vergleich zu jener, die mit Cytochrom c aus Pferdeherz bestimmt wurde, etwa 14-mal höher. Die Struktur von AaCcO konnte mittels cryo EM mit einer Auflösung von 3.4 Å ermittelt werden. Die Struktur zeigt, dass die drei Untereinheiten des AaCcO-Komplexes, CoxA2, CoxB2 und IIa, einen stabilen Komplex formen, welchen ein Homodimer mit einem zweiten AaCcO-Komplex bildet. Auch konnte die vorhergesagte Untereinheit III, welche aus nur einer Transmembranhelix besteht, in der Struktur identifiziert werden. Die Struktur zeigt die Cofaktoren, Häm a_3, Häm b, Cu_A und Cu_B innerhalb des AaCcO-Komplexes. Im direkten Vergleich zu der veröffentlichten Kristallstruktur des Cytochrom c Oxidase Dimers aus Rind, stellt die cryoEM Struktur von AaCcO einen nativen Zustand dar. Die cryoEM-Struktur erlaubte es, zwei Moleküle 1,4-Napththochinon und ein Cardiolipin im Dimerinterface zu identifizieren. Basierend auf den strukturellen Daten benutzt AaCcO nur den K-Pfad

für den Protonentransport zum aktiven Zentrum bzw. durch die Membran.

2) Strukturelle Charakterisierung von Aabc_1

Der Cytochrom bc_1-Komplex spielt eine wichtige in der Katalyse des Transfers von vier Elektronen von Chinol auf Cytochrom c und den Protonentransfer über den sogenannten Q-Zyklus. Strukturen des Cytochrom bc_1-Komplex aus verschiedensten Organismen konntne schon erfolgreich aufgeklärt werden. Mithilfe dieser Strukturen konnten Einblicke in den Aufbau und den katalytischen Mechanismus von Cytochrom bc_1 Komplexen gewonnen werden. Die Zusammensetzung des Komplexes variiert zwischen den verschiedenen Spezies, jedoch sind die drei Hauptuntereinheiten, Cytochrom b (Cyt. b) und Cytochrom c_1 (Cyt. c_1) und das Rieske Eisen-Schwefel Protein (ISP) in allen Spezies konserviert. Cyt. b enthält die beiden Häme b_L und b_H, Cyt. c_1 Häm c_1 und ISP den Eisen-Schwefel-Cluster [Fe_2S_2]. Der Cytochrom bc_1-Komplex hat zwei Bindungsstellen für Chinol, eine für die Oxidierung (Q$_o$) und eine für die Reduzierung (Q$_i$), welche oftmals zu, Design spezifischer Inhibitoren oder Medikamente herangezogen werden. Alle verfügbaren Strukturen stammen jedoch von mesophilen Organismen. Gerade der Elektronentransport in thermophilen Organismen unter extremen Bedingungen ist noch nicht ausreichend verstanden.

Im Zuge dieser Arbeit wurde der Cytochrom bc_1-Komplex (Komplex III) aus *A. aeolicus* aufgereinigt und seine Struktur mittels cryoEM aufgeklärt. Es konnte eine Apo und eine inhibierte Struktur mit einer Auflösung von 3.3 Å ermittelt werden. Die Analyse der Strukturen zeigt, dass das die drei konservierten Untereinheiten Cyt. b, Cyt. c_1 und ISP in engem Kontakt stehen und den Komplex bilden, welcher wiederum eine Homodimer bildet. Mittels Sequenzanalysen des Cytochrom bc_1-Komplexes konnten Aminosäuren identifiziert werden, welche nur in thermophilen Bakterien, nicht aber in mesophilen vorhanden sind. In Cyt. b wurden die Aminosäuren Tyr 38, Tyr 64, Phe 83 und Arg 222 als thermophilenspezifisch identifiziert. Tyr 38 stabilisiert die Carboxylgruppen von Häm b_H. Die Hydroxylgruppe von Tyr 61 in Transmemban helix (TMH) I in einem Protomer bindet an den Stickstoff von Arg 197 in TMH IV eines zweiten Protomers um die Bindung der beiden Cyt. b Protomere zu verstärken. Die

X

Interaktionen zwischen Tyr 61 und Val 31 in TMH I der ISP Untereinheit stabilisieren diese Untereinheit im Enzymkomplex. Phe 83 in Cyt. b verstärkt die Affinität zu 1,4-Naphthochinon durch hydrophobe Wechselwirkungen mit dem Benzolring mit des Naphthochinons. Arg 222 stabilisiert die Bindung von 1,4-Naphthochinon am Q_i-Zentrum Q_i, um einen effizienten Elektronenfluss zu Häm b_H herzustellen. Die Struktur zeigt auch eine weitere TMH am N-Terminus von Cyt. c_1, welche die Interaktionen zwischen Cyt. b und Cyt. c_1 verstärkt. Diese zusätzliche TMH bindet auch ein Phospholipid, welches den Komplex in der Membran stabilisiert. Die Ergebnisse liefern wichtige Erkenntnisse über die Thermostabilität und den Katalysemechansimus des Cytochrom bc_1-Komplexes unter extremen thermischen Bedingungen.

3) Bestimmung des Oligomerzustandes von AaHAS

Häm A Synthasen (HASs) sind integrale Membranproteine, welche die Biosynthese von Häm A aus Häm O katalysieren. Der Katalysemechanismus beinhaltet drei Schritte; (i) ein monohydroxyliertes Häm O (Häm I) wird mittels Oxygenierung der C8-Methylgruppe des D-Pyrrolrings von Häm O hergestellt, (ii) Häm I wird weiter zu einem dihydroxyliertem Zwischenprodukt oxidiert, (III) die spontane Dehydratation des geminalen Diols zur Aldehydgruppe an Position C8 des Häm A. Studien zeigten, dass HAS Homoligomere bildet und dass ihre Oligomerisierung, welche in Pro- und Eukaryoten vorhanden ist, entscheidend für ihre Funktion ist. Trotz ihrer biologischen Bedeutung ist nur wenig über die strukturellen Eigenschaften von HAS-Oligomeren bekannt. In dieser Arbeit wurde der Oligomerisierungszustand der HAS aus *A. aeolicus* mittels Größenausschlusschromatographie, gekoppelter Mehrwinkel-Lichtstreuungs spektroskopie (SEC-MALS, cross-linking, Laser induzierter Ionendesorptionsmassenspektrometrie (LILBID-MS) und cryoEM untersucht. Die Ergebnisse zeigen, dass AaHAS thermostabile Trimere bildet.

4) Untersuchung des Zusammenhangs der Oligomerisierung mit der Funktion von AaHAS.

Die einzige veröffentlichte HAS-Struktur ist die Struktur des HAS-Monomers aus

Zusammenfassung

Bacillus subtilis. Jedoch zeigen eine Vielzahl von Studien, dass HASs nativ als Oligomere vorliegen und ihre Oligomerisierung entscheidend für die Funktion von HASs ist. Die Struktur des HAS Oligomers und die Rolle der Oligomerisierung im Reaktionsmechanismus konnten noch nicht aufgeklärt werden. In dieser Arbeit wurde die Struktur des AaHAS Oligomers aufgeklärt und die Implikationen auf den katalytischen Mechanismus untersucht. AaHAS ist ein integrales Membranprotein und das Molekulargewicht das AaHAS-Monomers beträgt nur 33.34 kDa. Beides stellt große Herausforderungen an die Strukturaufklärung mittels cryoEM. In dieser Arbeit gelang es, AaHAS in Detergensmizellen aufzureinigen und zu kristallisieren, jedoch erlaubten die Kristalle eine Strukturaufklärung nur bis maximal 7 Å. Daher wurde die AaHAS in Nanodiscs rekonstituiert und mittels cryoEM untersucht. Dieser Ansatz erlaubte es, die Struktur des AaHAS-Trimers mit einer Auflösung von 2.8 Å aufzuklären. AaHAS bildet ein N-terminales Bündel aus vier TMHs, welches das Substrat Häm O bindet, während ein C-terminales Bündel ebenfalls aus vier TMHs den Kofaktor Häm B gebunden hat. Hydrophobe Wechselwirkungen zwischen den C-terminalen Helixbündeln führen zur Bildung eines kompakten 3-Flügel-Propeller-förmigen AaHAs-Trimers. Es zeigte sich außerdem, dass jedes AaHAS-Monomer ein Phosphatidylglycerollipid (PG) gebunden hat. Dieses PG vermittelt die Interaktion zwischen Tyr 211 eines Monomers mit der extrazellulären Schleife II (ECLII) eines anderen Monomers. Im Vergleich zu der veröffentlichten Kristallstruktur des Monomers zeigte die Struktur des AaHAS-Trimers einen Knick in TMH IV und eine vergrößerte Substratbindungsstelle. Die Struktur impliziert dabei, dass Glu138 in *A. aeolicus* wahrscheinlich den katalytischen Rest bildet, welcher für die Formylierungsreaktion verantwortlich ist. Die Bestimmung der Struktur des AaHAS-Trimers verhalf damit zu neuen mechanistischen Einblicken in den katalytischen Zyklus von HAS und die Rolle der Oligomerisierung.

Zusammengefasst, im Zuge dieser Arbeit konnten die Strukturen der *ba₃*-Typ AaCcO, des Cytochrom *bc₁*-Komplexes und der AaHAS aus *A. aeolicus* mittels cryoEM aufgeklärt werden. Dadurch konnten neue Erkenntnisse über den katalytischen

Mechanismus dieser wichtigen membranständigen Enzyme und über ihre Thermostabilität gewonnen werden. Die Ergebnisse zeigen deutlich die Vorteile von cryoEM für die strukturelle Charakterisierung von Atmungskettenkomplexen aus extremophilen Organismen.

Summary

The electron transport chain (ETC) is used by cells to create an electrochemical proton gradient which can be used by the ATP synthase to produce ATP. ETC, also called respiratory chain, is formed in mitochondria by four complexes (complex I-IV) and mediated by two electron carriers: cytochrome c and ubiquinone. Electrons are passed from one complex to another in a series of redox reactions coupling proton pumping from the negative (N) side of the membrane to the positive (P) side. Complex I can introduce electrons into the ETC by oxidizing NADH to NAD^+ and reducing quinone (Q) to quinol (QH2). The process accomplishes pumping of four protons across the membrane. Complex II is another electrons entry point. It catalyzes the oxidation of succinate to fumarate while reducing Q to QH2. Complex III, also called cytochrome bc_1 complex, can transfer the electrons from QH2 to cytochrome c and couple to proton pumping. In complex III the Q-cycle contributes four proton translocations: two protons are required for the reduction of one quinone to a quinol and two protons are released to the P side. Complex IV (cytochrome c oxidase), the terminal complex of the ETC, catalyzes the electron transfer to oxygen and pumps four protons to the P side. Structures of ETC complexes are available. However, the structure of a hyperthermophilic cytochrome bc_1 complex has not been elucidated till now. Additionally, the dimeric crystal structure of cytochrome c oxidase from bovine has been discussed controversially.

To build up a functional complex, cofactors are required. The active site of A- and B-type cytochrome c oxidases contain the high spin heme a which is synthesized by the integral membrane protein heme A synthase (HAS). HAS can form homooligomeric complexes and its oligomerization is essential for the biological function of HAS. HAS is evolutionarily conserved among prokaryotes and eukaryotes. Despite its importance, little is known about the detailed structural properties of HAS oligomers.

Summary

During my PhD studies, I focused on the cytochrome c oxidase (AaCcO), the cytochrome bc_1 complex (Aabc_1) and the heme A synthase (AaHAS) from *Aquifex aeolicus*. This organism is one of the most hyperthermophilic ones and can live at extremely high temperatures, even up to 95 °C. Respiratory chain complexes provide energy for the metabolism of organisms, and their structures have been studied extensively in the past few years. However, there has been a lack of atomic structures of complexes from hyperthermophilic and ancient bacteria, so little is known about the mechanism of these macromolecular machines under hyperthermophilic conditions. Therefore, my PhD studies had four main objectives: 1) to structurally and functionally characterize AaCcO, 2) to reveal the mechanism of Aabc_1 thermal stability based on its structure, 3) to determine the oligomerization of AaHAS, 4) to provide valuable insights into the relationship between function and oligomerization of AaHAS.

1) Structure of AaCcO

Heme-copper oxidases (HCOs) catalyze the oxygen reduction reaction being the terminal enzymes in the plasma membranes in many prokaryotes or of the aerobic respiratory chain in the inner mitochondrial membrane. By coupling this exothermic reaction to proton pumping across the membrane to the P side, they contribute to the establishment of an electrochemical proton gradient. The energy in the proton electrochemical proton gradient is used by the ATP synthase to generate ATP. HCOs are classified into three major families: A, B and C, based on phylogenetic comparisons. The well-studied aa_3-type cytochrome c oxidase from *Paracoccus denitrificans* (*P. denitrificans*) represents A-family HCOs. So far, the only available structure of the ba_3-type cytochrome c oxidase from *Thermus thermophilus* represents the B-family of HCOs. This family contains a number of bacterial and archaeal oxidases. The C-family contains only cbb_3-type cytochrome c oxidases.

The AaCcO is one of the ba_3-type cytochrome c oxidases. Based on the genomic DNA sequence analysis, it has been revealed that *A. aeolicus* possesses two operons coding for cytochrome c oxidases (two different subunit I genes, two different subunit II genes and one subunit III gene). So far, only subunits CoxB2 and CoxA2 were identified. The

presence of the additional subunit IIa was reported in 2012. Moreover, a previous paper reported that AaCcO can use horse heart cytochrome c and decylubiquinol as electron donors and the typical cytochrome c oxidase inhibitor cyanide does not block the reaction completely.

In the course of my PhD studies, I performed heterologous expression of AaCcO in *Pseudomonas stutzeri* (*P. stutzeri*) and co-expression with AsHAS in *Escherichia coli*, respectively. The subcomplex CoxA2 and CoxB2 can be purified from *P. stutzeri*, however, it lacks heme A. Additionally, a protocol for the heterologous production of cytochrome c_{555} from *A. aeolicus* was established. In parallel, I also purified the AaCcO from native membranes according to previously reported methods with some modifications. The activity of AaCcO with its native substrate, cytochrome c_{555}, was 14 times higher than with horse heart cytochrome c.

To enable a detailed investigation and comparison of AaCcO and other cytochrome c oxidases, the cryo-EM structure of AaCcO was determined to 3.4 Å resolution. It shows that the three subunits CoxA2, CoxB2, and IIa are tightly bound together to form a dimer in the membrane. Surprisingly, CoxA2 contains two additional TMHs (TMH13 and TMH14) to enhance the protein stability. The cofactors heme a_3, heme b, Cu$_A$ and Cu$_B$ are also identified. Interestingly, two molecules of 1,4-naphthoquinone and cardiolipin were observed in the dimer interface. Based on the structure analysis, the AaCcO possesses only the K-pathway for proton delivery to the active site and proton pumping.

2) Structure of Aabc_1

The cytochrome bc_1 complex plays a key role in the catalysis of the electron transfer from quinol to cytochrome c and proton transfer across the membrane according to the "Q-cycle" mechanism. Up to date, various structures of cytochrome bc_1 complexes from vertebrates, yeast, α-proteobacteria are available. They have provided many details to understand the structural composition and the catalytic mechanism. The subunit composition of this complex varies among species but the three core subunits are always present, including cytochrome b (cyt. b) with cofactors heme b_L and heme b_H, cytochrome c_1 (cyt. c_1) with cofactor heme c_1, and the Rieske iron-sulfur protein

Summary

(ISP) with the cofactor [Fe_2S_2]. Each cytochrome bc_1 complex contains two quinol binding sites, the oxidation site Q_o and the reduction site Q_i, which are used as drug targets to design site-specific inhibitors. However, all known structures of the cytochrome bc_1 complexes are derived from mesophilic species. There is no structure available from thermophiles, which hinders us to study its unique thermal stability to maintain the electron transfer reaction under extreme conditions.

As one of the most thermophilic bacteria known, *A. aeolicus* belongs to the oldest species of bacteria. It grows in hydrothermal environments at land and in oceans throughout the world, like hot composts or deep gold mines. *A. aeolicus* is recognized as the representative organism not only of the *Aquifex* genus, but also of the *Aquificaceae* family and the order *Aquificales*. Interestingly, its cytochrome bc_1 complex uses a special substrate, a 1,4-naphthoquinol, for electron transport, which is formed by electron transfer from hydrogen in previous reactions.

During my PhD studies, I purified the cytochrome bc_1 complex (respiratory complex III) of *A. aeolicus* and performed single particle cryo-EM trials leading to the structure determination of its apo and inhibitory structures at 3.3 Å resolution. The structural analysis revealed that the three core subunits of cytochrome *b* (cyt. *b*), cytochrome c_1 (cyt. c_1) and the Rieske iron-sulfur protein (ISP) are tightly bound together to form a dimer in the membrane. Their cofactors and unique substrates of 1,4-naphthoquinones in the Q_i sites are involved in the Q-cycle reactions.

According to the sequence alignment, several unique residues are conserved in thermophilic bacteria but not in mesophilic species. In the cyt. *b* subunit, these thermophilic-specific residues include Tyr 38, Tyr 61, Phe 83 and Arg 222. The carboxyl groups of heme b_H are further stabilized by the interaction with Tyr 38. The phenolic hydroxyl of Tyr 61 in TMH1 of one protomer binds to the nitrogen atom of Arg 197 in TMH4 of another protomer, to enhance the interactions between two cyt. *b* protomers. The interaction of Tyr 61 and Val 31 in TMH1 of the ISP subunit enhances the interactions between these two subunits in the complex. Phe 83 of the cyt. *b* subunit may help to enhance the exchange of quinones and quinols between the cytochrome bc_1

complex and the Q-pool in the membrane by hydrophobic interactions with the benzene ring of 1,4-naphthoquinone. Arg 222 could help 1,4-naphthoquinone to stay at the center of the Q_i site, to form a preferential orientation and distance to the heme b_H cofactor.

Moreover, an extra transmembrane helix at the N-terminus of the cyt. c_1 subunit is found to largely enhance the interaction between cyt. b and cyt. c_1 subunits and to bind a phospholipid molecule to stabilize the complex in the membrane. These results provide the structural basis for the hyperstability of the cytochrome bc_1 complex in an extreme thermal environment.

3) Oligomerization of AaHAS

The integral membrane protein HAS catalyzes the biosynthesis of heme A that is a prerequisite for cellular respiration in a wide range of aerobic organisms. HAS catalyzes the biosynthesis of heme A from heme O in three sequential steps: (i) a monohydroxylated heme O (heme I) is produced by oxygenation of the C8 methyl group on pyrrole ring D of heme O, (ii) heme I is further oxidized to a dihydroxylated intermediate, (iii) spontaneous dehydration of the geminal diol produces the C8 aldehyde substituent of heme A. Previous studies have revealed that HAS can form homooligomeric complexes, and this oligomerization is essential for the biological function of HAS and is evolutionarily conserved among prokaryotes and eukaryotes. Despite its importance, little is known about the detailed structural properties of HAS oligomers. To analyze the oligomeric state of HAS from AaHAS a combination of different techniques was used, including size-exclusion chromatography coupled to multi-angle light scattering (SEC-MALS), cross-linking, laser-induced liquid beam ion desorption mass spectrometry (LILBID-MS) and single-particle cryo-electron microscopy (cryo-EM). Our results show for the first time that HAS forms a thermostable trimeric complex.

4) Structure of AaHAS

So far, only a crystal structure of a HAS monomer was reported. However, all characterization data from bacteria to mitochondria suggest that oligomerization of

Summary

HAS is important for its function and C*c*O assembly. The oligomeric structure of HAS, its reaction mechanism and the role of oligomerization remained unknown. AaHAS is an integral membrane protein and its molecular mass is only 33.34 kDa which is a big challenge for getting a high resolution cryo-EM structure. This major limitation was addressed with varying the sample preparation. In this thesis, a framework for purification and structural characterization of AaHAS is described. Firstly, the full-length protein was purified in detergent micelles and subjected to extensive crystallization trials. As the best crystals diffracted only up to 9 Å, the protein was reconstituted into nanodiscs and subsequently used for the cryo-EM studies. This approach led to the structure determination of AaHAS at an overall 2.8 Å resolution as a C3-symmetric trimer. The N-terminal four-helix bundle is for substrate heme O binding and the other four-helix bundle at the C-terminus is responsible for binding the cofactor heme B. Hydrophobic interactions between the C-terminal four-helix bundles of AaHAS generate a compact three-blade propeller-shaped trimer. Three molecules of the polar lipid phosphatidylglycerol (PG) were identified in the monomer. Tyr 211 in TMH6 strongly interacts with Arg 137 on ECL2 from another monomer via PG. Comparing to the previously published monomeric crystal HAS structure, we found that the TMH4 is kinked outwards and the substrate heme binding site is expanded. The AaHAS trimer architecture provides mechanistic insights into the substrate free state and provides valuable insights into the relationship between function and oligomerization.

In conclusion, this PhD work led to the cryo-EM structure determination of the dimeric *ba*₃-type AaC*c*O and the cytochrome *bc*₁ complex from the hyperthermophilic bacterium *A. aeolicus*. The latter one reveals the mechanism of its thermal stability. Moreover, AaHAS is a trimer and its cryo-EM structure reveals the roles of its oligomerization for binding the substrate heme O. This approach may be broadly applicable to understand the electron transfer chain.

Abbreviations and Symbols

The abbreviations used in this work are listed in the following table

1 Chemical abbreviations.

ADP	adenosine-5′-diphosphate
AP	alkaline phosphatase
APS	ammonium persulfate
ATP	adenosine-5′-triphosphate
BCA	bicinchoninic acid
BCIP	5-bromo-4-chloro-indolyl-phosphatase
ddH$_2$O	double-distilled water (=Milli-Q ultrapure water, Millipore)
dNTP	deoxyribonucleotide triphosphate
DDM (=LM)	n-dodecyl-β-D-maltoside
DMSO	dimethyl sulfoxide
DMF	*N,N*-dimethylformamide
DM	n-decyl-β-D-maltoside
DNA	deoxyribonucleic acid
EDTA	ethylendiaminetetracetic acid
EtBr	ethidium bromide
EtOH	ethanol
HABA	2-(4'-hydroxy-benzeneazo)-benzoic acid
HEPES	4-(2-hydroxyethyl)-piperazine-1-ethanesulfonic acid
IPTG	isopropyl β-D-1-thiogalactopyranoside
β-ME	2-mercaptoethanol
MOPS	3-(*N*-morpholino)-propanesulfonic acid
NADH	nicotinamide adenine dinucleotide
NBT	nitro blue tetrazolium
Ni-NTA	nickel nitrilotriacetic acid
PVDF	polyvinylidene difluoride
SDS	sodium dodecyl sulfate
TEMED	*N,N,N',N'*-tetramethylethylenediamine
TMBZ	3,3',5,5'-tetramethylbenzidine
TMPD	*N,N,N',N'*-tetramethyl-*p*-phenylenediamine
Tris	tris-hydroxymethyl-aminomethane

2 Biomolecules and non-chemicals

AOX	alternative oxidase
BN	blue-native
C*c*O	cytochrome *c* oxidase
CMC	critical micelle concentration

Abbreviations and Symbols

Cryo-EM	Electron cryomicroscopy
CV	column volume
Cyt	cytochrome
DNase	deoxyribonuclease
HAS	heme A synthase
HCO	heme-copper oxidase
HPLC	high-performance liquid chromatography
IMAC	immobilized-metal affinity chromatography
IEC	ion exclusion chromatography
ISP	iron sulfur protein
LILBID-MS	laser induced liquid beam ion desorption mass spectrometry
MALDI	matrix-assisted laser desorption/ionization
MS	mass spectroscopy
NanoDSF	nano differential scanning fluorimetry
NOR	nitric oxide reductase
OD	optical density
RCF ($\times g$)	relative centrifugal force
PAGE	polyacrylamide gel electrophoresis
PCR	polymerase chain reaction
PDB	protein data bank
pI	isoelectronic point
r.m.s.d.	root-mean-square deviation
SEC	size exclusion chromatography
SEC-MALS	size exclusion chromatography combined with multiangle light scattering
QOX	quinol oxidase
Rev	reverse (primer design)
Tm	transition temperature
TMH	transmembrane helix
TOF	time-of-flight
UQ	oxidized form of quinone
UQH2	reduced form of quinone, also hydroquinone or quinol
UV/Vis	ultraviolet/visible
WT	wild type

3 Symbols for measures and units

3D	three-dimensional
Å	angstrom
bp	base pair(s)
°C	degrees celsius
Da	dalton
h	hour

Abbreviations and Symbols

L	liter
M	molar
Min	minute
Rpm	rotations per minute
V	volt
v/v	volume/volume
w/v	weight/volume
w/w	weight/weight
Σ	standard deviation

1 Introduction

All living organisms are open systems that need energy to keep a highly ordered state. Phototrophs get light energy from the sun, chemotrophs capture energy by oxidizing chemical compounds. The universal energy carrier of the cell is adenosine-5'-triphosphate (ATP). During the catabolic processes, light or chemical energy is converted into an electrochemical gradient across membranes which can be used by the ATP synthase to generate ATP from ADP (1). At the same time, electron transfer is coupled to the proton (ion) translocation across the mitochondrial inner membrane or the bacterial cytoplasmic membrane.

1.1 The electron transport chain

The electron transport chain (ETC), also known as respiratory chain (Figure 1-1), consists of four membrane-embedded protein complexes (complex I-IV) in mitochondria (2). The electrons are transferred from the initial donor (a reduced compound) to low a redox potential acceptor (-320 mV for $NADH/NAD^+$) and then through the ETC finally to the high redox potential acceptors (+815 mV for O_2/H_2O). Throughout these steps, cells can maximize conservation of chemical energy and minimize heat dissipation. Electron transport between those four protein complexes is mediated by two mobile electron carriers: ubiquinone and cytochrome c.

The ECT is embedded in the phospholipid membrane of mitochondria and many bacteria. Complex I, complex III and complex IV have a proton-pumping activity.

Complex I (NADH: ubiquinone oxidoreductase) is one of the electron entry points into the ETC of eukaryotes and bacteria (3). It catalyzes the electron transfer from NADH to quinone. During the reduction, two electrons from NADH are transferred through flavin mononucleotide (FMN) and multiple iron-sulfur clusters to the quinone (4). The electron transport is coupled to the translocation of 4 protons across the inner mitochondrial membrane or the cytoplasmic membrane of bacteria (5). Through that

process, a transmembrane electrochemical potential difference of protons is generated. Complex I is the largest enzyme in the ETC and comprised of up to 46 subunits with a molecular weight of about 1,000 kDa (6). Seven core subunits form the membrane domain, and 6-7 core subunits form an extramembrane domain containing all the redox-active cofactors (7). So far, the structures of the whole complex I from *T. thermophilus* (8) and *Bos taurus* (*B. taurus*) (9) have become available. Complex I is moreover believed to be the major producer of reactive oxygen species in cells, and it is therefore relevant for understanding processes such as aging and cancer formation (10,11).
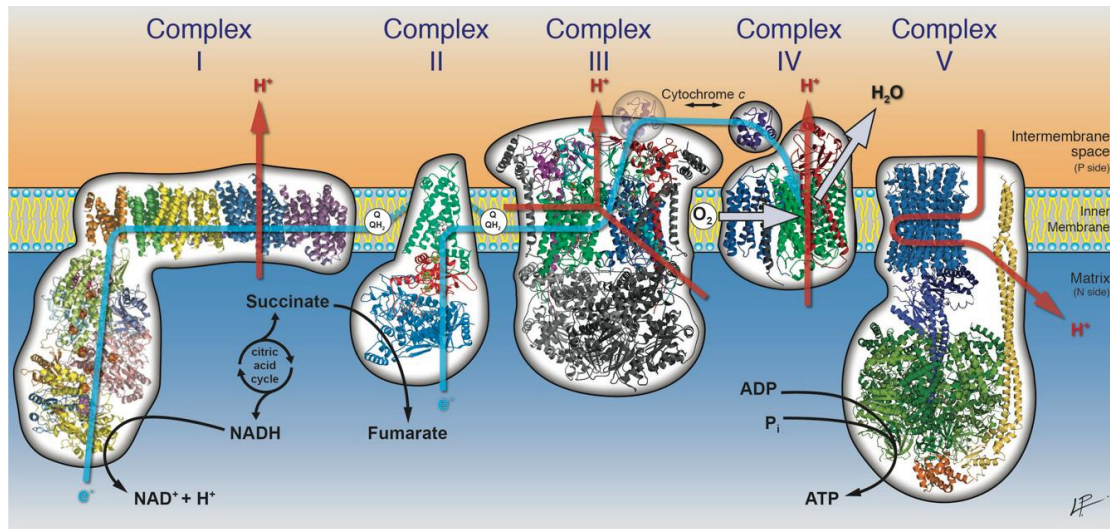
Figure 1-1: Schematic diagram of the mitochondrial electron transport chain. The electron transport chain is composed of four redox-active membrane protein complexes (complex I-IV) that transfer electrons to the ultimate electron acceptor, molecular oxygen. Complex I (NADH:quinone oxidoreductase) oxidizes NADH to NAD$^+$ and reduces quinone (Q) to quinol (QH$_2$). Complex II (succinate:quinone oxidoreductase) oxidizes succinate, which is a product of the citric acid cycle, to fumarate and reduces Q to QH$_2$. There is no proton pumping during this reaction. Complex III (quinol:cytochrome *c* oxidoreductase) transfers electrons from QH$_2$ to cytochrome *c*. Complex IV (cytochrome *c* oxidase) transfers electrons from cytochrome *c* to the final electron acceptor, molecular oxygen (O$_2$), to produce water. Electron flow and proton pumping are shown as blue and red arrows, respectively. The generated electrochemical gradient can be utilized by F$_O$F$_1$-ATP synthase (complex V) to generate ATP. Structural representation of complex I-IV was generated using PDB entries 3M9S, 1NEK, 3CX5 and 1QLE, respectively. This figure was kindly provided by Paolo Lastrico (MPI of Biophysics, Frankfurt am Main).

Complex II (succinate-ubiquinone oxidoreductase or succinate dehydrogenase) can act as the second electron entry point into the ETC. However, complex II has no proton-pumping activity (12). It is also a component of the citric acid cycle, and bound to the inner mitochondrial membrane due to the membrane location of its electron acceptor

ubiquinone (13).

Complex III (cytochrome bc_1 complex or ubiquinol:cytochrome c oxidoreductase) is structurally related to the cytochrome b_6f complex that mediates the electron transfer between photosystem II and photosystem I (14). A unique feature of complex III is the bifurcation of the electron transfer upon ubiquinol oxidation (15). According to the Q-cycle mechanism, ubiquinol undergoes a two-cycle oxidation, in which two separate active sites (Q_0 for the oxidation of ubiquinol, Q_i for reduction of ubiquinone) are involved. Two protons are released to the outside upon ubiquinol oxidation at the Q_0-site. Two protons are taken up from the inner side upon the ubiquinone reduction at the Q_i-site. After a cycle, complex III can get four electrons from ubiquinol. Two electrons are transferred to Rieske center and then via cytochrome c_1 to the final electron acceptor cytochrome c. The other two electrons are transferred to the high potential heme b_H though low potential heme b_L, where one ubiquinol is regenerated by a two-step reduction and protonation of ubiquinone (16). By coupling the reduction of cytochrome c and deprotonation of ubiquinol, protons are translocated across the membrane to the positive side. The stoichiometry is thermodynamically equivalent to 2 H^+/2 e^- (5).

Complex IV (cytochrome c oxidase) is the terminal enzyme in the ETC. It catalyzes the reduction of molecular oxygen (O_2) accompanied by proton pumping. Since it was found in 1924, its mechanism of its action has been one of the most important subjects in bioinorganic chemistry (17). The overall reaction can be described as following:

$$4 \text{ cyt.}c^{2+} + (n+4) \text{ H}_N^+ + O_2 \rightarrow 4 \text{ cyt.}c^{3+} + n \text{ H}_P^+ + 2 \text{ H}_2O$$
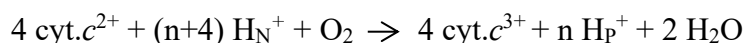
It catalyzes the electron transfer from the reduced cytochrome c to the O_2 which diffuses through the membrane to the active site as the electron sink. During this process, the reduced cytochrome c, which is located in the intermembrane space of mitochondrial matrix or in the bacterial periplasmic space (P side), subsequently supply four electrons. At the same time, eight protons are taken from the mitochondrial matrix or bacterial cytoplasm (N side). All these results suggest that the stoichiometry is thermodynamically equivalent to 4 H^+/2 e^- (18-20).

Heme A is the essential cofactor for cytochrome a-containing respiratory oxidases in mitochondria, plants and many aerobic microbes. Heme A synthase catalyzes the

production of heme A from heme O (21) and, additionally, plays a role in the cytochrome c oxidase assembly, which is not dependent on the function as heme A synthase (22). Despite its physiological importance, the reaction mechanism of the integral membrane protein heme A synthase is poorly understood.

This work focus on complex III, IV and heme A synthase. More details about these enzymes are presented in the following sections.

1.2 Heme-copper terminal oxidases

1.2.1 Classification of heme-copper terminal oxidases

Heme-copper oxidases (HCOs), the terminal enzymes of the respiration chain, catalyze the reduction of molecular oxygen (O_2) to water. This reaction is coupled to proton translocation across the membrane and contributes to the energy conversation. HCOs are quite diverse in terms of subunit composition, heme type, electron donor and proton pathways (23-25). HCOs are generally subdivided into two main groups based on their electron donors, the quinol oxidases (QOXs) and cytochrome c oxidases (CcOs or COX). One major difference between QOXs and CcOs is the electron pathway. In CcOs, electrons are first transferred from cytochrome c to the Cu_A metal center of subunit II, and subsequently transferred to the binuclear center. QOXs lack the Cu_A metal center in the hydrophilic domain of subunit II and electrons are transferred directly from ubiquinol to the oxygen.

HCOs are characterized by the presence of a transmembrane catalytic subunit, which has a low-spin heme and a binuclear center composed of a high-spin heme and Cu_B. The three cofactors are coordinated by six conserved histidine residues. According to the structure of the proton pathways and the types of heme, HCOs are classified into three families, A-family (mitochondrial-like oxidase), B-family (ba_3-like oxidase) and C-family (cbb_3-like oxidases) (26,27).

The A family CcOs are found in mitochondria and many bacteria. They contain at least two proton pathways, the D-and K-pathways. It has been shown that D-pathway is used

for transfer of both pumped and substrate protons, whereas the K-pathway is used only for the uptake of substrate protons during the initial reductions (28). Based on the presence or absence of a conserved glutamate residue in the D-pathway, the A-family can be further divided into A1- and A2-type (29). In A1-type C*c*Os, the D-pathway contains several hydrophilic residues ending at Glu 278 in *P. denitrificans* (30,31). In the A2-type C*c*Os, this glutamate residue is replaced by a tyrosine residue. The proton-pumping stoichiometry was determined to be 1.0 H^+/e^- in both A1- and A2-type family (32,33)

The B-family C*c*Os is represented by the C*c*O from *T. thermophilus.* B-family C*c*Os have only one proton pathway (K-pathway analog) (34). It is used for the transfer of both substrate and pumped protons, and a reduced proton-pumping stoichiometry of 0.5 H^+/e^- was determined (35). It has been reported that B-family C*c*Os can reduce nitric oxide (NO) and nitrous oxide (N_2O) at low levels (36).

The C-family only comprises the *cbb3*-C*c*Os and lacks the D-pathway. This family has a distinctly different subunit composition and redox centers (37). The proton-pumping stoichiometry of *cbb3*-C*c*Os is 0.5 H^+/e^- (38).

The differences between C*c*Os families are listed in table 1-1. Nitric oxide reductases (NORs) share structural similarities with HCOs. They are considered to be included in the HCOs superfamily.

Table 1-1: Diversity in HCOs

	Family name			
	A1	A2	B	C
High spin heme	A(O)[1]	A	A	B
Low spin heme	A(B)[1]	A	B	B
Proton pathway	D, K (H)[2]	D, K	K	K
Intial electron entry site	Cu_A (Q)[3]	Cu_A	Cu_A	Heme *c*
The proton pumping efficiency (H^+/e^-)	1	1	0.5	0.5

[1] *bo3*-type ubiquinol oxidase. [2] Mitochondrial cytochrome *c* oxidase. [3]Ubiquinol oxidase has Q-binding site.

1.2.2 Structure of heme-copper terminal oxidases

To understand the catalytic mechanism of C*c*Os, the determination of the protein structure is needed. So far, crystal structures of all types of HCOs have become available.

The structure of *aa*$_3$-C*c*O from *P. denitrificans* was determined at 2.8 Å resolution in 1995 (39). Afterwards, the metal center structure of bovine C*c*O was reported (40) and followed by the whole structure of the mitochondrial *aa*$_3$-C*c*O (41). Since then, several high-resolution structures from different organisms have been reported (42-44). The *aa*$_3$-C*c*O from *P. denitrificans* has four redox-active metal sites, designated as Cu$_A$, heme *a*, Cu$_B$, and heme *a*$_3$ (Figure 1-2A). It has four subunits. Subunit I has twelve transmembrane helices (TMHs) and three redox active metal sites, heme *a*, heme *a*$_3$ and Cu$_B$. There are two additional metal centers (Mg^{2+}/Mn^{2+} and Ca^{2+}). Previous work suggested that the Mg^{2+} (or Mn^{2+}) center may be involved in water exit from the reaction center and in the proton pumping (45), whereas the function of the Ca^{2+} is not clear (46).

Subunit II has two TMHs and a C-terminal hydrophilic domain, which is located on the P side of the membrane. It has the dinuclear Cu$_A$ site, which functions as the primary electron acceptor receiving electrons from cytochrome *c* and transferring them to the heme *a*. Trp 121 and Tyr 122 on subunit II of *aa*$_3$-C*c*O from *P. denitrificans* are reported to play roles in forming the transient complex with cytochrome *c* (47,48).

Subunit III and subunit IV do not have a reactive site. Subunit III has seven TMHs which are divided by a large V-shaped cleft into two bundles (39). Subunit III has been suggested to play roles as proton antenna used by the D-pathway and to help the *aa*$_3$-type C*c*O to adapt different physiological environments (49). Subunit III may also be involved in the stabilization of the whole enzyme. Deletion of the subunit IV dose not affect the stability or activity of the enzyme (50).

In the A2 family, an X-ray structure has been reported only for the *caa*$_3$-type C*c*O from *T. thermophilus* at 2.36 Å resolution (Figure 1-2B) (51). The *caa*$_3$-oxidase contains three subunits, subunit I/III, subunit IIC and subunit IV. Subunit I/III is a fusion

of the canonical, subunits I and II, while subunit IIC is a fusion of the classical subunit II and a cytochrome c domain (52). Subunit IV has two TMHs. The overall structure of caa_3-CcO is similar to that of aa_3-CcO. However, in caa_3-type CcO, the heme a is replaced by heme a_s, which has a hydroxygeranylgeranyl tail. Subunit I/III contains the D- and K-pathways for proton transfer from the cytoplasmic space to the O_2-reduction site.

The B-family HCOs are represented by the ba_3-CcO from *T. thermophilus* (53). The X-ray structure in the fully oxidized state has been reported at 1.8 Å resolution (54). The structure resembles the structure of the two-subunit aa_3-CcO from *P. denitrificans* and *Rhodobacter sphaeroides* (*R. sphaeroides*) (Figure 1-2 C). Members of this family have only one proton pathway (K-pathway), its location is similar to the K-pathway of A-family HCOs but shows no sequence similarity (34). Subunit II has only one TMH, while subunit IIa replaces the missing TMH of the canonical subunit II, suggesting a critical role of subunit IIa (53). The *T. thermophilus* ba_3-CcO contains heme a_{s3} instead of heme a_3. Furthermore, the efficiency of energy coupling in B-family CcOs ($H^+/e^- = 0.5$) is lower than that of A-famliy CcOs ($H^+/e^- = 1$) (55).

The C family contains only cbb_3-type CcOs. Compared to CcOs from other family, cbb_3- CcOs have a different subunit composition. The canonical cbb_3-CcO is composed of the central subunit N, subunit O, P and a small membrane-spanning subunit Q. In 2010, an X-ray structure of the cbb_3-CcO from *P. stutzeri* has been determined at 3.2 Å resolution (37). Subunit N contains twelve TMHs, a low-spin heme b and a binuclear center formed by a high spin heme b_3 and a copper (Cu_B) ion (56). Subunit O has only one TMH and is a membrane anchored mono c-type cytochrome, which is covalently linked to a low spin heme c. Subunit N and O together are defined as the core complex (57). Subunit P has two TMHs and a C-terminal globular domain. Subunit Q was not observed in the structure. The smallest subunit Q, has one TMH with a hydrophilic stretch at the C-terminus protruding into the cytoplasm. Only K-pathway is found in the C-family CcOs (58).
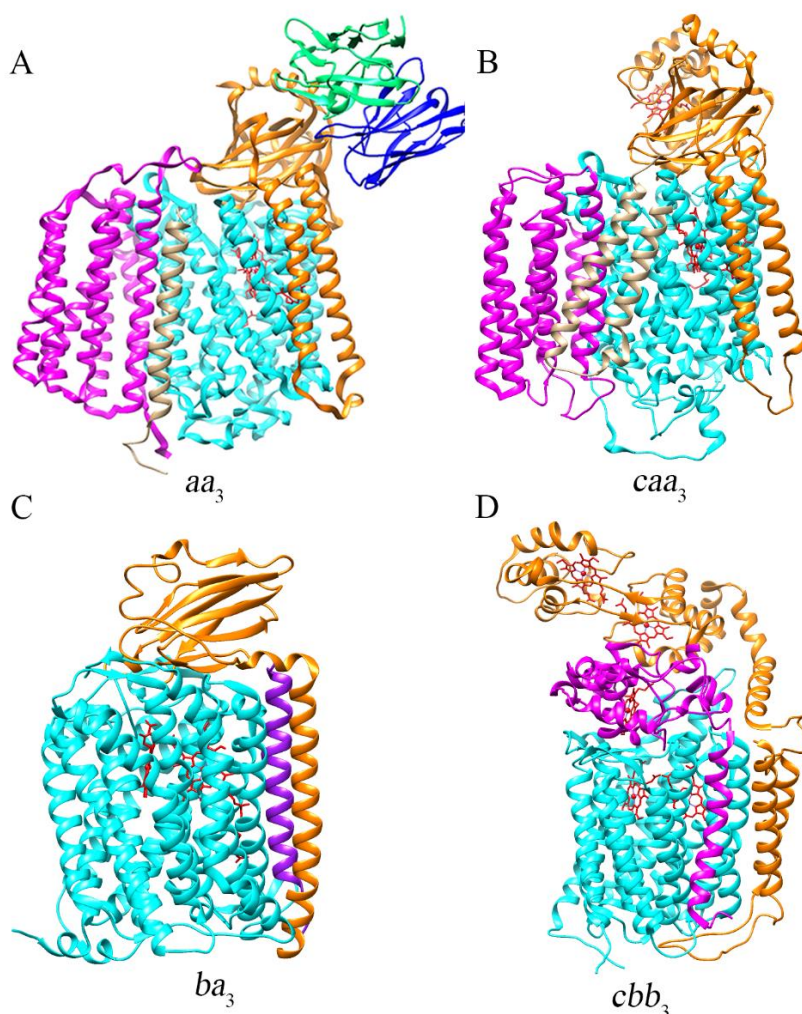
Figure 1-2: X-ray structures of HCOs. (A) aa_3-CcO from *P. denitrificans* (1QLE); (B) caa_3-CcO from *T. thermophilus* (2YEV); (C) ba_3-CcO from *T. thermophilus* (1XME); (D) cbb_3-CcO from *P. stutzeri* (3MK7). The catalytic subunit I, subunit II and subunit III are shown in cyan, orange and magenta, respectively. The catalytic subunit of caa_3-CcO is a fusion of a canonical subunit I and subunit III. The subunit IIa of ba_3-CcO is shown in purple. Hemes are represented as red sticks. 3D structural images were generated using the Chimera software.

According to the electron donors, NORs can be divided into two major groups cytochrome c dependent (cNOR) (Figure 1-3A) and quinol dependent NOR (qNOR) (Figure 1-3B). The cNOR has a large NorB subunit, which shows strong homology to the subunit I of all CcOs, and a small NorC subunit (59). The subunit NorB contains 12 TMHs, two b-type hemes and an Fe$_B$ center. Subunit NorC which contains a heme c has only one TMH. Neither D- nor the K- pathway was observed in cNOR (59).

The structure of qNOR is similar to that of cNOR (27). It is a single subunit enzyme consisting of 14 TMHs and an α-helical hydrophilic domain. The qNOR has a potential

hydrophilic channel translocating protons to the active site from the cytoplasm (60).
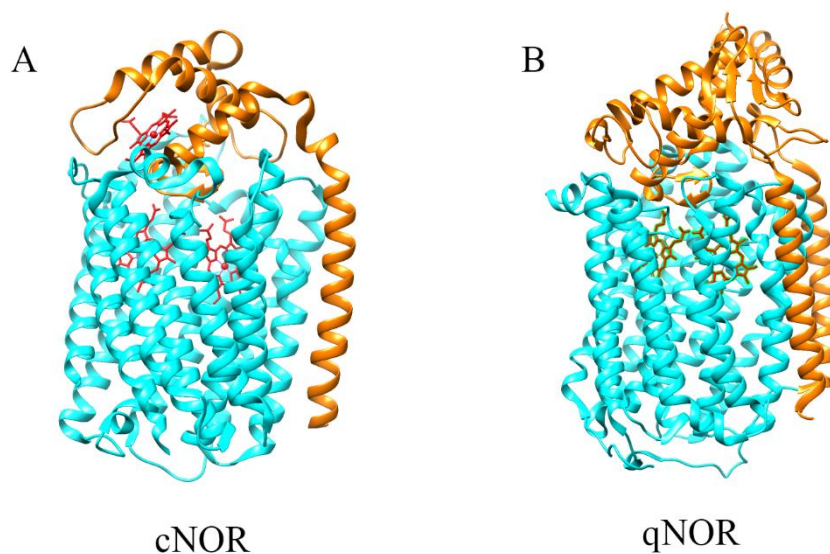
Figure 1-3: The structure of NORs. (A) cNOR from *Pseudomonas aeruginosa* (3O0R). (B) qNOR from *Geobacillus stearothermophilus* (3AYF). Hemes are represented as red sticks. 3D structural images were generated using the Chimera software.

1.2.3 Major function of cytochrome *c* oxidase

An introduction to the catalytic cycle, electron transfer process and the proton pumping of aa_3-CcO from *P. denitrificans* is given in the following section.

The reaction cycle of C*c*O can be divided into two parts (Figure 1-4): one is the binding and reduction of O_2 (oxidative phase) and the other is the rereduction of the binuclear center (reductive phase). During the catalytic cycle, the binuclear center undergoes different redox state changes. In 1981, the existence of the P (peroxy) and F (ferryl) states was reported (61). As the investigation of proton pumping, a first model of the reaction cycle was established, in which proton pumping only occurs during the oxidative phase (62). This model suggested that there is no proton pumping coupled to the first two electron transfer steps. With consideration of the electroneutrality principle (63), Michel proposed a modified model (64). This model suggests that each of the four electron transfer steps in the catalytic cycle is coupled to the proton pumping.

In the O state, both metal ions are oxidized and in a ferric/cupric state. Based on the presence of a continuous electron density between both metal ions in the crystal

structure of aa_3-CcO from *Paracoccus* (42), it was proposed that Fe^{3+} and Cu_B^{2+} are bridged by a water molecular and a hydroxide ion (state O) (64).The first electron arrives in the binuclear center and Cu_B^{2+} is reduced to Cu_B^+ (E state). After receiving a second electron, heme a_3 is reduced, and the state R is formed. When the molecular O_2 binds to the binuclear center, the state R transits to state A. The results of resonance Raman spectroscopy confirmed the presence of a ferrous-oxy adduct in this state (65). During the binding of O_2 to the heme a_3 iron, two water molecules are released. The P state was originally proposed to be a peroxy intermediate (61). However, the P state was found to be an oxyferryl state ($Fe^{4+}=O^{2-}$) with a hydroxide ion bound to Cu_B^+, which was revealed by resonance Raman spectroscopy (66). This process needs four electrons and a proton. Two electrons are provided by heme a_3 and one is derived from Cu_B^+. The fourth electron equivalent and one proton are thought to be donated by the nearby Tyr 280, yielding a tyrosine radical (67). The F state is formed by the transfer of a third electron from reduced cytochrome c to the active center, which reduces the tyrosine radical. During the last step of the catalytic cycle, the active center receives the fourth electron and changes to the state O, which is accompanied by proton pumping (68).
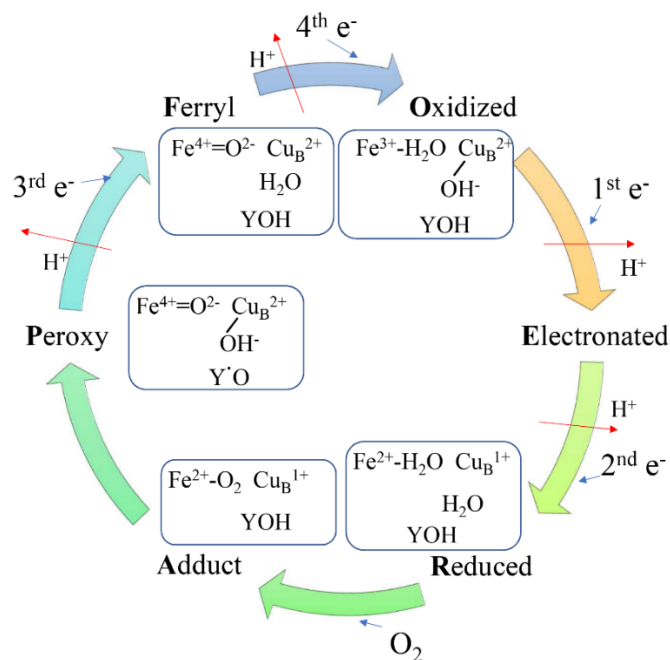
Figure 1-4: A catalytic cycle of cytochrome c oxidase. The rectangle represents the binuclear heme-copper center. The blue and red arrows indicate the electron input from the cytochromes c to the active site and the proton pumping, respectively. A dot represents the tyrosine radical in the "peroxy" state (also

called P_M state). This Figure is drawn based on the reaction mechanism proposed by Michel and modified from von der Hocht *et al.*, 2011.

One of the major roles of C*c*O is to reduce molecular O_2 to water for which four electrons are reguired. The electrons are transferred from cytochrome *c* one at a time to the electron accepter Cu_A. The rate-limiting step is the formation and dissociation of the cytochrome *c* and the C*c*O complex (69). The interaction between the C*c*O and cytochrome *c* oxidase has been described to follow a two-step model (48,70). The first step is to get two proteins together, which is controlled by electrostatic interactions. Subunit II has a set of acidic residues on the surface of its hydrophilic domain. It has been indicated by site directed mutagenesis studies that these acidic residues are involved in the initial docking (47). The second step is controlled by hydrophobic interactions, which optimizes the interactive geometry between both redox partners (47). Once a stable complex is formed, the electron is transferred from cytochrome *c* to Cu_A, with a time constant of ~15 µs (71).

Subsequently, the electron is transferred to the low spin heme *a*. It has been shown that this process occurs with a time constant of ~10 µs in bacterial C*c*Os (28,72). In the next stage, the electron is transferred from heme *a* to heme a_3, with a time constant of ~3 µs (73). Finally, the electron is transferred from heme a_3 to Cu_B, which is coupled to proton translocation, with a time constant of several hundreds of microseconds (74).

In the ba_3-C*c*O, the existence of a second electron transfer pathway was suggested by Soulimane et al. (53). It was suggested that electrons could be transferred from Cu_A to Cu_B via the aromatic rings of several amino acids (Figure 1-5).
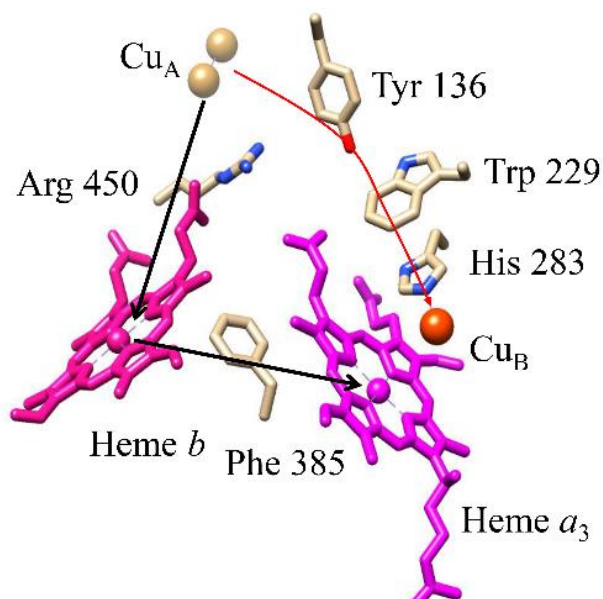
Figure 1-5: Scheme of electron transfer in ba_3-CcO. The black arrows show the pathway, where electron is transferred from Cu_A via heme b to the binuclear reactive center; the red arrow shows that the electron is directly transferred from Cu_A to Cu_B.

For the mitochondrial CcO, the existence of three proton pathways has been proposed. K-, D- and H- pathways, named after key lysine, aspartate and histidine residues. D-pathway is only found in the type A CcOs, while analogues of the K-pathway are found in all CcOs- families.

The end point of the D- pathway in all A1 type CcOs is a glutamate residues near the middle of the membrane, while, in the A2 type CcOs, the end point of the D- pathway is a tyrosine (75). A single mutation of the conserved Asp 124 strongly inhibits the enzymatic activity and proton pumping (76). Including Asp 124 and Glu 242, there is a set of conserved polar residues (Asn 11, Asn 199 and Ser 193) (77). A vast amount of experimental evidences has suggested that all pumped protons and one to two chemical protons are taken up via the D-pathway (78). When Asn 131 was mutated to Asp, the enzyme still possesses oxygen-reducing activity but loses the proton translocation ability (79).

The K-pathway is found in all A-, B-, and C-type CcOs. The K-pathway leads directly to the binuclear center via the highly conserved residues Lys 354, Thr 351 and Tyr 280. It is lined by hydrophilic residues from TMH8 of subunit I in the crystal structure of aa_3-CcO from *P. denitrificans* (80). It has been suggested that at least one chemical

proton is taken up by the K-pathway in the reductive phase of the reaction cycle, which is important for the initial reduction of the metal center and subsequent oxygen binding (81).

It has been suggested, based on the crystal structure data of the mitochondrial aa_3- CcO from bovine heart, that a third proton pathway (H-pathway) is present which consists of water-filled cavities and numerous polar residues (82). However, the existence of this proton pathway has been excluded for the bacterial aa_3-CcOs, because mutations in the putative H-channel showed that there is no influence on the proton translocation (76,83).

1.3 Cytochrome bc_1 complex

The cytochrome bc_1 complex plays key roles in respiration. It is a dimeric multi-subunit complex which is located in the inner mitochondrial membrane of eukaryotes or the cytoplasmic membrane of prokaryotes. The subunit composition of the cytochrome bc_1 complex is different between species, but three core subunits are always present. The catalytic core of the cytochrome bc_1 complex is composed of cytochrome b (cyt. b) which contains the cofactors heme b_L and heme b_H, cytochrome c_1 (cyt. c_1) which contains cofactor heme c_1 and the Rieske iron-sulfur protein (ISP) containing the cofactor Fe_2S_2 (14,84-87). The function of the cytochrome bc_1 complex is to catalyze the electron transfer from quinol to cytochrome c, which couples the proton transfer across the membrane, thereby contributing to the generation of electrochemical potential (88). The "Q-cycle" mechanism was proposed to described the action of the cytochrome bc_1 complex (15,89). The presence of two quinone/quinol binding sites were confirmed by biochemical data, mutagenesis studies and localization of site-specific inhibitors (14,90-92). Quinol oxidation occurs at the Q_o site, where two protons are released to the outside upon oxidation of one ubiquinol, whereas the two electrons use two different routes. The first electron is transferred to cytochrome c_1, which is achieved by a movement of ISP. The head group of ISP can accept electrons form quinol (b-position) when it connects to cyt. b and then donates the electrons to cyt. c_1 (c-

position). Subsequently, the electron is used to reduce cytochrome c. The second electron is transferred via heme b_L to heme b_H then to the Q_i site where a quinone is reduced to a semiquinone and finally to a quinol. In addition, the cytochrome bc_1 complex can produce reactive oxygen species which trigger apoptosis in animal cells (93,94).

1.3.1   Structure of cytochrome bc_1 complex

Subunit cyt. b was identified in 1922 (95) and the method to isolate this complex was established in 1965 (96). However, it took 22 years to determine the first complete crystal structure of a cytochrome bc_1 complex. Since then, structures of the cytochrome bc_1 complex from yeast (86), *Rhodobacter capsulatus* (*R. capsulatus*) (85), *R. sphaeroides* (97) and *P. denitrificans* (98) have become available. More recently, the atomic structure of this enzyme has been determined by cryo-EM from different organisms (99-101). In the cryo-EM structure of a functional obligate complex III2IV2 respiratory supercomplex from *Mycobacterium smegmatis,* a menaquinone bound in the Q_o site was observed which was suggested previously only on the basis of inhibitor binding in crystal structures (100). In the cryo-EM structure of the yeast respiratory supercomplex, the location of subunit Qcr10 which was missing in the crystal structure of the cytochrome bc_1 complex was determined (101). The cryo-EM structure of the respiratory supercomplex not only revealed the structure of the cytochrome bc_1 complex, but also showed the interaction between different complexes (99). A detailed introduction to each core subunit is given in the following section.

Cyt. b is the central core subunit of cytochrome bc_1 complex. All determined structures of cyt. b contain 8 TMHs and the two catalytic centres heme b_L and heme b_H (Figure 1-6A). Cyt. b is composed of two bundles of 4 TMHs. The two b-type hemes are located in the N-terminal bundle. In *P. denitrificans*, heme b_L is coordinated by His 97 and His 198 and heme b_H is coordinated by His 111 and His 212. The TMH5 is close to the THM of ISP and arranges in an anti-parallel orientation to the TMH of cyt. c_1. The P-side of THM5 interacts with the head group of ISP from the other monomer. The major

differences of cyt. *b* between bacteria and mitochondria are found on the matrix side (102). There are several supernumerary subunits present at the matrix side of cyt. *b* in mitochondria, whereas the cyt. *b* from bacteria has extended N-and C-termini (98). Comparison of the N-terminal sequence of cyt. *b* from bacteria and mitochondria showed that both enzymes possess a small helix oriented towards the other monomer of cyt. *b* along the surface of the membrane. However, the small helices from both cyt. *b* monomers do not connect to each other, because there is a right-angle turn caused by a short helical stretch. Another significant difference of cyt. *b* between bacteria and mitochondria is the presence of a longer linker between TMH4 and TMH5 near the Q_i site in bacteria, whereas a shorter linker allows cyt. *b* to connect more easily to subunit 7 in mitochondria (85).

Cyt. *b* also contains the quinone binding sites Q_i and Q_o which are located on opposite sides of the membrane. The density for a quinone was only observed at the Q_i site in crystal structures of cyt. *b* (86,87), whereas the quinol binding in the Q_o site has been observed in the cryo-EM structure of cyt. *b* (100).

ISP is composed of three parts (Figure 1-6B). According to the Q-cycle mechanism, electron transfer from cyt. *b* to cyt. c_1 is achieved by movement of the ISP functional domain. In *P. denitrificans*, the functional group possesses an Fe_2S_2 cluster which coordinates to the evolutionary conserved residues His 134, His 155, Cys 132 and Cys 152 (98). The N-terminus of the ISP forms a TMH which aids in anchoring the ISP to the complex and membrane. The functional domain is connected by a hinge region which contains the ADV motif (Ala-Asp-Val). Mutations of this hinge region impair enzyme activity (103,104). Hydrophobic interactions are responsible for keeping the ISP bound to the surface of the cytochrome *bc*$_1$ complex. The interactions can be abolished by detergents (105).

Cyt. c_1 is anchored to the membrane by the C-terminal TMH. Its cofactor heme c_1 is coordinated by His and Cys residues from the CXXCH motif with Met as the sixth heme ligand (Figure 1-6C). The first structure of cyt. c_1 has been determined from chicken (87). The hydrophilic domain of cyt. c_1 is located on the P side of the membrane (85-87,90).
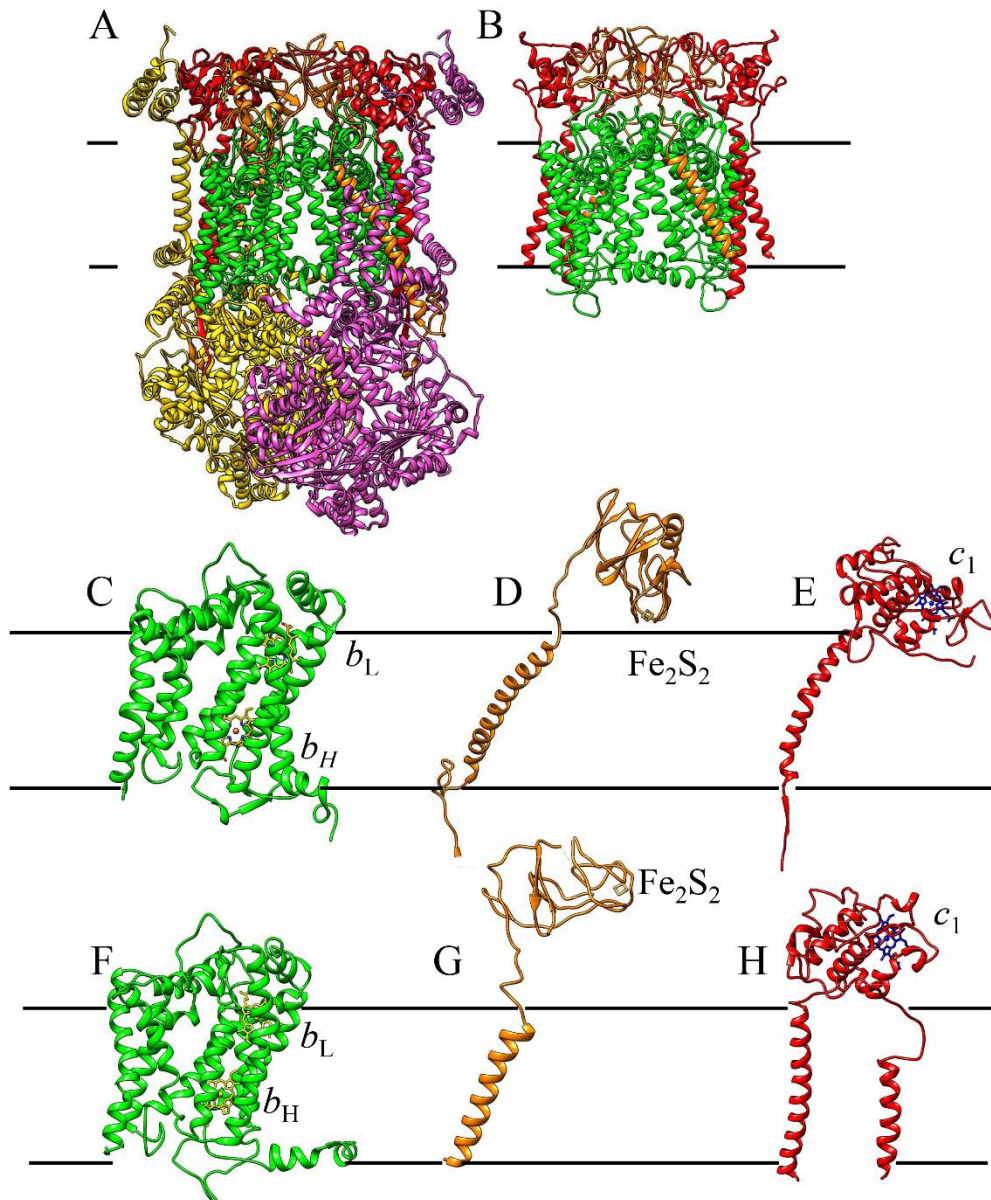
Figure 1-6: Structures of mitochondrial and bacterial cytochrome bc_1 complex in ribbon representation. Subunit of cyt. b, cyt. c_1 and ISP are indicated in green, red and orange, respectively. (A) Crystal structure of the cytochrome bc_1 complex from bovine mitochondria. (B) Cryo-EM structure of the cytochrome bc_1 complex from *A. aeolicus*. (C) Structural model of monomeric bovine cyt. b. 8 transmembrane helices are labeled. Two hemes are shown in yellow and as stick models. (D) Ribbon diagram showing the structure of ISP from the bovine complex. The Fe_2S_2 cluster is shown as stick model. (E) Ribbon presentation of the structure of bovine cyt. c_1. Heme c_1 is shown as stick models. (F) Ribbon diagram of the cryo-EM structure of *A. aeolicus* cyt. b. (G) Ribbon presentation of the structure of cryo-EM structure of *A. aeolicus* ISP. There is no extra loop at the N terminal side out of the membrane. The cofactor Fe_2S_2 is shown as a stick. (H) Ribbon diagram of the cryo-EM structure of *A. aeolicus* cyt. c_1. Both N-terminus and C-terminus are located at the negative side of the membrane. Two transmembrane helices are observed in the structure. The cofactor heme c_1 is shown as a stick model.

Atomic models of cytochrome bc_1 complexes from different organisms determined by

X-ray crystallography and cryo-EM explained the experimental results on the Q_o and Q_i binding pockets (14,86,87,90,99-101). The Q_i pocket which is located close the N side of the membrane is found near heme b_H. The pocket is surround by TMHs 1, 4, 5, the amphipathic small helix and heme b_H. The binding pocket has a hydrophilic surface outside and a hydrophobic surface in side. The conserved residues involved in quinol interaction are shown in the Figure 1-7. These residues are identified by their interaction with inhibitors and substrate at the Q_i site. The most conserved residues His 201 and Asp 228 in *B. taurus* are equivalent to Arg 221 and Glu 253 in *A. aeolicus.*
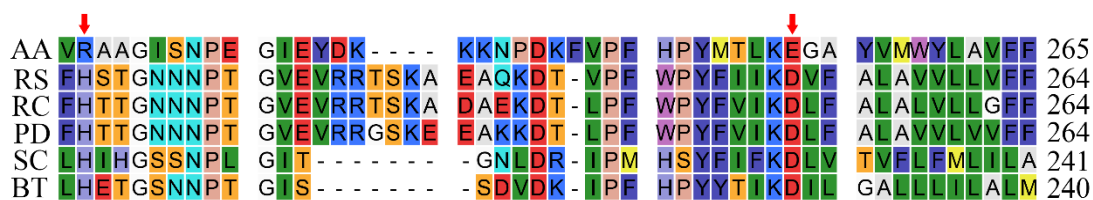
Figure 1-7: Sequence alignments of Q_i pocket residues of cyt. *b* subunits from different species: BT (*B. taurus*), SC (*S. cervisiase*), RS (*R. sphaeroides*), RC (*R. capsulatus*), PD (*P. denitrificans*) and AA (*A. aeolicus*). The conserved residues involved in quinone binding are marked by red arrows.

1.3.2   Functional mechanism of the cytochrome bc_1 complex

As described above, the cytochrome bc_1 complex catalyzes ubiquinol reduction and oxidation, which is coupled to proton transfer across the membrane and contributes to the generation of an electrochemical gradient. The mechanism of this reaction is called Q-cycle (15,89). The experimental data that the oxidant-induced cyt. *b* can be reduced in the presence of the inhibitor antimycin is in support of the Q-cycle mechanism (106,107). Later critical experiments showed that each electron transfer is coupled to two proton translocations across the membrane (108). Then the movement of iron-sulfur protein, which plays an important role in the electron transfer from ubiquinol to cytochrome c_1, was found (109). The Q-cycle was described in details in 1990 (89). The subunit composition of the cytochrome bc_1 complex is different from species to species. However, the Q-cycle mechanism is conserved (110).

The redox potentials of heme b_L, heme b_H and the iron-sulfur cluster are -190 mV, -60 mV and +210 mV, respectively (111). Normally, the redox potential of cyt. c_1 is around +260 mV (112). The reaction catalyzed by cytochrome bc_1 complex is shown in figure

1-8. As described above, one electron from the quinol which binds at the Q_o site is transferred to ISP and then to cyt. c_1. Finally, the electron is used to reduce oxidized cytochrome c. The second electron from the ubiquinol is transferred to the low spin heme b (heme b_L) then to the high spin heme b (heme b_H). It ends up at a quinone or a semiquinone anion in the Q_i site. The reduced quinol takes two protons from N side of the membrane and can be usded at the Q_o site as electron donor. After one reaction cycle, the ubiquinol is oxidized to a quinone and the two protons are released to the P side of the membrane. The enzyme catalyzes the quinone reduction at the Q_i site to a quinol which can take two protons from N side. Thus, a complete Q cycle translocates 4 protons to the P side and two molecules of quinol are used at the Q_o site and one molecule of quinol is generated at the Q_i site.
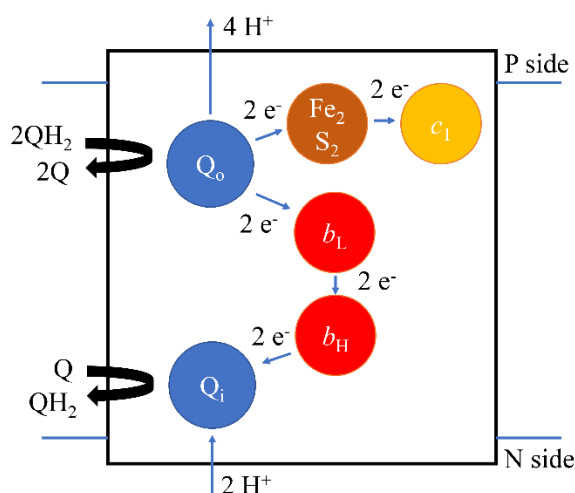
Figure 1-8: Q-cycle mechanism. The cytochrome bc_1 complex is represented by the black box. Heme b_L (red), heme b_H (red), Fe_2S_2 (orange) and heme c_1 (yellow) are represented by circles. Electron transfer steps, proton release and uptake are shown by blue narrow arrows, binding and release of quinone species by broad curved arrows. The position of Q_o and Q_i are marked and represented by blue circles. The short blue lines represent the position of membrane. The negative side of the membrane is marked by N side and the positive side is indicated by P side.

1.4 Heme A synthase

Heme A is a highly specialized heme variant and is found across different organisms (113). It is a prosthetic group in the mitochondrial and many bacterial cytochrome c oxidases (114-116). Therefore, heme A is essential for aerobic respiration and energy

conversion of all eukaryotes and most bacteria. Heme A is synthesized by the heme A synthase (HAS) that is located in the inner membrane of mitochondria and the cytoplasmic membrane of bacteria. Two reactions are involved in the biosynthesis of heme A from heme B with heme O as intermediate. Heme O synthase catalyzes the farnesylation of heme B to produce heme O (117,118), while HAS catalyzes the synthesis of heme A from heme O by three oxidative steps (21,119) (Figure 1-9). First, a monohydroxylated heme O (heme I) is produced by oxygenation of the methyl group at position C8 of the porphyrin ring of heme O. Second, a dihydroxy group (heme II) is formed. Third, the dihydroxy group of heme II is converted to a formyl group with the subsequent release of a water molecule. Studies of HAS from *Bacillus subtilis* (BsHAS) produced in *E. coli* demonstrated that HAS utilizes oxygen from water to oxidize the methyl group (120).
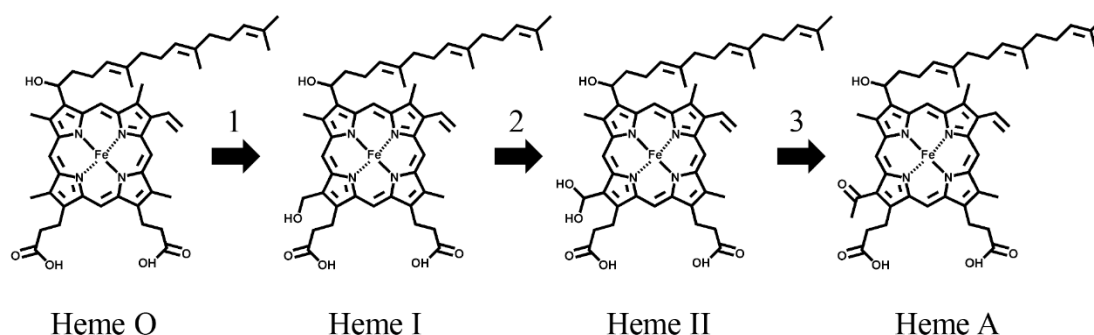
Figure 1-9: Heme A biosynthesis pathway. The proposed three reaction steps are supported by experimental data obtained from BaHAS. Steps 1 and 2 are single-electron oxidation reactions resulting in a germinal diol. Subsequently, dehydration at the 8-substituant group yields the formyl group resulting in the production of heme A.

HASs are integral membrane proteins, which are classified into four types according to their transmembrane topology and the number of conserved cysteine residues (Figure 1-10). The invariant cysteine residues are not only important for the activity of HAS, but also play a structural regulatory role (121). Class A HAS is the smallest HAS consisting of only four predicted TMHs, while other classes (B-D) possess eight predicted TMHs. Class B and class C HASs have four and two cysteine residues, respectively. The class D HASs, *e.g.*, the mitochondrial heme A synthase (Cox 15), has no cysteine residue (121). Class A HAS from bacterium *Aeropyrum pernix* (*A. pernix*)

and class B HAS from *B. subtilis* are relatively well studied (113,120,122-125). Previous results suggested that the homo-oligomerization is a conserved feature of HASs. Heterologous production of HAS from *B. subtilis* and *A. pernix* in *E. coli* showed that proteins form higher oligomeric complexes (125). It was found that the mitochondrial Cox 15 (class D) is also present in multiple oligomeric states (126). The oligomeric state is not influenced by the concentration of heme or the catalytic activity. However, the region between two heme-binding domains is critical for the formation of the oligomeric state (126). For class C HASs, limited information is available about the oligomeric state of the protein.
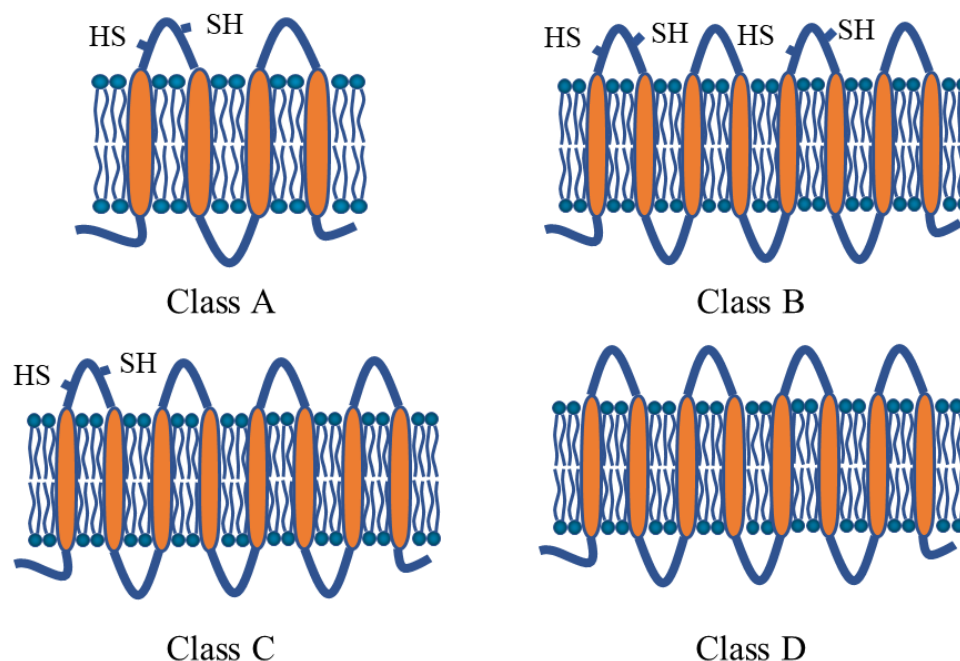
Figure 1-10: Membrane topology models of heme A synthases from different classes. The suggested classification is based on the protein size and complement of cysteine residues present in loops. SH indicates the cysteins.

Several mutations in HAS have been linked to malfunction of cytochrome *c* oxidase and several diseases, such as fatal infantile hypertrophic cardiomyopathy (127-130). There are two production systems used for the expression of HAS. One is the heterologous production in *Escherichia coli* (*E. coli*) and another one is a homologous expression system using *B. subtilis*. Previous mutagenesis studies focused mostly on the characterization of the strictly conserved cysteine and histidine residues

(113,121,126). Previous reported data for the BsHAS variants are summarized in table 1-2.

Table 1-2: Characterization of variants of heme A synthase from *B. subtilis* overproduced using heterologous (124,131) or homologous (113,131) expression system.

	CtaA variants	Produced in *B. subtilis*		Produced in *E. coli*
		Activity[1]	Heme content	Heme content
Wild type		+	B, A	B, (O)
C35	A	±	B, O, (I), (II), (A)	
C42	A	-	ND	
C191	A	+	ND	
C197	A	+	ND	
C35/C42	A	-	B, O	B, O
C35/C191	A	-	B, O	
C35/C197	A	-	B, O	
C35/C42/C191	A	-	B, O	
C35/C42/C191/C197	A	-	B, O, II	
Cys191+Cys197	A	+	B, I, A, II, (O)	B, O
H60	A			B, O
	L	-	B, O	
	M	+	B, (A)	
	Q			B, (O)
H123	A			B, (O)
	L	-	B, O	
	M	-	B, O	
	Q			B, (O)
H216	A			B, O, I
	L	No expression		
	M	+	B, O, I, (A)	
	Q			B, O, I
H278	A			B, (O)
	L	+	(B), (A)	
	M	+	(B), (A)	
	Q			B, O, I
W39	A			B, (O)
E57	A			B, O
	Q			B, O
R217	A			B, (O), I
	Q			B, (O), I
Q257	A			B, (O), (I)

1: Activity was determined by TMPD oxidation activity of cells; +: normal activity; ±: low activity; -: no activity. (): low amounts of the indicated type of heme. ND: not determined.

The crystal structure of BsHAS (class B) has been determined (132). The structure confirmed that the cofactor heme B is present in the C-terminal domain. Its N-terminal and C-terminal halves contain four helices each and are arranged in a pseudo twofold symmetric manner (Figure 1-11).
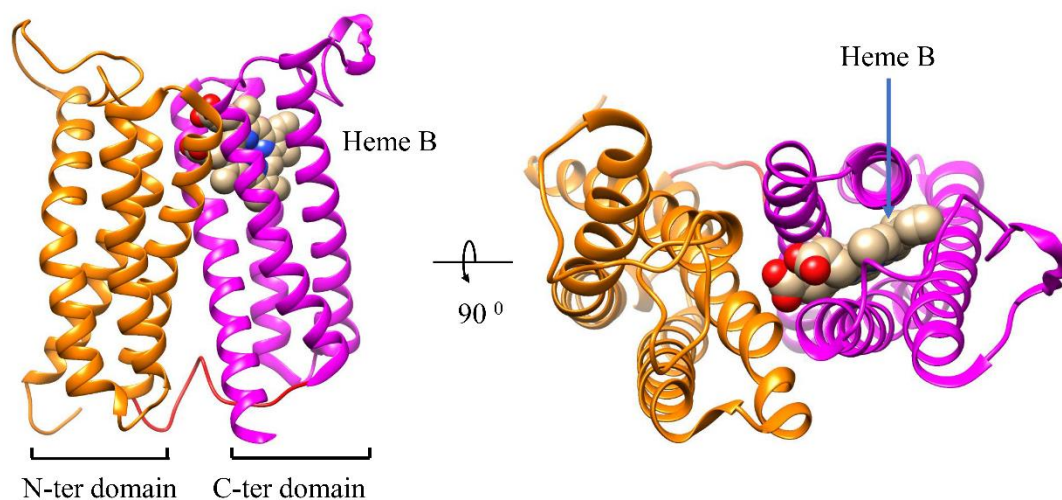
Figure 1-11: Overall structure of heme A synthase from *B. subtilis* (PDB:6A2J). Views from the membrane and from the extracellular side are shown as a ribbon drawing. Heme B was identified in the C-terminal domain.

A conserved residue, Gly 65, is identified at the bending site of TM2 and was suggested to be responsible for mediating the bending motion upon the binding of the substrate heme O. It was proposed that the conformation change of TM2 from a kinked state to a straight state leads to movement of the residue Glu 57 towards heme O. A catalytic mechanism of HAS was proposed based on the crystal structure (Figure 1-12). This reaction scheme contains four steps in the synthesis of heme A: two steps of hydroxyl radical formation, followed by dehydration, and the final heme B oxidation. In the first hydroxyl radical formation step, heme O yields a heme radical, which generates an ester cross-link of the C-8 methyl group of heme O with the carboxylate group of Glu 57. Following hydrolysis of the ester cross-link, heme I is generated. Then the second single-electron oxidation step takes place in a manner similar to the first step and generates a geminal diol. Subsequently, spontaneous dehydration at the 8-substituent group yields heme A. In the final heme oxidation step, both heme A and B are reoxidized by the electron acceptor.
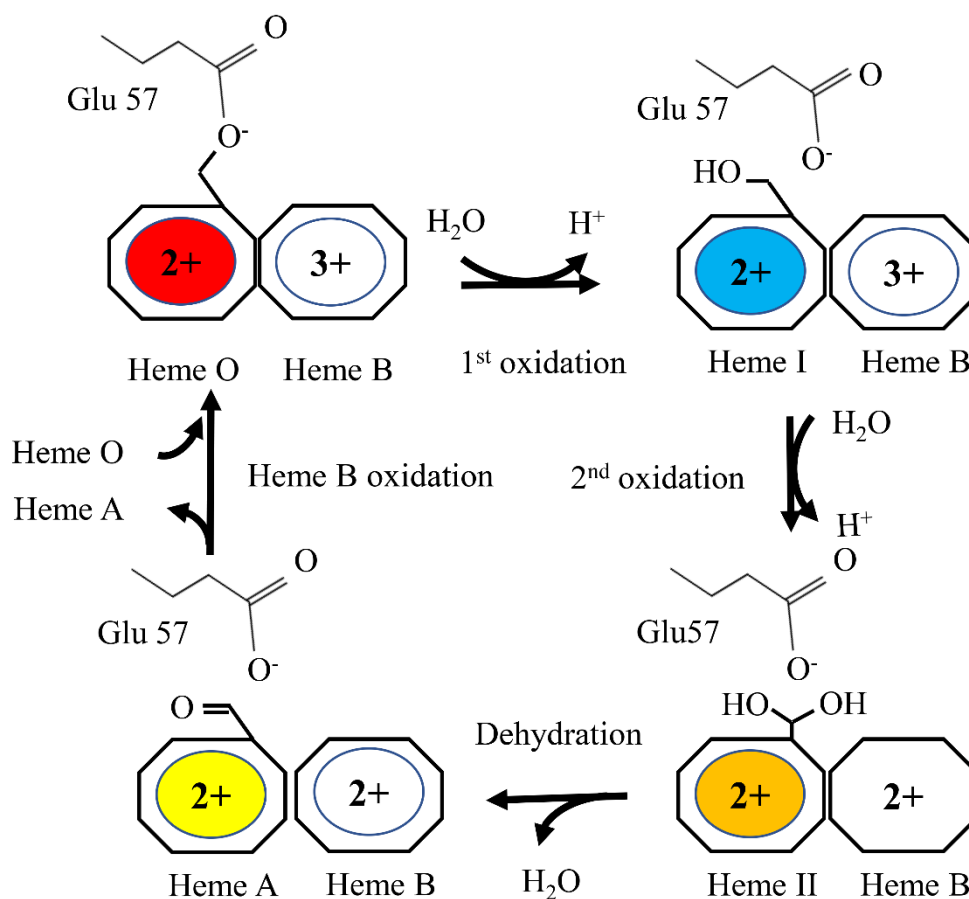
Figure 1-12: Proposed reaction mechanism of heme A synthesis (132). In the first step, heme O yields a heme radical, which generates an ester cross-link of the C-8 methyl group of heme O with the carboxylate group of Glu57. The cross-link can be hydrolyzed to produce heme I. The second step is the second single-electron oxidation which is similar to the first step and generates a geminal diol. Then the third step is the spontaneous dehydration at the 8-substituent group of heme II to yield heme A. In the final heme oxidation step, both heme A and B are oxidized.

1.5 *A. aeolicus* (VF5)

A. aeolicus belongs to the phylum *Aquificae*, which is an extremely thermophilic or hyperthermophilic Gram negative bacterium. It grows optimally between 85-95°C and was isolated from shallow hydrothermal volcanic areas in the Aeolian Islands, Italy (133). It can be artificially cultured in liquid SME medium supplemented with thiosulfate. It uses inorganic carbon sources for biosynthesis and inorganic chemical energy sources. It is an obligate aerobic bacterium that cannot tolerate high oxygen concentrations but can survive at levels of oxygen as low as 7.5 ppm (133). It can use hydrogen as the sole electron donor and oxygen as an electron accepter to produce water

by the "knallgas" reaction (134). Instead of hydrogen, it can use thiosulfate as an energy source, producing sulfuric acid and hydrogen sulfide.

Its genome consists of one chromosome and one extrachromosomal element (ECE), both were sequenced in 1988 with a calculated sequence redundancy of 4.83 (135). The genome size (1,551,335 base pairs in length) is only one-third of that of the *E. coli* genome. Interestingly, many genes that are functionally grouped within operons in other organisms or that encode subunits of the same enzyme, are often separated in *A. aeolicus.* No introns or inteins were detected in the genome (135). Recently, *A. aeolicus* became a model organism to test new culturing approach for microaerophilic hyperthermophilic bacteria (136).

1.5.1 *A. aeolicus* respiration

A. aeolicus is a chemolithoautotrophic bacterium, which can fix carbon dioxide through the reductive citric acid cycle (133). Several enzymes involved in electron transport and energy conservation were previously characterized, including hydrogenase I (137), hydrogenase II (134), sulfur reductase (134), cytochrome $c_{555}{}^m$ (138), cytochrome c_{555} (138), NADH:quinone oxidoreductase (complex I) (139), sulfide:quinone oxidoreductase (SQR) (140), cytochrome bc_1 complex (141), cytochrome c oxidase (142) and ATP synthase (143). However, the whole picture of *A. aeolicus* respiration is still incomplete, because only a limited number of proteins can be purified and characterized and 38 % of the encoded proteins of the genome have unknown functions.

1.5.2 Electron transport in *A. aeolicus*

A number of oxidoreductases, using alternative electron donors and acceptors have been identified in *A. aeolicus*. Naphthoquinone (NQ) forms the quinone pool in *A. aeolicus* (144). Based on this information, a model of electron transport was proposed (Figure 1-13)
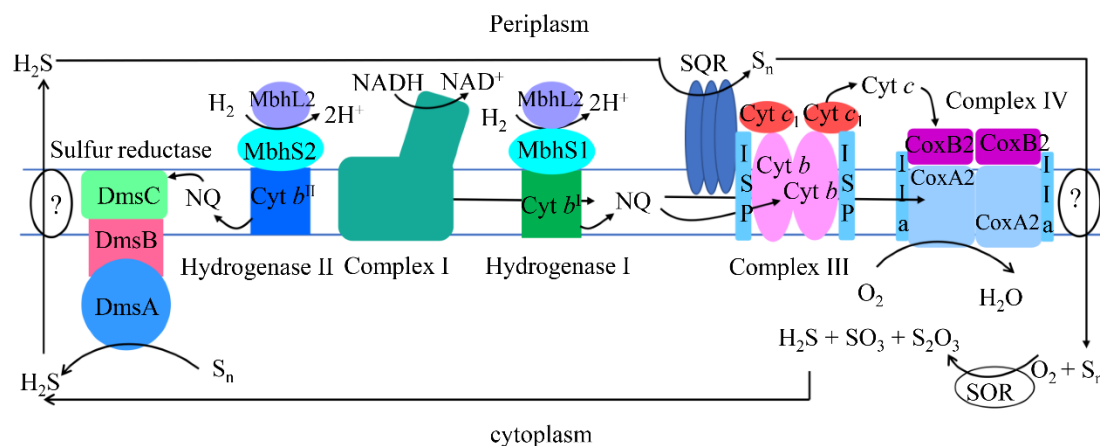
Figure 1-13: Model of electron transfer in the *A. aeolicus* membrane. S_n stands for sulfur which is the substrate of sulfur reductase. Cyt b^I and Cyt b^{II} are the cytochrome b^I of hydrogenase I and cytochrome b^{II} of hydrogenase II, respectively. The H_2S and H_2S/O_2 respiratory enzymes are structurally organized in supercomplexes, which contain complex IV (ba_3-type cytochrome *c* oxidase), complex III (cytochrome bc_1 complex), sulfide quinone reductase (SQR) and cytochrome c_{555}.

The electron of H_2 is first transferred to NQ by the enzyme hydrogenase II (145,146). Electrons are further transferred to S by the Sulfur reductase to produce H_2S. H_2S is subsequently transferred to the periplasmic side (146). Sulfide quinone reductase catalyzes the electron transfer from H_2S to NQ (147). The naphthoquinol found is the electron donor for the cytochrome bc_1 complex (111). The electrons of naphthoquinol are transferred to cytochrome *c* by the cytochrome bc_1 complex. Finally, the reduced cytochrome *c* delivers electrons to molecular oxygen through the cytochrome *c* oxidase. The electrons of H_2 can be also transferred to NQ directly by hydrogenase I (146). Complex I also can catalyze the electron transfer from NADH to NQ (148). Reduced NQ can be used by the cytochrome bc_1 complex and cytochrome *c* oxidase (149).

1.6 Aim of this work

The knowledge about the *A. aeolicus* cytochrome *c* oxidase and cytochrome bc_1 complex is quite limited. The cytochrome *c* oxidase was detected within supercomplexes in 2009 (150) and 2010 (151). In 2012, Gao reported that the cytochrome *c* oxidase (Cox2) can use both cytochrome *c* and quinol as electron donor (142), however, the mechanism of this reaction is still has to be elucidated. On the other

hand, the structure of HAS from *A. aeolicus* is unknown and its role in C*c*O assembly is unclear. The aim of my project was to determine the structure of the cytochrome *c* oxidase (AaC*c*O) and of the cytochrome *bc*$_1$ complex (Aa*bc*$_1$) and to heterologously express, purify, identify and investigate the structure and function of heme A synthase (AaHAS).

More specifically, this work aims to: (1) characterize the natural electron donors of cytochrome *c* oxidase; (2) structurally and functionally characterize the AaC*c*O; (3) structurally and functionally characterize the Aa*bc*$_1$; (4) biophysically, biochemically and functionally characterize AaHAS; (5) investigate the structure of AaHAS.

2 Materials and Methods

2.1 Material

2.1.1 Chemicals

If not stated otherwise, all chemicals and enzymes were bought from Sigma-Aldrich (Taufkirchen Germany), New England Biolabs (Ipswich USA), Carl Roth (Karlsruhe Germany), Thermo Scientific (Bonn Germany) and Invitrogen (Carlsbad, USA). Primers were synthesized by Sigma-Aldrich and Eurofins MWG Operon (Ebersberg, Germany). DNA sequencing was performed by Eurofins MWG Operon.

2.1.2 Bacterial strains

P. stutzeri, *A. aeolicus* and *E. coli* strains used in this work are listed in Table 2-1.

Table 2-1: List of strains

Strains	Genotype	Reference
A. aeolicus VF5	Wild type	(Huber *et al.,* 1988)
P. stutzeri ZoBell (ATCC14405)	Wild type	(ZoBell and Upham 1944)
E. coli DH5α	F⁻ *gyrA96* (Nalʳ) *recA1 relA1 endA1 thi-1 hsdR17* (r$_K^-$ m$_K^+$) *glnV44 deoR* Δ(*lacZYA-argF*) *U169* [Φ80dΔ(*lacZ*)M15]	(Hanahan 1983)
E. coli BL21 Star™ (DE3)	F⁻ *ompT hsdS$_B$* (r$_B^-$ m$_B^-$) *gal dcm rne131* (DE3)	Invitrogen
E. coli TOP10	F⁻ *mcrA* Δ(*mrr-hsdRMS-mcrBC*) Φ80lacZΔM15 Δ*lacX74 nupG recA1araD139* Δ(*ara-leu*)7697 *galE15 galK16 rpsL(StrR) endA1* λ-	Invitrogen

2.1.3 Plasmids

The plasmids used in this work are listed in table 2-2.

Table 2-2: List of plasmids

Plasmid	Relevant features	Reference
pEC86	Tet^R, Cam^R, *ccmABCDEFGH* genes	(Thöny-Meyer *et al.,* 1995)
pXH22	pBBR1 derivative, multiple cloning site, Cam^R, T7 promoter, T3 promoter, mobilization gene (mob), pBBR replication origin	(Hao *et al.,* 2014)
pET-22b (+)	Amp^R (Tn3), T7 promoter, *pelB* coding sequence, *lacI* coding sequence, pBR322 replication origin, f1 origin	Novagen
pJET1.2	Amp^R, T7 promoter, lethal gene *eco47IR*, pMB1 replication origin, insertion site for blunt end ligation	Thermo Fisher Scientific
pBADA2	pBAD/His derivative *ara*BAD promoter, pBR322, Amp^R, C-terminal His$_{10}$-tag	(Surade *et al.,* 2006)
pBADC3	pBAD/His derivative *ara*BAD promoter, pBR322, Amp^R, C-terminal Strep-tag II	(Surade *et al.,* 2006)
pETDeut	T7*lac*^{g} promoter, pBR322, Amp^R, N-terminal His$_6$-tag and C-terminal S-tag	Novagen
pJET1.2-C$_{555}$^{s}	pJET1.2 derivative, Amp^R, *cycB2* (cytochrome *C*$_{555}$^{S}) gene	This work
pJET1.2-C$_{555}$^{m}	pJET1.2 derivative, Amp^R, *cycB1* (cytochrome *C*$_{555}$^{m}) gene	This work
pJET1.2-C$_{552}$^{m}-ΔN18	pJET1.2 derivative, Amp^R, *cycB1* (cytochrome *C*$_{555}$^{m}) gene, deletion of 18 N-terminal residues	This work
pJET1.2-CtaA	pJET1.2 derivative, Amp^R, *ctaA* (heme A synthase) gene	This work
pJET1.2-C*c*O	pJET1.2 derivative, Amp^R, *coxA2* (subunit I) gene, *coxB2* (subunit II) gene and *IIa* (subunit IIa) gene	This work
pZH-22- C$_{555}$^{s}	pET-22 derivative, Amp^R, *CycB2* gene	This work
pZH-22- C$_{555}$^{m}	pET-22 derivative, Amp^R, *CycB1* gene	This work
pZH-22- C$_{555}$^{m}-ΔN18	pET-22 derivative, Amp^R, *CycB1* gene, deletion of 18 N-terminal residues	This work
pZH-22-C*c*O	pET-22 derivative, Amp^R, *coxA2* (subunit I) gene, *coxB2* (subunit II) gene and *IIa* (subunit IIa) gene	This work
pZH-22-C*c*O-CoxA2-C-His	pET-22 derivative, Amp^R, *coxA2* (subunit I with C-terminal His$_6$) gene, *coxB2* (subunit II)	This work

	gene and *IIa* (subunit IIa) gene	
pZH-22-C*c*O-CoxA2-C-Strep II	pET-22 derivative, Amp^R, *coxA*2 (subunit I with C-terminal Strep II) gene, *coxB*2 (subunit II) gene and *IIa* (subunit IIa) gene	This work
pZH-22-C*c*O-CoxA2-N-His	pET-22 derivative, Amp^R, *coxA*2 (subunit I with N-terminal His$_6$) gene, *coxB*2 (subunit II) gene and *IIa* (subunit IIa) gene	This work
pZH-22-C*c*O-CoxA2-N-Strep II	pET-22 derivative, Amp^R, *coxA*2 (subunit I with N-terminal Strep II) gene, *coxB*2 (subunit II) gene and *IIa* (subunit IIa) gene	This work
pZH- CtaA-C-Strep II-C*c*O-CoxA2-C-His	pETDeut detivative, T7*lac*^{g} promoter, pBR322, Amp^R, *coxA*2 (subunit I with N-terminal Strep II) gene, *coxB*2 (subunit II) gene, *IIa* (subunit IIa) gene and *ctaA* (heme A synthase with C-terminal Strep II) gene.	This work
pZH-C*c*O-CoxA2-C-His	pXH22 derivative, Cam^R, *coxA*2 (subunit I with C-terminal His$_6$) gene, *coxB*2 (subunit II) gene and *IIa* (subunit IIa) gene	This work
pZH-C*c*O-CoxA2-N-His	pXH22 derivative, Cam^R, *coxA*2 (subunit I with N-terminal His$_6$) gene, *coxB*2 (subunit II) gene and *IIa* (subunit IIa) gene	This work
pZH-C*c*O-CoxA2-N-Strep II	pXH22 derivative, Cam^R, *coxA*2 (subunit I with N-terminal Strep II) gene, *coxB*2 (subunit II) gene and *IIa* (subunit IIa) gene	This work
pZH-C*c*O-CoxA2-C-Strep II	pXH22 derivative, Cam^R, *coxA*2 (subunit I with C-terminal Strep II) gene, *coxB*2 (subunit II) gene and *IIa* (subunit IIa) gene	This work
pZH-C*c*O-IIa2-N-Strep II	pXH22 derivative, Cam^R, *coxA*2 (subunit I) gene, *coxB*2 (subunit II) gene and *IIa* (subunit IIa with N-terminal Strep II) gene	This work
pBAD-CtaA-C-His	pBAD/His *ara*BAD promoter, pBR322, Amp^R, *ctaA* gene,C-terminal His$_{10}$-tag	This work
pBAD-CtaB-C-His	pBAD/His derivative *ara*BAD promoter, pBR322, Amp^R, *ctaB* gene, C-terminal His$_{10}$-tag	This work
pBADC3-CtaA-C-Strep II	pBAD/His derivative *ara*BAD promoter, pBR322, Amp^R, *ctaA* gene, C-terminal Strep II	This work

Amp^R: resistance to ampicillin; Cam^R: resistance to chloramphenicol; Tet^R: resistance to tetracycline

The plasmid pBADC3-CtaA-C-Strep II was used for the production of recombinant AaHAS.

2.1.4 Bacterial growth media and solutions

All microbiological media were prepared in deionized water and autoclaved at 121°C for 20 min. All bacterial growth media used in this work are listed in table 2-3. Agar plates were made by adding 1.5% (w/v) agar to the media before autoclaving. Antibiotics were added into autoclaved media ($\approx$40°C) to make agar plates. Stock solutions of medium supplements listed in table 2-4 were stored at - 20°C.

Table 2-3: List of bacterial media

Medium	Composition	Preparation
Lysogeny broth (LB) broth medium	1% (w/v) tryptone 0.5% (w/v) yeast extract 1% (w/v) NaCl H_2O Adjust pH to 7.0 with NaOH	10 g 5 g 10 g Add to 1 L
SOC medium	2% (w/v) tryptone 0.5% (w/v) yeast extract 10 mM NaCl 2.5 mM KCl 10 mM $MgCl_2$ 10 mM $MgSO_4$ 20 mM glucose H_2O Adjust pH to 7.0 with NaOH	5 g 1.25 g 0.146 g 0.047 g 1 M $MgCl_2$/2.5 ml 1 M $MgSO_4$/2.5 ml 1 M glucose/5 ml Add to 250 ml
Asparagine medium[a]	0.2% (w/v) L-asparagine 0.7% (w/v) $Na_3C_6H_5O_7 \cdot 2H_2O$ 0.2% (w/v) KH_2PO_4 0.2% (w/v) $MgSO_4 \cdot 7H_2O$ 0.01% (w/v) $CaCl_2 \cdot 2H_2O$ 1% (w/v) NaCl 1$\times$ trace element mix (see below). Adjust pH to 8.0 with NaOH.	0.5 g 1.75 g 0.5 g 0.5 g 0.025 g 2.5 g
Trace element mix (1000×) for asparagine medium	3.2% (w/v) $FeCl_3 \cdot 6H_2O$ 0.017% (w/v) $CuCl_2 \cdot 2H_2O$ 0.16% (w/v) NH_4NO_3 2.2% (w/v) KBr 2.0% (w/v) $MnCl_2 \cdot 2H_2O$ 2.5% (w/v) $ZnCl_2$ H_2O	8 g 0.0425 g 0.4 g 0.55 g 5 g 6.25 g Add to 1 L

a: According to Urbani (152) and further modified by Sabine Buschmann (MPI of Biophysics, Frankfurt am Main) concerning the supplementation of trace elements.

Table 2-4: List of medium supplements.

Medium supplement	Composition
Ampicillin (Amp), 1000×	10% (w/v) Amp in 50% (v/v) H_2O + 50% (v/v) glycerol
Chloramphenical (Cam), 1000×	3.4% (w/v) Cam in EtOH
IPTG	1M IPTG in H_2O
L-arabinose	1M L-arabinose in H_2O

2.1.5 Enzymes, proteins, markers and kits

All restriction enzymes and DNA modifying enzymes, proteins, markers and kits used in this work are listed in Table 2-5.

Table 2-5: List of enzymes, proteins, markers and kits.

Name	Supplier	Application
Albumin standard (bovine serum)	Pierce	Protein concentration assay
Albumin fraction V (bovine serum, biotin-free)	Carl Roth	Western blot
Avidin (egg white)	Gerbu	Avidin-biotin interaction
CloneJET™ PCR Cloning Kit	Thermo Fisher Scientific	Molecular cloning
Crimson™ *Taq* DNA Polymerase	NEB	PCR
Cytochrome *c* (equine heart)	Biomol	Protein activity assay
DNA Clean & Concentrator™-25 Kit	Zymo Research	DNA purification
Fast-Link™ DNA Ligation Kit	Epicentre	Molecular cloning
GeneRuler™ 1 kb Plus DNA Ladder	Thermo Fisher Scientific	DNA ladder
GeneRuler™ 100 bp Plus DNA Ladder	Thermo Fisher Scientific	DNA ladder
G-spin™ Genomic DNA Extraction Kit (for bacteria)	iNtRON	Genomic DNA extraction
In-Fusion® HD Cloning Kit	Clontech	Molecular cloning
Lambda DNA-Mono Cut Mix	NEB	DNA ladder
Lysozyme (egg white)	Fluka	Protein purification
NativeMark™ Protein Standard	Invitrogen	Protein ladder
PageRuler™ Prestained Protein Ladder	Thermo Fisher Scientific	Protein ladder
PageRuler™ Prestained Protein Ladder Plus	Thermo Fisher Scientific	Protein ladder
SeeBlue® Plus2 Prestained Standard	Invitrogen	Protein ladder
PeriPreps™ Periplasting Kit	Epicentre	Protein purification

Phusion® High-Fidelity DNA Polymerase	Finnzymes	PCR
QIAGEN® Plasmid Plus Midi Kit	Qiagen	DNA extraction
QIAprep® Spin Miniprep Kit	Qiagen	DNA extraction
QIAquick® Gel Extraction Kit	Qiagen	DNA purification
QIAquick® PCR Purification Kit	Qiagen	DNA purification
QuickExtract™ DNA Extraction Solution 1.0	Epicentre	DNA extraction
QuikChange® Lightning Site-Directed Mutagenesis Kit	Stratagene	Cloning and mutagenesis
Ribonuclease A	Roche	DNA extraction
SilverQuest™ Staining Kit	Invitrogen	Protein staining
Zymoclean™ Gel DNA Recovery Kit	Zymo Research	DNA purification
Complete protease inhibitor cocktail tablets	Roche	Protease inhibitors

2.1.6   Chromatographic columns and matrices

The chromatographic columns and matrices used in this work are listed in Table 2-6.

Table 2-6: Chromatographic columns and matrices

Column name	Matrix	Type	Supplier
MonoQ 10/100 GL	Polystyrene/divinyl benzene	Strong anion exchanger	GE Healthcare
TSK-GEL G4000SW 21.5/30	Silica	Size exclusion chromatography	TOSOH Bioscience
Yarra SEC-4000	Silica	Size exclusion chromatography	Phenomenex
Superdex® 200 10/300 GL	Cross-linked agarose and dextran	Size exclusion chromatography	GE Healthcare
Superdex® 200 3.2/30 GL	Cross-linked agarose and dextran	Size exclusion chromatography	GE Healthcare
HisTrap HP 1 ml	Cross-linked agarose	IMAC affinity chromatography	GE Healthcare
Ni-NTA agarose	Cross-linked agarose	IMAC affinity chromatography	Qiagen
Strep-Tactin Superflow® high capacity column	Strep-Tactin Superflow	IMAC affinity chromatography	IBA
Disposable PD-10 desalting column	Sephadex G-25 medium	Size exclusion chromatography	GE Healthcare

Zeba™ Spin Desalting Columns (0.5 ml Spin Column)	Proprietary resin	Size exclusion chromatography	Thermo Fisher Scientific
Zeba™ Spin Desalting Columns (Micro Spin Column)	Proprietary resin	Size exclusion chromatography	Thermo Fisher Scientific

2.1.7 Databases, servers and software

The databases and servers used in this work are listed in Table 2-7.

Table 2-7: Databases, servers and software

Database and server URL	
EMBL	http://www.embl.org
ExPASy: SIB Bioinformatics Resource Portal	http://www.expasy.org
HCO: Heme Copper Oxygen reductase classification tool	http://www.evocell.org/hco
Mascot	http://www.matrixscience.com
Membrane Protein Data Bank MPDB	http://www.mpdb.tcd.ie
MultAlin	http://multalin.toulouse.inra.fr
NCBI: National Center for Biotechnology Information	http://www.ncbi.nlm.nih.gov
PDB: Protein Data Bank	http://www.rcsb.org
PROMISE	http://bioinf.leeds.ac.uk/promise
Proteopedia	http://www.proteopedia.org
ScanProsite	http://prosite.expasy.org/scanprosite
SignalP Server	http://www.cbs.dtu.dk/services/SignalP
Compute pI/Mw	http://web.expasy.org/compute_pi
Signal Peptide Database	http://www.signalpeptide.de
UniProt: Universal Protein Resource	http://www.uniprot.org
Web of Knowledge	http://www.webofknowledge.com
Dali server	http://ekhidna2.biocenter.helsinki.fi/dali
PPM server	https://opm.phar.umich.edu/ppm_server
I-TASSER server	https://zhanglab.ccmb.med.umich.edu/I-TASSER

The software used in this work is listed in Table 2-8.

Table 2-8: List of software

Software	Version	Application	Company or reference
BioTools	3.1	MS data analysis	Bruker Daltonics
Chromas Lite	2.01	Chromatogram editor	Technelysium
Clone Manager	Professional 9	Cloning simulation	Sci-Ed Software
CLC Sequence viewer	8	Multiple-sequence alignment	Qiagen
Compass/Hystar	3.2	MS data analysis	Bruker Daltonics
Endnote	X8	Reference management	Thomson Reuters
Geneious	Basic 5.6.5	Phylogenic tree viewing	Biomatters Ltd
Microsoft Office	2016	Microsoft office software	Microsoft
Origin	9	Data processing and analysis	OriginLab
Photoshop	CS6	Image editor	Adobe
PyMOL	Anaconda 2	3D molecular visualizer	Schrödinger, LLC
Unicorn	5.11	Äkta control system	GE Healthcare
Gautomatch	0.56	Image processing	Jack (Kai) Zhang
Coot	0.8	Manual model building	Paul Emsley
Chimera	X	3D molecular visualizer	Pettersen EF et *al.,* (2004)
RELION	2.1/3.0-beta	Data processing	Sjors Scheres (153,154)
EMAN2	2.3	Image processing	Tang G et *al.,* (155)
Resmap	1.1.5	Data processing	Alp Kucukelbir et *al.,* (156)

2.2 Methods

2.2.1 Molecular Biology

General molecular biological techniques were performed according to standard protocols described by the manufactures, unless otherwise stated. The growth of

bacteria was monitored by measuring the optical density (OD) of the bacterial culture in an Ultrospec^{TM} 2100 pro UV/Vis spectrophotometer (Amersham).

2.2.1.1 Isolation of genomic DNA from *A. aeolicus*

10 mg of wet *A. aeolicus* cells were taken to isolate genomic DNA using the G-spin^{TM} Genomic DNA Extraction Kit for Bacteria (iNtRON Biotechnology), according to the manufacturer's protocol for Gram-negative bacteria. The typical yield of genomic DNA was 2 µg per 10 mg of wet *A. aeolicus* cells. The genomic DNA was stored at at 4°C in TE buffer (10 mM Tris/HCl, pH 8.0, 1 mM EDTA) for long-term storage.

2.2.1.2 Isolation of plasmid DNA

A single bacterial colony was cultured in Asparagine (*P. stutzeri*) or LB (*E. coli*) medium containing appropriate antibiotics and incubated at 32°C (*P. stutzeri*) or 37°C (*E. coli*) with shaking at 220 rpm overnight. 5 ml or 50 ml bacterial cultures were used for isolation of high-copy-number or low-copy-number plasmids, respectively. Plasmid DNA was isolated using the Qiagen plasmid mini/midi kit according to the manufacturer's protocols, which are based on a modified alkaline lysis procedure and anion exchange chromatography. The plasmid DNA was stored at -20°C in elution buffer at for long-term storage.

2.2.1.3 DNA amplification

The polymerase chain reaction (PCR) was used in this work to amplify DNA fragments for cloning and screening of constructs. Primers were designed according to gene sequences from NCBI (NC_000918) and synthesized by Sigma-Aldrich or Eurofins, which are listed in table 2-9. Phusion DNA polymerase (Finnzymes) was used for PCR amplifications of variant amplicons (0.5 to 7 kb). Gradient PCR was used to optimize the amplification condition. The QuikChange lighting site-directed mutagenesis kit (Stratagene) was used to introduce a point mutation or deletion (up to 120 bp) according to the protocol supplied by the manufacturer. Working concentrations of primer was 10 µM. For a reproducible and effective PCR amplification, analytical and preparative PCR cycles were performed in a volume of 10 µl and 5×10 µl, respectively. A typical

PCR reaction mixture is listed in table 2-10.

Table 2-9: List of primers used in this work

Primers	Sequence (5'-3')	Restriction site
IIa-NdeI-F	CGCCATATGAATGAAAAGCATGAAC	NdeI
CoxA2-XhoI-R	CCGCTCGAGTTTCTGAGTGATACCC	XhoI
CycB1-NdeI-F	GCCATATGCCATGAAGTTAAGATATG	NdeI
CycB1-NSP-NcoI-F	CGCCATGGAGCAACCACAAAAGAAAGAGG	NcoI
CycB1-R	GTCTCGAGCTTGTGGGACATTATAAAG	XhoI
CycB2-NcoI-F	CTACCATGGCTGACGGAAAAGC	NcoI
CycB2-XhoI-R	GGCTCGAGTTTGTGAGAAAGG	XhoI
CoxA2-N-Strep II-F	GTTGAATAAAGGAGGTGTGGAGCCACCCGCAGTTCGAAAAGTGGGTGATGCAGGTGAG	
CoxA2-N-Strep II-R	CTCACCTGCATCACCCACTTTTCGAACTGCGGGTGGCTCCACACCTCCTTTATTCAAC	
CoxA2-N-His-F	GAATAAAGGAGGTGGCTAGCAGAGGATCGCATCACCATCACCATCACGGCGCCTGGGTGATGCAGGTG	
CoxA2-N-His-R	CACCTGCATCACCCAGGCGCCGTGATGGTGATGGTGATGCGATCCTCTGCTAGCCACCTCCTTTATTC	
CoxA2-C-His-F	AGCTGAAGGGGGTATCACTCAGAAAGCTAGCAGAGGATCGCATCACCATCACCATCACTGAATCGATACCG	
CoxA2-C-His-R	CGGTATCGATTCAGTGATGGTGATGGTGATGCGATCCTCTGCTAGCTTTCTGAGTGATACCCCCTTCAGCT	
CoxA2-C-Strep II-F	CCGCAGTTCGAAAAATGAATCGATACCGTCG	
CoxA2-C-Strep II-R	GTGGCTCCAAGCGCTTTTCTGAGTGATACC	
pXH22-F	ATCGATACCGTCGACCTC	
pXH22-R	GTATGGGCTTCCAT	
CcO-sequencing -1	ATGCAGGTGAGCAATG	
CcO-sequencing -2	CGGACTCGTTGACGAGATTAACC	
CcO-sequencing -3	TCGCACCCTACTTCTGGATG	
CtaA BamHI-F	CACGGATCCATGAACACCAACCTC	BamHI

CtaA EcoRI-R	GTG<u>GAATTC</u>TGCCAGCTCTCCTC	EcoRI
CtaA NcoI-F	CAT<u>CCATGG</u>ATGAACACCAACCTC	NcoI
CtaA EcoRI-R	GTG<u>GAATTC</u>CGTGCCAGCTCTCCTC	EcoRI
CtaA-Del36-40-F	GTATAGTTACCTCTACGGGTCCCGACTGGCC	
CtaA-Del36-40-R	GGCCAGTCGGGACCCGTAGAGGTAACTATAC	
CtaA-Del41-45-F	GGTTCAGGGCTCGGATGTTGTCACGGACAACT	
pBDAC3-CtaA-Del41-45-R	AGTTGTCCGTGACAACATCCGAGCCCTGAACC	
CtaA-Del46-50-F	TCCCGACTGGCCCCTGCTTCCTTTTCAGTTAA	
CtaA-Del46-50-R	TTAACTGAAAAGGAAGCAGGGGCCAGTCGGGA	
CtaA-Del51-56-F	TGTGTCACGGACAACTCGAACAAATTCCCACACC	
CtaA-Del51-56-R	GGTGTGGGAATTTGTTCGAGTTGTCCGTGACACA	
CtaA-Del64-67-F	ACAAATTCCCACACCTGTAGCTCCAACTCCCC	
CtaA-Del64-67-R	GGGGAGTTGGAGCTACAGGTGTGGGAATTTGT	
CtaA-Del76-82-F	CCCCTCCAGCCCTGGATACTCGGAGGAATA	
CtaA-Del76-82-R	TATTCCTCCGAGTATCCAGGGCTGGAGGGG	
CtaA-C40A-F	CGGGTTCAGGGCTCGGAGCTCCCGACTG	
CtaA-C40A-R	CAGTCGGGAGCTCCGAGCCCTGAACCCG	
CtaA-C46A-F	CCGACTGGCCCCTGGCTCACGGACAACTCC	
CtaA-C46A-R	GGAGTTGTCCGTGAGCCAGGGGCCAGTCGG	
CtaA-Del-loop1-F	CTCTACGGGTTCAGGGCACAGGATACTCGGAG	
CtaA-Del-loop1-R	CTCCGAGTATCCTGTGCCCTGAACCCGTAGAG	

Table 2-10: Typical PCR reaction mixture

Component	Volume (μl)/50 μl	Final concentration
5× Phusion® HF Buffer	10	1×
2.5 mM dNTPs	4	200 μM
primer A (10 μM)	2.5	0.5 μM
primer B (10 μM)	2.5	0.5 μM
Template	X	50 ng (plasmid)/100 ng (genomic DNA)
Phusion® Hot Start DNA Polymerase (2 U/μl)	0.5	0.02 U/μl
H$_2$O	Add to 50	

All reactions were set up on ice and performed using a Biometra T Gradient thermocycler. A typical PCR cycling program is shown in table 2-11. Agarose gel electrophoresis was used to analyze the PCR results and QuickExtract™ DNA extraction kit (Epicentre) or the PCR purification kit was used to isolate the PCR fragments. The final correctness of the PCR products were confirmed by sequencing.

Table 2-11: Typical PCR cycling programs.

Cycle step		Temperature (°C)	Duration	Number of cycles
1	Initial denaturation	98, 95	30 s, 2 min	1, 1
2	Denaturation	98, 95	10 s, 20 s	30-35, 18
	Annealing	55-70, 65	30 s, 10 s	
	Extension	72, 68	30 s/kb, 30 s/kb	
3	Final extension	72, 68	10 min, 5 min	1, 1
4	Refrigeration	4, 4	-	-

Routine PCR programs and mutagenesis PCR program are showed in black and red, respectively.

2.2.1.4 Agarose gel electrophoresis of DNA

1% (w/v) agarose (NEEO ultra quality, Carl Roth) gel electrophoresis was performed to separate supercoiled or linear DNA (0.5 kb–10 kb) using 0.5× TBE or 1× TAE buffer. The sample was prepared by mixing DNA with 10× loading buffer prior to the electrophoretic run. Electrophoresis was performed using PowerPac™ Basic power suppliers (Bio-Rad) and a self-made horizontal gel chamber. Typically, the electrophoresis was performed at 120 V (6V/cm) for 60-90 min and the running of visible colored dyes represented the progress of the separation. 100 bp or 1 kb DNA ladders (NEB) were used to determine the size of the DNA fragments. Gel was stained in 0.5 μg/ml ethidium bromide (Roth) solution for 10-30 min and destained in water for

5-10 min. The gels were subsequently visualized and photographed using a Bio-Rad gel documentation system with a 302 nm UV transilluminator or visualized under UV light (312 nm, Biometra TI1 transilluminator). The buffers used for electrophoresis of DNA are listed in Table 2-12.

Table 2-12: List of agarose gel electrophoresis buffer

Buffer	Components	Preparations
TAE (50×)	2 M Tris 1 M glacial acetic acid 50 mM EDTA H_2O	242 g 57.1 ml 100 ml 0.5 M EDTA (pH 8.0) Add to 1 L
TBE (5×)	445 mM Tris 445 mM boric acid 10 mM EDTA H_2O	54 g 27.5 g 20 ml 0.5 M EDTA (pH 8.0) Add to 1 L
DNA loading buffer (10×)	50 % glycerol 10 mM EDTA 0.25% (w/v) bromophenol blue 0.25% (w/v) xylene cyanolFF H_2O	2.5 ml glycerol 100 µl 0.5 M EDTA 1.25 mg bromophenol blue 1.25 mg xylene cyanolFF Add to 5 ml

2.2.1.5 Purification of DNA fragments from agarose gels

After agarose gel electrophoresis, the gel was visualized under UV light (312 nm, Biometra TI1 transilluminator) and the band with the desired DNA fragment was excised from the gel with a clean scalpel. The DNA fragments were extracted and purified using the Zymoclean gel DNA recovery kit (Zymo Research) according to the manufacturer's protocols. The gel was dissolved in a chaotropic agent at 50°C. The mixture was mixed every 3 minutes until the gel was completely dissolved. The mixture was added to a spin column and washed with 80% ethanol. The DNA fragments were eluted with 15 µl elution buffer.

2.2.1.6 Quantification of nucleic acid concentration and purity

DNA concentration was determined using a NanoDrop® ND-1000 spectrophotometer (NanoDrop Technologies), recording the absorbance at 260 nm. The measurement was performed according to the manufacturer's guidelines. Typically, 1.5 µl of DNA sample was used for the measurements and one A_{260} unit of double stranded DNA is equal to a

concentration of 50 μg/ml. The purity of the DNA samples was estimated by the ratio A_{260}/A_{280} and A_{260}/A_{230}. Pure DNA generally has a A_{260}/A_{280} absorption ratio of approximately 1.8, and a A_{260}/A_{230} absorption ratio of approximately 2.0-2.2.

2.2.1.7 Restriction digestion

A typical DNA double digestion was prepared as shown in Table 2-13, as described in the manufacturer's guidelines. For the downstream purposes a preparative scale protocol was used to digest the DNA, while the analytical scale was used for screening purposes.

Table 2-13: Typical restriction digestion mixture

	Analytical scale	Preparative scale	
	Plasmid DNA	Plasmid DNA	PCR product
Reaction buffer (10×)	1×	1×	1×
DNA	200 ng	5 μg	1 μg
Restriction enzyme A	1 μl	2.5 μl	2.5 μl
Restriction enzyme B	1 μl	2.5 μl	2.5 μl
H$_2$O	Add to 20 μl	Add to 50 μl	Add to 50 μl

2.2.1.8 Ligation and ligation independent cloning

The ligation mixture was prepared according to the manufacturer's guidelines of the T4 DNA ligation kit (NEB) or of Fast-Link DNA ligation (Epicentre). T4 DNA ligation reaction was performed at 16°C overnight (Thermomixer comfort, Eppendorf). The Fast-Link DNA ligation was performed at RT for 5 to 15 min. Normally a molar ratio of 3:1 and 5:1 (insert:vector) was used for cohesive-end and blunt-end ligations, respectively. Conversion of double stranded DNA (μg to pmol) was calculated as one basepair is equal to 660 g/mol. To prevent DNA self-ligation, dephosphorylation was performed by incubation the linearized vector DNA with calf intestinal alkaline phosphatase (CIAP). T4 polynucleotide kinase was used to phosphorylate the 5' hydroxyl group of the blunt-end amplicons prior to ligation at 37°C for 20 min. Heat inactivation was optionally performed when the conventional T4 DNA ligase was used, but was avoided when the Fast ligation protocol was used. The ligation reaction was prepared as shown in table 2-14.

Table 2-14: Typical ligation reaction (20 µl)

	T4 ligase	Fast-link ligation
T4 DNA ligase Buffer (10×) / Quick ligation Buffer (2×)	2 µl	10 µl
Linearized vector DNA	50-200 ng	50-200 ng
Insert DNA	50-200 ng	50-200 ng
T4 DNA ligase / Quick T4 DNA ligase	1µl	1µl
H_2O	Add to 20 µl	Add to 20 µl

Ligation independent cloning was performed for directional cloning without restriction digestion and ligation. The primers for amplification of target inserts were designed to have lengths between 28 and 35 bases including 15 bases that are homologous to the last 15 bases of the vector the 3' end. The insert was amplified, and the vector was linearized by PCR using Phusion DNA polymerase. The amplified insert and vector were analyzed by gel electrophoresis and afterwards purified from agarose gel. The ligation independent cloning reaction was carried out as described elsewhere (157) or using the In-Fusion HD cloning kit following the supplier's instructions (Clontech), followed by transformation into chemically competent cells.

2.2.1.9 Preparation of chemically competent cells

Chemically competent cells were prepared according to the rubidium chloride method as described elsewhere (158). A single colony from a rich plate was used to inoculate 5 ml of LB medium and incubated at 37°C with shaking at 220 rpm overnight as a pre-culture. 2.5 ml of the pre-culture were added into 250 ml SOC medium in a 1 L baffled flask. The culture was incubated at 37°C with shaking at 180 rpm until an OD_{600} of 0.4-0.6 was reached. The cells were then chilled on ice and pelleted at 4,400 × g at 4°C for 15 min (Sigma 4K15 centrifuge, 6 × 40 ml in 50 ml tubes). The cell pellets were resuspended in 96 ml RF1 buffer and incubated on ice for 20 min. The cells were then centrifuged again at 1,600 × g at 4°C for 5 min (Sigma 4K15 centrifuge). The cell pellets were gently resuspended in 9.6 ml RF2 buffer and incubated on ice for 15 min. The chemically competent cells were distributed into pre-chilled microfuge tubes in 50 µl

aliquots, flash frozen in liquid nitrogen and stored at -80°C. The RF1 and RF2 buffer are listed in table 2-15.

Table 2-15: Buffers used to prepare chemically competent cells

	Working concentration	Stock solution	Preparation
RF1	30 mM KOAc, pH 5.8	1 M KOAc	15 ml
	100 mM RbCl		6.046 g
	50 mM $MnCl_2$	1 M $MnCl_2$	25 ml
	10 mM $CaCl_2$	1 M $CaCl_2$	5 ml
	15 % glycerol (v/v)		75 ml
	H_2O		Add to 500 ml
RF2	100 mM MOPS/KOH, pH 6.8	1 M MOPS, pH6.8	0.5 ml
	10 mM RbCl	1 M RbCl	0.5 ml
	75 mM $CaCl_2$	1 M $CaCl_2$	3.75 ml
	15 % glycerol (v/v)		7.5 ml
	H_2O		Add to 50 ml

2.2.1.10   Transformation of chemically competent *E. coli* cells

Transformation of plasmid DNA into chemically competent cells was performed by heat shock. 10 to 30 ng of plasmid DNA or 7% volumes (normally 3.5 µl) of the ligation reaction was added to 50 µl of competent cells. The DNA/cells mixture was incubated on ice for 30 min. Then the mixture was treated at 42°C for 90 sec without shaking (Thermomixer compact, Eppendorf). Afterwards, the cells were incubated on ice for 10 min before adding 900 µl SOC medium. The culture was transferred into a 13 ml culture tube and finally incubated at 37°C and 220 rpm for 1 h to allow the bacteria to recover. The cells were transferred to a sterile 1.5 ml microfuge tube and pelleted at 12,000 × g at room temperature for 1 min (Centrifuge 5415D, Eppendorf) and plated on LB agar plates containing the appropriate antibiotic. The plates were incubated at 37°C overnight.

2.2.1.11   Transformation of *P. stutzeri*

Freshly prepared *P. stutzeri* electrocompetent cells were used, according to a modified protocol (159). A fresh single clone from the LB plate was inoculated into a 5 ml of LB medium and incubated at 37 °C and 220 rpm until early stationary phase (OD_{550} = 1.5 to 2.0). 1 ml of pre-culture was transferred to a 1.5 ml microfuge tube and the cells were pelleted by centrifugation at 16,000 × g at RT for 2 min (Centrifuge 5415D, Eppendorf).

The cell pellet was washed twice with 1 ml of 300 mM sucrose and centrifugated as described above. The cell pellet was finally resuspended in 100 µl of 300 mM sucrose. Electroporation was performed in a 1 mm electroporation cuvette (PEQLAB or Bio-Rad) with the mixture 100 to 500 ng of plasmid DNA and 100 µl electrocompetent cells at 25 µF, 200 Ω and 2.5 kV (Bio-Rad Gene Pulser®). After electroporation, 900 µl of SOC medium was added to the cells immediately. The culture was transferred to a 13 ml culture tube and incubated at 37°C at 220 rpm for 1 h. Cells were plated on LB agar plates with appropriate antibiotic and incubated at 32°C. The colonies were visible after 2 to 3 days.

2.2.1.12 Screening for positive clones and DNA sequencing

Before subcloning and protein production, all positive clones were screened and confirmed by DNA sequencing. Colonies were screened in two steps. (1) Isolation of the plasmids from a single clone, and (2) digestion of the plasmids with the appropriate restriction enzyme. Afterwards, DNA sequencing was performed by Eurofin MWG Operon to confirm the correctness of the plasmid sequence. For one sequencing reaction, normally, 700 ng plasmid DNA is needed. Sequencing primers used in this work are listed in table 2-16.

Table 2-16: List of sequence primers

Primers	Sequence (5' – 3')
pBAD-7	AGATTAGCGGATCCTACCTG
pBAD-8	CAGACCGCTTCTGCGTTCTG
T7	AATACGACTCACTATAG
T7-term	GCTAGTTATTGCTCAGCGG
pJET1.2-F	CGACTCACTATAGGGAGAGCGGC
pJET1.2-R	AAGAACATCGATTTTCCATGGCAG
DuetDown1	GATTATGCGGCCGTGTACAA
DuetUp2	TTCTACACGGCCGCATAATC
C_CO-F1	ATGCAGGTGAGCAATG
C_CO-F2	CGGACTCGTTGACGAGATTAACC
C_CO-F3	TCGCACCCTACTTCTGGATG

2.2.1.13 Site-directed mutagenesis

Site-directed mutagenesis was performed according to the manufacturer's guidelines of

the QuikChange Lighting kit (Agilent Technologies) or PCR site-directed mutagenesis.

a) The QuikChange® lightning Site-Directed Mutagenesis kit (Agilent Technologies) was used for site-directed mutagenesis i.e. insertion or deletion of multiple nucleotides, following the manufacturer's specifications. Site-directed mutagenesis was used for generating pZH-CtaA-C-Strep II mutants using pZH-CtaA-C-Strep II as the template, and primers were designed on the website https://www.agilent.com/store/primerDesignProgram.jsp.

b) PCR site-directed mutagenesis: PCR site-directed mutagenesis was used to construct the pZH-CtaA-C-Strep II mutation, during which PCR products were purified using the QIAquick PCR purification kit (Qiagen), and linearized DNA was self-ligated using the Quick ligation kit (NEB) and subsequently transformed into host cells using standard transformation protocol.

After site-directed mutagenesis, the correctness of all constructs was confirmed by DNA sequencing.

2.2.1.14   Preparation of bacterial glycerol stocks

Glycerol stocks were made for *E. coli* and *P. stutzeri* strains at -80°C. 350 µl of late exponential phase bacteria was mixed with 150 µl of pre-sterilized 50% glycerol in a 1.5 ml cryovial. The mixture was flash frozen in liquid nitrogen and stored at -80°C.

2.2.2 Protein expression and isolation

2.2.2.1 Positive expression screening

0.5 ml of overnight bacterial culture was used for inoculation of 50 ml LB medium in Erlenmeyer flasks, (a ratio of culture/flask volume). The culture was incubated at 37°C with 180 rpm until OD_{600} of 0.6 was reached. 1 ml of cell suspension was pelleted by centrifugation at 16,000 × g at 4°C for 5 min (Centrifuge 5415D, Eppendorf) before induction and as a control stored at -20°C. Expression was induced by adding 1 mM IPTG (for vectors pET22b and petDuet derivatives) or 0.2% (w/v) arabinose (for vector

pBAD derivatives). The cells were cultured for different time periods (1, 2, 3, 4 and 16 h) at 37°C. 1 ml of cells were harvested by centrifugation at each time point as described above and stored at -20°C. Protein production was analyzed in whole cell lysates under denaturing condition. The corresponding cell pellets were resuspended in 100 µl of 20% (w/v) SDS solution at room temperature with vigorous shaking for 15 min. The suspension was centrifuged at 16,000 × g, at room temperature for 20 min (Centrifuge 5415D, Eppendorf) to remove cell debris and genomic DNA. The supernatant was analyzed by SDS-PAGE and Western blot analysis.

2.2.2.2 Determination of the cellular localization of protein

Small-scale membrane preparations were performed to identify the target protein localization (membrane-inserted, cytoplasm or inclusion bodies). 50 ml induced cells were pelleted at 5,000 × g at 4°C for 5 min (Sigma 4K15 centrifuge). The pellet was resuspended in a buffer (20 mM Tris-HCl, pH 7.4, 150 mM NaCl, 1 mM phenylmethyl sulfonyl fluoride [PMSF] and DNaseI) and 1g of 0.5 mm glass beads were added. The mixture was vortexed 8 times for 20 s, keeping on ice with intermediately for 1 min. A low-speed centrifugation (12,000 × g) was used to separate the cell debris and the supernatant (Rotor GSA/SS34, Sorvall RC5B) followed by a high-speed centrifugation (214,000 × g) to separate the soluble fractions and membranes (Ultracentrifuge Optima L-90K). The membranes, soluble fractions and cell debris were analyzed by SDS-PAGE and Western blot with anti-His-tag or anti-step II tag antibodies.

2.2.2.3 Protein production in *E. coli*.

Heterologous production and purification of AaHAS, cytochrome c_{555}^{s}, cytochrome c_{555}^{m} and AaCcO in *E. coli* BL21(DE3) or Top10 was performed using the following steps:

a) 50 ml LB medium (100 ml unbaffled Erlenmeyer flask), supplemented with 100 µg/ml Amp (68 µg/ml Cam also added in the medium for the expression of cytochrome *c*), was inoculated with a single *E. coli* colony isolated from an LB agar plate. This preculture was incubated at 160 rpm and 37°C overnight

(Lab-Shaker, Adolf Kühner).

b) 3×1 ml of the overnight culture were added to 3×50 ml (100 ml unbaffled Erlenmeyer flask) LB medium supplemented with 100 µg/ml Amp (68 µg/ml Cam was also added to the medium for the expression of cytochrome *c*) and incubated at 32°C with shaking at 180 rpm until OD_{600} of 1.0 to 1.4 was reached (8 to 10 h in Shaker CH-4103, Infos-HT).

c) 6×2 liter of LB medium (5 liter unbaffled Erlenmeyer flask), supplemented with 50 µg/ml Amp (34 µg/ml Cam additionally added to the medium for the expression of cytochrome *c*), were inoculated with 6×20 ml of the subculture and incubated at 37°C with shaking at 160 rpm till the OD_{600} reached 0.5. L-arabinose was added to the medium to a final concentration of 0.2% (w/v) for pBAD derived vectors and IPTG was added to the medium to a final concentration of 0.5 mM for pET derived vectors. The culture was incubated at 37°C with shaking at 160 rpm for another 4 h (Shaker CH-4103, Infos-HT).

2.2.2.4 Protein production in *P. stutzeri*

For large-scale heterologous production and purification of AaC*c*O in *P. stutzeri* cells, the culture was grown using a modified protocol for microaerobic growth (152), which was adapted by Sabine Buschmann (MPI of Biophysics, Frankfurt am Main) concerning the contents of trace elements in the asparagine medium (Table 2-4). Cultivation of *P. stutzeri* for large-scale production and purification of AaC*c*O was performed as described below:

a) Single colony selection: 50 µl from glycerol stock of *P. stutzeri* cells were plated on LB agar plates containing 100 µg/ml Amp and 170 µg/ml Cam. The plates were incubated at 32°C overnight (Incubator Biotherm 37, Julabo).

b) Cultivation of a pre-culture: 50 ml of asparagine medium containing 100 µg/ml Amp and 170 µg/ml Cam in a 100 ml baffled Erlenmeyer flask was inoculated with a single colony of *P. stutzeri* and incubated at 180 rpm and 32°C for 4 to 6 h (LabShaker, Adolf Kühner). Then, 2×25 ml of the preculture were added to 2×100 ml of asparagine medium containing 100 µg/ml Amp and 170 µg/ml

Cam in a 300 ml baffled Erlenmeyer flask. The subculture was incubated at 180 rpm and 32°C overnight (Shaker CH-4103, Infors-HT).

c) Lage-scale protein production: 6 × 40 ml of pre-culture was inoculated in 6 × 2 liter of asparagine medium containing 50 µg/ml Amp and 68 µg/ml Cam in a 5 liter baffled Erlenmeyer flask. The culture was incubated at 160 rpm and 32°C for 24 h (Shaker CH-4103, Infors-HT).

The cells were harvested by centrifugation at 10,540 × g at 4°C for 15 min (Centrifuge Avanti J-26XP, Rotor JLA-8.1000, Beckman Coulter). A typical cell yield of *P. stutzeri* was 6 to 10 g of wet cells per liter of asparagine culture. The cells were either directly used for membrane preparation or flash frozen in liquid nitrogen and stored at -80°C.

2.2.2.5 Membrane preparation

For large-scale membrane preparations, cell pellets were resuspended in cell lysis buffer in a ratio of 5 ml lysis buffer (20 mM Tris-HCl, pH 7.4, 150 mM NaCl, 1 mM PMSF, DNAase grade II) for 1 g of wet cells. A dispenser tool (Ultra-Turrax® T25 basic, IKA) was used to homogenize the cell suspension. The homogenized cell suspension was filtered through a porous membrane to remove cell clumps and then passed through a French Press at a pressure of 19,000 psi (40K cell, Thermo Fisher Scientific) for 3 cycles. Alternatively, when the volume of the cell suspension was above 200 ml, a microfluidizer (Microfluidics Corp) was used to disrupt the cells at a pressure of 12,000 psi for 3 cycles. After cell disruption, the cell lysate was centrifuged at 10,000 × g, 4°C for 1 h to remove the cell debris (Rotor GSA/SS34, Sorvall RC5B superspeed centrifuge). The supernatant was then ultracentrifuged at 214,000 × g and 4°C for 3 h (Rotor 70 Ti) or at 450,000 × g for 3 h (Rotor 45 Ti) (Ultracentrifuge Optima L-90K, Beckman Coulter) to get the membranes. The membrane fraction was pelleted and resuspended in the purification buffer (20 mM Tris-HCl, pH 7.4, 150 mM NaCl) to a typical protein concentration of 10 mg/ml. The membrane was directly used for membrane preparation or flash frozen in liquid nitrogen and stored at -80°C.

2.2.2.6 Solubilization of membrane proteins

The crude membranes were resuspended in solubilization buffer (20 mM Tris/HCl, pH 7.5, 150 mM NaCl and 1 mM PMSF) at a protein concentration of 10 mg/ml. The total protein concentration was determined using the bicinchoninic acid assay or the Bradford protein assay. The membrane proteins were solubilized by moderate stirring of the resuspended membranes (10 mg/ml) with 1% (w/v) n-dodecyl-β-D-maltoside (DDM, GLYCON Biochemicals) at 4°C for 1 h. Then, the protein solution was centrifuged at 214,000 × g and 4°C for 60 min (Ultracentrifuge Optima L-90K, Rotor 45 Ti or 70 Ti, Beckman Coulter). The obtained supernatant containing solubilized membrane proteins were filtered through a 0.45 μm polyethersulfone (PES) membrane prior to further purification.

Detergent screening was performed for further studies. The concentration of the total protein in the membrane suspension, the insolubilized pellets and the solubilized membrane were determined by the BCA method.

The detergents used in the membrane solubilization trials are listed in Table 2-17.

Table 2-17: List of detergents used for solubilization screens.

Detergent	Abbreviation	CMC % (w/v)	Concentration for solubilization % (w/v)	Concentration for purification % (w/v)	Company or reference
n-dodecyl-β-D-maltoside	DDM	0.0087	1-2	0.02-0.05	Glycon
n-decyl -β-D-maltoside	DM	0.087	1-2	0.1	Glycon
n-nonyl-β-D glucopyranoside	NG	0.2	1-2	0.3	Glycon
n-octyl-β-D glucopyranoside	OG	0.53	2-6	0.8	Glycon
n-dodecyl-N,N dimethylamine-N-oxide	LDAO	0.026	1-2	0.1	Anatrace
nonaethylene glycol monododecyl ether	$C_{12}E_9$	0.006	1-2	0.01	Sigma
cyclohexyl-hexyl-β-Dmaltoside	Cymal-6	0.028	1-2	0.05	Anatrace
octaethylene glycol monododecyl ether	C10E8	0.11	1-2	0.3	FLUKA
dodecyl-phosphorylcholine	FOS-12	0.053	1-2	0.08	Anatrace
digitonin		0.08	1	0.1	SERVA

2.2.2.7 Protein purification

Cytochrome c_{555}^s and Cytochrome c_{555}^m: Batch purification with Ni-NTA resins (Qiagen) was used to purify cytochrome c_{555}^s and cytochrome c_{555}^m. A final size exclusion chromatographic run was performed using a Superdex 200 10/300 GL column (GE healthcare) and the ÄKTA Purifier system (GE healthcare). Proteins were concentrated using Amicon Ultra devices (Ultra-4 & Ultra-15, 10K MWCO, Millipore).

Heme A synthase: AaHAS production with different vectors was performed (see 2.2.2.3). After membrane preparation and solubilization (see 2.2.2.5 and 2.2.2.6), two chromatographic steps were used to obtain pure and homogeneous heme A synthase. The first step was affinity purification (see 2.2.2.7.1), followed by the second step which was size exclusion chromatography (see 2.2.2.7.3). AaHAS was concentrated using Amicon Ultra devices (Ultra-4 & Ultra-15, 100K MWCO, Millipore).

Cytochrome bc_1 complex and cytochrome c oxidase: Aabc_1 and AaCcO were purified from native *A. aeolicus* membranes. Cultivation of *A. aeolicus* was performed at 85 - 90 ºC in SME medium supplemented with 0.1% thiosulfate under a gas phase of $H_2/CO_2/O_2$ (79/20/1) according to the methods described elsewhere (160,161) by the "Archaeenzentrum" (Regensburg, Germany). *A. aeolicus* cells were stored at -20 °C and resuspended in 20 mM Tris-HCl (pH 7.4) with 5 ml buffer per gram of cells. Cells disruption and membrane preparation are described in 2.2.2.5 and 2.2.2.6. Membrane solubilization was performed according to a previously described protocol for the isolation of ubiquinone oxidoreductase (162). The purification was performed as described below:

a) The membrane was solubilized by moderate stirring (300 rpm) of suspension with 2.5 g DDM per gram of protein at 50°C for 1 h. The detergent solubilized membranes were centrifuged at 40,000 × g for 1 h (Ultracentrifuge Optima L-90K, Rotor 45 Ti or 70 Ti, Beckman Coulter).

b) Ion exchange chromatography (IEC): The supernatant was loaded onto a MonoQ 10/100 GL column (GE Healthcare) which was pre-equilibrated with buffer A listed in table 2-18. Detailed information of IEC is described in

2.2.2.7.2. According to the absorption at 415 nm and 280 nm and the results of Western-blot, fractions containing target proteins were collected and concentrated using Amicon concentrators (Ultra-4 & Ultra-15, 100K MWCO, Millipore) for further purification.

c) Size exclusion chromatography (SEC): The selected and concentrated fractions from IEC were loaded onto a TSK-GEL G4000SW 21.5/30 column (TOSOH Bioscience) connected to an ÄKTA purifier chromatography system (GE Healthcare). Detailed information of SEC is described in 2.2.2.7.3. The main peak fractions were collected for buffer exchange immediately or stored at 4°C. Buffer A listed in table 2-18 was used as running buffer. Afterwards, buffer A was exchanged to buffer B (table 2-18) using a Yarra SEC-4000 column (Phenomenex).

2.2.2.7.1   Affinity purification

Purification of Strep-tagged AaHAS: 0.6 mg avidin per 10 mg solubilized membrane proteins were added to prevent nonspecific binding of free biotin and biotinylated proteins to Strep-Tactin® resins (IBA). Strep-Tactin resins, pre-equilibrated with purification buffer, was added to the detergent solubilized membrane protein solutions (2 ml resin per 100 mg total membrane proteins). The mixture was incubated at 4°C for 60 min with moderate stirring for sufficient binding. Afterwards, the mixture was loaded onto a gravity column (TERUMO) with a flow rate of 0.5 ml/min. The purification was monitored by a single path monitor UV-1 (Pharmacia Biotech) and recorded with a data chart recorder (BD41, Kipp & Zonen). Unbound proteins were washed until the absorbance at 280 nm returned to the baseline, at a flow rate of 1 ml/min. The bound proteins were eluted with buffer C listed in table 2-18 at a flow rate of 1 ml/min. The Strep-Tactin resins were regenerated with buffer D listed in table 2-18. 5 CV, 100 mM Tris buffer at pH 10.5 were used to remove HABA and followed by washing with 5 CVs of degassed water. The regenerated column was stored in 20% ethanol at 4°C.

Purification of His-tagged AaHAS: solubilized membrane proteins were incubated with

Ni-NTA resin (Qiagen), which was pre-equilibrated with buffer E listed in table 2-18, were added into the solubilized membrane proteins solution (2 ml resin per 100 mg total membrane proteins). The mixture was incubated at 4°C for 1 h. The mixture was loaded onto a gravity column (TERUMO) with a flow rate of 0.5 ml/min. The purification was monitored by a single path monitor UV-1 (Pharmacia Biotech) and recorded with a data chart recorder (BD41, Kipp & Zonen). Unbound proteins were washed until the absorbance at 280 nm returned to baseline, at a flow rate of 1 ml/min. The bound proteins were eluted with buffer F listed in table 2-18, at a flow rate of 1 ml/min. The Ni-NTA resins was regenerated with buffer G listed in table 2-18. The regenerated column was stored in 20% ethanol at 4°C.

2.2.2.7.2   Ion exchange chromatography

The sample was directly loaded onto a 10 ml MonoQ 10/100 GL column (GE Healthcare) which was pre-equilibrated with buffer H listed in table 2-18. After washing with 10 column volumes (CV) of buffer H, the bound proteins were eluted with buffer I listed in table 2-18 with a segmented salt gradient. The eluted protein was concentrated using Amicon concentrators (Ultra-4 & Ultra-15, MWCO, Millipore).

2.2.2.7.3   Size exclusion chromatography

Size exclusion chromatography (SEC) was performed according to the manufacturer's guidelines. The protein solution was loaded onto a Superdex 200 10/300 GL column (GE Healthcare), TSK TSK-GEL G4000SW 21.5/30 column (TOSOH Bioscience) or Yarra SEC-4000 column, which was pre-equilibrated with buffer A. The gel filtration chromatography was performed at a flow rate of 0.5 ml/min and the absorbances at 280 nm and 415 nm were monitored. The target protein fractions were collected and concentrated using Amicon concentrators (MWCO, Millipore) and stored at 4°C for further studies. All buffers used are listed in table 2-18.

Table 2-18: List of buffers used for membrane preparation, solubilization and protein purification

Buffer	
Solubilization buffer	20 mM Tris/HCl, pH 7.4, 150 mM NaCl and 1 mM PMSF
Purification buffer	20 mM Tris-HCl, pH 7.4, 150 mM NaCl
Buffer A	Purification buffer + 0.05% DDM
Buffer B	Purification buffer + 0.1% digitonin
Buffer C	Buffer A + 5 mM desthiobiotin
Buffer D	100 mM Tris/HAc, pH 8.0, 1 mM EDTA, 4 mM HABA
Buffer E	Buffer A + 50 mM imidazole
Buffer F	buffer A + 400 mM imidazole
Buffer G	1M imidazole, pH 7.4
Buffer H	20 mM Tris-HCl pH 7.4, 50 mM NaCl, 0.05% DDM
Buffer I	buffer H + 1 M NaCl

2.2.3 Protein characterization methods

2.2.3.2 Determination of protein concentration

The protein concentration was determined by the three methods described as follows:

a) NanoDrop protein quantification: For a rough measurement, protein concentration was determined at absorbance 280 mm using a NanoDrop ND-1000 spectrophotometer measurement (one A_{280} unit = 1 mg/ml).

b) Bicinchoninic acid (BCA) protein assay: This method was performed as published (163). The BCA protein assay buffer was prepared by mixing reagents A and B with a ratio of 1:50 (v/v) (Pierce). The concentration of bovine serum albumin (BSA) ranges from 0.01 to 0.1 mg/ml or from 0.1 to 1 mg/ml were used as a standard. The mixture containing 10 µl of water and BSA standard or of protein sample were pipetted into a 96-Well plate (Nunc) and 200 µl BCA protein assay buffer was added into each well. The plate was incubated at 37°C for 30 min. Measurements were performed two times. The absorbance at 562 nm was recorded with a microtiter plate reader (Trista LB 941 Multimode, Berthold). The protein concentration was calculated by

comprising with the BSA standards. This assay was not used for samples containing imidazole.

c) Bradford protein assay: The Bradford protein assay is based on the binding of the Coomassie dye to protein residues (Arg, Trp, Tyr, His and Phe). Five BSA standard solutions (1 ml each) were prepared (10, 20, 30, 40 and 50 μg/ml). 800 μl of each standard and sample solution were pipetted into clean cuvettes (Sarstedt) and mixed with 200 μl reagent (Bio-Rad), The mixtures were incubated at room temperature from 5 min – 60 min. The absorbance at 595 nm was measured with a spectrophotometer (Spectronic BioMate 3, Thermo). The average of protein concentration was taken from duplicates. This assay was used to determine the concentration of the purified protein in buffers containing imidazole.

Nanodrop protein quantification was used during the membrane preparation and the protein purification. BCA and Bradford protein assay were performed with the purified protein before crystallization and cryo-EM.

2.2.3.2 Denaturing gel electrophoresis (SDS PAGE)

Sodium dodecyl sulfate polyacrylamide gel electrophoresis (SDS-PAGE) was used to analyze the proteins under denaturing conditions. The protein samples mixed with 4 × sample buffers were incubated at RT, 70°C or 90°C for 10 min. The samples were run on NuPAGE® 4-12% Bis-tris gel (Invitrogen) with MES running buffer in a commercial gel chamber (XCell SureLock Mini-Cell, Invitrogen), at 200 V (PowerPac HC power supply, Bio-Rad). The components of 4% and 12% Bis-tris gels are listed in table 2-19 and the solutions used for SDS-PAGE are shown in table 2-20.

Table 2-19: Components of 4% and 12% Bis-tris gels.

Chemicals	4% stock gel	12% resolving gel
30% (w/v) acrylamide/bis solution	340 µl	2 ml
1 M Tris/HCl pH 6.8	350 µl	-
1.5 M Tris/HCl pH 8.8	-	1.25 ml
10 % (w/v) SDS	20 µl	50 µl
TEMED	2 µl	2 µl
10% (w/v) APS	20 µl	50 µl
ddH2O	1.36 ml	1.65 ml
Total volume	2 ml	5 ml

Table 2-20: Solutions used for the SDS-PAGE.

Solutions	Components
4× sample buffer	106 mM Tris HCl
	141 mM Tris Base
	2% LDS
	10% glycerol
	0.51 mM EDTA
	0.22 mM SERVA Blue G250
	0.175 mM phenol red
MES buffer (pH 7.3)	50 mM MES
	50 mM Tris Base
	0.1% SDS
	1 mM EDTA

Coomassie blue staining solution was used to stain the gel at RT and gel destaining was performed with the destaining buffer until the protein bands were clearly visible. The staining and destaining buffer components are described in table 2-21.

Table 2-21: Gel staining and destaining buffer.

Buffer	Components
Staining buffer	0.02% (w/v) Coomassie R-250
	30% (v/v) methanol
	10% (v/v) acetic acid
Destaining buffer	30% (v/v) ethanol
	8% (v/v) acetic acid

2.2.3.3 Non-denaturing polyacrylamide gel electrophoresis (Native PAGE)

Blue native polyacrylamide gel electrophoresis (BN-PAGE) was used to separate protein complexes under native conditions (164). BN-PAGE was performed with precast Native PAGE™ 4-16% Bis-Tris gels with the native PAGE buffer in an XCell

SureLockTM Mini-Cell chamber (Invitrogen). The anode buffer was BN-PAGE running buffer and the cathode buffer was dark blue BN-PAGE buffer (BN-PAGE running buffer + NativePAGE™ Cathode Additive). The protein samples were mixed with 4× BN-PAGE sample buffer and with G-250 (The G-250 concentration was 1/4th of the detergent concentration). A NativeMark protein standard (Invitrogen) was used as the sample proteins. At the beginning, electrophoresis was performed at 150 V at 4°C for 60 min and then changed to 250 V for 90 min (Pharmacia LKB ECPS 3000/150 power supply). The solutions used in the Native PAGE are described in table 2-22.

Table 2-22: Solution used in the Native PAGE.

Solution	Components
4× BN-PAGE sample buffer (pH 7.2)	50 mM Bis-Tris
	6 N HCl
	10% w/v glycerol
	0.001% Ponceau S
	50 mM NaCl
20× BN-PAGE running buffer (pH 6.8)	50 mM Bis-Tris
	50 mM tricine
20× Cathode Additive	0.4% G-250 Coomassie
Cathode buffer	2.5 mM Bis-Tris
	2.5 mM Tricine
	0.02% G-250

2.2.3.4 Heme staining

Heme staining is a specific method to detect c-type hemes after sodium dodecyl sulfate polyacrylamide gel electrophoresis. This method was performed as described elsewhere (165,166). After SDS-PAGE, heme staining solution III was used to briefly wash the gel and then the gel was incubated in freshly prepared 10 ml heme staining solution I and 24 ml heme staining solution II at RT for 60 min with gentle shaking (Orbital-Rocking Shaker 3011, GFL). After washing 2 times with the heme staining solution III, the colour reaction was triggered by adding 204 μl of 30% H_2O_2 and stopped when the bands were visible (2 to 20 min). The solutions used in heme staining procedure are shown in table 2-23.

Table 2-23: Heme staining solution.

Solution	Component
Heme staining solution I	6.3 mM TMBZ in MeOH
Heme staining solution II	0.25 M sodium acetate/HAc, pH 5.0
Heme staining solution III	40% (v/v) MeOH + 60% (v/v) heme staining solution II

2.2.3.5 Western blot

After gel electrophoresis, the gel was washed briefly with ddH$_2$O. The proteins from the gel were transferred to polyvinylidene difluoride (PVDF) membranes using the iBlot® 7-minute Blotting System (Invitrogen) and iBlot® Transfer Stack according to the manufacturer's protocol. Later, the PVDF membranes were incubated in blocking buffer at RT for 1 h or overnight at 4°C. After blocking, the membrane was washed 3 times for 5 min each with 1× TBST buffer. For His or Strep II tagged proteins, the membrane was subjected to immuno-detection using conventional methods with alkaline phosphatase conjugated antibodies at RT for 1 h. Then the membrane was washed three time for 5 min each with 1× TBST buffer and subsequently, with alkaline phosphatase (AP) buffer 3 times under gentle agitation for 5 min. The developer colorimetric reaction was observed according to the colorimetric BCIP-NBT detection system (Thermo Fisher Scientific) until an optimal signal to background ratio was achieved. The reaction was stopped by washing with ddH$_2$O.

For the native proteins, the membrane was incubated with primary antibodies for 2 h, then washed with 1× TBST buffer 3 times for 5 min. Subsequently, the membrane was incubated with the second AP-conjugated antibodies for 1 h. Then the membrane was washed with 1× TBST buffer for 5 min (3 times), and washed with AP buffer 3 times for 5 min. The colour development was performed as described above. The solutions used for the Western blotting are described in table 2-24.

Table 2-24: List of solutions used in Western blot.

Solution	Component
TBST buffer (10×)	100 mM Tris/HCl, pH 8.0
	1.5 M NaCl
	0.5% (v/v) Tween-20
Western blot blocking buffer	2% BSA in 1× TBST buffer
Western blot blocking buffer for Strep II	2% BSA (biotin free) in 1× TBST buffer

Western blot AP buffer	100 mM Tris/HCl, pH 9.5
	100 mM NaCl
	5 mM $MgCl_2$
BCIP-NBT detection buffer	250 µg/ml BCIP (in DMF)
	500 µg/ml NBT (in 70 % DMF)
	in $1\times$ AP buffer

2.2.3.6 Nano differential scanning fluorimetry

Nano differential scanning fluorimetry (NanoDSF) was performed using the Prometheus NT.48 (NanoTemper Technologies) to characterize the stability and folding of protein. This method is based on the fluorescence of tryptophan residues. The concentration of protein used is between 0.5 mg/ml and 2 mg/ml. Measurements were performed using the following settings: 15 to 98°C, 0.5°C/min. The data was analyzed using Origin 9 software.

2.2.3.7 Ultraviolet/visible spectroscopy

Ultraviolet/visible (UV/Vis) spectroscopy was used to determine the concentration and redox state of the heme-containing proteins. The measurements were performed using a Lambda 35 UV/Vis spectrometer (Perkin Elmer) and 10 mm quartz micro-cuvettes (104.002-B, Hellman). Absorption spectra were measured between 380 and 700 nm with a scan rate of 120 nm/min (data interval: 0.2 nm; slit width: 1 nm). For measuring the spectroscopic changes in different redox states, as-isolated protein was oxidized with a 10-fold molar excess of potassium hexacyanoferrate (III) and fully reduced by adding a small amount of sodium dithionite (crystalline powder). The spectra were recorded after different incubation times. The obtained spectra were analyzed using the software Origin 9.

2.2.3.8 Size exclusion chromatography-multi angle light scattering (SEC-MALS)

SEC-MALS measurements were performed at 4°C and the differential refractive-index as well as the UV absorption were recorded (Viscotek SEC-MALS 20, Malvern). A superdex 200 10/300 GL column was used for SEC-MALS analysis at a flow rate of 0.5 ml/min. The column was equilibrated with purification buffer A supplemented by

0.05 %(w/v) DDM or 0.15% (w/v) DM for 16 h, and 150 μl (~ 2 mg/ml) of the protein were loaded onto the column. Data analysis was performed with OmniSEC (Malvern). The specific refractive index increment of the protein was 0.187 ml g^{-1}. The dn/dc value of DDM and DM were taken as 0.133 ml g^{-1} (167) and 0.1473 ml g^{-1} (168) respectively. The extinction coefficient of the protein at 280 nm was calculated using the ProtParam server to 50435 $M^{-1}cm^{-1}$. BSA was used for calibration of the refractometer.

2.2.3.9 Cross-linking

Chemical cross-linking with BS^3 and DSS (Thermo Fisher Scientific) were performed according to the manufacturer's instructions. The cross-linking products were analyzed by SDS-PAGE.

2.2.3.10   Laser-induced liquid bead ion desorption-mass spectrometry

LILBID-MS was performed in collaboration with Nina Morgner (Johann Wolfgang Goethe University of Frankfurt, Germany). Ionization of the biomolecules from the "native solution" into vacuum was achieved by irradiating micro droplets (Ø ~ 50 μm; V ~65 pL) with pulsed infrared laser light (λ= 3 μ). The droplets were passed one by one under pressures of 300 Torr though reduction apertures into 10^{-6} Torr. These are generated in a home-built optical parametric oscillator using $LiNbO_3$ crystals and a ND-YAG laser pump. Afterwards, the ionized biomolecules were analyzed by time-of-flight mass spectrometry. Ultrasoft or harsh operation conditions were used for membrane proteins. AaHAS was degassed and ultrafiltrated before analyzing by LILBID-MS (169). Three independent experiments were performed. The mass analysis was performed by a time of flight mass spectrometer with a Wiley-McLaren-type acceleration region and an ion reflector. The protein concentration used for LILBID-MS was about 2 mg/ml.

2.2.4   Protein Crystallization

Initial crystallization screening of His or Strep II-tagged AaHAS was performed on the Rigaku CrystalMation system in the crystallization unit of the department of molecular

membrane biology (ESFRI-INSTRUCT Core Centre, MPI of Biophysics, Frankfurt am Main). After gel filtration, the purified homogeneous protein was concentrated to a final concentration of 10 mg/ml. For screening, 100 nl protein solution was added to 100 nl reservoir solution using the Phoenix drop setter (Rigaku). The drops were equilibrated against 50 μl reservoir solutions by sitting-drop vapor diffusion at 18 °C. Sparse matrix screens, which were used to test initial conditions for protein crystallization, are listed in Table 2-25. Crystallization trials were incubated over a period of three months and imaged on an automated and regular basis. Evaluation of the crystallization outcome was performed using the software CrystalTrak web (Rigaku) and by manual inspection on a Leica M165C microscope.

Table 2-25: List of crystallization trials.

Trial	Company or reference
MemGold ECO	Molecular Dimensions
MemGold 2 ECO	Molecular Dimensions
PGA Screen CF	Molecular Dimensions
MemSys and Sigma Membrane Kit	Molecular Dimensions
MemStart + MemPlus CF	Molecular Dimensions
MbClass Suite	Qiagen
MbClass II Suite	Qiagen
MPI pHScreen	MPI of Biophysics, Frankfurt am Main
JBScreen Pentaerythritol HTS	Jena Bioscience
PGA Screen	Molecular Dimensions
LCP_Screen_PEG400_Citrate	MPI of Biophysics, Frankfurt am Main
LCP_Screen_Salts	MPI of Biophysics, Frankfurt am Main
Additive Screen / HR2-138	Hampton Research
Detergent Screen HT / HR2-406	Hampton Research
MemAdvantage / MD1-70	Molecular Dimensions

2.2.5 Electron microscopy

2.2.5.1 Negative staining

For even distribution of protein particles carbon coated TEM grids were first negatively glow discharged under H_2 and O_2 mixtures in a Gatan Solarus glow discharge system for 1 min, which creates a hydrophilic surface on the grids. To allow the protein absorb to the carbon, 5 μl of a 0.01 mg/ml protein sample was loaded on the grid for 1 minute.

Blotting the gird with filter paper was performed to remove excess sample. The grid was washed 5 times with ddH2O which was filtered by 0.22 µm filter. A drop of 2% (w/v) uranyl acetate (pH 4.5) was loaded to cover the grid for 1 min and the excess uranyl acetate was removed by carefully blotting with filter paper from the side. Digital micrographs were collected on a FEI Biotwin microscope operated at 120 kV.

2.2.5.2 Cryo freezing

Protein vitrification was achieved using a FEI vitrobot 3 µl of the freshly purified complex sample (1.5 mg/ml) was applied to glow-discharged holy carbon film grids (GIG Au R 1/1, 300 mesh), which were treated under H_2 and O_2 mixtures in Gatan Solarus for 1 min. Grids were blotted at 16°C and 100% humidity for 3 s. To get high resolution protein structures, grids were frozen in liquid ethane to make vitrified samples in a thin layer of ice and then stored in liquid nitrogen.

2.2.5.3 Cryo-EM Data Acquisition

For cryo-EM, high resolution images were collected on a 300 kV FEI Titan Krios transmission electron microscope using SerialEM software (170) on a K2 detector, with super-resolution counting mode at a calibrated magnification of 59,000 × (yielding a pixel size of 0.52 Å) and a dose rate of 8.45 e-/ $Å^2$/s. A quantum energy filter (Gatan, 107 Pleasanton, CA), whose energy slot was set to 20 keV, was applied to remove any inelastic scattering. Defocus values varied from -1.5 to -2.5 µm. Frame alignment, exposure weighting, and contrast transfer function parameters estimation were performed using Center for Bio-imaging platform's automated data collection scripts (Institute of Biophysics Chinese Academy of Sciences) integrated with Motioncor2 (171) and CTFFIND4 (172) during movie data collection.

2.2.5.4 Cryo-EM Data processing

Image processing was performed using RELION (version 2.1 and version 3.0-beta) (153,154) and EMAN2 (155). A low-resolution reconstruction of the complex was built from negatively-stained sample. Particle picking was performed using Gautomatch (http://www.mrc-lmb.cam.ac.uk/kzhang/Gautomatch/) without template. Reference-

free classification was performed. One class was selected as initial model for subsequent cryo-EM data processing. Gautomatch was used to pick around 20k particles of 200 good quality images without template matching. After one round of reference-free 2D classification, 10 representative classes were used as reference for automatic particle picking of all micrographs. The particles were extracted using a 128 × 128 pixel-box and sorted by two rounds of 2D classification. Then particles from good 2D classes were selected and used for the 3D classification, with the previously generated initial model as reference. After a second round of 3D classification without alignment, one best class was selected for the final refinement.

Refinement with those particles yielded the cryo-EM density map. Then CtfRefine and Bayesian polishing were used to further optimize the resolution.

2.2.5.5 Model building and refinement

The regions and side chains of the protein in the map were checked using COOT (173). The ligands and phospholipids were docked into densities and refined using COOT and Phenix (174).

2.2.6 Activity assay

Quinol oxidation/cytochrome *c* reduction

Oxidation of decylubiquinol and reduction of cytochrome *c* were recorded at 80 °C using a spectroscopic system (Agilent 8453 UV-visible) following a procedure described elsewhere (175) with slight modifications. The reaction buffer contained 30 mM KPi (pH 7.0) and 0.05% DDM. The activity assay was started by adding 6 μl of decylubiquinol (final concentration 45 μM) to the reaction mixture (94 μl of reaction buffer containing 23 pM (0.5 µg) Cox2, 60 μM air oxidized cytochrome c_{555}^{m} or cytochrome c_{555}^{s}, 0.2 mM EDTA, 1 mM KCN and 250 mM sucrose). Activities were calculated using extinction coefficients of 12.5 $mM^{-1}cm^{-1}$ for ubiquinol (176) and of 19 $mM^{-1}cm^{-1}$ for cytochrome *c* (177).

3 Results

Several structures of supercomplexes containing cytochrome c oxidase and cytochrome bc_1 complexes have been reported and those structures suggested a mechanism of ECT (99,100,178,179). Previous work suggested that the AaCcO and the Aabc_1 can form a supercomplex in *A. aeolicus* (149,180). However, so far, the structures of AaCcO and Aabc_1 were missing. To better understand their functions, the structures of these two enzymes were determined in this work. At the same time, I also set up a heterologous expression system to investigate the function and structure of AaHAS which plays very important role in cytochrome c oxidase assembly. The cryo-EM structure of AaHAS trimer was determined at 2.8 Å resolution.

3.1 Characterization of AaCcO

3.1.1 Heterologous expression and purification of AaCcO and cytochrome c_{555}

3.1.1.1 Construction of expression vectors

The genome sequence of *A. aeolicus* has been published (135). *A. aeolicus* contains two CcO operons (*Cox1* and *Cox2*). The function of Cox2 was characterized (149,180,181), while Cox1 has never been detected. Cox2 possesses three subunits: CoxA2, CoxB2 and IIa (149). The following primers pairs were designed to amplify Cox2: IIa-NdeI-F/CoxA2-XhoI-R.

There are two genes encoding cytochrome c: *cycB1* and *cycB2* (135,182-184). The gene product of *cycB1* is cytochrome c_{555}^{m} (hereafter named c_{555}^{m}) which is a membrane attached cytochrome. *cycB2* encodes the soluble cytochrome c_{555}^{s} (hereafter named c_{555}^{s}). Following primers were used: CycB1-NdeI-F/CycB1-R for *cycB1*, CycB1-NSP-NcoI-F/CycB1-R for *cycB1*Δ18 (without the first 18 amino acids which are responsible for attachment to the membrane), and CycB2-NcoI-F/CycB2-XhoI-R for *cycB2*.

To construct the expression vectors for AaCcO, c_{555}^{m}, $c_{555}^{m}\Delta18$ and c_{555}^{s}, the amplified DNA fragments containing *Cox2*, *cycB1*, *cycB1Δ18* and *cycB2* were cloned into plasmid pJET1.2, respectively, resulting in the four subcloning vectors pJET1.2-CcO, pJET1.2-C$_{555}^{m}$, pJET1.2-C$_{552}^{m}$-ΔN18 and pJET1.2-C$_{555}^{s}$. The subcloning vectors pJET1.2-CcO and pJET1.2-C$_{555}^{m}$ were digested with the NdeI and XhoI endonucleases, and subcloned into the same site of pET-22b (+), resulting in pZH-22-CcO and pZH-22- C$_{555}^{m}$ (Figure 3-1). The subcloning vectors pJET1.2-C$_{555}^{m}$-ΔN18 and pJET1.2-C$_{555}^{s}$ were digested with NcoI and XhoI endonucleases, and subcloned into the same site of pET-22b (+), resulting in pZH-22- C$_{555}^{m}$-ΔN18 and pZH-22- C$_{555}^{s}$, respectively (Figure 3-1). For AaCcO, His$_6$-tag or Strep-tag II was fused to different subunits by site-directed mutagenesis (Figure 3-1). The *ctaA* (encoding for AaHAS) gene was also amplified using primers CtaA NcoI-F/CtaA EcoRI-R. The co-expression vector pETDuet contains two multiple cloning sites (MCS), each of which is preceded by a T7 promoter/lac operator and a ribosome binding site (rbs). Subsequently, the amplified DNA fragment *ctaA* was digested with NcoI and EcoRI endonucleases, subcloned into the same site of pETDuet in one MCS, resulting in vector pETDuet-CtaA. Subsequently, a Strep-tag II was fused to the C-terminal end of AaHAS by site-directed mutagenesis, generating the subcloning vector pETDuet-CtaA-C-Strep. The amplified DNA fragment *Cox2* was digested with NdeI and XhoI endonucleases, subcloned into the same site of pETDuet-CtaA-C-Strep in another MCS, generating vector pZH- CtaA-C-Strep II-CcO-CoxA2. Finally, a His$_6$ tag was fused to the C-terminal end of CoxA2 by site-directed mutagenesis, generating the expression vector pZH- CtaA-C-Strep II-CcO-CoxA2-C-His.

In this work, *P. stutzeri* strain ZoBell was also tested as an expression host. Primers pXH22-F/pXH22-R were used to linearize the vector pXH22. With pZH-22-CcO as template, primers CoxA2-N-Strep II-F/CoxA2-N-Strep II-R, CoxA2-N-His-F/CoxA2-N-His-R, CoxA2-C-His-F/CoxA2-C-His-R and CoxA2-C-Strep II-F/CoxA2-C-Strep II-R were used to amplify DNA fragments encoding N-terminal Strep- and His-tagged, and C-terminal Strep- and His-tagged Cox2, respectively. Those DNA fragments were cloned separately into the linearized pXH22 using ligation independent cloning method

to construct the expression vectors pZH-C*c*O-CoxA2-N-Strep II, pZH-C*c*O-CoxA2-N-His, pZH-C*c*O-CoxA2-C-Strep II and pZH-C*c*O-CoxA2-C-His (Figure 3-1).
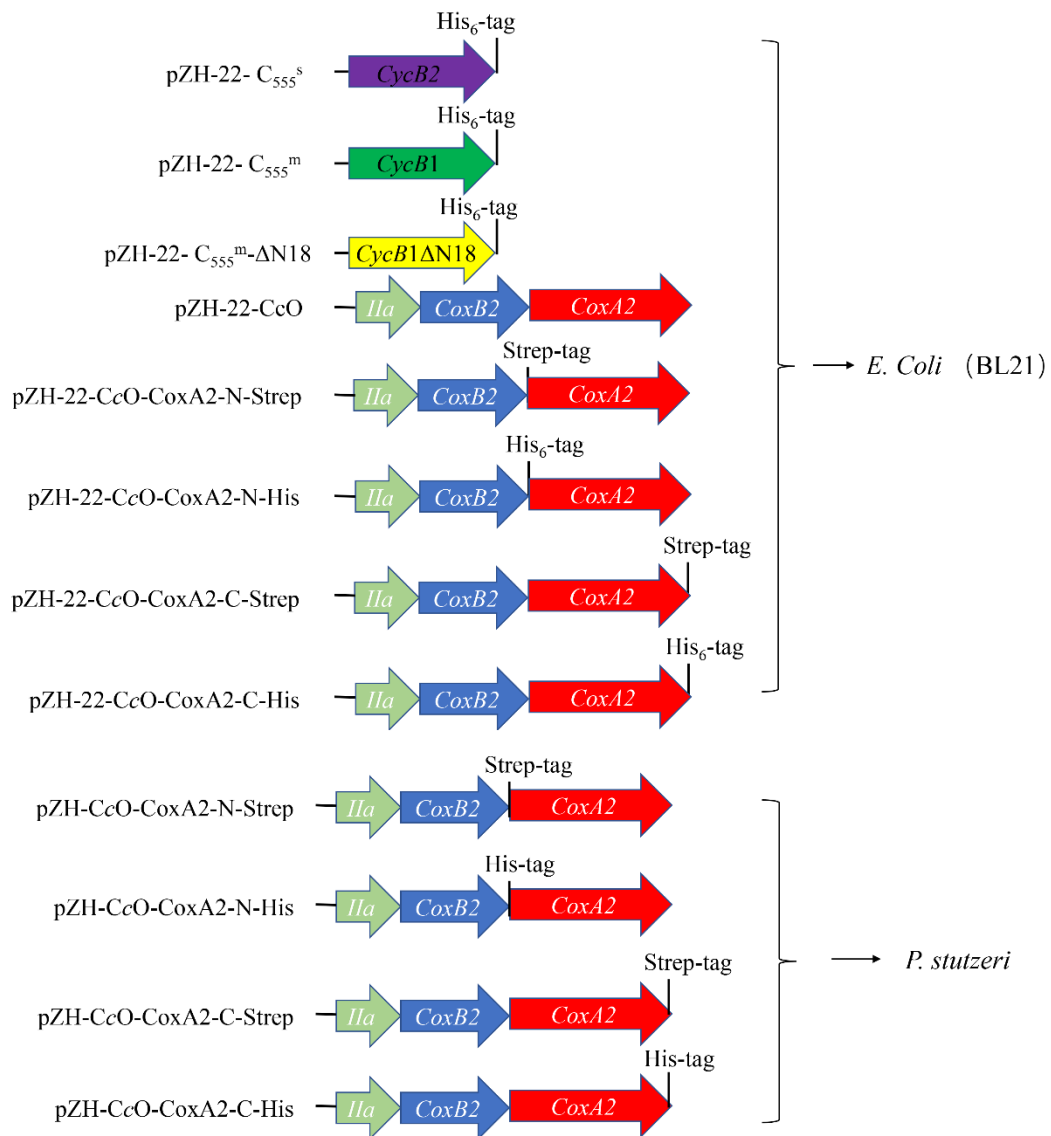

Figure 3-1: Schematic summary of the expression vectors used for the expression of AaC*c*O, c_{555}^{m}, $c_{555}^{m}\Delta18$ and c_{555}^{s}. Only the target operon sequence region is shown. The tag and its position are shown. The pET-22 and pXH derivative vectors are transferred into *E. coli* (BL21) and *P. stutzeri* cells, respectively.

For using the *E. coli* (BL21) expression system, all constructed expression vectors were transferred into competent cells using the heat shock method. For the expression of cytochrome c_{555}, the proteins were coexpressed with the *ccm* proteins from pEC86 (kindly provided by Linda Thöny-Meyer). The *ccm* proteins are responsible for heme insertion and cytochrome *c* maturation (185). The pXH derivative expression vectors

were electroporated into *P. stutzeri* cells. All the recombinant strains were used to produce target proteins.

3.1.1.2 Production of cytochrome c_{555} and AaCcO

For production of cytochrome c_{555}, only the *E. coli* system was used. The production of cytochrome c_{555} was detected by Western-blot analysis with α-poly-histidine-alkaline phosphatase conjugated antibody. Heterologous production of c_{555} could be achieved by all expression vectors and the pelleted cells were red, suggesting that heme c is incorporated successfully in the target cytochrome c_{555} (Figure 3-2). The production conditions of cytochrome c_{555} were further optimized by screening IPTG concentration (0-1 mM) and induction time (3-16 h), and cultivation temperature (18°C, 30°C, 37°C). Finally, the highest yield was achieved using 0.05 mM IPTG at 37°C for 4 h.
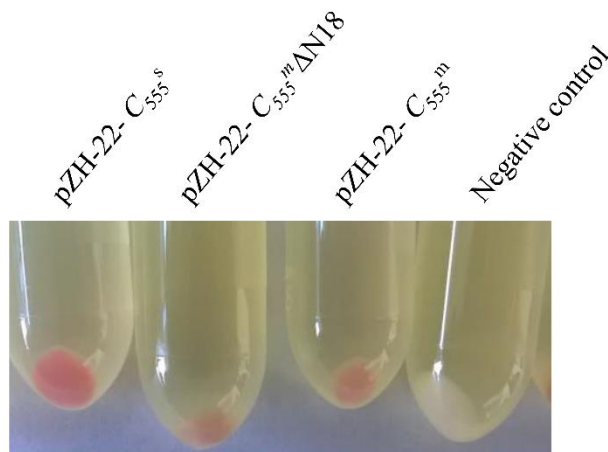

Figure 3-2: Production of cytochrome c_{555}. Cells were pelleted from 2 ml culture after induction with 0.5 mM IPTG for 4 h by centrifugation at $12,000 \times g$ for 20 min.

Two systems with related expression vectors (pXH derivative vectors for *P. stuteri*, pET22 derivative vectors for *E. coli*) were used to express AaCcO. The production of Cox2 was detected by Western-blot analysis with an anti CoxA2 antibody. Only C-terminal His-tagged Cox A2 was produced in *E. coli* (BL21) strain (Figure 3-3A). Interestingly, production of C-terminal or untagged CoxA2 can be detected using *P. stutzeri*, while no production of N-terminal tagged CoxA2 can be detected (Figure 3-3 B) can be detected. The different results of N- and C-terminal CoxA2 suggested that the tag positions influence the protein production. Compared to the *E. coli* (BL21) system, the Western-blot results also suggest that C-terminal Strep-tag II may also influence CoxA2 production. Therefore, the results suggest that pZH-CcO-CoxA2-C-

His is the best vector to produce AaC*c*O in *P. stutzeri*.
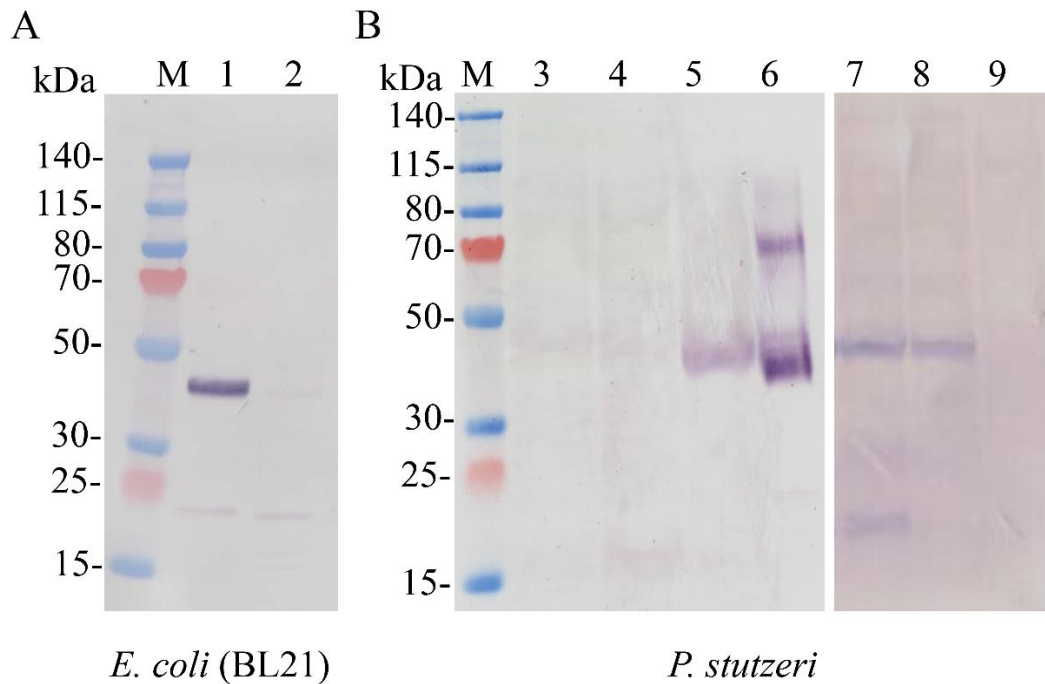

E. coli (BL21) P. stutzeri

Figure 3-3: Production of AaC*c*O. (A) Only C-terminal His-tagged CoxA2, which was expressed in *E. coli* (BL21), was detected by Western-blot. (B) CoxA2 can be detected when the expression vectors pZH-C*c*O, pZH-C*c*O-CoxA2-C-His and pZH-C*c*O-CoxA2-C-Strep II are used. Purified CoxA2 from the native membrane as positive control and wild type *P. stutzeri* lysate as negative control. All Western-blot were performed using Anti-CoxA2 antibody. M: PageRuler Prestained protein standard. 1: pZH-22-C*c*O-CoxA2-C-His; 2: Empty vector (negative control); 3: pZH-C*c*O-CoxA2-N-His; 4: pZH-C*c*O-CoxA2-N-Strep II; 5: vector of pZH-C*c*O; 6: Native AaC*c*O (positive control); 7: pZH-C*c*O-CoxA2-C-His; 8: pZH-C*c*O-CoxA2-C-Strep II; 9: Empty vector (negative control).

Considering that there is no heme A synthase in *E. coli*, the expression vector pZH-CtaA-C-Strep II-C*c*O-CoxA2-C-His was used to co-express AaHAS and Cox2 (Figure 3-4).
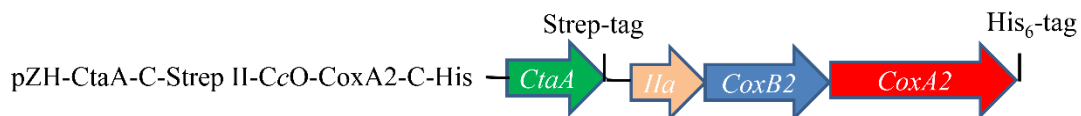

Figure 3-4: Schematic summary of the co-expression vector for AaC*c*O and AaHAS. Only the target operon sequence region is shown. The tags position are shown.

The expression vector pZH-CtaA-C-Strep II-C*c*O-CoxA2-C-His was introduced into *E. coli* (BL21). The production of the target proteins was induced by adding 0.5 mM IPTG

when the OD_{600} reached 0.5. The culture was incubated at 160 rpm, 30°C, for 4 h and the cells were harvested by centrifugation at 10,540 × g at 4°C for 15 min. Then cell lysate was analyzed by Western-blot. CoxA2 expression was detected using Anti-CoxA2 antibody. Strep-tagged AaHAS was detected by chemiluminescence reaction using Strep-Tactin horse radish peroxidase (HRP) conjugate. The results showed that AaHAS can be expressed, however, no Cox2 can be detected (Figure 3-5).
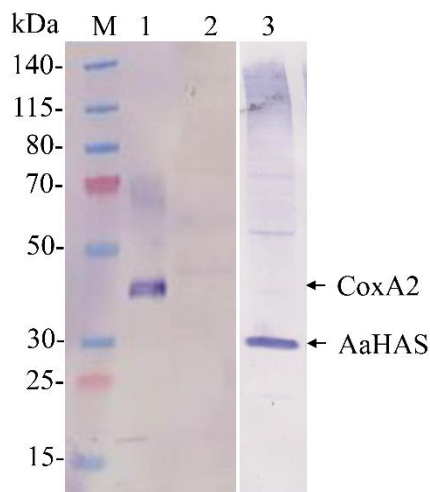

Figure 3-5: Co-expression of AaC*c*O and AaHAS in *E. coli* (BL21). The position of CoxA2 and AaHAS are marked. Lane 1: Native AaC*c*O. After inducing with IPTG, cell lysates of *E. coli* (BL21) were analyzed by Western-blot with Anti-CoxA2 antibody (lane 2) and Strep-Tactin horse radish peroxidase (HRP) conjugate (lane 3). M: molecular mass marker.

3.1.1.3 Purification of AaC*c*O from *P. stutzeri* and recombinant cytochrome c_{555} from *E. coli*

The co-expression results showed that there is no chance to get functional AaC*c*O from the *E. coli* (BL21) heterologous system. Therefore, I focued on the *P. stutzeri* system for the heterologous production of AaC*c*O. After screening the expression vectors, the *P. stutzeri* strain containing vector pZH-C*c*O-CoxA2-C-His was used to express AaC*c*O. For details on the production of AaC*c*O see the method section 2.2.2.4. Membrane preparation and solubilization were performed as described in method section (2.2.2.5 and 2.2.2.6). The supernatant contained the solubilized AaC*c*O. Imidazole was added to the supernatant containing the solubilized AaC*c*O, to a final concentration of 20 mM to avoid unspecific binding. Immobilized metal-ion affinity chromatography (IMAC) resin was added to the solution with a ratio of 1:10 (v/w). The binding was performed at 4°C for 1 h with constant rotation. Stepwise elution with different concentrations of imidazole was used to elute the His-tagged AaC*c*O. The eluate of His-tagged AaC*c*O was analyzed by Western-blot (Figure 3-6). CoxA2 and CoxB2 were only detected in

the elution fraction with 150 mM imidazole, suggesting that this fraction may contain
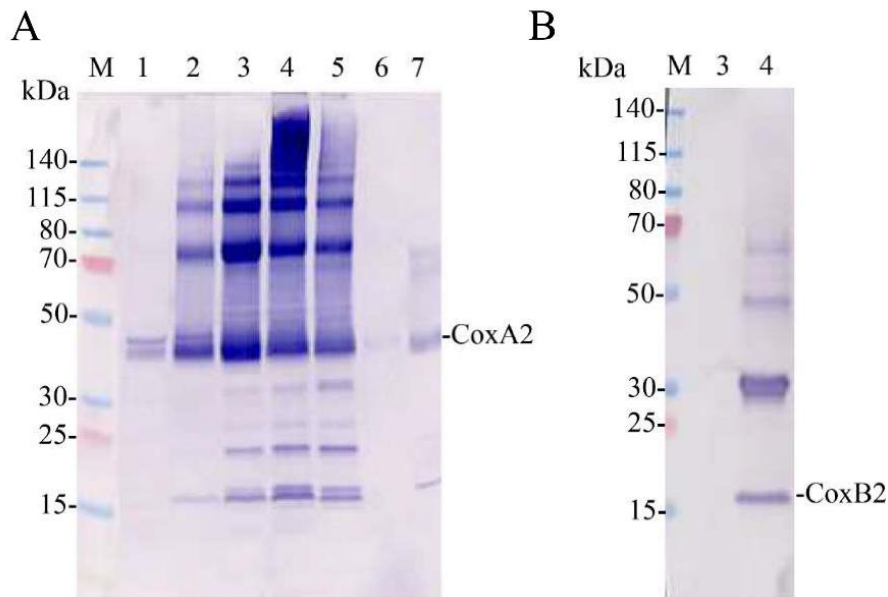Cox2.

Figure 3-6: CoxA2 and CoxB2 can form a subcomplex. (A) Anti-CoxA2 antibody was used to detect the
expression of CoxA2. (B) Anti-CoxB2 antibody was used to detect the expression of CoxB2. M:
PageRuler Prestained protein ladder) are indicated on the left. 1: 5 mM imidazole eluate; 2: 50 mM
imidazole elution; 3: 100 mM imidazole eluate; 4: 150 mM imidazole eluate; 5: 250 mM imidazole
elution; 6: 500 mM imidazole eluate; 7: Native AaCcO. Bands of interest (subunit CoxA2 and CoxB2)
are indicated.

The fraction was pooled and loaded on to a superdex 200 10/300 GL column. The
profile of SEC shows three main peaks according to the absorption at 280 nm, however,
only one peak shows to absorption at 415 nm (Figure 3-7 A). The main peak fractions
were analyzed by Western-blot with anti-CoxA2 and anti-CoxB2 antibodies (Figure 3-
7 B and C). Both CoxA2 and CoxB2 can be detected in the fraction 3 and 4, suggesting
that CoxA2 and CoxB2 can form a complex. Fraction 3 was eluted at 8 ml, suggesting
that it contained aggregated protein. The proteins in fraction 4 do not show heme
absorption. Fraction 4 was analyzed by Native-PAGE. The main band was observed at
around 480 kDa (Figure 3-7 D).
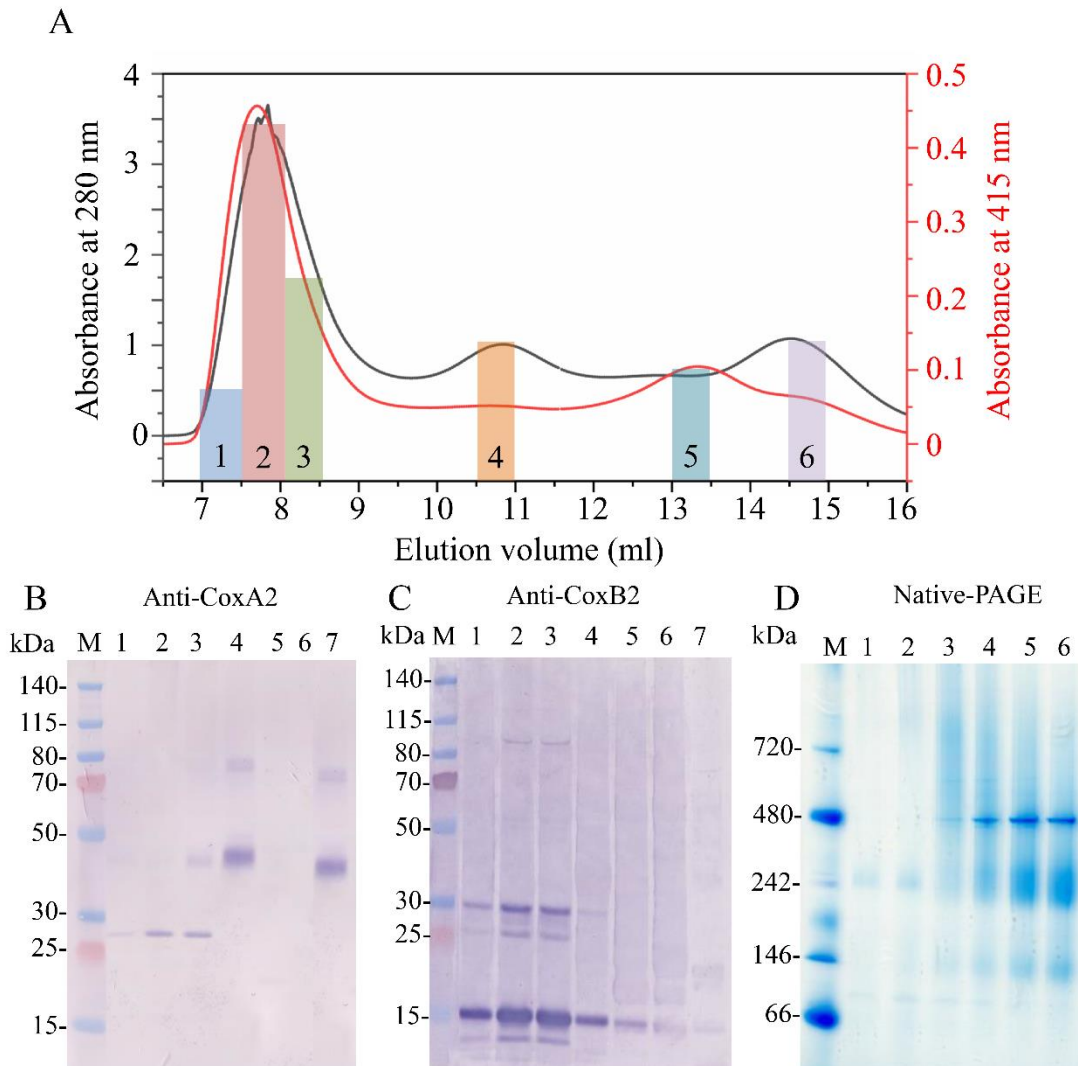
Figure 3-7: Purification of recombinant AaC*c*O from *P. stutzeri*. (A) SEC profile of 150 mM imidazole elution. The absorption at 280 nm and 415 nm were monitored. The fractions marked in different colors (1, 2, 3, 4, 5 and 6) were used for Western blots with anti-CoxA2 antibody (B) and anti-CoxB2 (C), and native-PAGE analysis. M: PageRuler Prestained protein ladder and Native marker are indicated on the left. 7: Native AaC*c*O.

To confirm the expression of Cox2, the fraction 4 was sent for mass spectrometric analysis. Peptides of CoxA2 and CoxB2 were detected in the fraction (data not shown). The UV-vis difference spectra were recorded (Figure 3-8). The typical heme A absorption at 451 nm was missing (149), suggesting that there is no heme A in the heterologously expressed AaC*c*O. The result of UV-vis spectroscopy is in line with the observation of SEC. All results permit the following conclusion: AaC*c*O can be expressed and may form a complex which misses heme A.

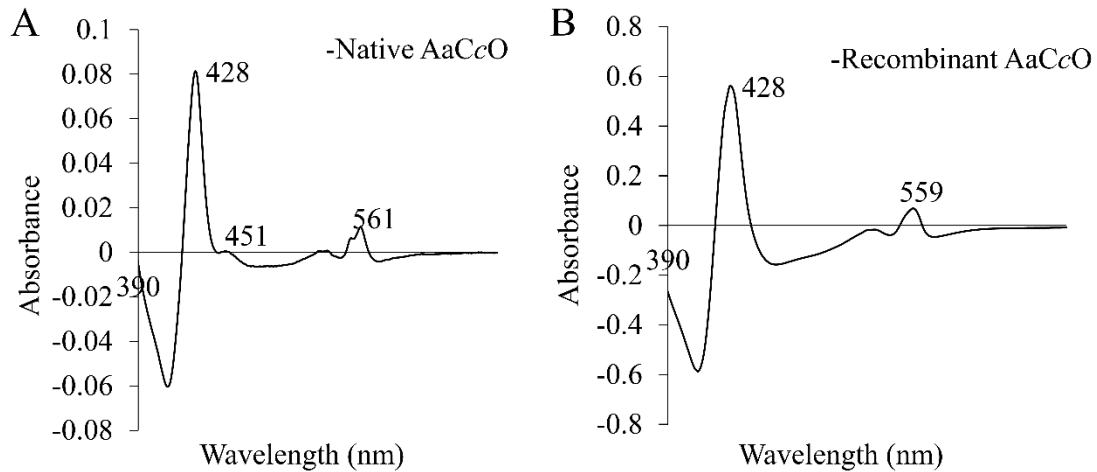Figure 3-8: UV-visible redox difference spectra of the native AaC*c*O and recombinant AaC*c*O. (A) UV-visible redox difference spectra of the native C*c*O. (B) difference spectrum of recombinant AaC*c*O. The typical high spin heme a_3 absorption band was shown at 451 nm.

Recombinant cytochrome c_{555} was purified using affinity chromatography and subsequent size exclusion chromatography. Three different cytochrome c_{555}'s were incubation with nickel-charged resin in a buffer with 100 mM imidazole and eluted with 400 mM imidazole, respectively. The peak fractions were collected and subjected to SEC. Figure 3-9A-C shows the typical SEC profiles of c_{555}^m, $c_{555}^m\Delta18$ and c_{555}^s, respectively. After a two-step purification, the recombinant c_{555}^m and c_{555}^s were purified to highest homogeneity, as only single dominant bands can be observed on SDS-PAGE gels stained for hemes and proteins (Figure 3-9 D-E). However, heme staining (Figure 3-9 D) and Coomassie staining (Figure 3-9 E) showed that $c_{555}^m\Delta18$ was degraded. Purified $c_{555}^m\Delta18$ could not be detected with anti-his antibody using Western blot analysis (Figure 3-9 F). All results suggest c_{555}^m and c_{555}^s can be expressed and purified.
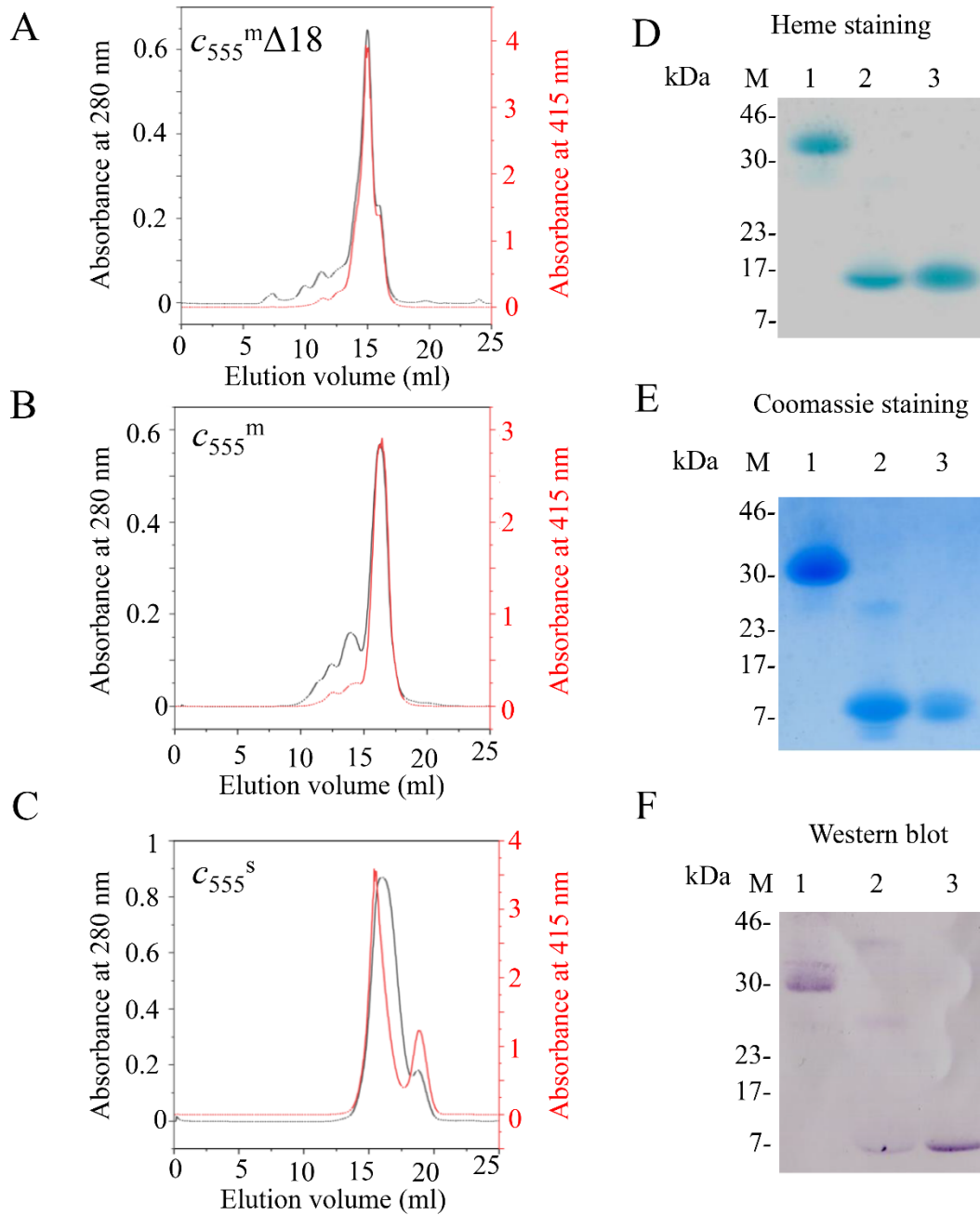
Figure 3-9: Purification of cytochrome c_{555}. Size exchange chromatography (superdex 200 column) elution profile of $c_{555}^m\Delta18$, c_{555}^m and c_{555}^s are shown in (A), (B) and (C), respectively. During all purification steps, fractions were monitored at 280 nm (black) and 415 nm (red). Heme staining (D), Coomassie staining (E) and Western blot (F) were used to visualize the protein bands. "M" is the PageRuler Prestained Protein Ladder and the molecular weights of the marker proteins are shown in kDa.

MALDI-MS was used to identify c_{555}^m and c_{555}^s (Figure 3-10). c_{555}^m and c_{555}^s can be detected as 18247.564 m/z and 11060.970 m/z, respectively.
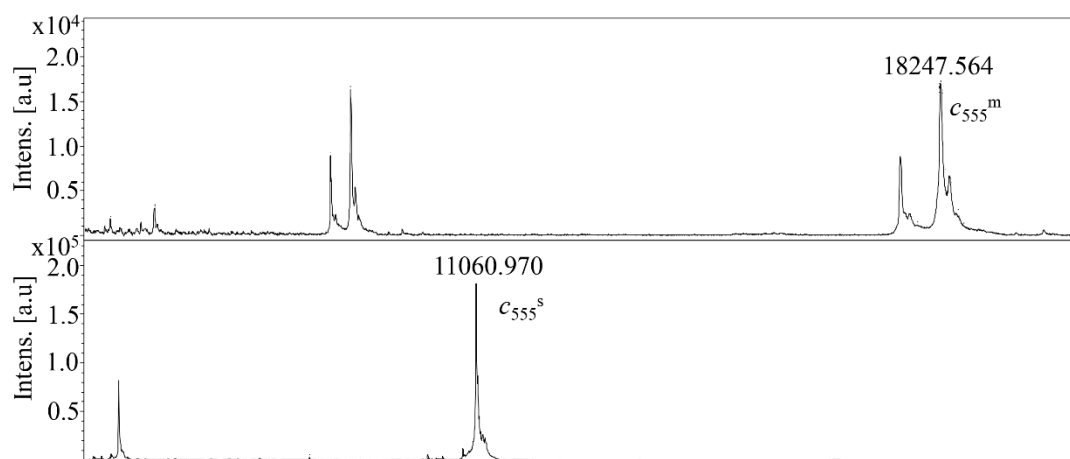
Figure 3-10: MALDI-MS spectra of cytochrome c_{555}^m and cytochrome c_{555}^s. The m/z values of the main peaks are marked and correspond to c_{555}^m and c_{555}^s, respectively.

3.1.2 Purification of AaC*c*O from native membranes

In order to investigate the structure and function of AaC*c*O, I also tried to purify AaC*c*O from the native *A. aeolicus* membranes. AaC*c*O from *A. aeolicus* was solubilized and purified as described previously (162) with minor modifications. Membrane proteins were solubilized using DDM and separated by MonoQ exchange chromatography (Figure 3-11). Fractions from MonoQ 10/100 GL were analyzed by SDS-PAGE and MALDI-MS. Those fractions, which contain Aa*bc*$_1$ and AaC*c*O, were collected ("I" for Aa*bc*$_1$ and "II" for AaC*c*O in Figure 3-11).

Figure 3-11: Separation of native *A. aeolicus* membrane proteins by ion exchange chromatography. Fractions "I" colored in green were used to purify cytochrome *bc*$_1$ and fractions "II" colored in purple were used to purify cytochrome *c* oxidase.

Fractions "II" were subjected to TSK-GEL G4000SW 21.5/30 SEC (Figure 3-12 A). Then yellow marked fractions B10 and B11 were pooled and subjected to Yarra SEC-4000, shifting detergent from DDM to digitonin (Figure 3-12 B). The main fractions 13 and 14 were collected and used for functional and structural stud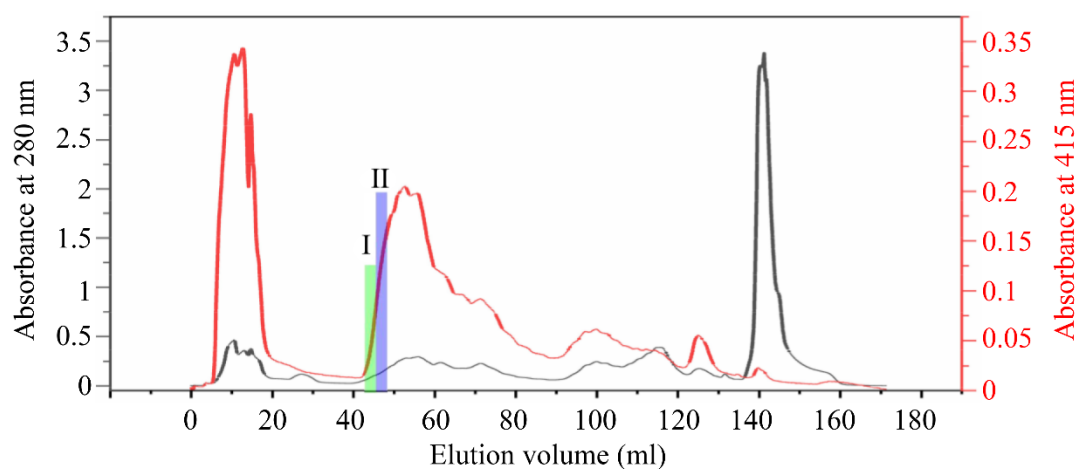ies. Proteins in fractions 13 and 14 were separated on SDS-PAGE. After staining with Coomassie blue, protein bands corresponding to CoxA2 and CoxB2 were observed (Figure 3-12 C). The subunit IIa can not be observed, because of its low molecular weight (5.2 kDa) and poor staining property.
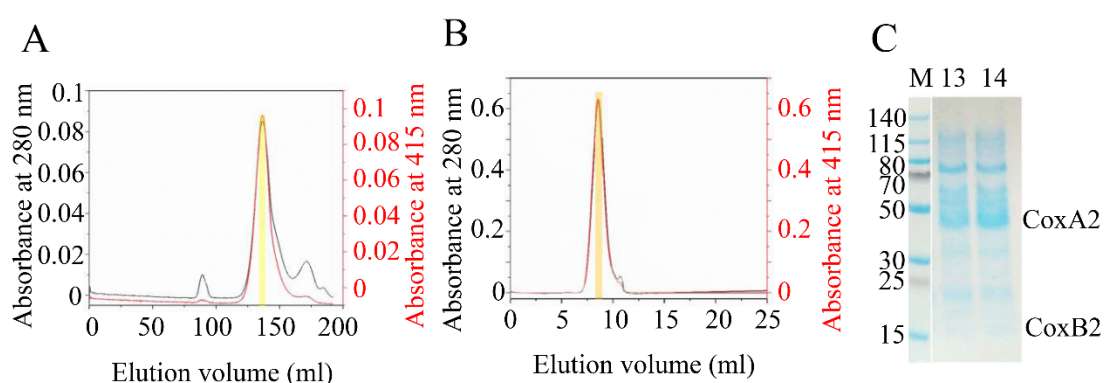
Figure 3-12: Purification of native AaCcO. (A) Separation of membrane proteins by size exclusion chromatography with TSK-GEL G4000SW 21.5/30 SEC. The fractions colored in yellow were pooled and used to purify native AaCcO. (B) Size exclusion chromatography profile of native AaCcO with Yarra SEC-4000. Fractions 13 and 14 are colored in orange and were analyzed by SDS-PAGE (C). M: PageRuler Prestained protein ladder. Bands of interest (CoxA2 and CoxB2) are marked on the right.

3.1.3 Functional analysis of AaCcO

The activity of Cox2 had been characterized previously (149). However, the horse heart cytochrome c used in that study is not the native electron donor of AaCcO. Here, I performed the activity assay of this enzyme with its native electron donor cytochrome c_{555}. The oxidation of cytochrome c was monitored by the absorption changes of cytochrome c in the UV-visible region. No significant difference in activity of Cox2 with c_{555}^{m} and c_{555}^{s} was observed. Therefore, only the c_{555}^{s} is shown as an example for the activity assay (Figure 3-13). As shown in the Figure 3-13, the activity can be further inhibited by adding 1 mM KCN.

Figure 3-13: Activity of Cox2 with its natural substrate cytochrome c_{555}. The activity was initiated by adding reduced cytochrome c_{555} (A) and the reaction can be inhibited by adding KCN (B). The reactions were recorded at 80 °C and the activity was determined by measuring the absorbance at 550 nm minus 540 nm.

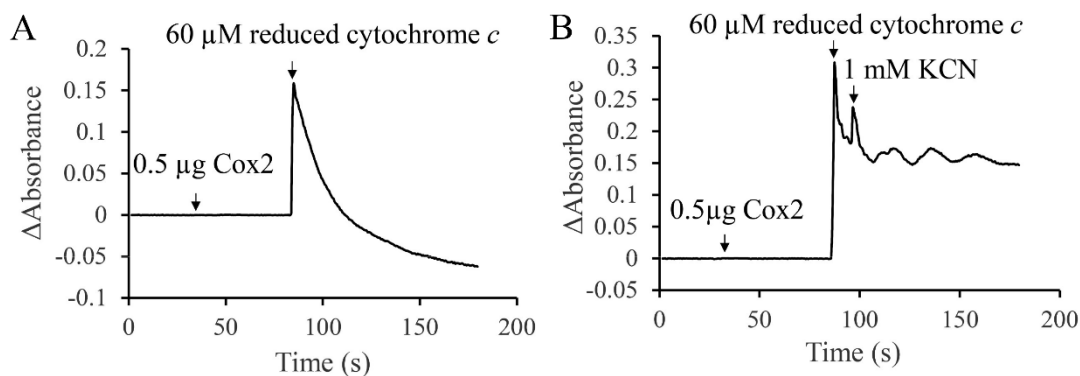After adding cytochrome c_{555}, the initial 20 s data were used to calculate the activity of Cox2. Turnover measured with cytochrome c_{555} is 24 e s^{-1} which is 14 times higher compared to the published data using heart cytochrome c as substrate (149). All results indicate that the purified Cox2 can use recombinant cytochrome c_{555} as electron donor.

3.1.4   Structure of AaCcO

3.1.4.1 Overall structure

The EM data collection, image processing and model building are summarized in table 3-1. After high-resolution refinement with 195,313 particles, the dimeric structure of AaCcO was determined at 3.4 Å according to the gold standard Fourier shell correlation (FSC$_{0.143}$) criterion. It has dimensions of ~84.7 Å in height and of 107.7 Å in length (Figure 3-14A). The length of monomeric AaCcO is 54.9 Å. The subunits CoxA2, CoxB2 and IIa are identified. Surprisingly, CoxA2 contains an extra domain composed of TMH13 and TMH14, probably to enhance the protein stability (Figure 3-14A). The cofactors Cu$_A$, Cu$_B$, heme a_3 and heme b are shown in Figure 3-14B. The distance between Cu$_A$ atom CU2 (located closer to the heme b) and heme b Fe is 19.76 Å which is larger than described for the ba_3-type cytochrome c oxidase from $T.$ $thermophilus$. Two molecules of 1,4-naphthoquinone (NQ) and cardiolipin (CL) are observed in the dimer face. Its overall structure is similar to that of the ba_3-type CcO from $T.$

thermophilus with root mean square deviations (r.m.s.d.) of the C_α-atoms of 1.02 Å.

Table 3-1: Statistics of data collection, image processing and model building

Sample	The *ba3*-cytochrome c oxidase
Data collection	
EM equipment	FEI Titan Krios
Voltage (KV)	300
Detector	Gatan Bioquantum K2
Energy filter	20 eV
Pixel size (Å/pixel)	1.04
Electron dose ($e^-/Å^2$)	60
Defocus range (μm)	-1.5~-2.5
Reconstruction	
Software	RELION 3.0-beta / RELION 2.0
Number of used particles	32,982
Accuracy of rotation	2.526
Accuracy of translations (pixel)	0.891
Symmetry	C2
Map sharpening B-factor ($Å^2$)	-85
Final resolution (Å)	3.41
Model building	
Software	Coot
Model Refinement	
Software	PHENIX
Map CC (whole unit cell)	0.80
Map CC (around atoms)	0.71
Rmsd (bonds) (Å)	0.005
Rmsd (angle) (°)	0.845
Model composition	
Protein residues	1,528
Heme groups	4
Cu center	4
Validation	
Ramachandran plot	
Outliers (%)	0.26
Allowed (%)	12.17
Favored (%)	87.57
Rotamer outliers (%)	1.48

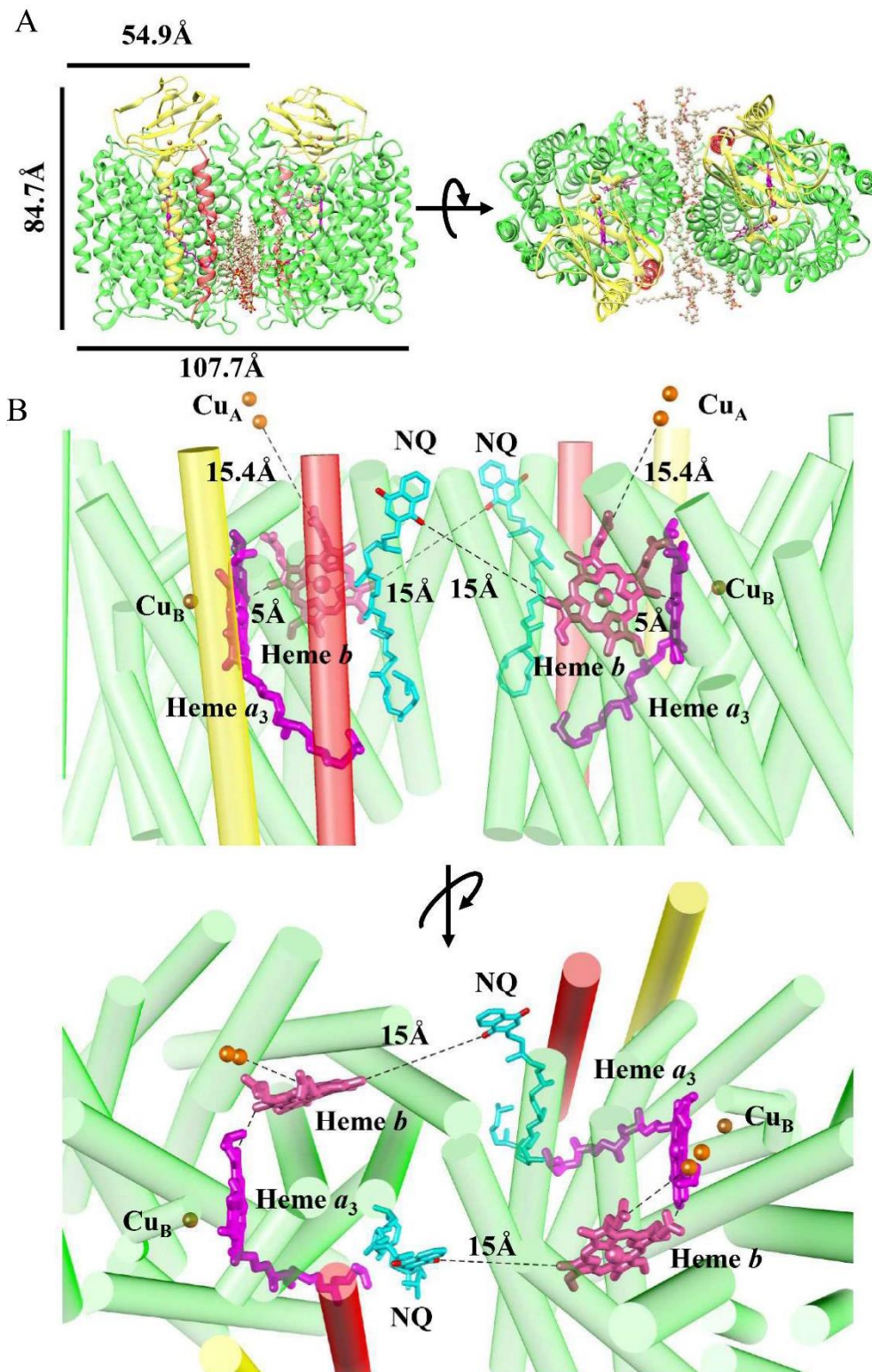Figure 3-14: Overall structure of AaC*c*O. (A) Protein structure of AaC*c*O is shown as ribbon model in two different views, with dimensions indicated. The subunits CoxA2, CoxB2, and IIa are colored in green, yellow and red, respectively. The structures of the cofactors and of NQ are shown as stick representations. (B) The edge-to-edge distances between NQ from one monomer and heme *b* from the other monomer are labeled.

3.1.4.2 Subunit I: CoxA2

Normally, subunit I of the heme copper oxidases consists of 12 TMHs (53) (Fig 3-15C). However, subunit I of B-family ba_3-CcO from *T. thermophilus* contains 13 TMHs (Fig 3-15B). Surprisingly, CoxA2 contains 14 TMHs (Fig. 3-15A). Three pores, A, B and C, which have been described previously (53,186), can be observed from the periplasmic side (53,186). The N-terminus is at the cytoplasmic side and the first five residues (MWVMQ) are not visible in the cryo-EM density. The C-terminal part is observed on top of pore A. The dimer interface is mainly formed by TMH10 and TMH11 of CoxA2. In particular, CoxA2 has 592 residues and its TMH13 and TMH14 form the long C-terminal region (Fig.3-15D).
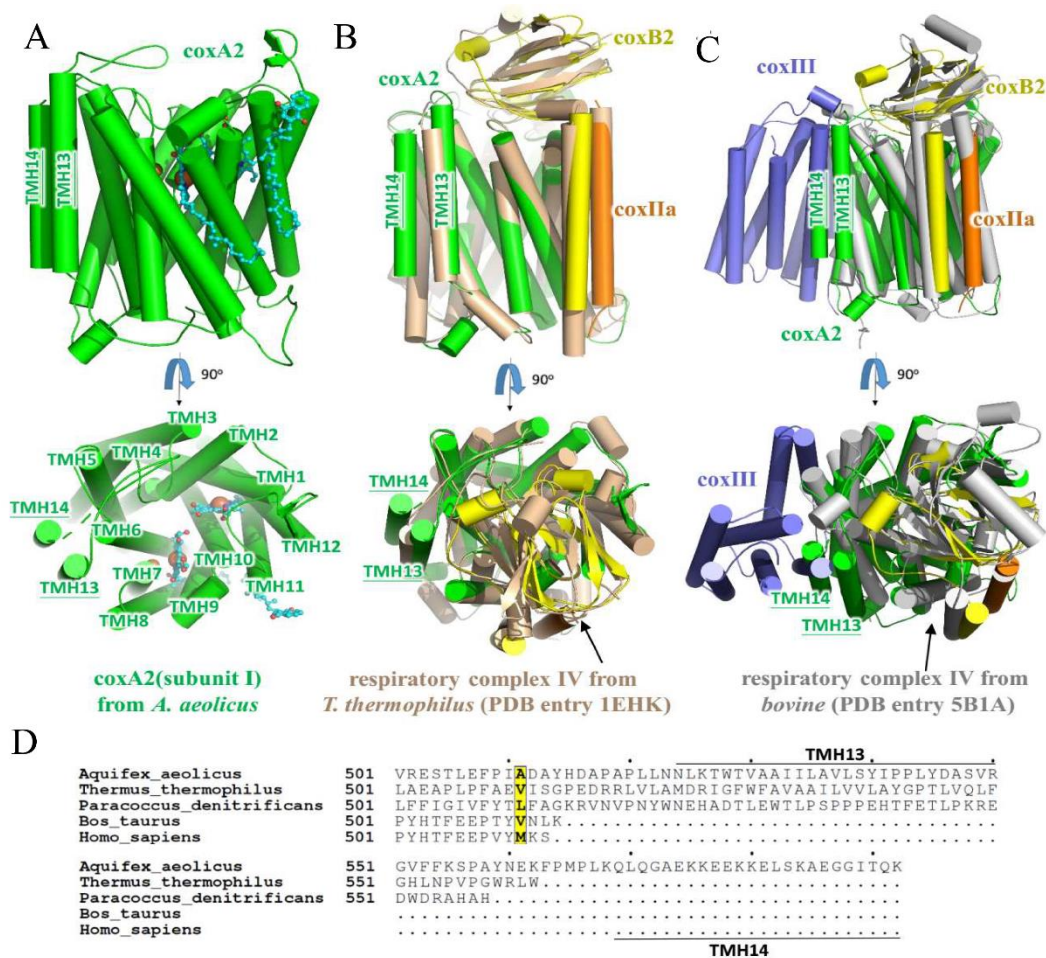
Figure 3-15: Structure of CoxA2. (A) Subunit I of *A. aeolicus* (green), (B) Subunit I of *A. aeolicus* and *T. thermophilus* (PDB entry 1EHK) are colored in green and wheat, respectively. (C) Subunit I of *A. aeolicus* and *bovine* (PDB entry 5B1A) are colored in green and blue, respectively. (D) Sequence alignment of the C-terminal domains of subunit I in different species.

The active site formed by heme a_3 and Cu_B is loacted in CoxA2 (Figure 3-14B). His

383 serves as an axial ligand for the high-spin heme a_3 with a distance of 2.4 Å, which is shorter than the distance reported for *T. thermophilus*. The covalent bond between His 233[T] and Tyr 237[T] (numbers alone correspond to the ba_3-type cytochrome c oxidase from *A. aeolicus* and numbers marked by T correspond to the numbering in the *T. thermophilus* crystal structure) is also observed between His 222 and Tyr 226, suggesting that the same proton pathway is present in AaCcO. Heme b is coordinated by His 60 and His 385 in CoxA2.

3.1.4.3 Subunit II: CoxB2 and Subunit IIa

CoxB2 contains only one TMH and a10 β-sheet (Figure 3-16A). The β-strands form a polar domain which is located at the periplasmic side. The binuclear Cu$_A$ cofactor is coordinated by the conserved residues His 96, His 139, Cys 131 and Cys 135. The distance between the two copper atoms is 2.4 Å. The distance is in good agreement with the distance determined for ba_3-type cytochrome c oxidase (53). However, the distance of 19.76 Å between Cu1 and the heme b is longer than the 19 Å observed in the ba_3-type cytochrome c oxidase from *T. thermophilus*.

The conserved residues Trp 121[P] and Tyr 122[P] (numbers marked by P correspond to the numbering in the *P. denitrificans* crystal structure) are proposed to play an important role in the electron transfer from cytochrome c to Cu$_A$ (187,188). As shown in Figure 3-16B, those two conserved residues are found in CoxB2, but are replaced by Phe 88[T] and Gly 89[T] in subunit II of *T. thermophilus*, suggesting that the electron transfer mechanism of AaCcO may be similar as in the A-type cytochrome c oxidases.

The presence of subunit IIa in AaCcO was reported in previous work (149) and its structure was determined (Figure 3-16A). It contains only one TMH which can be superimposed with the first TMH of subunit II of cytochrome c oxidase from *P. denitrificans*, but with opposite orientations. Soulimane and co-workers proposed that this TMH might be important for the function of ba_3-type cytochrome c oxidase (53). Sequence alignment suggests that subunit IIa corresponds to subunit SoxD of the SoxB-type quinol and cytochrome c oxidases from *S. acidocaldarius* (189).
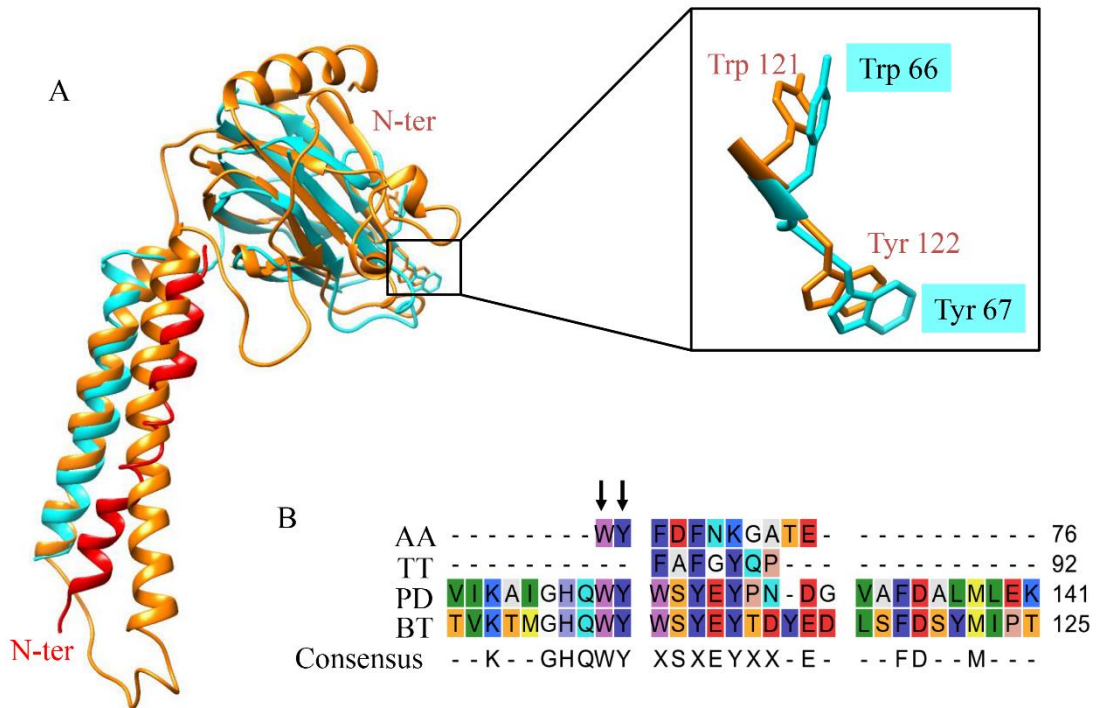
Figure 3-16: Structure of CoxB2 and IIa. (A) Comparison of subunit II from *A. aeolicus* (cyan), *T. thermophilus* (PDB entry 1EHK, cyan). *P. denitrificans* (PDB entry 1AR1, orange). The subunit IIa from *A. aeolicus* is shown as ribbon model in red. The N-terminus of subunit IIa from *A. aeolicus* and *P. denitrificans* are marked. (B) Sequence alignment of subunit II from *A. aeolicus*, *T. thermophilus* and *P. denitrificans*. The conserved residues Trp 66 and Tyr 67 are marked with arrows. PD: *P. denitrificans*; BT: *B. taurus*; AA: *A. aeolicus*. TT: *T. thermophilus*.

3.1.4.4 Only the K-proton pathway exists in AaC*c*O

Structural analysis of the B-type cytochrome *c* oxidase suggested the presence of three possible proton pathways: K-, D- and Q-proton pathway (53). Sequence (Figure 3-17A) and structure-based sequence (Figure 3-17B) alignment show that the residues for forming the D- and Q-proton pathways are not conserved. The sequence alignment result suggests that Tyr 91^T is conserved. However, the structure-based sequence alignment shows that it is not conserved. The sequence alignment results show that all polar residues forming D- and Q-proton pathways are substituted by hydrophobic residues in *A. aeolicus*. All these results suggest that there are no D- or Q-proton pathway in AaC*c*O. The results of mutagenesis studies also suggested that there is no D- or Q-proton pathway in *ba*₃-type cytochrome *c* oxidases (190).

Figure 3-17: D- and Q-pathways. (A) Sequence alignment analysis of D- and Q-pathway residues. The residues forming the D- and Q-pathways in *T. thermophilus* are marked with arrows. PD: *P. denitrificans*; BT: *B. taurus*; AA: *A. aeolicus*. TT: *T. thermophilus*. (B) Structure-based sequence alignment analysis of D- and Q-pathway residues from *A. aeolicus* and *T. thermophilus*. Residues marked in yellow are from *A. aeolicus* and in blue are from *T. thermophilus*.

The structure-based sequence alignment of subunit I shows that the functionally vital residues forming the proposed K-proton pathway are conserved (Figure 3-18A and B). The conserved residues Thr 351^P and Lys 354^P, of which mutations result in either lower or a complete loss of activity (191), are substituted by residues Ser 300 and Thr 303. The same residues replacement was found in *T. thermophus* (53). Therefore, the proton transfer efficiency may be largely reduced in AaC*c*O, which is important in achieving adaptation to the low oxygen tension and high temperature environment.
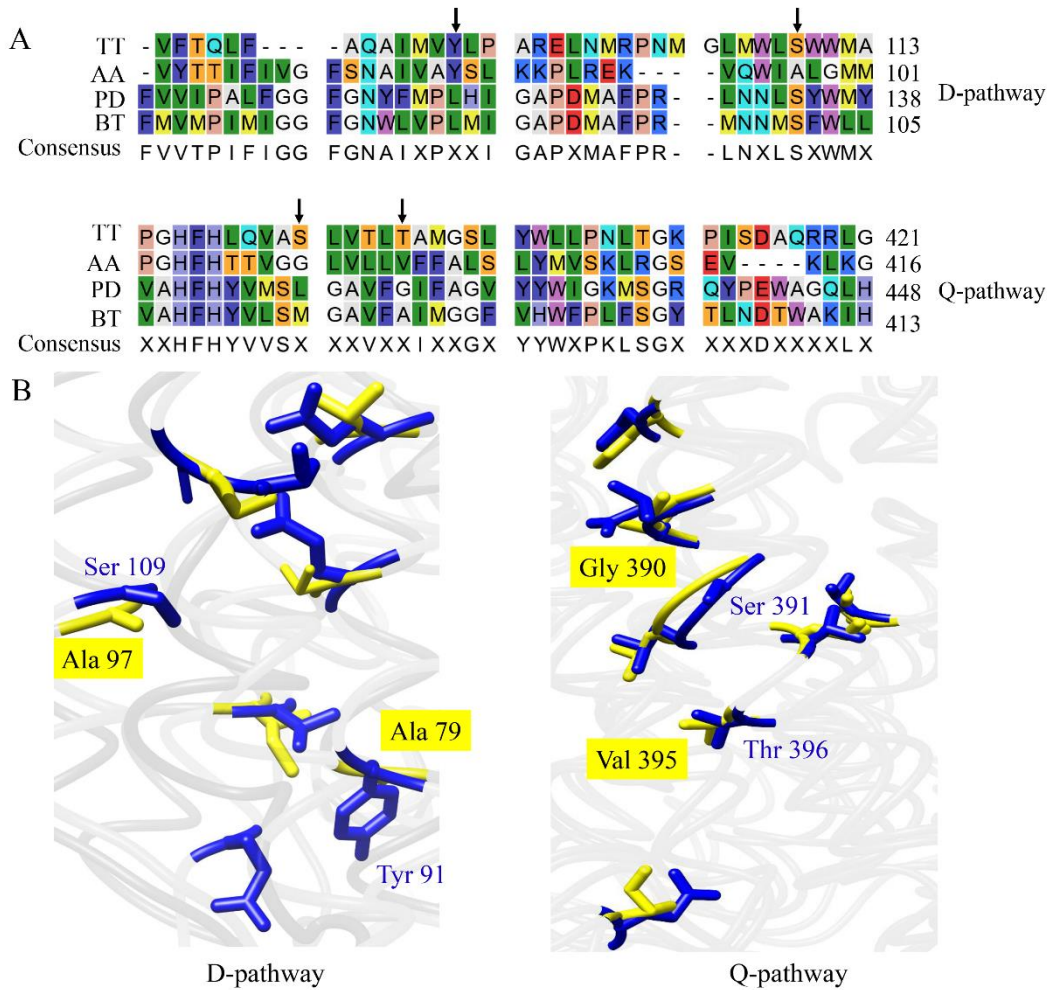
A

B
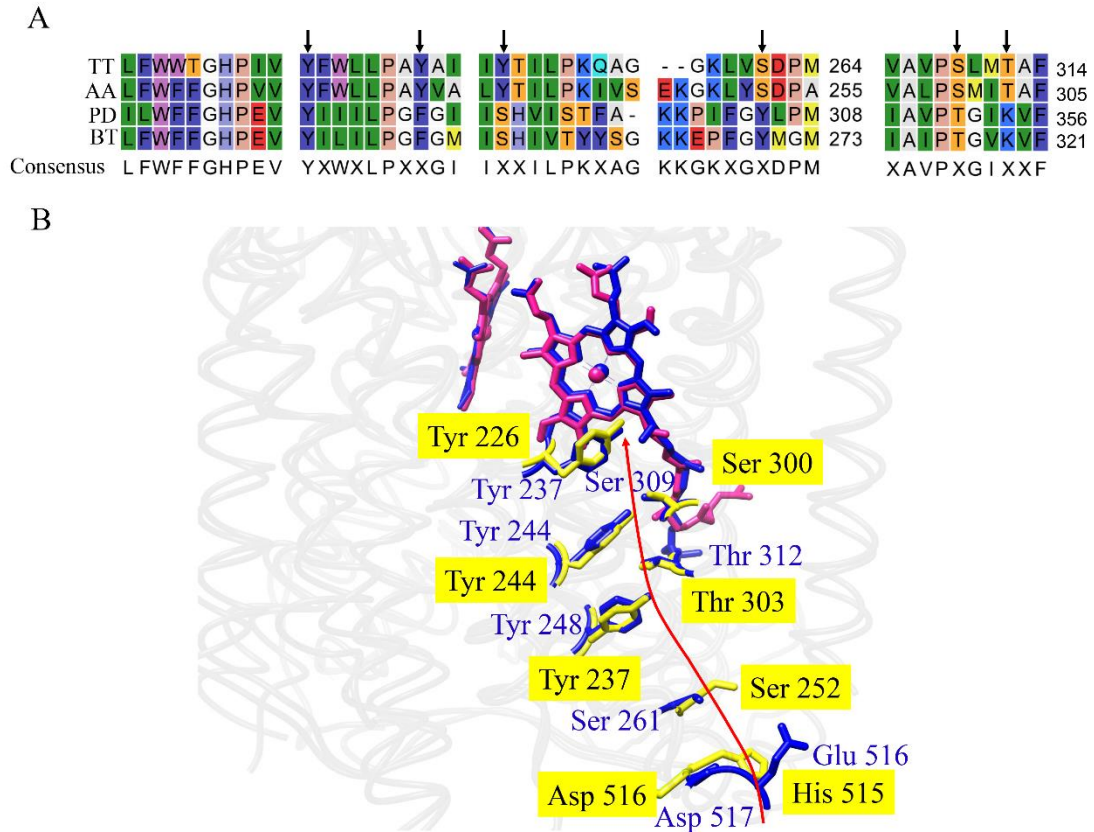
Figure 3-18: The K-proton pathway. (A) Sequence alignment analysis of K-pathway residues. The residues forming the K-pathway in *T. thermophilus* are marked with arrows. PD: *P. denitrificans*; BT: *B. taurus*; AA: *A. aeolicus*. TT: *T. thermophilus*. (B) Structure-based sequence alignment analysis of K-pathway residues from *A. aeolicus* and *T. thermophilus*. Residues marked in yellow are from *A. aeolicus* and in blue are from *T. thermophilus*.

In AaC*c*O, the distance from Asn 371 to the propionate-A of heme a_3 is 4.14 Å. Asn 371 was proposed to be critical for the proton-pumping mechanism (192). However, Asp 372 was identified in the same position in *T. thermophus*. The AaC*c*O structure are function, suggest that Asn 371 in AaC*c*O is not essential for oxidase activity. Similar results were also observed for the D399N mutation in aa_3-type cytochrome *c* oxidase from *P. denitrificans* (193), *R. sphaeroides* (194), and cytochrome bo_3 from *E. coli* (195).

3.1.4.5 Oxygen pathway

One putative oxygen channel leading from the middle of the membrane to the active site was observed (Figure 3-19A). However, a Y-shaped oxygen pathway with two entry points were identified in the ba_3-type cytochrome *c* oxidase from *T. thermophilus*

(Figure 3-19B). Sequence alignment shows that most of the residues forming the putative oxygen channels are conserved, except Phe 113 and Val 224 (Figure 3-19C). The presence of Phe 113 in the AaCcO blocks entry point 2 (Figure 3-19D). Another not conserved residue, Val 224, which is substituted by Ile 235[T] and Glu 278[P] (Figure 3-19C).

Figure 3-19: Oxygen pathway. (A) Oxygen pathway viewed from the periplasmic side in *A. aeolicus*. (B) Y shaped oxygen pathway viewed from the periplasmic side in *T.thermophilus*. The two oxygen pathways are named 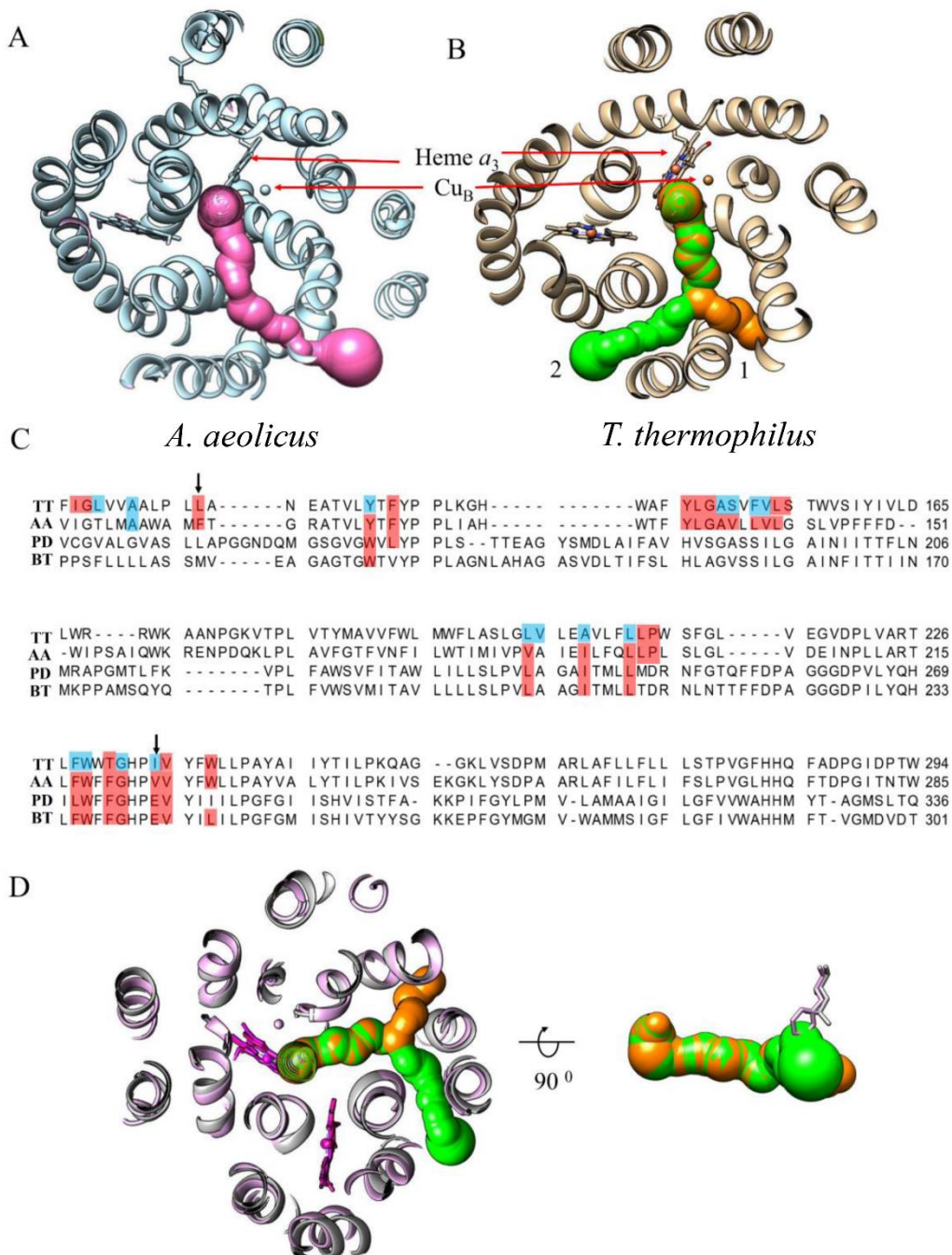1 and 2. (C) Sequence alignment of the oxygen pathways forming residues. The residues colored in red form the putative oxygen pathway and residues colored in blue are in contact with

Xeno atoms in the crystal structure. Phe 113 and Val 224 are marked with arrows. PD: *P. denitrificans*; BT: *B. taurus*; AA: *A. aeolicus*. TT: *T. thermophilus*. (D) Phe 133 blocks the oxygen pathway 2 in *T. thermophilus*.

A channel of considerably smaller volume was observed in the aa_3-type cytochrome *c* oxidase from *P. denitrificans* (196,197) and *B. taurus* (197). Oxygen channels from *A. aeolicus* and *T. thermophilus* connect the active site to the outside of the enzyme, while the active site is not connected to the outside in the channels from *P. denitrificans* and *B. taurus*.

Soulimane and co-workers suggested that, in water at high temperatures, the presence of Ile or Val in the ba_3-oxidases optimizes the oxygen pathway by reducing solubility of gaseous oxygen. The conserved Val was also found in aa_3-quinol oxidase from *S. acidocaldarius* which also grows at high temperatures with low oxygen concentrations. In contrast, the conserved Glu residues in aa_3 type oxidases from *P. denitrificans* and bovine play an essential role in proton pumping (196,198). All results suggest that the putative Val optimized oxygen channel is a conserved feature in thermophilic bacteria.

3.2.3.3 Dimer interface

The dimer interface in AaC*c*O is formed by CoxA2 but only with few protein-protein interactions. A hydrophobic cavity is observed in the interface near cytoplasmic side. Interestingly, CLs and PGs are identified in the dimeric cavity (Figure 3-20A). CL is negatively charged and contains a glycerol moiety as head group which is linked to two phosphatidyl-glycerol molecules. CL is proposed to play an important role in stabilizing the dimer interface (199). Two CLs can be identified in the dimer interface of AaC*c*O (Figure 3-14D, Figure 3-20B), which is in line with the previous reports of the dimeric crystal structure of cytochrome *c* oxidase from *B. taurus* (199,200). Two phosphatidylglycerols (PGs) are identified between the CLs in the interface and another four PGs are observed around the cavity (Figure 3-20B and E). All polar head groups are oriented toward to the negative membrane side (Figure 3-20C). Interestingly, two molecules of 1,4-naphthoquinone were observed upon those lipids with the head group

toward to the positive membrane side (Figure 3-20D). Considering that naphthoquinone is one of the substrates of AaC*c*O, all arrangements observed in the dimeric structure may be regulated by the lipid-naphthoquinone interactions.
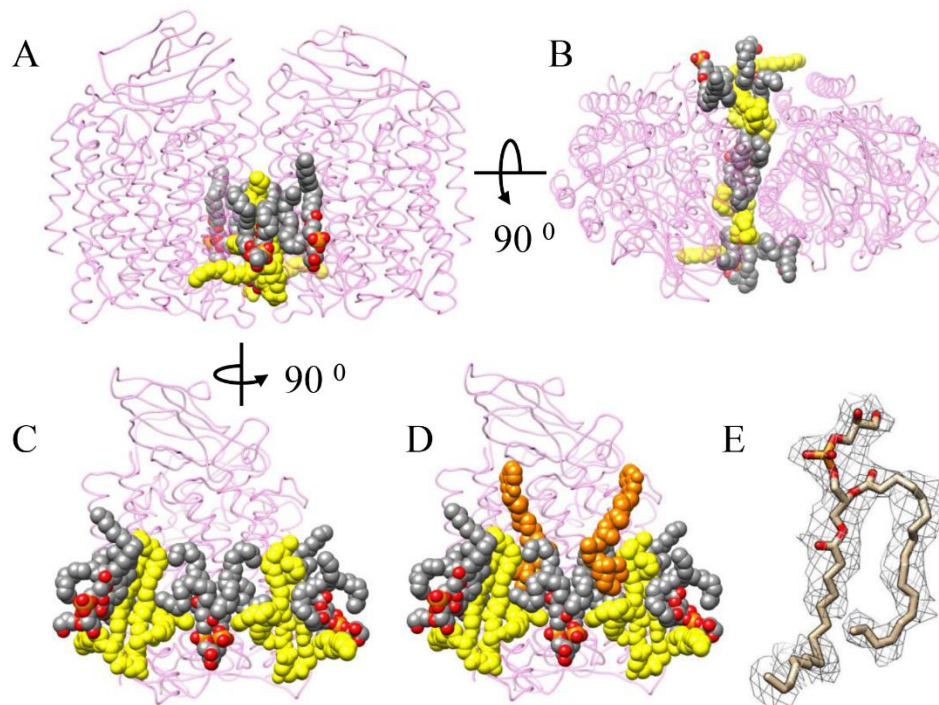
Figure 3-20: The dimer interface of AaC*c*O. (A) AaC*c*O is viewed perpendicular to the membrane and from the periplasmic side (B) and (C) viewed along the membrane. CoxA2 is coloured plum and semi-transparent. CL and PG are coloured yellow and gray, respectively. (D) Lipid-1,4-naphthoquinone interaction. The 1,4-naphthoquinone is colored light orange. (E) Cryo-EM density of PG.

3.2 Characterization of Aa*bc*$_1$

3.2.1 Purification of Aa*bc*$_1$ from native membrane

Fractions "I" (Figure 3-11) were subjected to TSK-GEL G4000SW 21.5/30 SEC (Figure 3-21A). Then green marked fractions B8 and B9 were pooled and subjected to Yarra SEC-4000 SEC, shifting the detergent from DDM to digitonin (Figure 3-21B). The main fraction 12, colored in blue, was collected and used for functional and structural studies. Proteins in fraction 12 were separated on SDS-PAGE. After staining with Coomassie blue, the protein bands corresponding to cyt. *b*, cyt. *c*$_1$ and ISP were observed (Figure 3-21C).
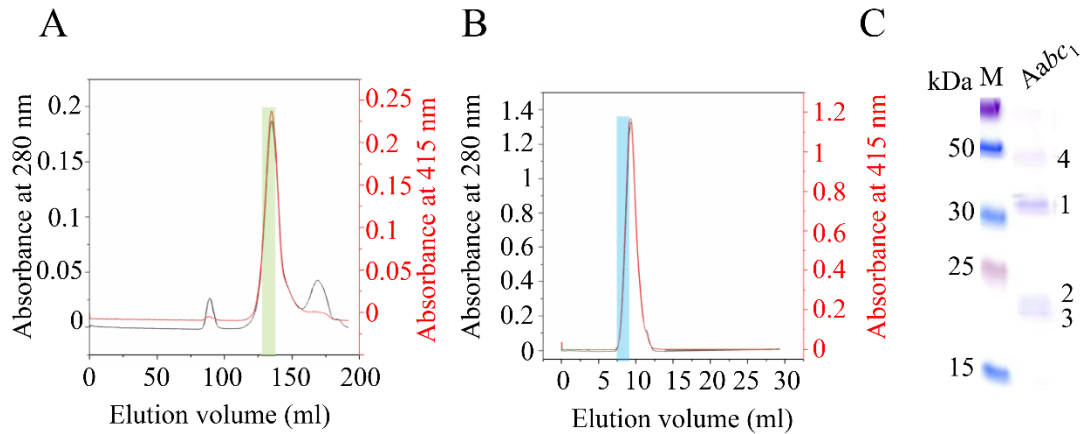
Figure 3-21: Purification of the native Aa*bc₁*. (A) Separation of membrane proteins by size exclusion chromatography with TSK-GEL G4000SW 21.5/30 SEC. The fractions colored in green were pooled and used to purify native Aa*bc₁*. (B) Size exclusion chromatography profile of native AaC*c*O with Yarra SEC-4000. Fractions 12 and 13 are colored in blue and analyzed by SDS-PAGE (C). M: PageRuler Prestained protein ladder. 1: cyt. *b*; 2: cyt. c_1; 3: ISP; 4: CoxA2.

3.2.2 Functional analysis of Aabc_1

Reduction of cytochrome *c* was recorded by measuring the absorption change in the UV-visible region, suggesting that recombinant cytochrome c_{555} can be used as electron accepter. No significance activity differences of Aabc_1 with c_{555}^m and c_{555}^s were observed (Figure 3-22). The reaction buffer contained 30 mM KPi pH 7.0, 0.1% digitonin and 1 mM KCN. The electron donor was 60 µM decylubiquinol and the electron acceptor was 45 µM air-oxidized cytochrome c_{555}. The activity of Aabc_1 (0.3 µg) was determined by monitoring the increase in absorbance at 550 minus 540 nm for 20 s.
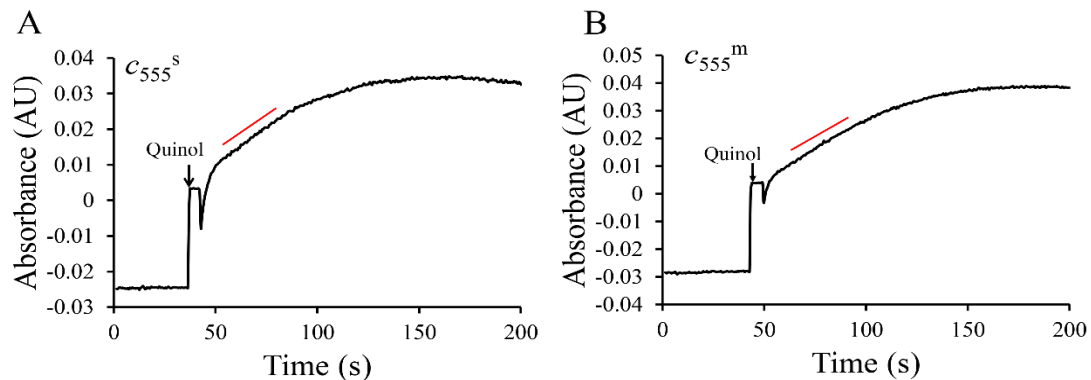
Figure 3-22: Activity assay of Aabc_1. The activity was initiated by adding quinol. The recombinant cytochrome c_{555}^s (A) and cytochrome c_{555}^m (B) were used as electron acceptor. The reactions were recorded at 80 °C.

3.2.3 **Structure of Aabc_1**

3.2.3.1 Structure determination and overall structure of Aabc_1

Aabc_1 was purified from native membranes (Figure 3-21). The cryo-EM data collection and processing are summarized in table 3-2. A representative cryo-EM micrograph is shown in Figure 3-23A. 12 most populated 2D classes (marked in red) were identified out of 379,000 selected particles (Figure 3-23C). After high-resolution refinement with 93,622 particles, the overall structure of the Aabc_1 dimer reached a resolution of 3.3 Å according to the gold standard $FSC_{0.143}$ criterion (Figure 3-23B).

Table 3-2: Statistics of data collection, image processing and model building

Sample	apo cytochrome bc_1 complex	Inhibitor cytochrome bc_1 complex
Data collection		
EM equipment	FEI Titan Krios	
Voltage (KV)	300	
Detector	Gatan Bioquantum K2	
Energy filter	20 eV	
Pixel size (Å/pixel)	1.04	
Electron dose (e^-/ Å^2)	60	
Defocus range (μm)	-1.5~-2.5	
Reconstruction		
Software	RELION 3.0-beta / RELION 2.0	
Number of used particles	93,622	81,350
Accuracy of rotation	1.748	
Accuracy of translations (pixel)	0.697	
Symmetry	C2	
Map sharpening B-factor (Å^2)	-140	-56
Final resolution (Å)	3.28	3.22
Model building		
Software	Coot	
Model Refinement		
Software	PHENIX	
Map CC (whole unit cell)	0.76	0.77
Map CC (around atoms)	0.73	0.74
Rmsd (bonds) (Å)	0.008	0.009
Rmsd (angle) (°)	1.181	1.249

Model composition		
Protein residues	1530	
Heme groups	6	
[Fe$_2$S$_2$] clusters	2	
Validation		
Ramachandran plot		
Outliers (%)	0.26	0.40
Allowed (%)	9.67	8.74
Favored (%)	90.07	90.86
Rotamer outliers (%)	0.77	1.23

A

B

C
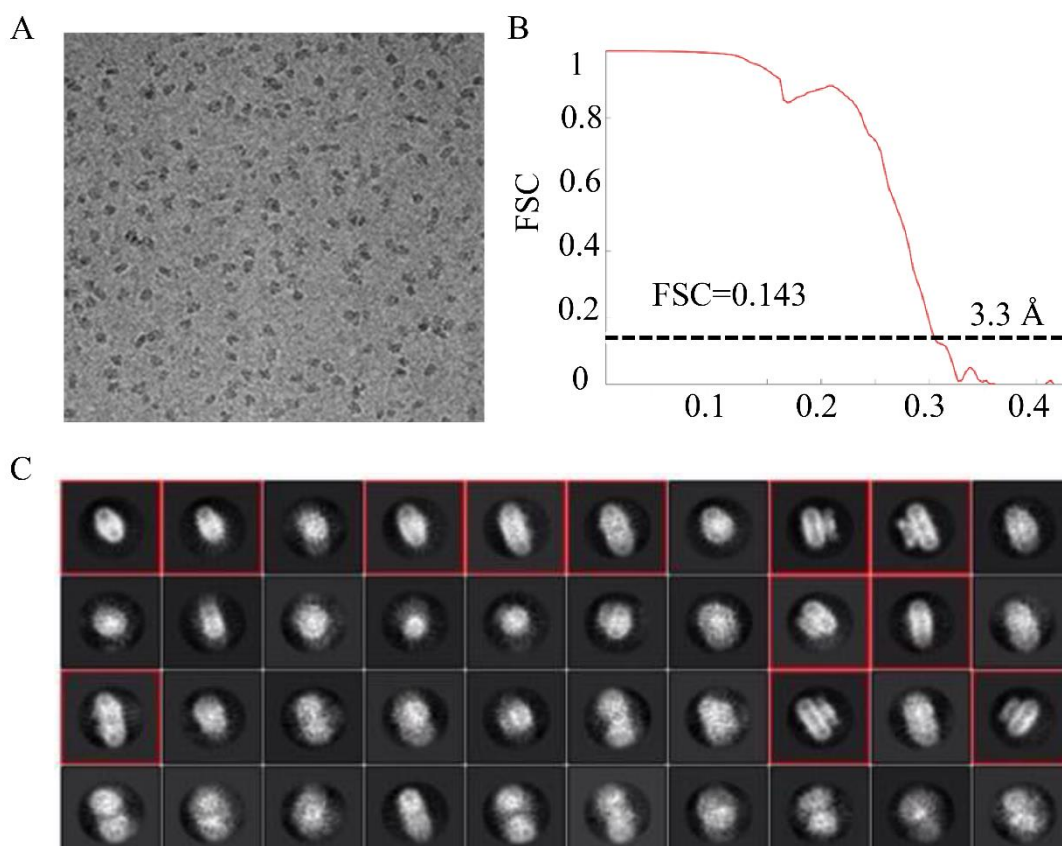
Figure 3-23: Structure determination of Aabc_1. (A) A representative micrograph. (B) Gold-standard FSC curve for the overall map. (C) Representative 2D class averages obtained from reference-free classification.

It is the first structure of a respiratory chain complex of *A. aeolicus*, as well as the first naphthoquinone oxidizing cytochrome bc_1 complex. It has a dimension of ~ 86.7 Å in height and 79.8 Å in length (Figure 3-24A). The subunits cyt. *b*, cyt. c_1 and ISP, and their respective cofactors hemes b_H, b_L, c_1 and Fe$_2$S$_2$ centers are observed in the structure (Figure 3-24B). Notably, two molecules of 1,4-naphthoquinone are observed

at the Q_i site (Figure 3-24C). The overall structure of this enzyme is highly similar to those of the core subunits of the mitochondrial (PDB 1BE3) (90) and bacterial (PDB 5KLI) (201) cytochrome bc_1 complexes when compared by superposition. Subunit cyt. b is similar to cyt. b of *R. capsulatus* with r.m.s.d. of the C_α-atoms of 2.2 Å and the subunit ISP of Aabc_1 is similar to the ISP of *R. sphaeroides* with r.m.s.d. of the C_α-atoms of 2.1 Å. Interestingly, the ISP is similar to PetC3 of the cytochrome b_6f complex from cyanobacteria. Higher deviations are observed for cyt. c_1 when compared to cyt. c_1 of cytochrome bc_1 complex from *P. denitrificans* (202). Interactions of the functional domains of cyt. c_1 and the ISP are observed at the periplasmic side.
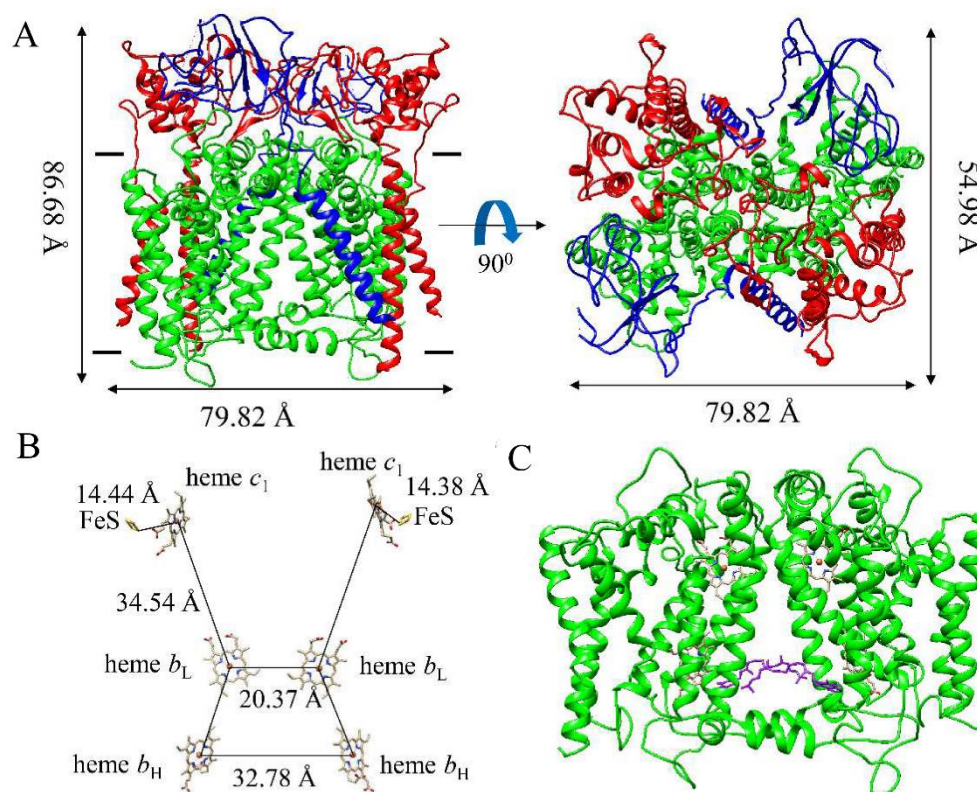
Figure 3-24: Architecture of cytochrome bc_1 complex from *A. aeolicus*. (A) overall structure of cytochrome bc_1 complex. Ribbon representation of two different views along with the membrane plane and matrix. The structure of subunits cyt. b, cyt. c_1 and ISP are colored green, red and blue, respectively. The dimensions are indicated beside the model and the horizontal lines represent the position of membrane. (B) The distances of relative location of the cofactors in the dimeric cytochrome bc_1 complex. (C) View into the Q_i binding site with one molecule of naphthoquinone for each monomer. Naphthoquinone is colored purple.

3.2.3.2 Iron sulfur protein

ISP is formed by three parts: The TMH part which acts as the anchor to cyt. *b* and is formed by 33 residues (Phe 2 - Glu 34), the functional part containing three β- strands and the part which connects the TMH and functional part (Figure 3-25A). All determined cytochrome bc_1 complex structures from bacteria show a connecting helix and an ADV (Ala-Asp-Val) motif. However, sequence alignment shows there is no ADV motif present in the Aabc_1 (Figure 3-25A and C). The connection of the functional domain and the anchor part is a loop in Aabc_1. There are three strands in the functional domain, and the Fe_2S_2 cluster is coordinated by the residues His 138, His 113, Cys 111 and Cys 135. The Fe_2S_2 cluster of ISP is observed in the *c* position. Furthermore, the conserved His 138 of the ISP is found between heme c_1 and Fe_2S_2 cluster (Figure 3-25B).
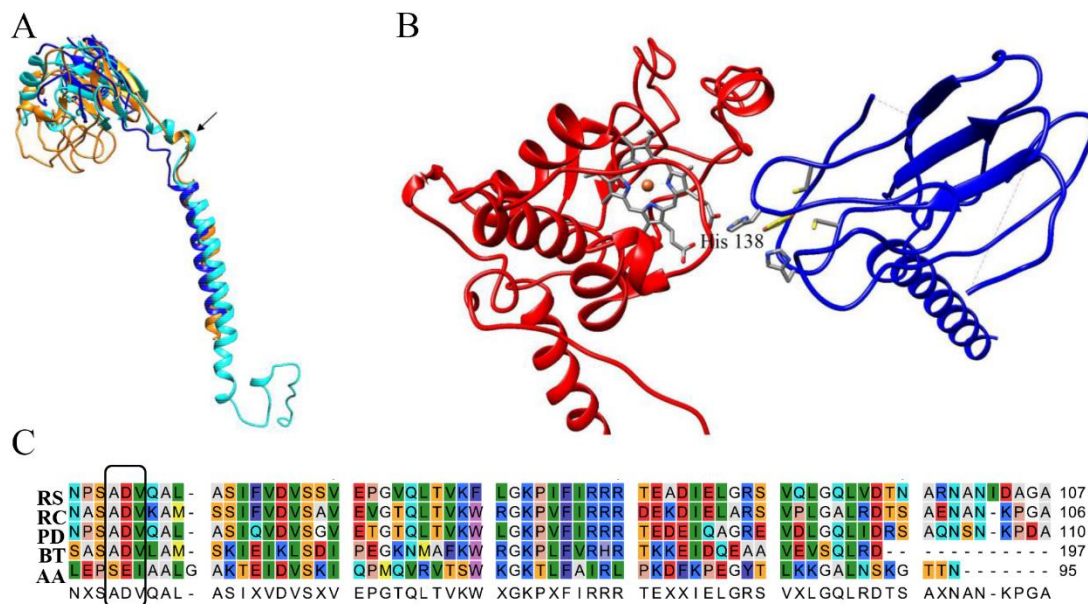
Figure 3-25: The folding of ISP. (A) Comparison of ISP from *A. aeolicus* (blue)*, B. taurus* (PDB entry 1BE3, cyan)*,* and *R. capsulatus* (PDB entry 1ZRT, orange). The short helix which is located between the functional domain and transmembrane helix is marked with an arrow. (B) ISP-cyt. c_1 interface. ISP and cyt. c_1 are colored blue and red, respectively. The His 138 found between the ISP and heme c_1 is marked. (C) Sequence alignment of ISP: The conserved "ADV" motif is marked. RS: *R. sphaeroides*; RC: *R. capsulatus*; PD: *P. denitrificans*; BT: *B. taurus*; AA: *A. aeolicus*.

3.2.3.3 Cytochrome c_1

Subunit cyt. c_1 contains 5 helices including 2 TMHs, 4 loops and one cofactor heme c_1

(Figure 3-26A). The N-terminal TMH consists of residues Trp 4 toTrp 24 and the C-terminal TMH is composed of residues Ser 205 to Leu 237. The cofactor heme c_1 is coordinated by Cys 70, Cys 73, His 74 and Met 171. Sequence identity between cyt. c_1 of *A. aeolicus* and cyt. c_1 of *P. denitrificans*, *R. sphaeroides*, *R. capsulatus* and *B. taurus* are 25%, 21%, 26% and 28%, respectively (Figure 3-26B). Many differences are found in the peripheral domain of this subunit between *A. aeolicus* and, *B. taurus* and *R. capsulatus* (Figure 3-26C). The low deviations are observed of loop1. Helix 1 was found between the loop 1 and loop 2 of cytochrome bc_1 complex from *B. taurus* and *R. capsulatus*. However, there is an antiparallel ß-sheet between loop 1 and loop 2 of Aabc_1. A short helix between loops 2 and 3 near the heme c_1 cleft is observed in Aabc_1. There is an additional short helix 2a in Aabc_1.

Figure 3-26: Structure of cytochrome c_1. (A) Ribbon model representing the monomer structure of cyt. c_1 viewed from the matrix side. Heme c_1 is shown as a stick model. The loops are marked. (B) Sequence

alignment of cyt c_1 of *A. aeolicus*, and cyt. c_1 of *P. denitrificans*, *R. sphaeroides*, *R. capsulatus* and *B. taurus* with secondary structure elements. Structure elements for *A. aeolicus* are indicated on top with black lines for α-helices, dot lines for β-strands and blue lines with arrows for loops. (C) Comparison of cyt. c_1 of *A. aeolicus* (red), *B. taurus* (PDB entry 1BE3, cyan), and *R. capsulatus* (PDB entry 1ZRT, orange). The differences of loops and helices are marked with arrows.

3.2.3.4 Cytochrome *b*

The cyt. *b* subunit of Aa*bc*$_1$ has 409 amino acid residues and consists of 13 helices including 8 TMHs (helices 1 to helices 8) and two catalytic centers heme b_L and heme b_H (Figure 3-27A). In line with determined structures of cytochrome bc_1 complexes, two 4-helix bundles (TMH 1-4 and TMH 5-8) are observed. Heme b_L and b_H are located in the first bundle close to the periplasmic and cytoplasmic side, respectively. The coordinating residues are identified as His 91 and His 202 for heme b_L, and His 105 and His 217 for heme b_H. The distance is 20.12 Å between the heme b_L and heme b_H in the monomer, and 20.37 Å between heme b_L and heme b_L, and 32.77 Å heme b_H and heme b_H, respectively, in the dimer Aa*bc*$_1$ (Figure 3-24B). One should note that helix ef2 in other bacterial cytochrome bc_1 complexes is missing in Aa*bc*$_1$ (Figure 3-27B).
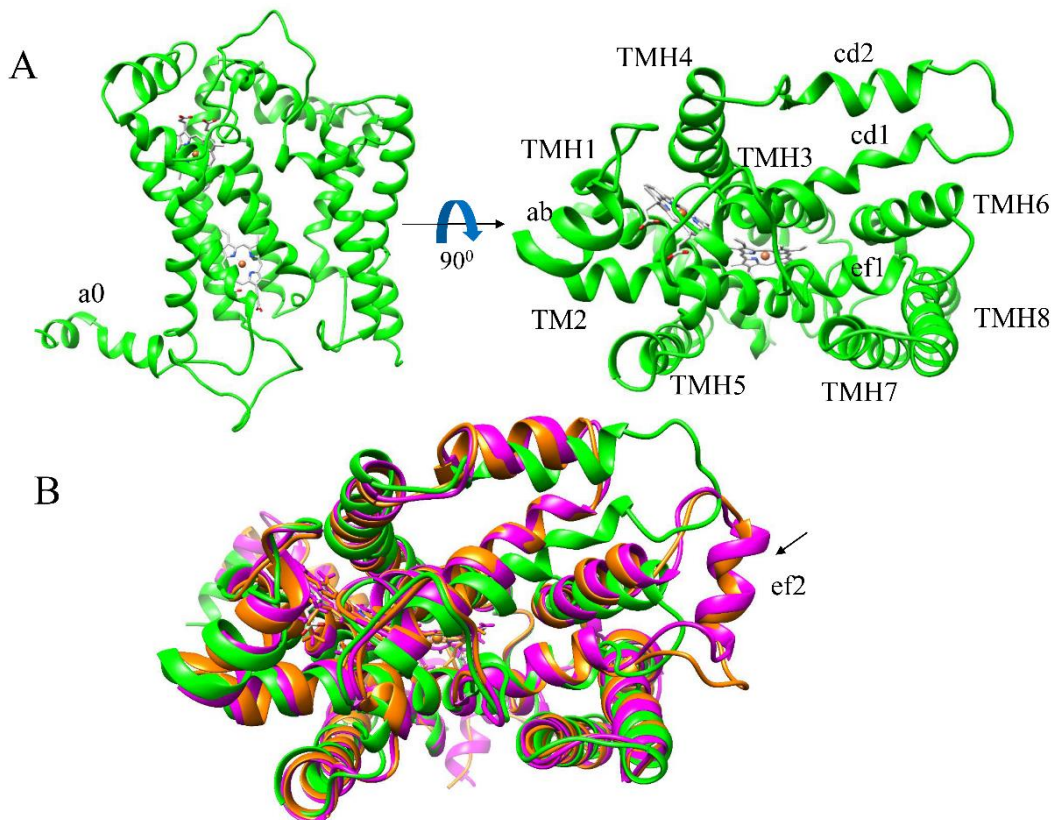

Figure 3-27: Structure of cyt. *b*. (A) Structure of cyt. *b*. Helix a0 is shown in the view along the membrane.

The other helices are shown in the view from the matrix. (B) Comparison of cyt. *b* from *A. aeolicus* (green), *R. capsulatus* (PDB entry 1ZRT, orange) and *R. sphaeroides* (PDB entry 5KLI, magenta). The helix ef2 is marked with arrow.

3.2.3.5   Binding sites of naphthoquinone and antimycin A

Aa*bc*$_1$ uses naphthoquinol as substrate (203). Cryo-EM structure presents a pronounced cryo-EM density close to the heme b_H. The position is in line with the reported Q$_i$ site (14,86,87,90). One molecule of 1,4-naphthoquinone was identified in each cyt. *b* monomer (Figure 3-28A). The well-defined density map of 1,4-naphthoquinol is clearly visible in a pocket formed by the TMH1, 4 and 5. The 1,4-naphthoquinone binding pocket was above helix a0 which is formed by positive charged residues. The distance between 1,4-naphthoquinone and the edge of heme b_H is 8.29 Å. Interestingly, the plane of the 1,4-naphthoquinone head-group is nearly perpendicular to the heme b_H porphyrin plane. The distances from the carbonyl oxygens O1 and O4 to the iron of heme b_H are 9.7 Å and 10.7 Å, respectively (Figure 3-28A). The tail of 1,4-naphthoquinone stretches toward the membrane core outside of the binding pocket. The 1,4-naphthoquinone is bound by Arg 222 and Glu 254, which are homologous to the highly conservatived His 201 and Asp 229 in the mitochondrial cytochrome *bc*$_1$ complex (86,204).

Antimycin A can block the electron transfer from the high spin heme b_H to the quinone or semiquinone. A well-ordered antimycin A was observed in the Q$_i$ site (Figure 3-28B). Briefly, the headgroup of antimycin A was found at the end of the Q$_i$ binding pocket and the tail bound at the entrance. Atoms OE1 and OE2 of Glu 254 in TMH5 are located 2.09 Å and 2.22 Å, respectively, away from the amide N1 and carbonyl oxygen O1 of antimycin. Ile 42 in the TMH1 is located 3.15 Å away from the carbonyl oxygen O7 of antimycin. CD1 of Leu 218 in TMH4 and Leu 45 in TMH1 are located 3.18 Å and 3.67 Å, respectively, away from the carbonyl oxygen O9 of antimycin A. Additionally, van der Walls interactions between antimycin A and cyt. *b* are also contributed by heme b_H, Phe 246, Arg 222, Lys 253 and Val 221.
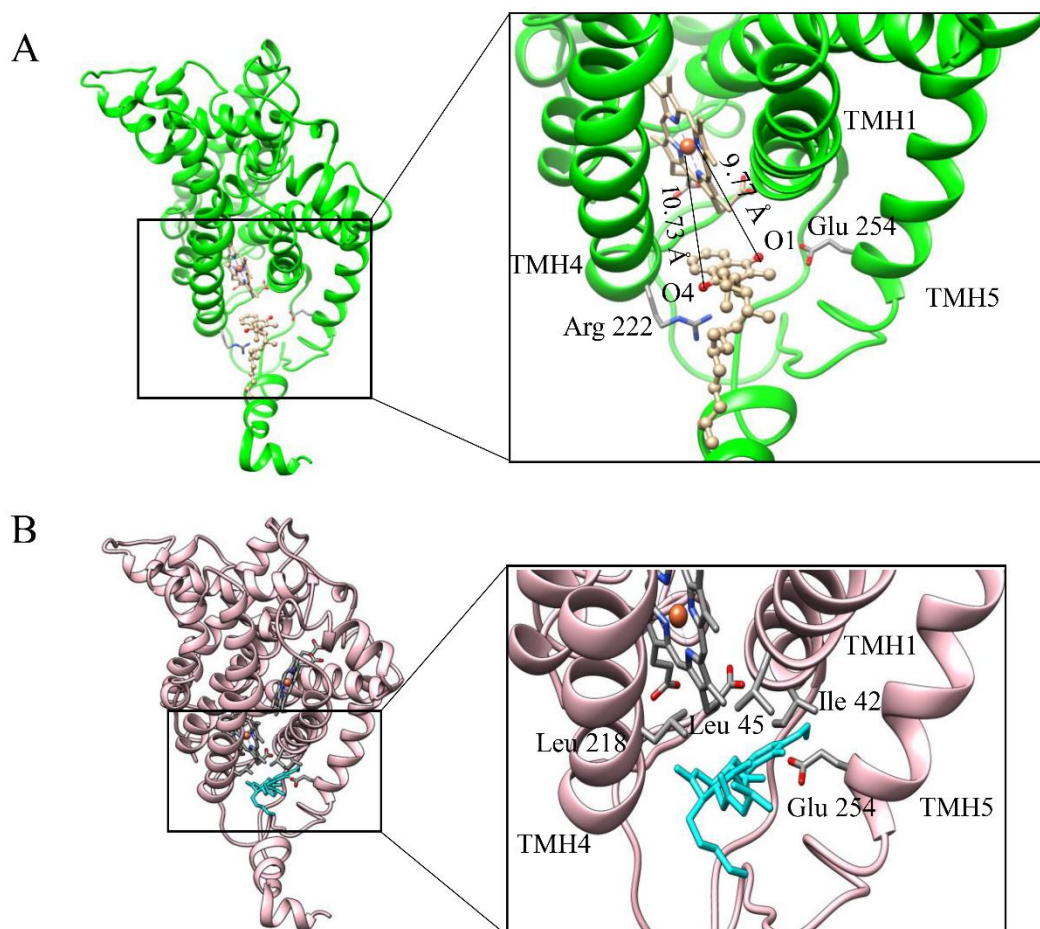
Figure 3-28: The binding sites of 1,4-naphthoquinone and antimycin A. (A) Interaction of 1,4-naphthoquinone and cyt. *b*. Zoom in on the interaction between 1,4-naphthoquinone and cyt. *b* (Right). The coordinating residues of cyt. *b* are shown as sticks. The distances from the center of heme b_H to O1 and O4 of naphthoquinone are shown. The helices around the binding pocket are helix 1, 4 and 5. (B) Binding interaction of antimycin A and cyt. *b*. Zoom in on the interaction between 1,4-naphthoquinone and cyt. *b* (right). The coordination residues of cyt. *b* are showed as sticks.

3.2.3.6 Sequence characterization of Aa*bc*₁

In order to study the mechanism of the cytochrome *bc*₁ complex under hyperthermophilic conditions, the amino acid sequences from different species, including thermophilic bacteria (*A. aeolicus, Hydrogenivirga sp, Thermocrinis albus, Thermocrinis minervae, and Hydrogenobacter thermophilus*), other prokaryotes (*R. sphaeroides and R. capsulatus*) and eukaryotes (*S. cerevisiae, Gallus gallus, Ovis aries, B. taurus and Homo sapiens*) were aligned and an evolutionary tree was constructed . The results show that the sequences of cytochrome *bc*₁ complex subunits between the three groups are significantly different (Figure 3-29A). All five thermophilic bacteria have closely related sequences as indicated in the evolutionary tree, suggesting that

their sequences might be correlated with their thermophilic environment.
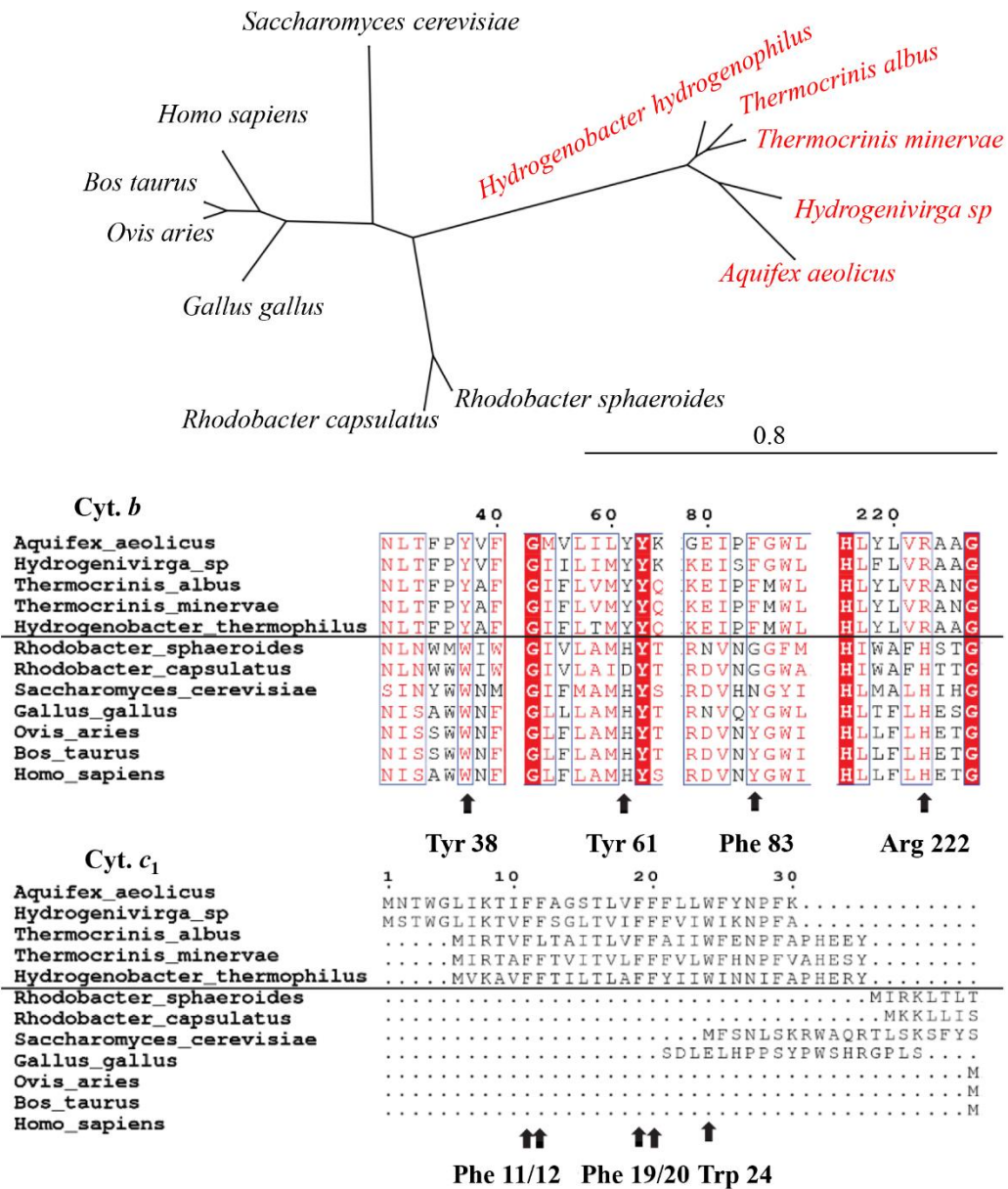
Figure 3-29: Sequence characterization of cytochrome Aabc_1. (A) Evolutionary tree of cytochrome bc_1 complexes from different species. (B) Sequence alignment of cyt. b subunits from different species, indicating important residues. (C) Sequence alignment of cyt. c_1 subunits from different species, indicating important residues.

According to the sequence alignment result, several unique residues are found in thermophilic bacteria but substituted in other species. In the cyt. b subunit, these residues include Tyr 38, Tyr 61, Phe 83 and Arg 222 (Figure 3-29B). In cyt. c_1, the whole N-terminal TMH1 spanning 1-30 amino acids, is completely absent in other mesophilic species (Figure 3-29C). There are seven phenylalanine and two tryptophan

residues in this helix, forming a unique "WF-rich motif". Based on the cryo-EM structure of Aabc_1 complex, the important functions of these unique residues in thermophilic bacteria are analyzed.

3.2.3.7 Heme b_H and naphthoquinone are further stabilized

In the cyt. *b* subunit of Aabc_1, heme b_H is stabilized by TMH1, TMH2 and TMH4 of cyt. *b* subunit. The highly conserved residues His 274 and His 105 of these TMHs interact with the iron atom inside the heme molecule. This interaction manner and spatial conformation of heme b_H are consistent in all cyt. *b* proteins from different species, to protect the electron transfer reaction at this Q_i site (Figure 3-30A). However, in the structure of cytochrome Aabc_1, another residue Tyr 38 in the TMH1 of the cyt. *b* subunit, binds to the two carboxyl groups of heme b_H to further stabilize this cofactor. This tyrosine residue is highly conserved in the thermophilic bacteria (Figure 3-29B), but replaced by tryptophan in other species. In the structure of the cytochrome bc_1 complex of *R. sphaeroides* (PDB entry 5KLI) or *B. taurus* (PDB entry 1BE3), Trp 45 or Trp 31 do not interact with the two carboxyl groups of heme b_H. This result suggests that heme b_H stays in more stable tightly bound in *A. aeolicus*.

In the Aabc_1 structure, there are two 1,4-naphthoquinone substrates in each Q_i site, one of them is located close to the heme b_H molecule with ~10 Å distance, ready for electron transfer. Interestingly, this 1,4-naphthoquinone is stabilized by a unique residue Arg 222 on TMH4 of cyt. *b* subunit for *A. aeolicus*, which is replaced by a histidine in *R. sphaeroides* or *B. taurus* (Figure3-28A). The positively charged guanidinium group of Arg 222 is close to the oxygen atom of 1,4-naphthoquinone. Sequence alignment result showe that Arg 222 is highly conserved in all thermophilic bacteria family but is replaced by a histidine residue in other species (Figure 3-29B). Therefore, Arg 222 many help the substrate to stay in the Q_i site, to ensure a favorable orientation and distance against the heme b_H cofactor.
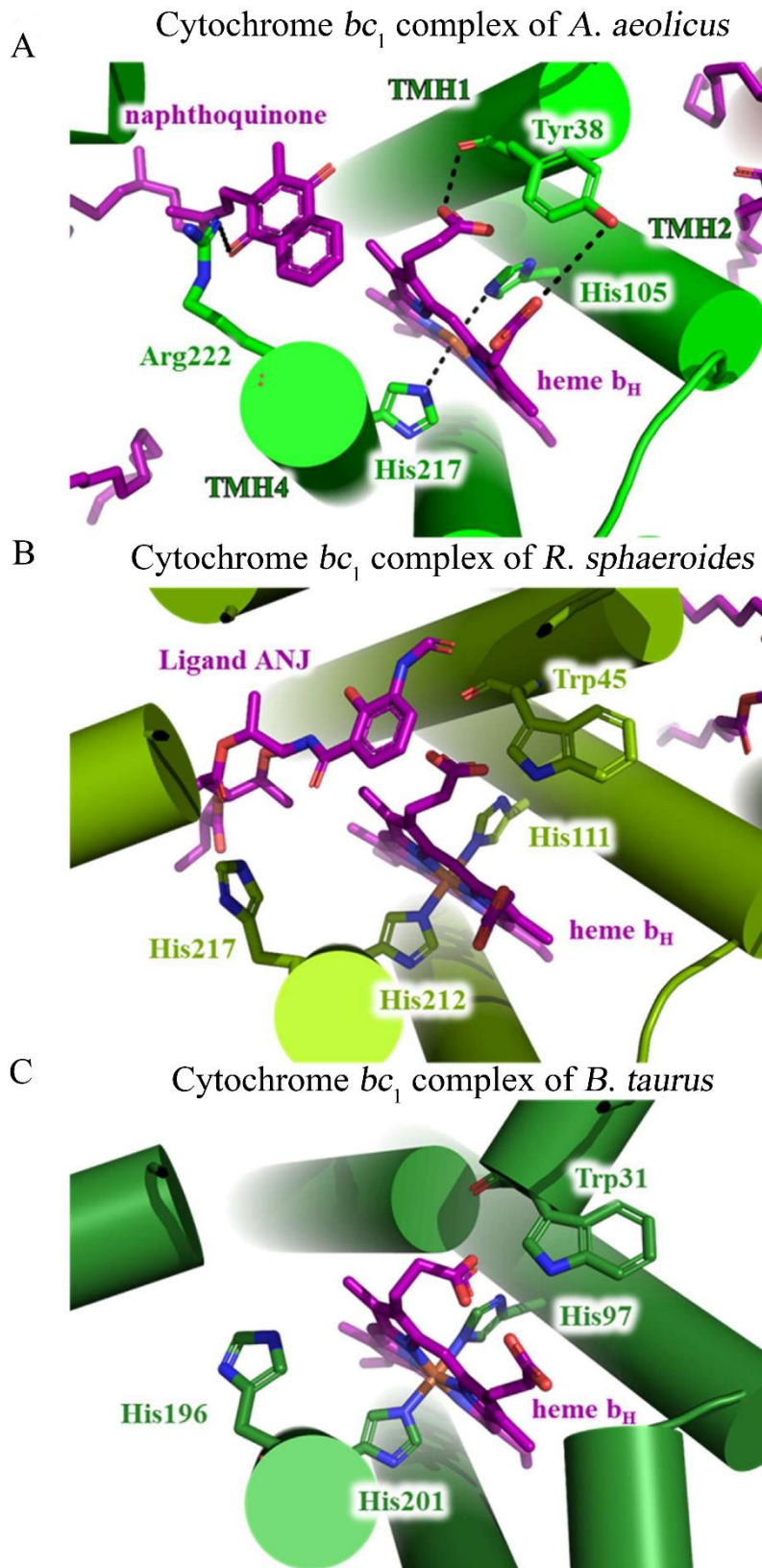
Figure 3-30: Structural comparison of the Q_i sites in cyt. *b* subunits of *A. aeolicus* (A), *R. sphaeroides* (B) and *B. taurus* (C). The proteins are shown in cartoon representations, while important residues and ligands are indicated and shown as sticks.

3.2.3.8 More stable TMHs and increased affinity with Q-pool in *A. aeolicus*

In the dimer structure of Aa*bc*$_1$, two cyt. *b* monomers bind to each other mainly through the TMHs regions. A unique residue, Tyr 61 of the cyt. *b* subunit, is involved in these dimer interactions. The oxygen atom of Tyr 61 of one monomer binds to the nitrogen atom of Arg 197 of another monomer, to stabilize of cyt. *b* dimer (Figure 3-31A). Moreover, Tyr 61 is also close to the main-chain oxygen of Val 31 of the ISP subunit, which enhances the interactions between these two subunits in the complex. In the cytochrome *bc*$_1$ complex from *R. sphaeroides* or *B. taurus*, Tyr 61 is replaced by a histidine residue (His 68 in *R. sphaeroides* or His 54 *B. taurus*), and this histidine shows no interaction with the adjacent arginine residue in TMH4 of the other protomer (Figure 3-31B and C). Tyr 61 is highly conserved in all thermophilic bacteria analyzed (Figure 3-29B). Consequently, Tyr 61 of cyt. *b* subunit helps to stabilize the TMH region in the complex.

Interestingly, there are two 1,4-naphthoquinone molecules buried in the hydrophobic pocket formed by TMH2 of cyt. *b*, TMH of ISP and TMH1of cyt. *c*$_1$ (Figure 3-31A). This pocket is located away from both Q$_i$ and Q$_o$ sites, but close to the phospholipid layer around the complex. These two 1,4-naphthoquinones are tightly bound to the Aa*bc*$_1$ because they are still present after the protein purification process, and come from the Q-pool in the phospholipid layer. This type of substrate-binding has not been found in other homologous structures (Figure 3-31B and C). Moreover, a highly conserved residue in thermophilic bacteria family, Phe 83 in TMH2 of *A. aeolicus* cyt. *b* subunit, is found to strongly bind the naphthoquinone molecule through hydrophobic interaction. In the cytochrome *bc*$_1$ complex from *R. sphaeroides* or *B. taurus*, this phenylalanine residue is replaced by a glycine or a tyrosine, respectively, which could not form strong hydrophobic interactions with the quinones. Therefore, there is no substrate binding in this region. Our structure suggests that Phe 83 of cyt. *b* helps to enhance the affinity of quinone to Aa*bc*$_1$.

A   Cytochrome bc_1 complex of *A. aeolicus*

B   Cytochrome bc_1 complex of *R. sphaeroide*
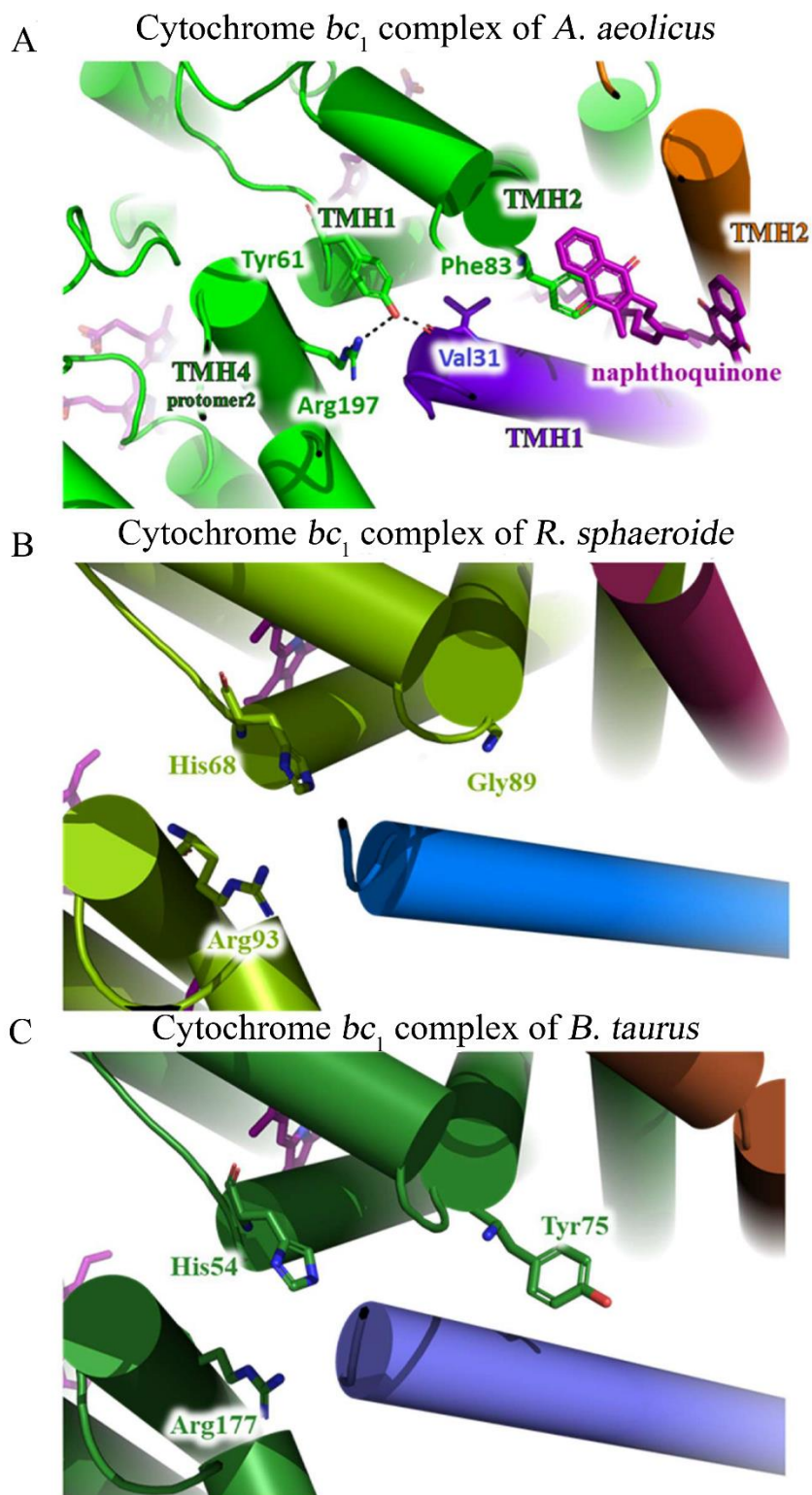

C   Cytochrome bc_1 complex of *B. taurus*

Figure 3-31: Structure comparison around TMH1 of ISP subunits of *A. aeolicus* (A)*, R. sphaeroides* (B) *and B. taurus* (C). The proteins are shown in cartoon representations, while important residues and ligands are indicated and shown as sticks.

3.2.3.9 TMH1 of cyt. c_1 improved the stability of complex in the membrane

In the structure of cyt. c_1 subunit of *A. aeolicus*, there are two TMHs, an N-terminal one and a C-terminal one. Both TMHs are bound to the cyt. *b* dimer. However, in other homologous structures, the cyt. c_1 subunit possesses only the C-terminal TMH in (Figure 3-32A). The sequence alignment shows that, this N-terminal TMH1 of the cyt. c_1 subunit of *A. aeolicus* contains a phenylalanine/tryptophan rich (WF-rich) motif, which can be found in all thermophilic bacteria but not in the other species (Figure 3-29C). This WF-rich TMH1 binds to the hydrophobic surface of the TMH region of the complex in the phospholipid layer. Importantly, a deep hydrophobic groove is formed by this kind of interaction and a phospholipid molecule is observed inside. The hydrophilic head group is bound to the positively charged region of the complex with its phosphate group, while its long hydrophobic tail is buried by a series of hydrophobic residues on TMH1 of cyt. c_1 subunit, including Phe 11, Leu 17, Phe 19 and Phe 20. Other hydrophobic residues of TMH1 interact with the hydrophobic surface of cyt. *b* to stabilize this pocket, including Tyr 4, Phe 12, Leu 23, Tyr 24 and Phe 25 (Figure 3-32C). By calculating the surface area of the protein complex, I found that the addition of this TMH1 motif largely increases the interface between cyt. *b* and cyt. c_1 subunits by 60%, from 1560 $Å^2$ to 2494 $Å^2$. Therefore, the unique N-terminal TMH1 motif of cyt. c_1 not only enhances the subunit interactions inside the cytochrome bc_1 complex, but also grab the phospholipid molecule inside the complex to stabilize the complex in the membrane.
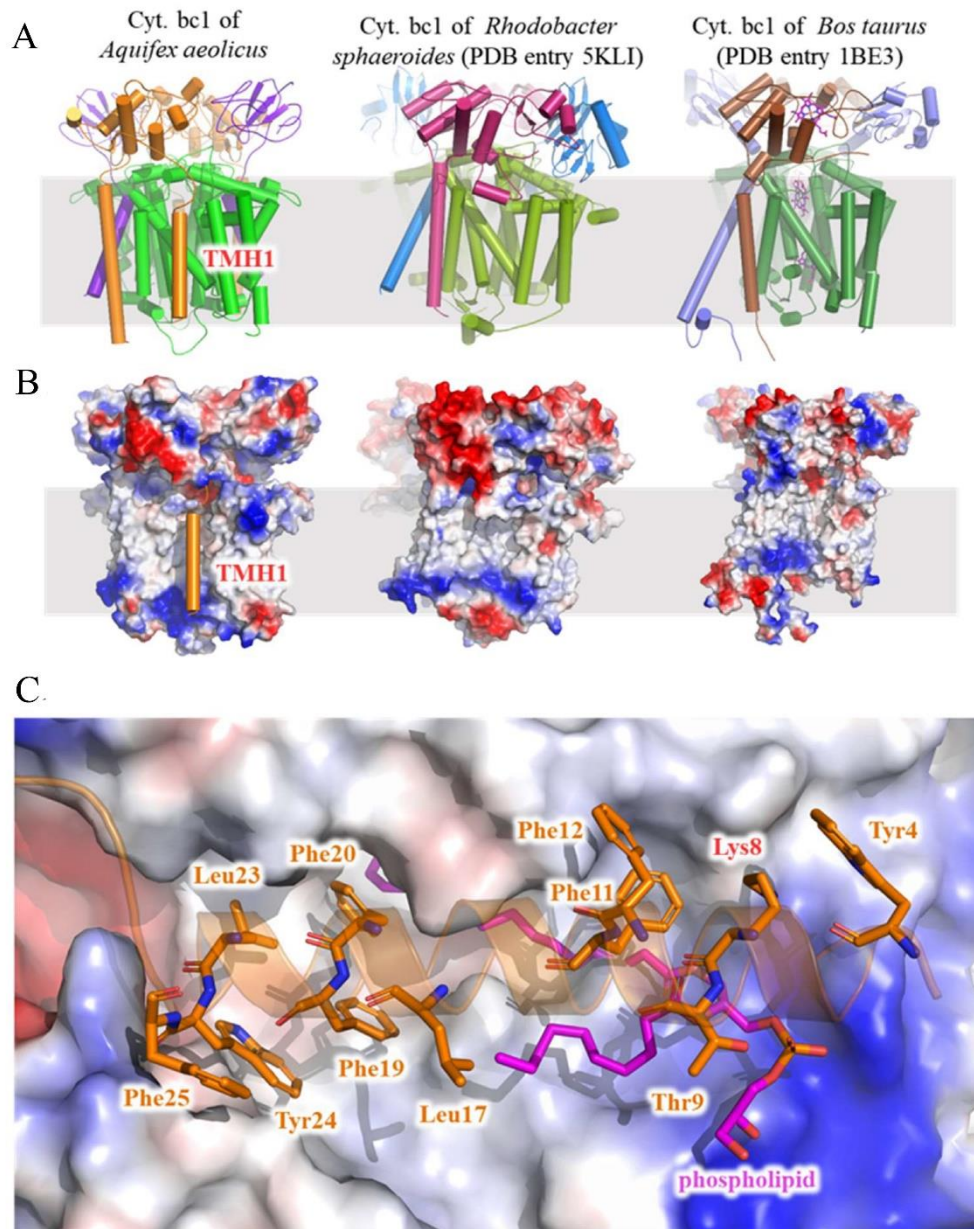
Figure 3-32: The extra TMH1 of the cyt. c_1 subunit of *A. aeolicus*. (A) The cytochrome bc_1 complex from *A. aeolicus*, *R. sphaeroides* and *B. taurus* are shown in cartoon representations, indicating the location of extra TMH1 motif of cyt. c_1 from *A. aeolicus*. (B) Electrostatics surface potential of the cytochrome bc_1 complexes from three species are shown as except for TMH1 motif of cyt. c_1. (C) Interaction details between TMH1 of cyt. c_1 with the complex and phospholipid ligand.

3.3 Characterization of AaHAS

3.3.1 Heterologous expression and purification of AaHAS

For constructing the expression vectors of AaHAS, a DNA fragment containing *ctaA* was PCR amplified from the genomic DNA of *A. aeolicus*, later digested with BamHI and EcoRI endonucleases, and subcloned into the corresponding sites of the pBAD vector. His-tag or Step-tag II were fused to the C-terminal end of AaHAS, resulting in pBAD-CtaA-His and pBDA-CtaA-Strep II, respectively. Production of His- or Strep II-tagged AaHAS in *E. coli* was detected by Western blotting (Figure 3-33).
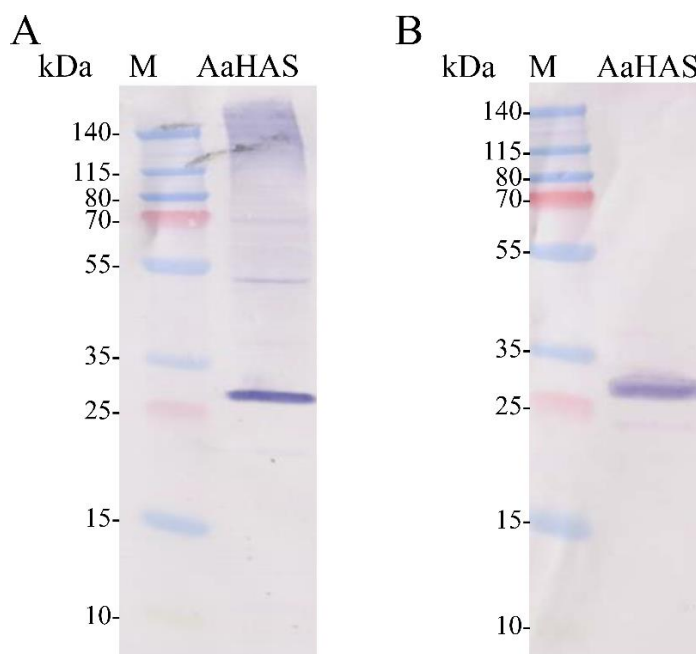
Figure 3-33: Western blot analysis of purified AaHAS. AaHAS was identified by Western blot analysis using anti-His (A) or anti-strep II antibody (B).

The His-tagged AaHAS was purified by affinity chromatography and SEC. Figure 3-34A shows the SEC profile. The main peak fractions were analyzed by SDS-PAGE (Figure3-34B). Two main bands were observed in the SDS-PAGE gel. His-tagged AaHAS was identified in both gel bands by electrospray-ionization mass spectrometry (ESI-MS) analysis. Furthermore, several bands were observed in the BN-PAGE (Figure 3-43C). All the results suggested that his-tagged AaHAS could be satisfactorily purified.

A

B

C
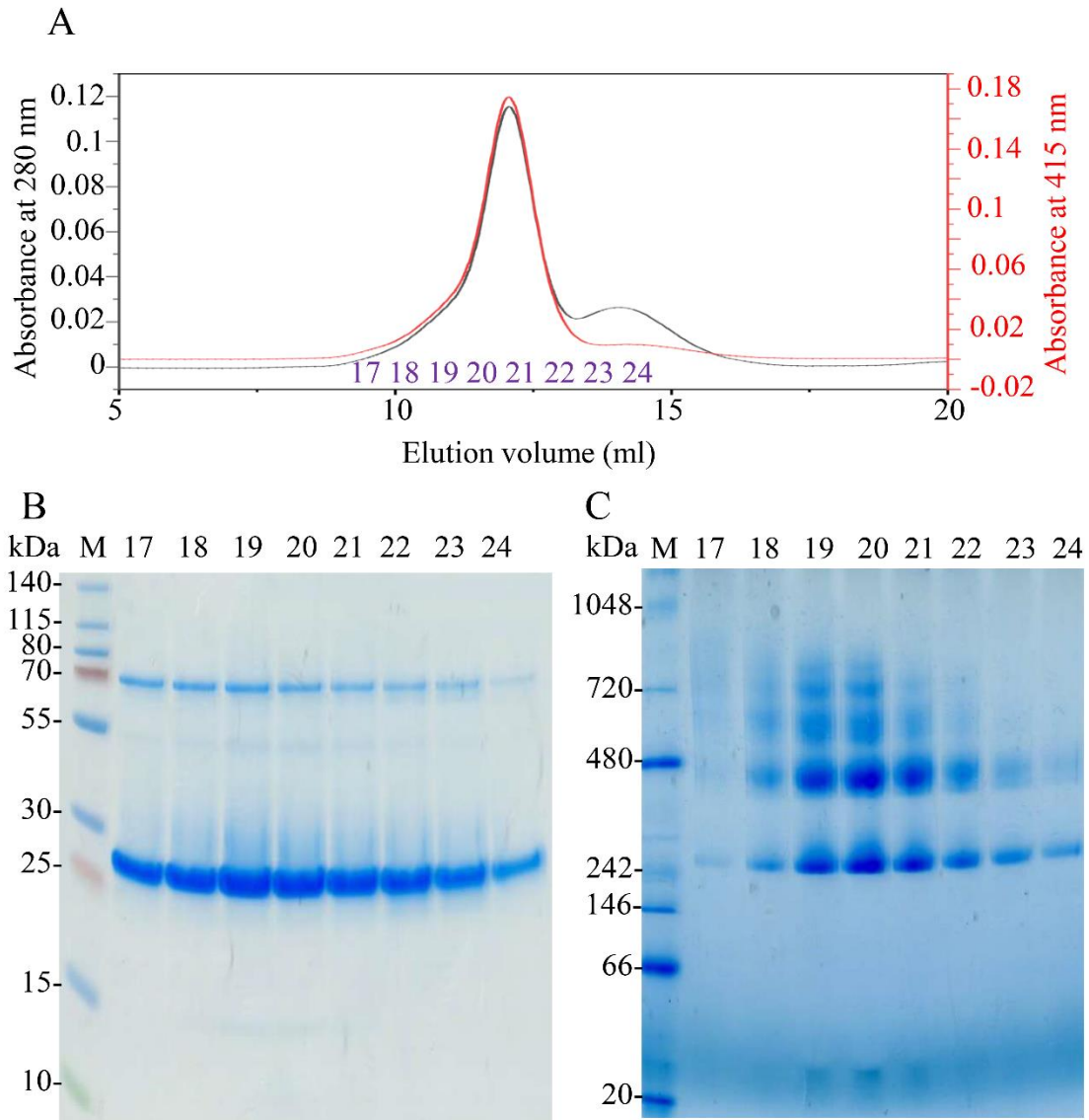
Figure 3-34: Purification of His-tagged AaHAS. The fractions from 17 to 24 are marked in the SEC profile (A). The fractions were analyzed by SDS-PAGE (B) and BN-PAGE (C). M: molecular mass marker.

Compared with his-tagged AaHAS, only one single peak was observed in the SEC profile of the strep II tagged AaHAS (hereafter AaHAS) (Figure 3-35B). The yield of the AaHAS was about 2 mg/L. To characterize the purified AaHAS, BN-PAGE was performed and a single dominant band with an approximate molecular mass of 200 kDa was observed (Figure3-35C). However, Coomassie blue-stained proteins incubated at 70°C and room temperature (RT) for 10 minutes prior to SDS-PAGE showed two distinct bands. The molecular mass was determined to be 34.95 kDa and 104.56 kDa, respectively, using matrix-assisted laser desorption/ionization time of flight mass

spectrometry (MALDI-TOF MS). Notably, only the lower band of 34.95 kDa was present when AaHAS was incubated at 90°C for 10 minutes (Figure 3-35A). Therefore, the two bands observed in SDS-PAGE might suggest that the AaHAS complex possesses two different thermal states. To confirm this hypothesis, differential scanning fluorimetry (DSF) was used to determine the transition temperature (T_m) of AaHAS. Indeed, a thermal unfolding curve was observed with two unfolding temperatures at 62.4°C and 75.3°C, respectively (Figure 3-35D).
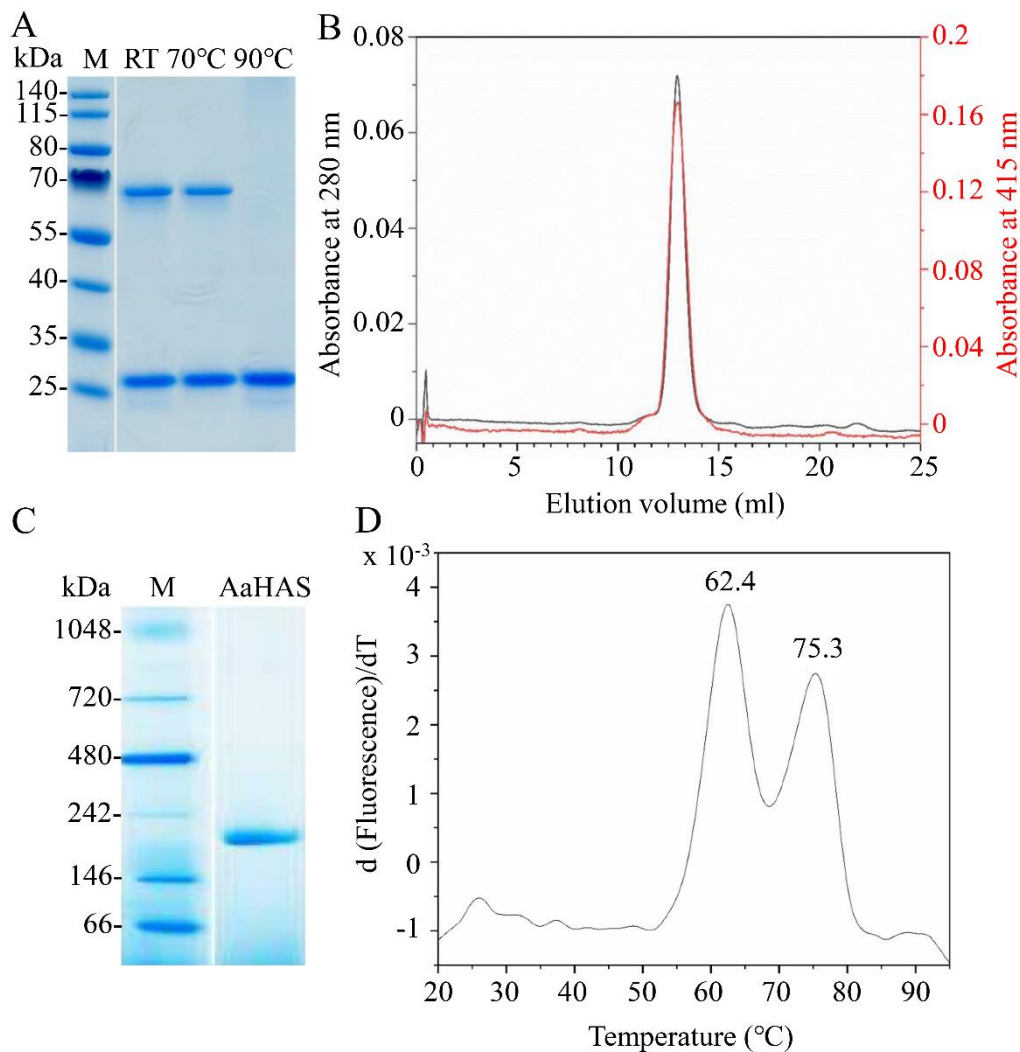
Figure 3-35: Heterologous production and purification of AaHAS. (A) SDS-PAGE analysis of AaHAS, M: molecular mass marker, AaHAS was incubated for 10 minutes at room temperature (RT), 70°C, and 90°C. Monomeric AaHAS has a calculated mass of 34.95 kDa and migrated at around 27 kDa during electrophoresis. (B) SEC elution profile of the strep II-tagged AaHAS. SEC elution profiles were monitored by absorbance at 280 nm (black) and 415 nm (red). (C) Analysis of the AaHAS complex by Blue Native PAGE, M: molecular mass marker, AaHAS: purified AaHAS. (D) Melting profile of AaHAS analyzed by DSF, Tm values are given.

To confirm that AaHAS was expressed in full-length, N-terminal sequencing was performed and the result verified the identity of the purified protein and the molecular mass of heterologously produced AaHAS is 34.95 kDa. Thus, the production and purification system of heme A synthase was established and AaHAS forms a highly thermo-stable complex.

In order to further characterize the cofactors, the absorption spectra of fully oxidized and fully reduced AaHAS were acquired. At the reduced state, AaHAS showed the Soret peak at 427 nm, the β-peak at 528 nm and the α-peak at 560 nm. After oxidation with potassium ferricyanide, the Soret peak shifted to 415 nm (Figure 3-36A). The reduced-minus-oxidized difference spectrum showed the Soret peak at 428 nm, the β-peak at 529 nm and the α-peak at 560 nm respectively (Figure 3-36B). However, the typical absorption maximum of the reduced heme A at 585 nm could not be observed, suggesting the absence of heme A in the sample.
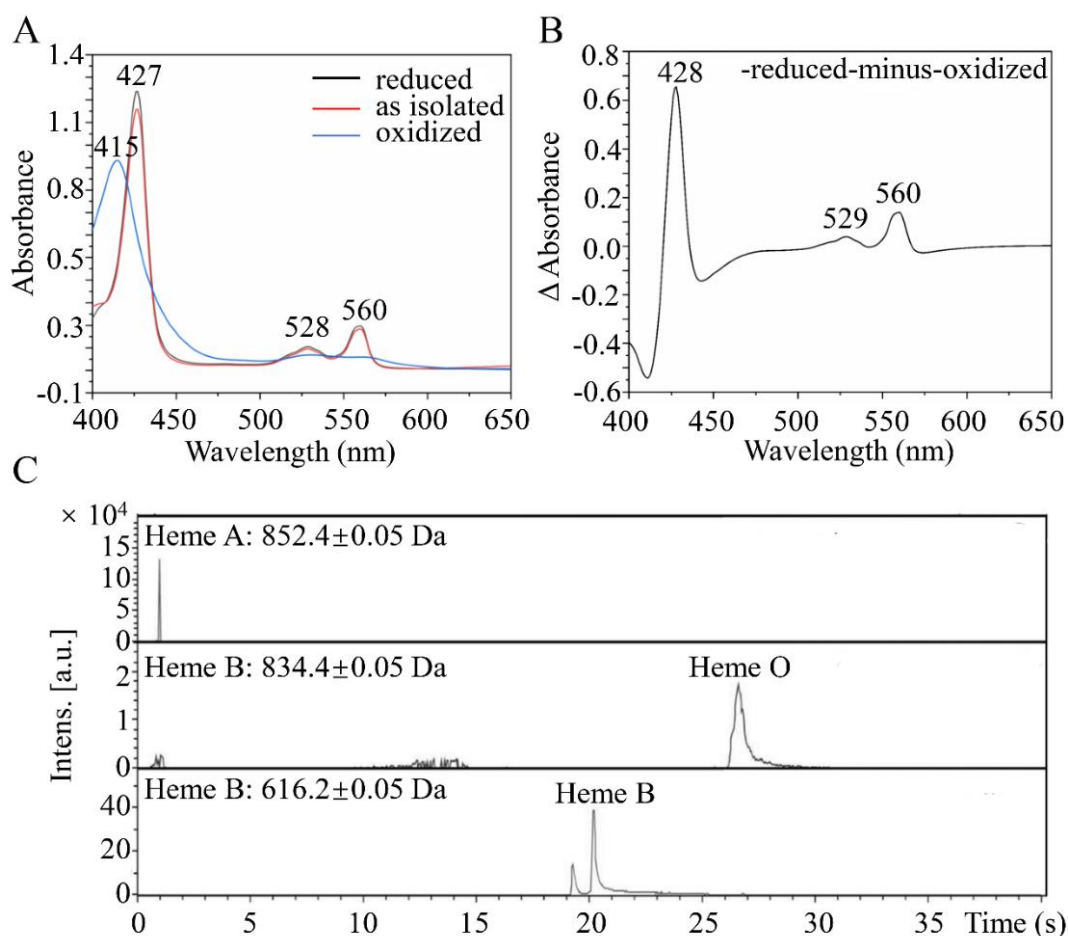

Figure 3-36: Purified AaHAS is a *bo*-form binding protein. (A) Spectra of the isolated (red line), dithionite-reduced (gray line) and potassium ferricyanide–oxidized (blue line) AaHAS. (B) Reduced-

minus-oxidized difference spectra of purified AaHAS showed a Soret peak at 428 nm, the ß-peak at 529 nm and α-peak at 560 nm. (C)The heme composition in the purified AaHAS was identified by HPLC-MS.

In addition, the high-performance liquid chromatography coupled to mass spectrometry (HPLC-MS) was used to identify the hemes in the purified AaHAS. Heme O and heme B but not heme A were detected (Figure 3-36C), which is in good agreement with the result obtained from the UV spectra. Taken together, these results show that purified AaHAS is a *bo*-form heme-binding protein.

3.3.2 Oligomerization of AaHAS

In this work, the oligomeric state of AaHAS was investigated by size exclusion chromatography-multi angle light scattering (SEC-MALS), chemical cross-linking, laser induced liquid beam ion desorption-mass spectrometry (LILBID-MS) and cryo-EM. The SEC-MALS elution profile showed one chromatography peak with the elution volume at 14.35 ml for AaHAS purified with dodecyl β-D-maltoside (DDM), suggesting the presence of a monodisperse complex. Based on the three detector method and the analysis using the OmniSEC software, the averaged mass of the AaHAS complex with and without bound DDM was calculated to be 280.99 kDa and 124.76 kDa respectively (Figure 3-37A). To rule out the possibility of the role of the detergent in oligomerization of the protein, AaHAS was purified in decyl β-D-maltoside (DM) and analyzed by SEC-MALS (Figure 3-37B). The SEC profile exhibited a similar behavior as the sample purified using DDM. The molecular mass of the AaHAS complex with and without bound DM was calculated to be 209.02 kDa and 124.36 kDa respectively (Table 3-3). The molecular masses of the AaHAS oligomer in different detergent-lipid micelles appeared to remain constant within experimental error, with an average of 124.56 kDa. Considering that the molecular mass of monomeric AaHAS is 34.95 kDa, these values suggest that AaHAS is a trimer.

Table 3-3: Molecular weight analysis by SEC-MALS

Detergent	Mw (kDa)	Wt Fr (P)	Mp(kDa)
DDM	280.99	0.444	124.76
DM	209.01	0.595	124.36
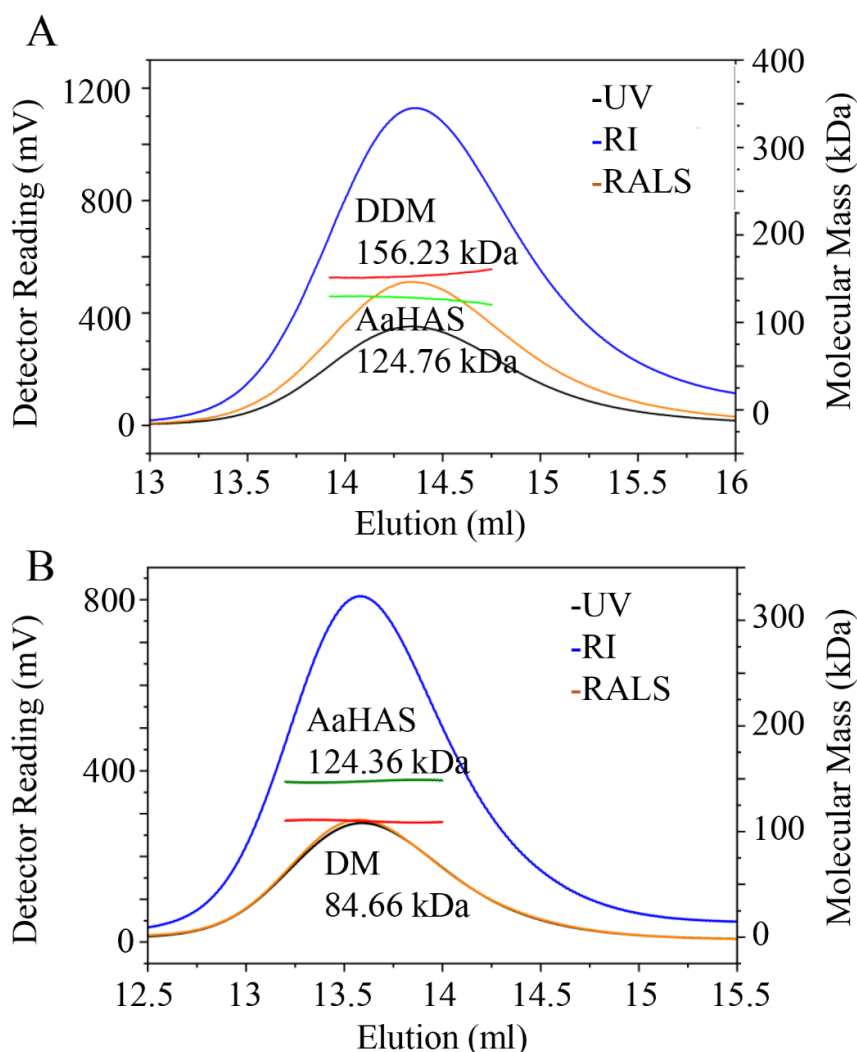
Figure 3-37: Elution profiles used for SEC-MALS analyses of AaHAS. The elution profiles of DDM-(A) and DM-purified (B) AaHAS are displayed. The reading of UV, refractive index and Light scattering are shown in black, purple and orange, respectively. The right axes represent the molecular mass. The red lines indicate the contribution of detergent components and the green lines show the calculated molecular mass of the AaHAS complex. Results are shown for one representative of three experiments.

To further analyze the oligomeric state of the AaHAS complex, chemical cross-linking experiments were performed. DM-purified AaHAS was treated with either Bissulfosuccinimidyl suberate (BS[3]) or disuccinimidyl suberate (DSS) and further analyzed by SDS-PAGE. These crosslinkers form covalent bonds between primary amino groups. The SEC profiles after the cross-linking reaction showed two peaks, one

at 12 ml elution volume and another at 20 ml. The heme absorbance at 415 nm was observed only in the peak at 12 ml retention volume. Further analysis of this peak's fractions by SDS-PAGE after incubation at 90°C for 10 minutes yielded three bands (Figure 3-38). Analysis of the cross-linked samples by MALDI-TOF MS showed three peaks of 36,214, 72,726 and 109,250 m/z for BS³ treated AaHAS and 35,451, 71,069 and 106,263 m/z for DSS treated AaHAS, respectively.
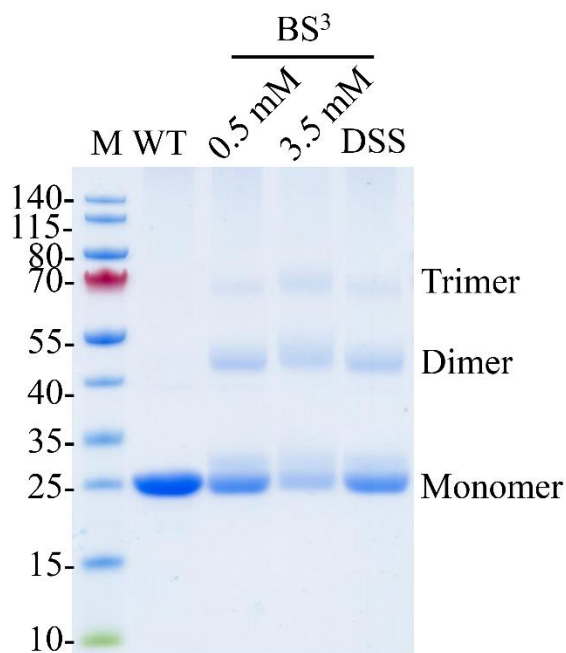
Figure 3-38: SDS gel for the determination of the oligomeric state of AaHAS via chemical cross-linking. SDS-PAGE of 70 μM AaHAS after incubation for 30 min with either 0.5 mM, 3.5 mM BS³ or 0.5 mM DSS at RT. Control (WT) was treated at room temperature for 30 minutes. All samples were incubated at 90°C for 10 minutes before loading onto the SDS-PAGE. Molecular weight markers (M) is indicated. The positions of monomer, dimer and trimer bands are indicated.

Identification of the trimeric AaHAS complex by LILBID-MS. LILBID-MS is an established method for the analysis of the oligomeric states of membrane proteins (205) . The results of SDS-PAGE and DSF (Figure 3-35) strongly suggest that AaHAS forms a thermostable complex. To remove the bound detergent and lipid molecules as much as possible, the measurements were performed at harsh laser conditions. Three individual measurements as biological replicates were performed (Figure 3-39). The singly negatively charged peaks of the monomer, dimer and trimer were observed. Small shoulders were also visible on the high m/z side of the main monomeric peak,

which may correspond to the monomer with bound cofactor (heme B, 616.487 Da), substrate (heme O, 838.854 Da) and detergents/lipids.
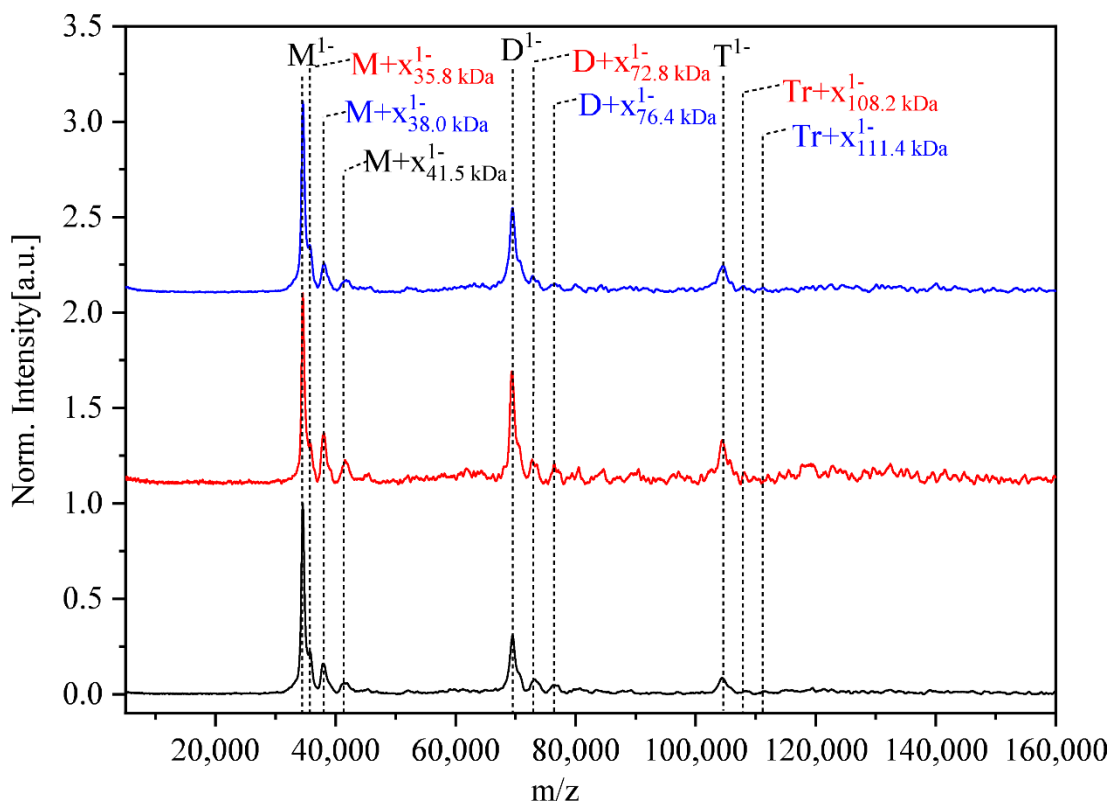
Figure 3-39: Identification of the trimeric AaHAS complex by laser induced liquid beam ion desorption mass spectrometry (LILBID-MS). The trimer of AaHAS with molecular mass of 104.3 kDa shows two different charge states. The molecular masses of dimer and monomer of AaHAS observed to be 69.5 kDa and 34.7 kDa, respectively. The molecular mass is taken from the left side of the peak position. The shoulder of the peaks indicates small molecules (x) binding to AaHAS. M, D and Tr represent the peaks of monomer, dimer and trimer of AaHAS. Three measurement results were shown in blue, red and black, respectively.

The DM-stabilized AaHAS was further analyzed by cryo-EM. The low-resolution cryo-EM structure confirmed that the AaHAS complex is trimeric. Electron images of the cryo-EM shown triangle-shaped particles in top view and rod-shaped particles in side view (Figure 3-40A). One of the classes after 2D classification clearly showed a particle of the top view with 24 TMHs (Figure 3-40B), pointing towards the trimeric state of AaHAS. In the 3D model, it was interesting to note that each protomer in the trimeric complex contacts each other tightly though interaction of the TMHs (Figure 3-40C). Furthermore, a high resolution cryo-EM structure of AaHAS was determined after reconstitution of the AaHAS in nanodiscs (3.3.4.2).
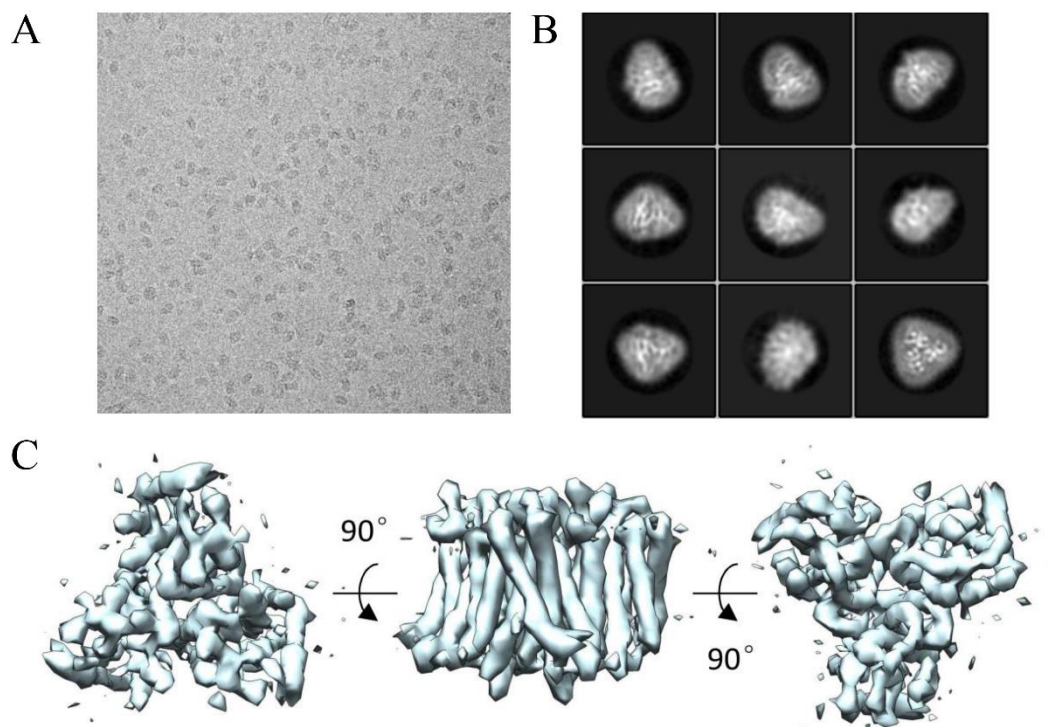
Figure 3-40: Electron micrographs of AaHAS. (A) Motion-corrected raw image of AaHAS particles recorded by FEI Titan Krios transmission electron microscope (300 kV). (B) 2D class averages obtained with the RELION (version 2.1 and version 3.0-beta). (C) Surface-rendered views of the final 3D map.

3.3.3 Mutations of AaHAS

Sequence alignment analysis of the heme A synthase from different bacterial species revealed two highly conserved cysteine residues. To gain additional insights into the functional roles of these two cysteine residues, mutagenesis studies were performed. Wild type AaHAS (WT) and, variants C46A/C40A, C46A and C40A were analyzed by SDS-PAGE after purification (Figure 3-41). The migration patterns of WT and C46A/C40A were observed to be quite similar. Monomer and trimer bands could be observed when the samples were incubated at RT and 70°C and the trimer bands were no longer evident when the sample was incubated at 90°C (Figure 3-41A). Interestingly, analysis of the variant C40A at RT and 70°C showed a dimer band as well, but only the monomer band was observed at 90°C (Figure 3-41A). Similar results are also obtained for C46A, but the dimer band was missing at RT (Figure 3-41A). The dimer bands were no longer resolvable at 70°C and 90°C after incubating the samples with dithiothreitol

(DTT) but the dimer band of C40A could still been observed at RT (Figure 3-41B). The samples that were incubated with 2-mercaptoethanol (ß-ME) showed the trimer band only at RT, while the dimer band was no longer evident (Figure 3-41C). Collectively, these results indicate that AaHAS has no inter disulfide bond and is more sensitive to ß-ME than DTT.
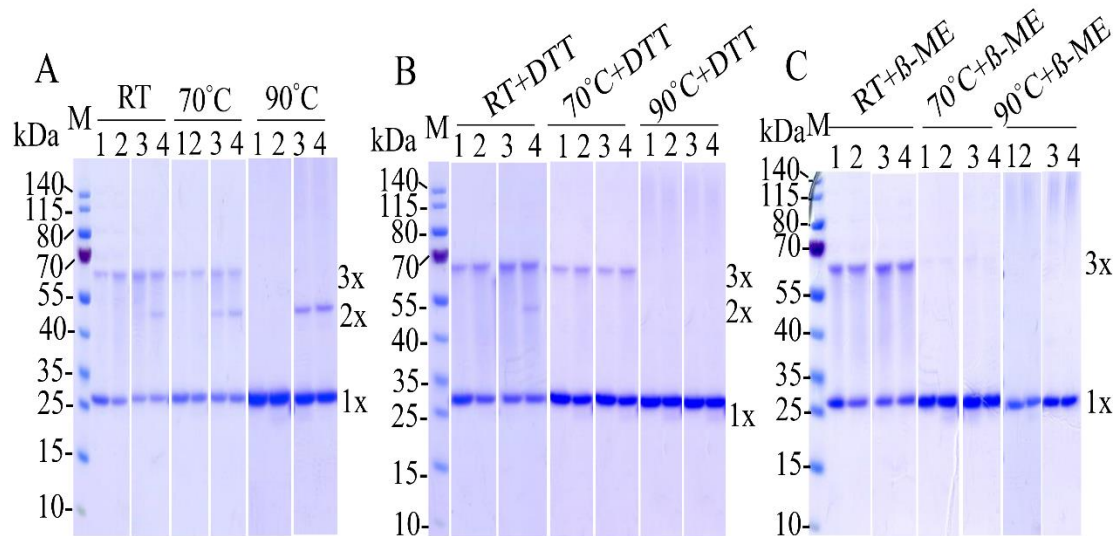
Figure 3-41: Disulfide bond in AaHAS. (A) WT and variants C46A/C40A, C46A and C40A were incubated for 10 minutes at RT, 70°C and 90°C, respectively, before 5 µg each treatment was subjected to 4-12 % SDS-PAGE. (B) WT and variants C46A/C40A, C46A and C40A were incubated with10 mM DTT at RT, 70°C and 90°C for 10 minutes, respectively, before 5 µg each treatment was subjected 4-12 % SDS-PAGE. (C) WT and C46A/C40A, C46A and C40A were incubated with 12 mM ß-ME at RT, 70°C and 90°C for 10 minutes, respectively, and then 5 µg of each mixture was analyzed by 4-12 % SDS-PAGE. The position of monomeric, dimeric and trimeric AaHAS in the gel is indicated at the right of the gel. 1: WT; 2: C46A/C40A; 3: C46A; 4: C40A.

The effect of physicochemical conditions on the oligomerization properties of AaHAS were further investigated. Independent of the purification buffer composition, containing 1M NaCl or 10 mM DTT or without NaCl, only one single band is observed in the BN-PAGE (Figure 3-42A). This result clearly suggests that the oligomeric state of AaHAS is influenced neither by the ionic strength nor by the oxidative environment. Analysis of those cysteine variants by BN-PAGE (data not shown) showed that the oligomerization of AaHAS does not depend on the disulfide bonds. However, a ladder pattern in the BN-PAGE was observed with the purified variant AaHAS-Δ_{37-79} which lacked the residues from 37 to 79 (Figure 3-42B). The result of this purified mutant was

significantly different to the single band observed for the wild type AaHAS and this observation strongly suggested that the first intracellular loop of AaHAS is critical for the maintenance of the trimeric complex.
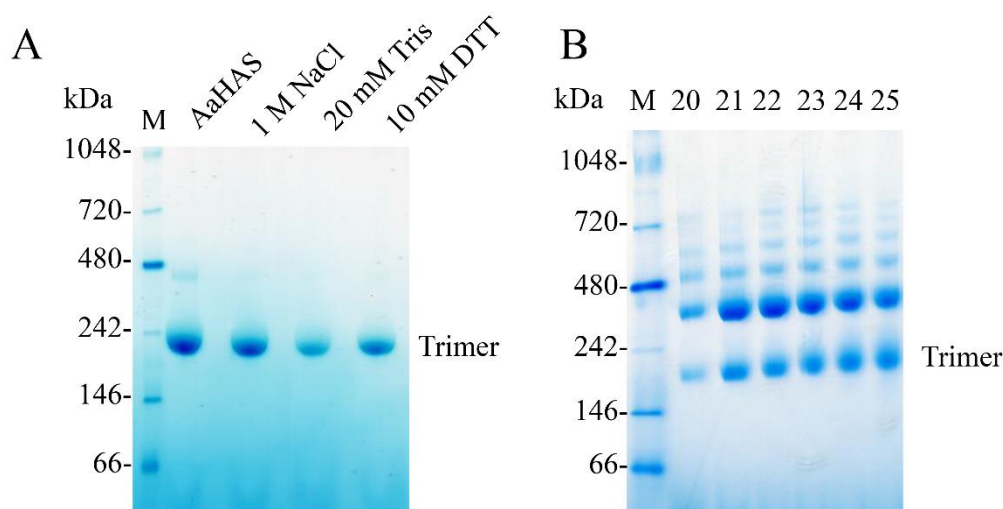
Figure 3-42: SDS-PAGE gels showing that the N-terminal loop is crucial for maintenance of the trimeric complex of AaHAS. (A) Analysis of AaHAS purified under different physicochemical conditions by BN-PAGE. (B) Analysis of different SEC fractions of AaHAS-Δ_{37-79} by BN-PAGE. The position of the AaHAS trimer in the gel is marked at the right side. M: molecular mass marker; samples from different fractions (20, 21, 22, 23, 24 and 25).

3.3.4 Structure of AaHAS

3.3.4.1 Crystallization of AaHAS

After successful purification of AaHAS, crystallization trials were conducted. Initial crystals were obtained from a variety of different conditions using commercially available and in-house designed crystallization screens using vapor diffusion and lipidic cubic phase methods. The crystals could be obtained at 10 °C and 18 °C. Table 3-4 lists the crystallization parameters, such as salts, temperature, precipitating agents and detergents, which can affect crystal morphology and diffraction quality.

Table 3-4: Screened crystal conditions of AaHAS

Screening parameter	Crystals	Best resolution (Å)
Heme A synthase		
AaHAS-C-His	Hexagonal, 2 - 5 days Rod shape, 2 - 30 days Plate, 15 days Triangular star like, 1day Cubic, 2 days	13
AaHAS-C40A-C-His	Rod shape Plate Triangular star like 3 days	17
AaHAS-C46A-C-His	Rod shape, 7 days Triangular star like, 3 - 14 days	16
AaHAS-$\Delta_{37\text{-}79}$-C-His	-	
AaHAS-C-Strep II	Hexagonal, 2 - 5 days Rod shape, 2 - 30 days Plate, 7 days Triangular star like, 1 day Cubic, 3 days	9
AaHAS-C40A-C-Strep II	Rod shape, 5 days Plate, 7 days Triangular star like, 2 days	20
AaHAS-C46A-C-Strep II	Rod shape Plate Triangular star like 3 days	16
AaHAS-C40AC46A-C-Strep II	Microcrystals <1 day Pentagon, 3 days Triangular star like, 1 day Prism, 60 days	17
AaHAS-TEV-C-Strep II	Microcrystals 2 days Rod shape 3 days	20
AaHAS-$\Delta_{37\text{-}79}$-C-Strep II	Rod shape <1 day Microcrystals	16
Temperature		
10°C	hexagonal, 1 - 3 days Rod shape <1 day Hexagonal, 2 - 5 days Prism, 60 days Triangular star like, 1 day Pentagon, 3 days Cubic, 3 days	9

18 °C	hexagonal, 1 - 3 days Triangular star like, 1 day Pentagon, 3 days	13
<mark>Buffer, pH</mark>		
Na-citrate, 3.3-4.7	Hexagonal	9
Na-acetate, 4-5.5	-	
Na-MES, 6-6.5	plate	-
Na-HEPES, 7-7.5	precipitate	
Na-Tris, 8-8.5	-	
Na-CHES, 9-9.5	precipitate	
<mark>Concentration</mark>		
7.5 mg/ml	hexagonal, 1 - 3 days Rod shape <1 day Hexagonal, 2 - 5 days Triangular star like, 1 day Pentagon, 3 days	18
10 mg/ml	hexagonal, 1 - 3 days Rod shape <1 day Hexagonal, 2 - 5 days Prism, 60 days Triangular star like, 1 day Pentagon, 3 days Cubic, 3 days	9
13 mg/ml	hexagonal, 1 - 3 days Rod shape <1 day Hexagonal, 2 - 5 days Triangular star like, 1 day Pentagon, 3 days	20
<mark>Precipitating agent (PEG)</mark>		
PEG 200 (19-29% v/v)	-	
PEG 250 DME (19-29% v/v)	-	
PEG 300 (19-29% v/v)	-	
PEG 400 (19-29% v/v)	hexagonal, 1 - 3 days Rod shape <1 day Hexagonal, 2 - 5 days Prism, 60 days Triangular star like, 1 day Pentagon, 3 days Cubic, 3 days	9
PEG 500 DME (19-29% v/v)	Rod shape <1 day Plate <1 day	25
PEG 600 (19-29% v/v)	Rod shape <1 day Plate <1 day Triangular star like, <1	33

	day	
PEG 1000 (19-29% v/v)	Triangular star like, 1 day Plate, 1 day	13
MPEG 350 (19-29% v/v)	-	
MPEG 500 (19-29% v/v)	Rod shape <3 days Cubic, 7 days	29
<mark>Detergents (after extensive detergent shift)</mark>		
UM	-	
α-DDM	Rod shaped Cubic Microcrystals Plate 3 days	16
ß-DDM	Hexagonal, 2 - 5 days Rod shaped 2 - 30 days Plate Triangular star like Cubic	10
NM	Microcrystals 15 days	-
OM	Rod shaped 20 days	20
DM	Hexagonal, 2 - 5 days Rod shape 2 - 30 days Plate 30 days Triangular star like < 1 day Cubic 2 days Pentagon 3 days	9
MANC12	-	
LMNG	Rod shape 43 - 63 days Microcrystals	18 -
Cymal-4	-	
<mark>Small molecules additives</mark>		
Small inorganic salts		
Calcium chloride	Plate, 48 days	14
Lithium sulfate	Rod shape, >48 days	18
Copper (II) chloride	Rectangular, >199 days	14
Manganese (II) chloride	Plate, >199 days	18
Ferric chloride	Plate, >48 days Rectangular, >48 days	18
Praseodymium (III) acetate	Rod shape, >48 days	23
Organic		

Ethanol	Hexagonal, 8 days	
2-propanol	Hexagonal, 22 days	20
	Rod shape, 8 days	18
2,2,2-trifluoroethanol	Microcrystals	-
1-butanol	Microcrystals	-
1-propanol	Hexagonal, 22 days	18
	Rod shape, 8 days	
	Plate, 4 days	
Tris(2-carboxyethyl) phosphine	Plate, >199 days	20
1,3-propanediol	Rod shape	22
	Plate	
	Triangular star like	
	>48 days	
Dichloromethane	Rectangular, >199 days	18
<mark>Others</mark>		
Dtergents (as additives)		
LDAO	plate	-
n-hexadecyl- ß -D-maltoside	Hexagonal, >100 days	16
n-tetradecyl- ß -D-maltoside	Hexagonal, >100 days	18
sucrose monolaurate	Microcrystals, >100 days	-
Reduced		
2 mM DTT	Microcrystals, 4 days	-
	Needle 29 days	
Lipidic cubic phase		
The CubicPhase II Suite	-	
The CubicPhase I Suite	- Microcrystals, 45 days	22
LCP_Screen_Salts	-	
LCP_Screen_PEG400_Citrate	-	

From the variety of the screened conditions, the best AaHAS crystals diffracted up to 9 Å resolution. It was grown in the presence of PEG 400 (22%) and 0.15% DM, in Na-citrate buffer (pH 3.5) at 10°C.

3.3.4.2 Cryo-EM structure of AaHAS

3.3.4.2.1   Overall cryo-EM structure of AaHAS

AaHAS is an integral membrane protein and the molecular mass of the AaHAS trimer is only 105 kDa. After the resolution revolution, numerous structures of smaller proteins are constantly being submitted to EMDB, but still it is a big challenge to get a high

resolution cryo-EM structure of such a small protein as AaHAS. These major limitations were addressed with varying sample preparation. Finally, the purified AaHAS reconstituted into nanodiscs which was prepared with MSP1D1 (Figure 3-43A) and a single band was observed in the BN-PAGE (Figure 3-43A). A representative cryo-EM micrograph is shown in figure 3-43C. 28 good classes were obtained after 2D classification (Figure 3-43D). A high resolution EM model of AaHAS at 2.8 Å resolution was finally obtained after refinement taking best classes with a total 72,345 particles and the local resolution is showed in Figure 3-43E.
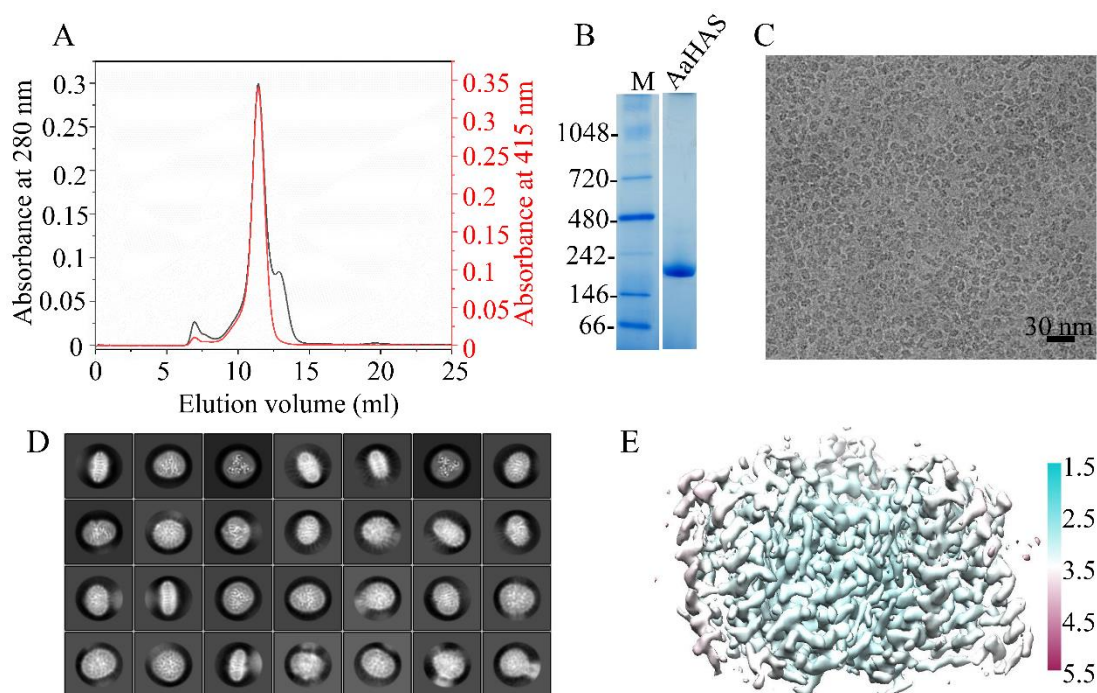
Figure 3-43: Cryo-EM sample preparation and overall structure of AaHAS. (A) Size exclusion chromatography of AaHAS which was reconstituted in nanodisc. The absorption at 415 nm (red) and 280 nm (black) were recorded. (B) Blue native PAGE was used to analyze the purified AaHAS. M: molecular mass marker, AaHAS: purified AaHAS. (C) Representative cryo-EM micrograph.D, Representative reference-free 2D class averages for AaHAS. (E) Local-resolution-filtered map for AaHAS is from 1.5 (blue) to 5.5 Å (red).

A C3-symmetric structure of AaHAS was determined at overall 2.8 Å resolution (Figure 3-44A and Table 3-5). The structure shows a three-blade propeller-shaped trimer with dimension of roughly 77 x 75 x 53 Å. Each protomer of AaHAS has eight TMHs (TMH1-TMH8) as shown in Figure 3-44B. The EM density for the residues from Leu 56 to Pro 75 of the long extracellular loop (ECL) is not quite visible in the map.

Previous work on this enzyme suggested classes B, C and D of HAS evolved from class

A by tandem gene duplication leading to one extracellular loop (ECL) at the N-terminal half and another one at the C-terminus respectively (121,125,206). In our structure of AaHAS, the N-terminal half contains ECL1 and a short extracellular loop (ECL2) (Figure 3-44B) while the C-terminal half contains two short extracellular loops. The heme O binding groove is observed in the N-terminal half domain formed by TMH1 to TMH4. The cofactor heme B was identified in the C-terminal half domain containing TMH5 to TMH8, in coordination with His 213 and His 216. ECL2 was found close to the C-terminal half of the adjacent monomer.
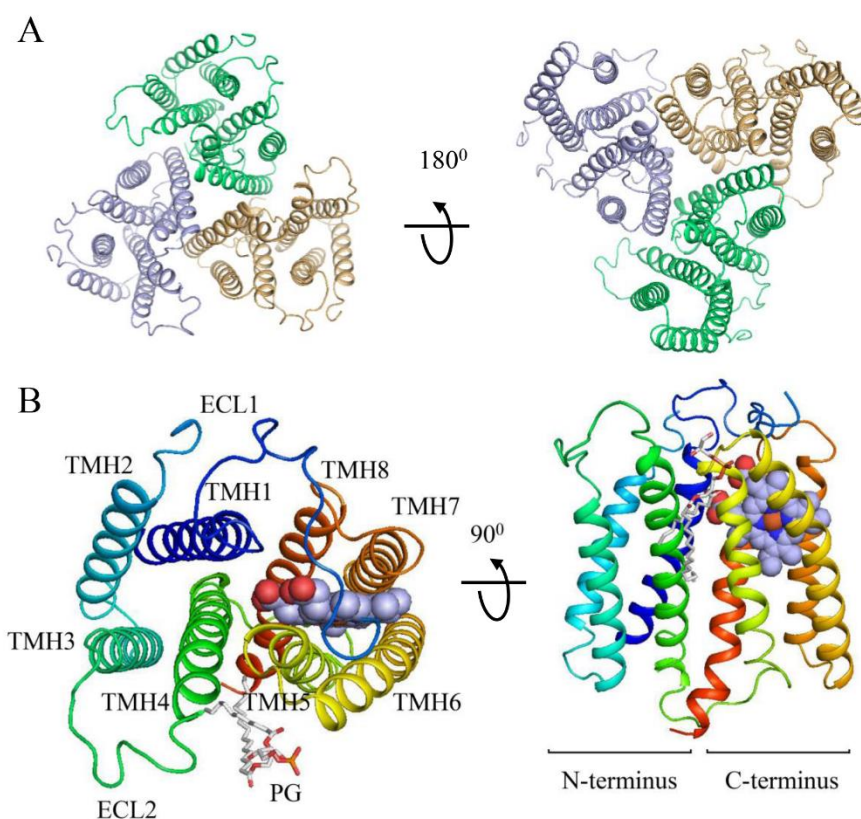
Figure 3-44: Structure of AaHAS in lipid nanodiscs. (A) Orthogonal views from the extracellular (left) and the intracellular (right) side of the trimeric AaHAS is shown as ribbons. AaHAS monomers are colored green, orange and blue, respectively. (B) The monomeric AaHAS structure is shown in two different views and colored in rainbow from the N-terminus (blue) to the C-terminus (red). Cofactor heme B is shown in blue spheres. PG near the extracellular side is shown as a stick model. The 8 TMHs and extracellular loops are labeled. The N-terminal half is formed by TMH1 to TMH4, ECL1 and ECL2, while the C-terminal half is formed by TMH5 to TMH8 and contains heme B.

Table 3-5: Cryo-EM data collection and processing of AaHAS

Sample	heme A synthase
Data collection	
EM equipment	FEI Titan Krios
Voltage (KV)	300
Detector	Gatan Bioquantum K2
Energy filter	20 eV
Pixel size (Å/pixel)	0.82
Electron dose (e$^-$/ Å^2)	70
Defocus range (μm)	-1.2~-2.2
Reconstruction	
Software	RELION 3.0-beta / RELION 2.0
Number of used particles	72,435
Accuracy of rotation	1.061
Accuracy of translations (pixel)	0.303
Symmetry	C3
Map sharpening B-factor (Å^2)	-68
Final resolution (Å)	2.78
Model building	
Software	Coot
Model Refinement	
Software	PHENIX
Map CC (whole unit cell)	0.81
Map CC (around atoms)	0.77
Rmsd (bonds) (Å)	0.006
Rmsd (angle) (°)	0.881
Model composition	
Protein residues	792
Heme groups	3
Validation	
Ramachandran plot	
Outliers (%)	0.13
Allowed (%)	10.26
Favored (%)	89.62
Rotamer outliers (%)	6.11

The quality of the cryo-EM map was sufficient to define lipids between TMHs (Figure 3-45). Though zwitterionic 1-palmitoyl-2-oleoyl-sn-glycero-3-phosphocholine (POPC) lipids were used for nanodisc reconstitution, a molecule of the polar lipid PG was observed close to TMH4 at the extracellular side (Figure 3-44B). PG tightly binds to

AaHAS, suggesting that the lipids play a crucial role in the maintenance of the structural and functional integrity of AaHAS.
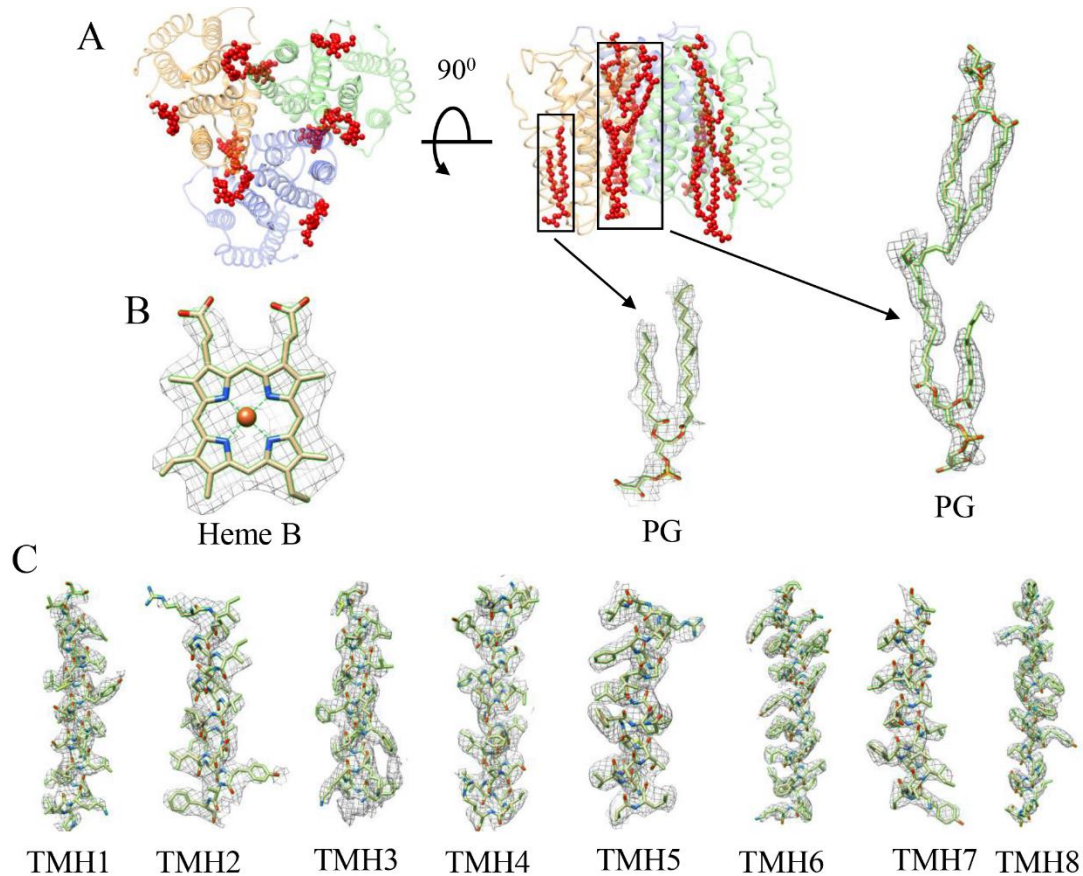
Figure 3-45: Fit of molecular model to cryo-EM density of AaHAS. (A) Extracellular (left) and membrane (right) views of trimeric AaHAS with molecular models of PG which are shown in sticks. The molecular models of PG also fit to the cryo-EM density with 3 σ. (B) Cofactor heme B is shown with cryo-EM density and σ value is 2.5 σ. (C) Transmembrane helices with sharpened maps of AaHAS are shown in mesh with 5 σ.

The crystal structure of BsHAS showed that the N- and C-terminal transmembrane domains superimpose well with Cα r.m.s.d. value of 2.3 Å by a pseudo twofold symmetry (207). However, superimposition of the N- and C-terminal domains of AaHAS showed a big difference, with Cα r.m.s.d. of 12.6 Å (Figure 3-46). TMH2 is straight. TMH4 was clearly observed to be kinked at a valine residue 153 in *A. aeolicus* (Figure 3-46).

Figure 3-46: Superimposition of the N- and C-terminal halfs of AaHAS. The N-and C-terminal domains of AaHAS are colored in orange and cyan. The gray box indicates the position of the membrane.

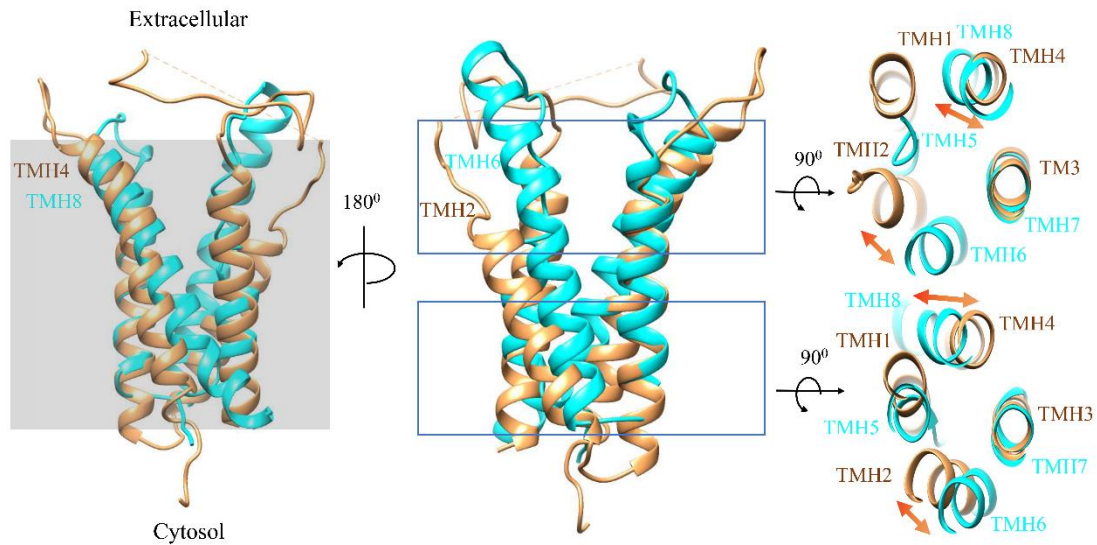### 3.3.4.2.2 The AaHAS trimer is formed by hydrophobic interactions

To get more details about how AaHAS forms a stable trimer, hydrophobicity analysis of AaHAS was performed and the result suggests that the AaHAS trimer is formed by hydrophobic interactions (Figure 3-47A). This result confirms the conclusion that HAS is formed via hydrophobic interaction (126). The trimeric interface is a tapered hole in the center of the trimeric cryo-EM structure (Figure 3-44A). TMH6 contains 8 hydrophobic residues with some highly conserved residues and is observed to be involved in the interactions of protomers in the trimeric complex. TMH6 is kinked at Gly 218 (Figure 3-47B). Interestingly, three kinked TMH6 from different monomers bend to pack together at the periplasmic side and partially close the tapered hole. An array of hydrophobic interactions between the adjacent TMH6 contribute to the stability of the trimer (Figure 3-47B). The residues Phe 208, Leu 212, Thr 215, Tyr 216 and Phe 219 in the TMH6 are the major contributors to the trimer formation and stability (Figure 3-47B). Phe 208 is near the periplasmic side and it forms the first hydrophobic belt. The distance between those three Phe 208 from different monomers is around 4 Å. The second hydrophobic belt is formed by Leu 212 and Thr 215 and the distance between Leu 212 to Thr 215 from the adjacent monomer is 3.8 Å. The third hydrophobic belt is near the middle of TMH6 and is formed by residues Tyr 216 and Phe 219 from the

neighborhood. The distance between Tyr 216 and Phe 219 is around 3.9 Å. We suggest that three hydrophobic belts ensure that the water or ion accessibility inside the tapered hole is under strict regulation and provide the high stability of the AaHAS trimer.
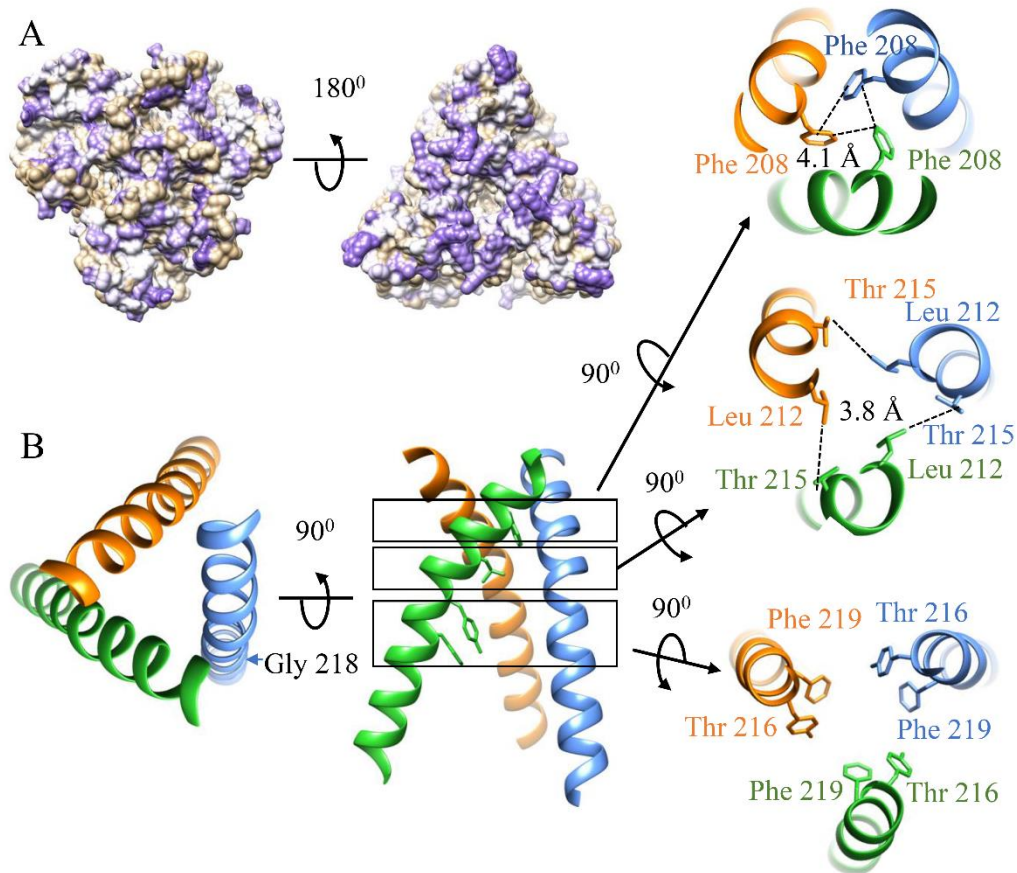
Figure 3-47: Hydrophobicity of AaHAS. (A) Extracellular (left) and intracellular side views of the trimeric AaHAS hydrophobic regions. The hydrophobicity surface is colored by amino acid hydrophobicity on the Kytr-Doolittle scale generated with Chimera software. The most hydrophilic residues are colored tan and the most polar are medium purple. The trimeric interface in the center is primarily tan. (B) TMH6 is kinked at the most conserved Gly 218 and involved in the trimeric interface (left). There are three hydrophobic belts from the beginning to the middle of TMH6 (middle). The first hydrophobic belt is formed by Phe208 and the second belt is formed by Leu 212 and Thr 215. Tyr 216 and Phe 219 form the third hydrophobic belt (right).

Additionally, the direct interaction of TMH6 via residues Tyr 205 and Thr 215 was observed in our structure (Figure 3-48). TMH5 also makes a big contribution to the trimeric interface (Figure 3-48). Leu 183 in TMH5 and Ile 227 in TMH6 form a strong hydrophobic interaction at the bottom of the tapered hole. Additionally, a strong hydrophobic interaction exists between Tyr 179 from TMH5 and Phe 226 in TMH6. TMH5 not only has an interaction with TMH6 from the same monomer, but also has a

strong interaction with the TMH6 from the adjacent monomer. Leu 192 in TMH5 can be seen interacting with Ile 222 in TMH6 from the adjacent monomer.
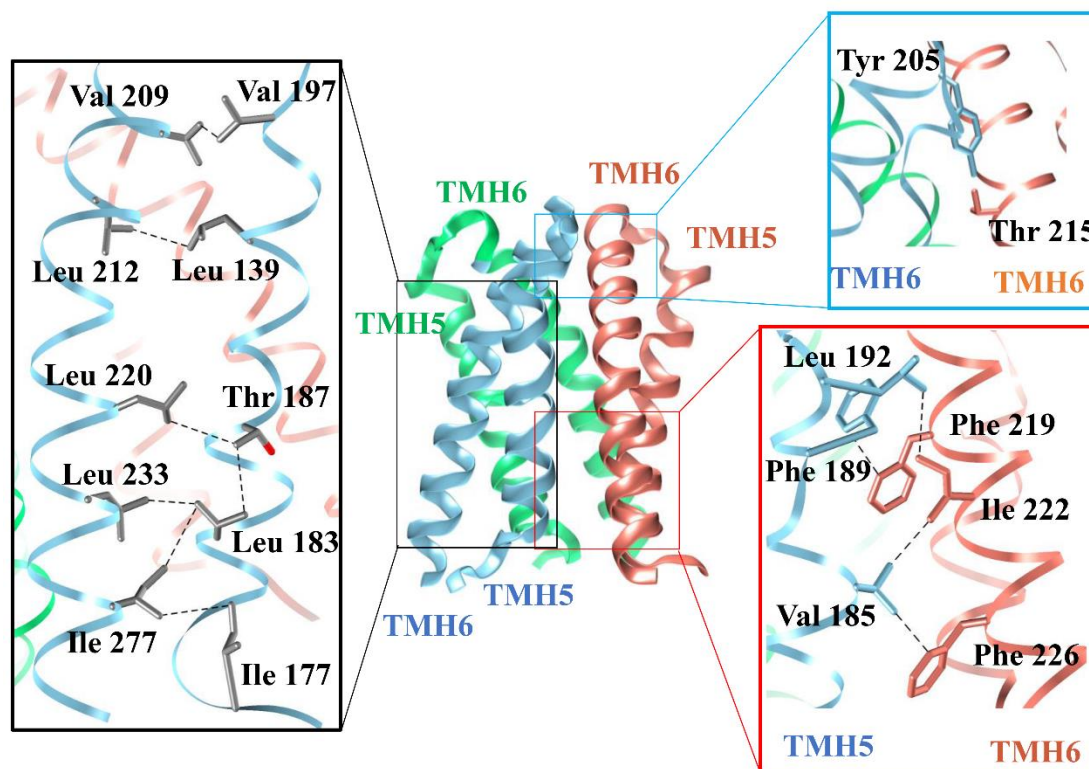
Figure 3-48: The interactions in the formation of the AaHAS trimer between TMH5, TMH6 and TMH6*. The trimeric interface is formed by TMH5 and TMH6 from different subunits. TMH5 and TMH6 in one monomer are colored in blue, green and orange, respectively. The hydrophobic interactions between TMH5 and TMH6 in one monomer is shown (left) and the residues involved in the hydrophobic interaction are labeled. The direct interaction between Tyr 205 on TMH6 and Thr 215 on TMH6* is shown. Leu 192, Phe 189 and Val 185 in TMH5 and Phe 219, Ile 222 and Phe 226 in TMH6* form an array of hydrophobic interactions (right).

3.3.4.2.3 Structure comparison reveals substrate binding groove conformation change

Crystal structure of BsHAS suggested that the substrate heme O binding depends on the conformation change of TMH2 which can open and close the binding groove open and close (207). To investigate the structural basis of a confirmation change, more details were analyzed by superimposing the structure of AaHAS and with that of BsHAS structure. The structure comparison suggests that the BsHAS superimposes well with the monomer AaHAS with a r.m.s.d. of 1.28 Å and reveals a similar position of the cofactor heme B. However, differences were found at the N-terminal domain and

TMH6. Superposition of AaHAS and BsHAS revealed that the heme O binding groove in AaHAS is slightly larger than in BsHAS (Figure 3-49A).

The cryo-EM map reveals that the ECL2 of AaHAS completely points to the exterior of the groove, which was not observed in the crystal structure of BsHAS (Figure 3-49A). ECL2 in AaHAS is longer than in BsHAS and its outward conformation makes the interaction with another monomer possible. There is one Arg 137 at the end of ECL2 and the TMH4 slightly is kinked at a highly conserved residue Val 153. Compared to the TMH4 in BaHAS, the extracellular end of TMH4 in AaHAS showed an outward shift by ~8.5° (Figure 3-49B). Moreover, compared to the TMH3 in BaHAS, the extracellular end of TMH3 was observed to be shifted outward by ~18.5° in AaHAS. These results suggest that ECL2, TMH3 and kinked TMH4 may be responsible for the conformational change during the heme O binding or heme A release.
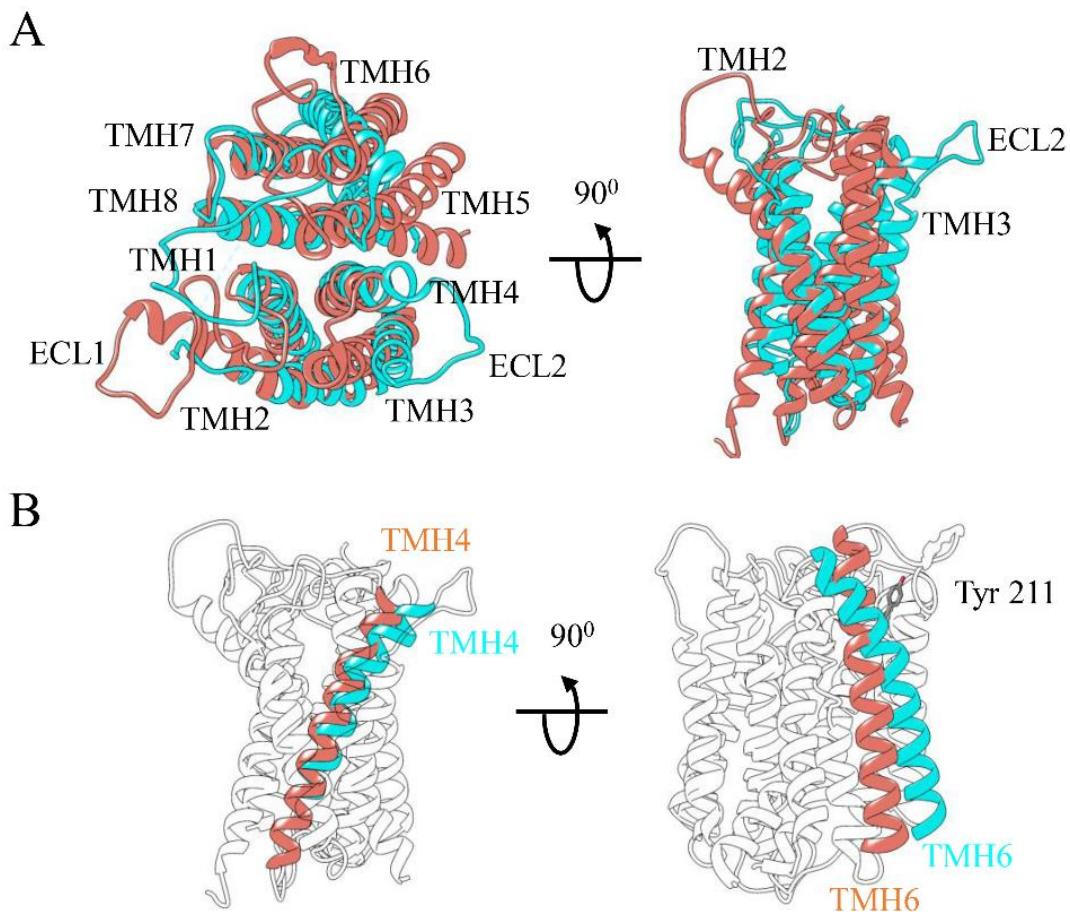

Figure 3-49: Superposition of BaHAS (salmon) and AaHAS (cyan). (A) Extracellular (left) and membrane (right) side views of the superposition. The number of helices from AaHAS are labeled and the extracellular loops at the N-terminal half are marked. (B) Details of the superposition differences of TMH4 and TMH6 from BaHAS (salmon) and AaHAS (cyan). Tyr 211 from AaHAS is shown as sticks.

A kinked TMH2 at Gly 65 is observed in BsHAS, while an almost straight TMH2 in AaHAS can be seen in our cryo-EM structure (Figure 3-49A). TMH6 which is the counterpart in the C-terminal domain is straight in BsHAS. However, TMH6 is kinked at Gly 218 in AaHAS (Figure 3-49B, Figure 3-47B). The kinked TMH6 results in the aromatic ring of Tyr 211 in TMH6 pointing to TMH4 from the adjacent monomer. All observed structural differences between AaHAS and BsHAS may explain why the heme O binding groove in AaHAS is bigger than in BsHAS. The biological implications of these differences are discussed further in the discussion section.

3.3.4.2.4   Arg 137-lipid-Tyr 211 interactions shape the conformational substrate binding domain

Oligomerization of HAS is believed to be important for the function of heme A biosynthesis (126,208) and Cox1 maturation (22,209). To understand the structural basis of the relationship between the oligomerization and function, structural details at the interface between the monomers are analyzed. Six robust densities are observed in the groove which is formed by one monomer and the C-terminal half of the adjacent monomer (Figure 3-45). The well-resolved densities are assigned as PG, though POPC were used in the reconstitution of AaHAS into nanodiscs (Figure 3-45). Many published membrane protein structures suggested that lipid-protein interactions play an important role in protein fold (210,211), oligomerization (212,213) and function (199,214,215). PG is tightly bound to AaHAS, which suggests that it plays a crucial role in structural and functional integrity (Figure 3-50). Most remarkably, Tyr 211 in TMH6 is present in the interfacial region and interacts with the PG phosphodiester group in combination with the positively charged Arg 137 in ECL2. This a typical tight protein-lipid interaction which was reported to keep proteins in a high oligomeric state (216-219). Considering that Arg 137 is located at the end of ECL2 where TMH4 begins, Arg 137-lipid-Tyr 211 interaction may explain the observation that the ECL2 bends outwards and TMH4 is kinked. These results also explain how oligomerization of AaHAS plays a critical role in functional integrity.
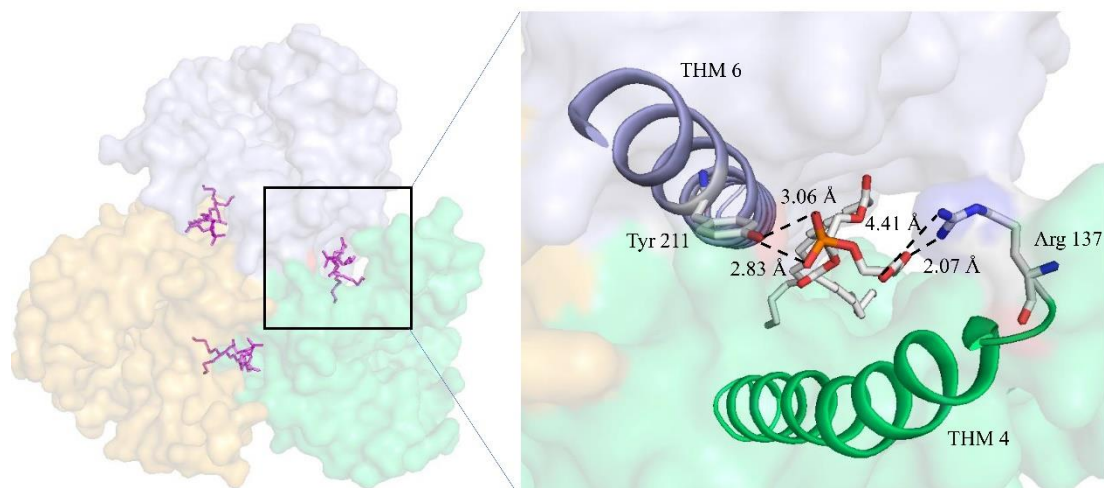
Figure 3-50: Dimer interface of AaHAS. The monomeric AaHAS is colored in bright orange, green and blue, respectively. Three molecules of PG located at the extracellular side between the monomer interface are shown (left). The details of the surrounding environment of the PG are shown (right). Tyr 211, Arg 137 and PG are shown as sticks. The distances from the side change of Tyr 211 and Arg 139 to the negative head group of PG are marked.

4. Discussion

4.1 Respiratory chain complexes of *A. aeolicus*

Aquifex aeolcius (VF5) is an extremely hyperthermophilic Gram-negative bacterium which belongs to the phylum Aquificae (160). The 16S rRNA gene sequence analysis suggested that it represents a very deep phylogenetic branch within the bacterial domain. It was isolated from a hydrothermal system of 102 °C (Porto di Levante, Vulcano, Italy) and can be cultured at 85 - 95 °C with inorganic components $H_2/CO_2/O_2$ (79:20:1) in the "SME" medium (161). *A. aeolicus* does not grow on a number of organic substrates, including sugars, amino acids, yeast extract or under strictly anaerobic condition in the laboratory (135,146). However, a gene, which is adjacent to the nitrate transporter gene, encoding putative nitrate reductase was identified in the *A. aeolicus* genome (135), suggesting that *A. aeolicus* may also use nitrate as an electron acceptor. *A. aeolicus* is a model organism to study the respiratory chains of microaerophilic hyperthermophiles (147,149,180).

The genes required for the respiratory chain complexes are often clustered in functionally related operons in *A. aeolicus*. The genome sequence indicates the existence of enzymes similar to other bacteria for oxygen respiration such as cytochrome bc_1 complex, cytochrome *c*, cytochrome *c* oxidase and the cytochrome *bd* quinol oxidase (135). Characterization of the cytochrome bc_1 complex from *A. aeolicus* was reported in 2003 and suggested that it is the only extant true naphthoquinol oxidizing cytochrome bc_1 complex (111). Characterization of ba_3-type cytochrome *c* oxidase from *A. aeolicus* suggested that it is so far the only known oxidase using both cytochrome *c* and ubiquinol as electron donors (149). It was previously proposed that there is an unusual aerobic respiratory pathway in this organism consisting of an electron transfer from hydrogen sulfide (H_2S) or hydrogen to molecular oxygen (181,220). Prunetti and co-workers confirmed the existence of this respiratory pathway and suggested the presence of an unusual supercomplex composed of dimeric

cytochrome bc_1, ba_3-type cytochrome c oxidase and one or two sulfide quinone reductases as well as traces of the monoheme cytochrome c_{555} and quinone molecules (180).

All results suggest that the respiratory chain in *A. aeolicus* is uncommon. Characterization of the protein complexes from this special respiratory chain has been partially done. However, the mechanistic details of electron transfer are unclear and atomic structures of cytochrome c oxidase and cytochrome bc_1 complex were still missing.

4.2 Cytochrome *c* oxidase

The overall protein structure and comparisons with other oxidases

The total Cα r.m.s.d. between our cryo-EM structure of AaC*c*O and the previously reported X-ray crystal structure of the ba_3-type cytochrome c oxidase from *T. thermophilus* (PDB entry 1EHK) is 1.02 Å, showing that the overall folds of both proteins are quite similar. One major difference is that one additional TMH14 was identified in the subunit CoxA2 of AaC*c*O (Figure 3-14). The result of a structural superposition showed that the additional TMH14 occupies nearly the same site as subunit III of the aa_3-type C*c*O (186). For the aa_3-type C*c*Os, the subunit III does not play a role in proton pumping or in binding of the redox-active prosthetic groups (221,222). In AaC*c*O, the presence of the extra TMH may enhance the thermal stability by stabilizing the core subunits of this complex. In addition, the membrane-anchored cytochrome c_{555} might bind to this TMH14, as proposed for the aa_3-type C*c*O from *P. denitrificans*.

Electron transfer pathway

It was shown that AaC*c*O can use both horse heart cytochrome c and ubiquinol as the electron donors (149). In this study, the activity assay was performed with the endogenous cytochrome c (c_{555}). By using the hyperthermostable cytochrome c_{555} as

electron donor, the turnover number was increased 14 times compared to the horse heart cytochrome c. The observed higher activity of AaCcO suggests that the thermo stability of the electron donor is important for the enzymatic activity of AaCcO.

In aa_3-CcO from *P. denitrificans*, two residues Trp 121[P] and Tyr 122[P] are involved in the electron transfer from cytochrome c to Cu$_A$ (187,188). Superposition and sequence alignment of subunit II from *P. denitrificans* and *A. aeolicus* showed that the corresponding residues in AaCcO are Trp 66 and Tyr 67 (Figure 3-16). Therefore, we propose that electrons can also be transferred from cytochrome c to Cu$_A$ via these two residues in AaCcO. The other electron donor, naphthoquinone, is identified in our structure (Figure 3-14). However, the distance between naphthoquinol and Cu$_A$ is 25.7Å, suggesting that Cu$_A$ may not be involved in the electron transfer from naphthoquinol to the active site.

CcO receives electrons from cytochrome c and transfers them to the binuclear center. (223,224). The electron transfer pathway from Cu$_A$ to the active site via low-spin heme a/b has been studied relatively well. The results indicate that the conserved residues Arg 450[T] and Phe 385[T] are involved in the one electron transfer from Cu$_A$ to the active site (53). The conserved residues Arg 447, Arg 448 and Phe 384 are also present in AaCcO, suggesting that this electron transfer pathway is also exist in AaCcO (Figure 4-1A). In ba_3-CcO from *T. thermophilus,* the tight interactions between Tyr 136[T] and Trp 229[T], and the π-system interation of the conserved residues Trp 229[T] and His 283[T] were observed. Therefore, a second electron transfer pathway was proposed in which the electrons are transferred from Cu$_A$ through Tyr 136[T], Trp 229[T] and 283[T] to the active site (225,226). The direct electron transfer from Cu$_A$ to the reaction center has never been tested by any kinetic experiments. However, Yoshikawa and co-workers proposed the same direct electrons pathway according to the crystal structure of cytochrome c oxidase from bovine heart (227). Interestingly, all isopositional residues Tyr 124, Trp 218 and His 274 are found in AaCcO (Figure 4-1A). This observation suggests that there may be a second electron transfer pathway from Cu$_A$ to the active site in AaCcO. Future studies are needed, to test the second electron pathway.

A previous study reported that AaCcO could use both cytochrome c and quinol as the

electron donors (149). Two molecules of NQ were observed in our cryo-EM structure (Figure 3-14). The edge-to-edge distance between NQ and heme b is 15.0 Å. Several residues which can mediate the electron transfer are observed between NQ and heme b. Therefore, three possible electron transfer pathways are proposed (Figure 4-1B). The first possible electron pathway allows electrons transfer from NQ to Phe 445, then to Arg 39, and finally to heme b, the second possible electron pathway is the transfer of electrons from NQ to heme b via Phe 37, the third hypothetical electron pathway might be used the electron transfer from NQ via Phe 37, Tyr 38 and Tyr 53, to heme b. Notably, the electron donor NQ is provided by the other protomer in the homodimer of AaCcO, suggesting that the dimerization is essential for this catalytic activity.
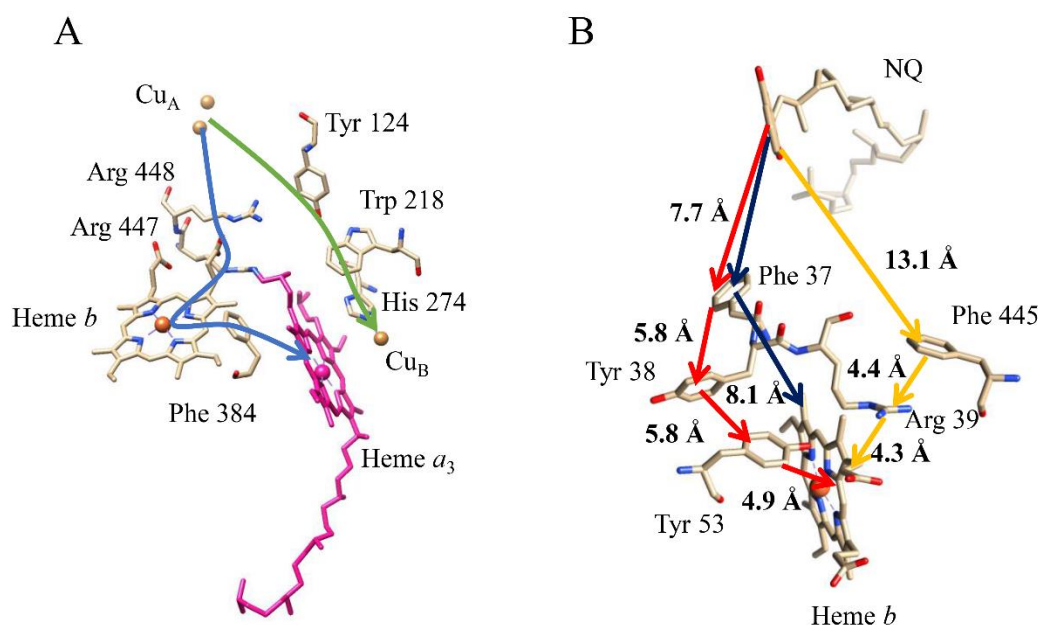
Figure 4-1: Electron transfer pathways: (A) The proposed direct electron transfer pathway is marked in green and the kinetic experiments confirmed the electron transfer pathway is shown in blue. (B) Three proposed electron transfer pathways from NQ to heme b are colored in orange, black and red, respectively. Heme a_3, heme b, Cu$_A$, Cu$_B$ and all the conserved residues involved in the electron transfer are showed in cartoon.

Proton transfer pathway

According to the crystal structure of ba_3-type CcO from *T. thermophilus*, three proton transfer pathways have been proposed: K, D and Q-pathway. However, mutations of critical residues (S109A in D-pathway and T396V in Q-pathway) have little influence on the activity or proton pumping (190,228). A structure-based sequence alignment

suggests that the polar residues Ser 109^T and Thr 396^T are substituted by the hydrophobic residues Ala 97 and Val 395, respectively, in AaCcO (Figure 3-17). These results suggest that neither D- nor the Q-pathway is present in AaCcO.

The cryo-EM structure of AaCcO supports the conclusion that the presence of only one proton pathway equivalent to the previously called the "K-pathway" (Figure 3-18). A previous study suggested that the area around Asp 372 was the location of proton pump site in *T. thermophilus* (192). However, the substitution of this Asp 399 by Asn in *P. dentrificans* did not significantly change the activity and proton pumping of the CcO (229). Similar result was obtained with the mutant D372N in *T. thermophilus* (228). Mutagenesis studies in *R. sphaeroides* suggested that Asp 407 does not play a critical role in proton translocation (230). The similar enzyme properties between the mutation Asp 135 and WT was reported within the cytochrome bo_3 from *E. coli* (195). The Asp 372^T is replaced by Asn 371 in AaCcO (Figure 3-18). A strong interaction between ND2 of Asn 371 and O1D of heme *a* is observed. The presence of Asn 371 in AaCcO may stabilize the environment of the proton-loading site.

Oxygen pathway

In contrast to electron and proton transfer pathways, details of the oxygen pathway by which oxygen reaches the heme a_3-Cu$_B$ active site are unclear. Hydrophobic cavities from the surface of protein to the reaction center are proposed to function as oxygen pathway. Conserved oxygen pathways have been suggested for the CcOs from *R. sphaeroides* (231) , *P. dentrificans* (186) and *B. taurus* (41). However, the geometry of oxygen pathway is very different (197). A Y-shaped oxygen pathway was reported in ba_3-type cytochrome *c* oxidase from *T. thermophilus*, suggesting that there were two entry points (197). One oxygen pathway in AaCcO is suggested based on the cryo-EM structure (Figure 3-19). Superposition of the CcO structures from *A. aeolcius* and *T. thermophilus* suggested that Phe 113 blocks the oxygen pathway 2 in AaCcO (Figure 3-19D). The larger the void in a protein, the smaller is its stability (232). Considering this, it is suggested one role of Phe113 is to increase the thermodynamic stability of

AaCcO by blocking the oxygen channel by decreasing the void inside.

In the A1-family CcOs, the conserved Glu (Glu278 in *P. dentrificans*, Glu286 in *R. sphaeroides* and Glu 242 in bovine heart) played an essential role in proton pumping and electron transfer (198). The conserved Glu was also suggested a role at this position in maintaining the O$_2$ channel (53,197). Sequence alignment suggested that the conserved Glu is replaced by Valine in oxidases from *Sulfolobus acidocaldarius* and *Natronobacterium pharaonis*. The presence of a Valine in these two oxidases was suggested to optimize the oxygen channel (53). The equivalent residues of Glu is Val 224 in AaCcO (Figure 3-19). This feature suggests that the presence of Val 224 may optimize oxygen channel of the *A. aolicus*, leading to adapt to the low oxygen and high temperature environment.

Dimer interface

The large contribution from lipids, especially CL, to stabilize the dimer interface of cytochrome c oxidase has been intensively studied (199,233-235). The dimerization of cytochrome c oxidase from bovine could still be observed even when all phospholipids were removed, except for the tightly bound cardiolipins (233). It was confirmed that CL plays an important role in proton pumping (234,236). CL can also influence the substrate quinone binding site by effecting the redox midpoint potential of Q$_A$ (237,238). but also for the function of cytochrome c oxidase. 2 CLs and 6 PGs were observed in the cryo-EM structure of AaCcO (Figure 3-20). This suggests that CL and PG are important for the dimerization of AaCcO. In addition, two molecules 1,4-naphthoquinones were observed in the dimer interface (Figure 3-20D). Strong interactions between the carbonyl oxygen O11 of naphthoquinone and Glu 39 OE1, and carbonyl oxygen O11 of 1,4-naphthoquinone and Gln 472 NE2 from another monomer can be observed (Figure 3-20E). Considering that 1,4-naphthoquinone is one of the substrates of AaCcO, the dimerization is essential for the catalytic activity of AaCcO.

4.3 Cytochrome bc_1 complex

In this work, the cryo-EM structure of the cytochrome bc_1 complex from *A. aeolicus*, which uses 1,4-naphthoquinone as substrate, was determined at 3.4 Å resolution (Figure 3-24A). The overall structure is in line with the previously determined crystal structures (Figure 3-32A). The hemes b_L and b_H are visible in the subunit cyt. *b*. Heme c_1 is found in subunit cyt. c_1. The ISP contains the Fe_2S_2 cluster. It is noteworthy to mention that the 1,4-naphthoquinone binds to the Q_i site (Figure 3-28B). The structure shown in this study allows an in-depth comparison of the enzyme to other cytochrome bc_1 complexes and suggests further insights into the mechanism of this complex. Details are discussed below.

ISP

ISP is one of the core subunits of cytochrome bc_1 complex (239). The connection part between the membrane anchor part and the catalytic domain contains a short helix in *R. capsulatus* and *B. taurus*. An "ADV" motif was observed in this helix. Mutagenesis studies suggested that affect length or rigidity of this part of the hinge region impair enzyme activity (240,241). This short helix is not present in the ISP subunit from *A. aeolicus* (Figure 3-35A), which might be due to the absence of the conserved ADV motif in *A. aeolicus*. This functional importance of the conserved His 161 in Bovine heart has been demonstrated for the cytochrome bc_1 complex (90). In our cryo-EM structure of Aabc_1, the isopositional residue is His 138 which was observed between the heme c_1 and Fe_2S_2 (Figure 3-35A). The distances between His 138 and Fe_2S_2 center, and the edge of heme c_1 are 2.36 Å and 3.86 Å, respectively, suggesting that His 138 may be involved in the electrons transfer between cyt. c_1 and ISP.

Cytochrome c_1

The cytochrome bc_1 complex from *A. aeolicus* was suggested to originate from ε-proteobacteria by lateral gene transfer (203,239), but the structure reveals the presence

of only one heme c in $A.$ $aeolicus$ cyt. c_1 which is unlike the diheme c feature of ε-proteobacteria.

Cyt. c_1 has to be post-translationally imported into the periplasmic side, because it is nuclear-encoded (242-244).The subunits cyt. c_1 from $R.$ $capsulatus$ and $B.$ $taurus$ have only a C-terminal TMH, while cyt. c_1 from $A.$ $aeolicus$ has one additional TMH at the N-terminus (Figure 3-26A). In previous studies, the crystal structure of cytochrome c_{555} from $A.$ $aeolicus$ was determined up to 1.15 Å resolution (184). Interestingly, the N-terminal TMH composed of 14 residues strongly binds to the core structure of c_{555} protein. This helix was demonstrated to contribute to the hyperstability of the c_{555} protein, and to help $A.$ $aeolicus$ adapt the hyperthermal environment. In the cryo-EM structure of the cyt. c_1 subunit, the extra N-terminal TMH1 is much longer than that of c_{555}, and the presence of various hydrophobic residues on TMH1 largely increases the interface between cyt. b and cyt. c_1 subunits by 60% (Figure 3-32). This extra TMH in cyt. c_1 could also contribute to the hyperstability of the overall complex. More importantly, TMH1 of cyt. c_1 subunit fixes one phospholipid molecule from the cell membrane into a unique hydrophobic groove, therefore the complex is firmly anchored in the membrane. This feature could help $A.$ $aeolicus$ to adapt the hyperthermal environment and has not been found in other mesophilic species.

Cytochrome b and the naphthoquinone binding site

In present structure, several unique residues and structural characteristics have been identified, which are not found in other homologous structures and could protect the catalytic site of the complex at extremely high temperatures.

On one hand, the cytochrome bc_1 complex from $A.$ $aeolicus$ exhibits enhanced overall stability in the membrane. Tyr 61 of cyt. b subunit interacts with ISP subunit and another cyt. b protomer to form a tighter complex (Figure 3-30). The substrate NQ is trapped inside a hydrophobic pocket and binds to a series of hydrophobic and hydrophilic residues in the three subunits of cytochrome bc_1 complex (Figure 3-31). Moreover, there is an extra TMH1 in the N-terminal of cyt. c_1 subunit of $A.$ $aeolicus$, which

interacts with the cyt. *b* subunit and traps a phospholipid molecule inside the complex. Therefore, the Aa*bc*$_1$ could grab the 1,4-naphthoquinone in the Q-pool and grab the phospholipid in the membrane (Figure 4-2), then form a more stable conformation under high temperature to provide a suitable environment for the internal electron transfer reaction.

Naphthoquinone

Naphthoquinone channel
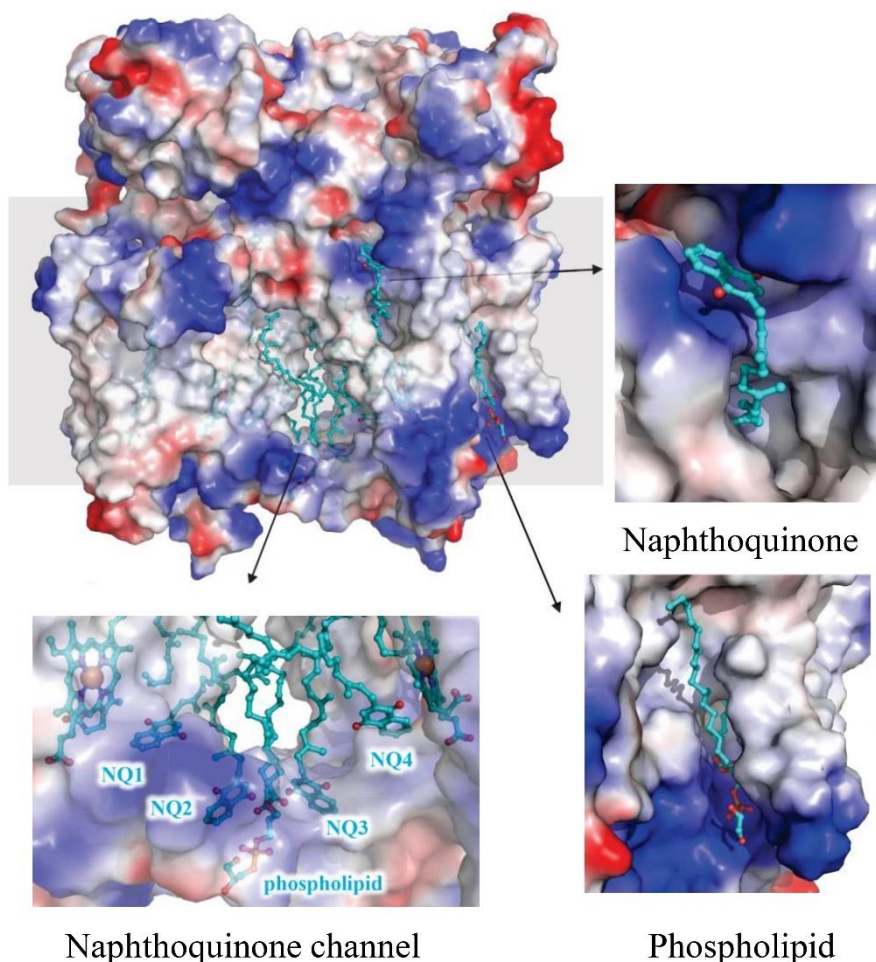
Phospholipid

Figure 4-2: The potential 1,4-naphthoquinone channel around the Q$_i$ site, with the embedded naphthoquinone and the phospholipid. The electrostatic surface of the cytochrome *bc*$_1$ complex from *A. aeolicus*, while the ligands are indicated and shown as stick models.

On the other hand, the Aa*bc*$_1$ has more stable electron transport pathway inside the complex. In the cyt. *b* subunit of Aa*bc*$_1$, Tyr 38 and Arg 119 bind to the two carboxyl groups of the cofactor heme *b*$_H$, while Glu 254 and Arg 222 bind to the two carbonyl oxygens groups of 1,4-naphthoquinone. Both cofactor and substrate in the Q$_i$ site are more stabilized in Aa*bc*$_1$. At high temperatures, the thermal motion of molecules is largely accelerated, so their relative positions and distances are change quickly, which

can reduce the electron transfer efficiency between them.

The highly conserved residues His 202 and Asp 229 in cyt. *b* from *R. sphaeroides* and *B. taurus* (86,204) are equivalent to Arg 222 and Glu 254 in cyt. *b* from *A. aeolicus*. The plane of the quinone ring is perpendicular to the heme b_H ring, but the shorter distance of OD1 of the naphthoquinone to the iron of heme b_H indicates that OD1 gets the electron first.

4.4 Heme A synthase

Mutations of HAS have been associated with several diseases, such as fatal infantile hypertrophic cardiomyopathy (127-130). Heme A synthases from bacteria, fungi, plants and animals are orthologous. Depending on the production conditions as well as the presence or absence of heme O synthase, heterologously expressed heme A synthase could have three different heme compositions (245). In this work, to investigate the oligomerization and structure of heme A synthase, a system for the heterologous production of AaHAS in *E. coli* was established. In this thesis, the presence of a trimeric complex of HAS was confirmed via a series of independent experiments, and its cryo-EM structure was determined at 2.8 Å. Several new features provide new insight into the structure and function of heme A synthase are found and are discussed below.

4.4.1 Oligomerization of AaHAS

AaHAS forms a highly stable trimer complex

The thermostability of the purified AaHAS was investigated by Nano DSF (Figure 3-35), which showed two transition temperatures, at 62.4℃ and 75.3℃, indicating its high thermo-stability. The stability of the purified AaHAS was also characterized by dynamic light scattering (DLS). The results of DLS performed with the purified AaHAS, stored at 4 ℃ for 1, 3, 5 and 7 days, suggested that AaHAS is stable at 4 ℃ for at least 7 days (Figure 4-3). All results demonstrated that AaHAS is highly thermo-stable. The "heme-induced fit" binding mechanism suggested that heme binding induces striking

conformational changes (246). The high thermo-stability of AaHAS may be essential to maintain its structural integrity during the catalytic cycle. In addition, oligomerization of AaHAS could reduce the surface area of each monomer, therefore providing the protection against thermal-denaturation (247-249). The evolutionary development of a highly stable trimeric AaHAS complex seems appropriate.
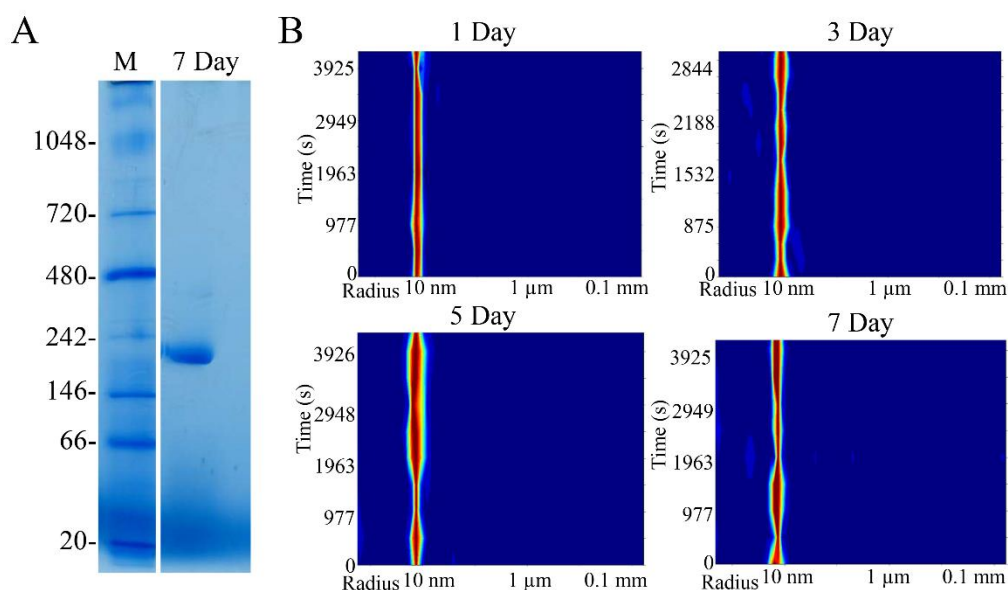

Figure 4-3: Stability of AaHAS. (A) BN-PAGE was used to analyze AaHAS. M: molecular mass. 7 day: the sample of AaHAS which was kept for 7 days at 4 ℃. The AaHAS which kept for 1, 3, 5 and 7 days at 4 ℃ were analyzed by DLS, separately (B).

Trimeric AaHAS is formed by the hydrophobic interaction

AaHAS was identified as a trimeric complex. The feature that heme A synthase can form a highly stable complex appears to be evolutionarily conserved. Heme A synthase from *A. pernix* (class A, 17 kDa) and *B. subtilis* (class B, 34 kDa) eluted as one peak with an apparent size of 380 kDa in detergents (125). Heme A synthase from *S. cerevisiae* (class D) functions as a complex containing multiple copies. In this work, purification of AaHAS was performed under different chemical conditions, *e.g.*, using a purification buffer with 1 M NaCl or without NaCl. Analysis of the AaHAS purified using different purification conditions by BN-PAGE showed the presence of only one dominant band at around 200 kDa corresponding to the trimeric AaHAS. This

observation indicated that the oligomerization of AaHAS is independent of the ionic strength (Figure 3-42). Those finding is consistent with the results obtained with the heme A synthase (Cox15) from yeast (126). Analysis of the cysteine mutations via BN-PAGE still showed the presence of the trimeric complex, suggesting that the disulfide bonds do not significantly contribute to the oligomer stability. Taken together, all data suggested that the trimeric complex appears to be stabilized by strong hydrophobic interactions. In addition, three hydrophobic belts at the trimer interface were observed in AaHAS (Figure 3-47). The hydrophobic interactions between three Phe 208 form the first belt. The interactions between Thr 215 and Leu 212 contribute to the formation of the second belt. The third hydrophobic belt is formed by the interactions between Tyr 216 and Phe 219. Moreover, the strong hydrophobic interactions between Leu 192 and Ile 222 at the dimeric interface are also observed in AaHAS (Figure 3-48). The interactions at the trimer interface of AaHAS confirmed the hypothesis that the trimeric complex of AaHAS is mainly formed by hydrophobic interactions.

Disulfide bond in AaHAS.

Sequence alignments show the presence of one pair of conserved cysteine in HAS from bacteria. Previous studies demonstrated that both cysteine residues can form an intra-molecular disulfide bridge that is important for the proper function of HAS (121). However, the significance of the two cysteine variants was different. In BsHAS, the heme A biosynthesis activity of the C35A variant (the counterpart of Cys 40 in AaHAS) was lower than that of the WT and trace amounts of the heme A could be still detected, while the C40A variant (the counterpart of Cys 46 in AaHAS) did not show any catalytic activity (121). In AaHAS, the dimer band was observed for the purified C40A variant which was incubated at RT, while the dimer band was absent with the purified C46A variant which was incubated at RT (Figure 3-41A). This observation suggests that the mutation of C40 decreased the stability of trimeric AaHAS.

Mutagenesis studies suggested that there is no inter-polypeptide disulfide bond in the AaHAS complex. A previous study demonstrated that the intra-molecular disulfide appears to be important for BsHAS activity (113). Considering the conservation of

these two residues in the bacterial heme A synthase, it is possible that an intra-molecular disulfide bond is also present in AaHAS, which is important for its activity.

The loop between TMH1 and TMH2 is critical for oligomerization

Studies of Cox 15 from yeast suggested that the 20 residues between TMH4 and TMH5 are critical for the oligomerization and function. Deletion of this region influenced the stability of the oligomeric complex but not of the monomeric Cox 15 (126). Mutagenesis studies also suggested that the residues from 37 to 79 in first loop between TMH1 and TMH2 are important for the oligomerization of AaHAS (Figure 3-42), since a ladder pattern was observed for the AaHAS-Δ_{37-79} variant in BN-PAGE. The lowest band observed in the BN-PAGE corresponds to the trimer of AaHAS. Several bands with apparent molecular weight higher than trimer were also observed which might be due to the aggregation of AaHAS-Δ_{37-79}. Altogether, these results suggest that the first loop between TMH1 and TMH2 is critical for the trimeric state of AaHAS.

Pet117 is one of the cytochrome *c* oxidase assembly factors. The physically interactions between Pet117 and Cox15 played an important role in stabilizing Cox15 oligomers (208). However, sequence blast with Pet117 shows there is no significant similarity found in *A. aeolicus*.

4.4.2 Structure of AaHAS

Recently, the crystal structure of the BsHAS monomer has been reported (207). Whereas all the characterization data suggested that HAS is present predominately as a homo-oligomeric complex (22,125,126,209), indicating that the reported crystal of BaHAS may not be biologically relevant. Previous studies suggested that oligomerization of HAS does not depend on its function of heme A biosynthesis (126), while the oligomerization of HAS is important for the function of heme A biosynthesis (22,126,208). In this thesis, the cryo-EM structure of AaHAS in lipidic nanodics

provides an atomic model of this protein complex in a native-like bilayer environment (Figure 3-44). The structure revealed many previously unseen features. A stable trimer of AaHAS is formed by intensive hydrophobic interactions between TMH6 (Figure 3-47 and Figure 3-48), which is in agreement with the reported data of HAS from yeast (126).

Heme B binding pocket in the trimeric AaHAS

The cofactor heme B is embedded in the C-terminal bundle where TMH8 and TMH6 provide His 266 and His 213 as heme B ligands (Figure 4-4A). Only the α-, β- and δ-*meso* edges of the heme B are buried in the protein, whereas the hydrophobic tail of PG prevents the exposure of the γ-*meso* edge of heme B to the solvent (Figure 4-4A). Moreover, the intense hydrophobic interactions between TMH6, TMH7 and γ-*meso* edge could stabilize heme B and optimize the orientation of heme B. It is obvious that the negatively charged carboxyethyl group at the α-*meso* edge of heme B strongly interact with the conserved positively charged Arg 198 on TMH5 (Figure 4-4C). Salt bridges contribute to the formation of the complementary electrostatic surfaces at the interface between heme B and heme O binding pockets (Figure 4-4B). Additionally, strong interactions between Gln 190 in TMH6 and His 213 in TMH5, and between the highly conserved Gln 246 in TMH7 and His 266 in TMH8 are observed, which can further stabilize the heme B binding site (Figure 4-4D). The optimized heme B binding pocket forms one-half of an elongated cleft leading to the substrate binding site of AaHAS. However, the cofactor heme B does not form close contacts with the substrate heme O in this cleft for electron transfer. Thus, solvent is able to access the channel between the two hemes, which has been reported in the crystal structure of BsHAS (207). The water molecules identified in the crystal structure of BsHAS were suggested to play a role in the conformational change of helices (207). Moreover, the conserved Gly 194 residue in TMH5 provides the required flexibility and allows the heme B binding pocket to get closer to the heme O binding pocket in AaHAS. Interestingly, the

presence of one Gly between two heme binding sites has also been reported in oxygenase-1 (250).
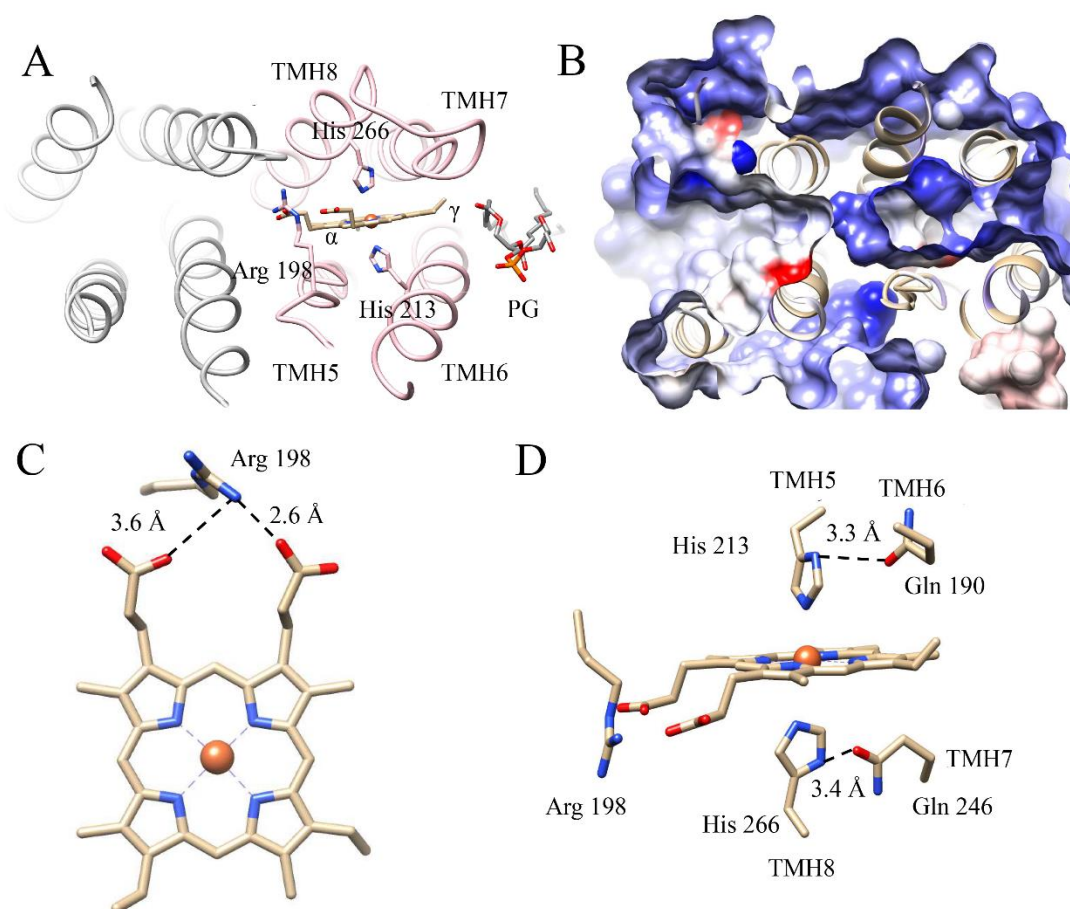

Figure 4-4：Heme B binding pocket. (A) The structure shown as a ribbon drawing as viewed from the extracellular side. The N-terminal bundle is shown in grey and C-terminal one in pink. The heme molecule is shown as atomic model. Heme B interaction residues Arg 198, His 213, His 266 and PG are showed as atomic model. (B) Electrostatic surface potential of AaHAS: A section of the surface representation of heme B binding site is shown. Coloring of the surface potential ranges from -10 kT (blue) to 10 kT (red). (C) Interaction of heme B propionate with Arg 198. (D) Conserved Gln 246 and Gln 190 play a role in stabilizing heme B ligands His 213 and His 266. TMHs are labelled. The distances between Gln 190 and His 213, and between Gln 246 and His 266 are marked.

Opened substrate heme O pocket in trimeric AaHAS

Based on the crystal structure of detergent-solubilized BsHAS, it was proposed that TMH2 of HAS undergoes a bent to straight conformational change (Figure 3-49). In this work, the trimeric AaHAS not only represents a physiological structure, but also explains how oligomerization is related to its function. A typical strong lipid-protein

interaction is mainly stabilized by polar interactions or hydrogen bond between lipid head groups , tyrosines and positively charged arginines (216,251). Indeed, a strong Tyr 211-lipid-Arg 137 interaction is observed in the trimeric AaHAS (Figure 3-50). Arg 137 is located at the end of ECL2 which is followed by TMH4. Tyr 211 is located in the kinked TMH6 which contributes to the stability of the AaHAS trimer (Figure 3-49). The substrate heme O binding groove is formed by TMH1 to TMH4, ECL1 and ECL2. Therefore, the conformation of heme O binding groove might be controlled by the Tyr 211-lipid-Arg 137 interaction which can regulate the conformational changes of TMH4, ECL2 and TMH3. A mechanism of heme O binding and heme A release is proposed in Figure 4-5. TMH6 located at the trimer interface provides a stable lipid binding site (Tyr 211) for protein-lipid interaction between the monomers. In the closed state of the reaction cycle, the ECL 1 and ECL 2 completely plug the substrate-heme O binding site, which might also contribute to the protection of the binding site by blocking it. Afterwards, ECL 1 and ECL 2 may move from the heme O binding site which results in the open state. During this step, the conserved Gly 86 TMH2 allows an outword kinking or to remove ECL 1, and TMH4 kinked outwards at Val 153 and pushes the side chain of Arg 137 in the TMH4 forming a strong interaction with PG which has stable interaction with Tyr 211. Subsequently heme O binds to the proposed binding site (substrate binding state). The conversion from the open state to the heme O binding state could be achieved by the interaction between hydrophobic residues of TMH2 and TMH3 with the polyprenyl side chain of heme O. Subsequently, the porphyrin ring of heme O is tugged to the binding site and the Fe atom interacts with Nε2 atoms of His 81 and His 141, resulting in the straight conformation of TMH2 and TMH4 straight. The conformational change of TMH4 increases the distance between Arg 137 and PG abolishing the interaction. Finally, heme A is released to finish the catalytic cycle (product release). In the last state, the interaction of Tyr 211-lipid-Arg 137 can be expected to participate in the product heme A release by removing ECL 2.
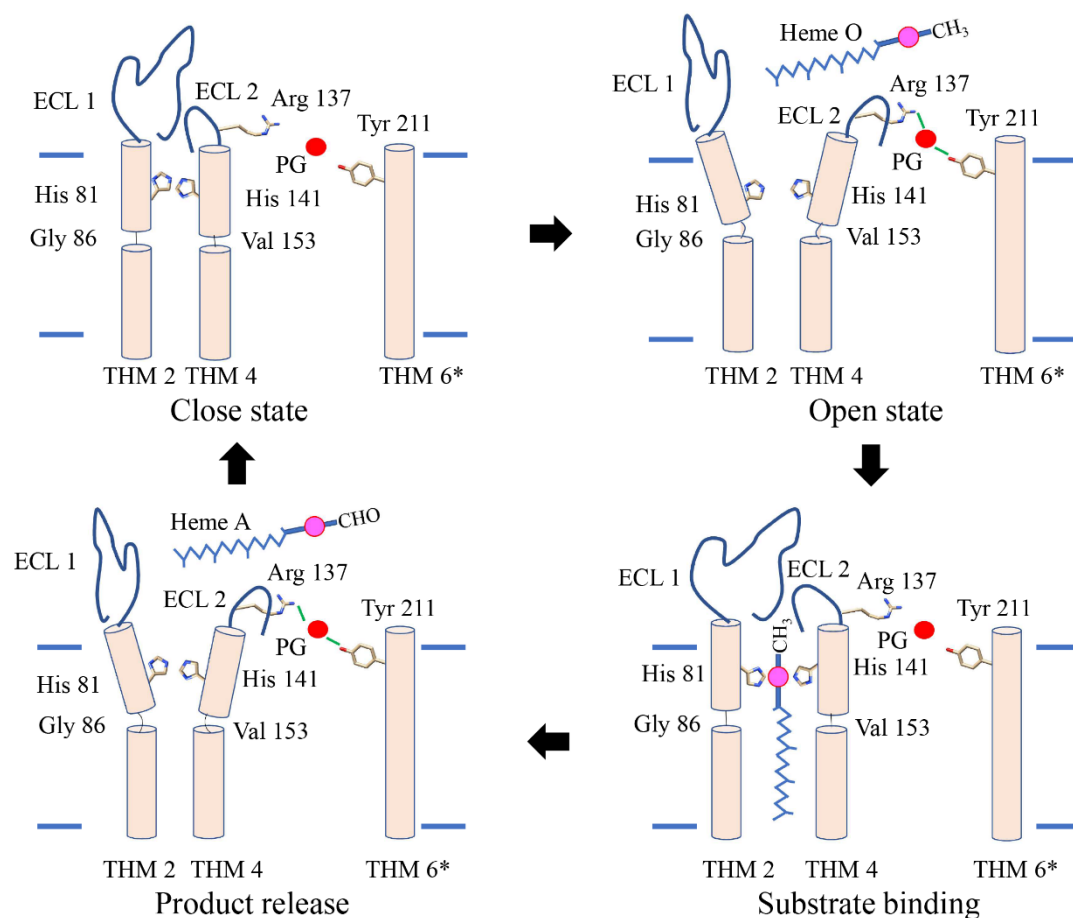
Figure 4-5: Schematic representation of the AaHAS alternating protein-lipid interaction heme binding and release mechanism. Side-view schematic representation of different conformational states. TMH2, TMH4 and TMH6* (*: from adjacent monomer) are indicated in light orange. The proposed heme O binding sites (His 81 and His 141), the kink sites of TMH2 (Gly 86) and TMH4 (Val 153), and protein-lipid interaction site (Arg 137 and Tyr 211) are showen. The ECL 1 and ECL 2 completely plugs the substrate-heme binding site and moves away for heme O binding and heme A release.

5. References

1. Mitchell, P. (1961) Coupling of Phosphorylation to Electron and Hydrogen Transfer by a Chemi-Osmotic Type of Mechanism. *Nature* **191**, 144-148

2. Saraste, M. (1999) Oxidative phosphorylation at the fin de siecle. *Science* **283**, 1488-1493

3. Verkhovskaya, M., and Bloch, D. A. (2013) Energy-converting respiratory Complex I: on the way to the molecular mechanism of the proton pump. *The international journal of biochemistry & cell biology* **45**, 491-511

4. Brandt, U. (2006) Energy converting NADH: quinone oxidoreductase (complex I). *Annu. Rev. Biochem.* **75**, 69-92

5. Wikström, M., and Hummer, G. (2012) Stoichiometry of proton translocation by respiratory complex I and its mechanistic implications. *Proceedings of the National Academy of Sciences* **109**, 4431-4436

6. Hirst, J., Carroll, J., Fearnley, I. M., Shannon, R. J., and Walker, J. E. (2003) The nuclear encoded subunits of complex I from bovine heart mitochondria. *Biochimica et Biophysica Acta (BBA)-Bioenergetics* **1604**, 135-150

7. Efremov, R. G., Baradaran, R., and Sazanov, L. A. (2010) The architecture of respiratory complex I. *Nature* **465**, 441-445

8. Baradaran, R., Berrisford, J. M., Minhas, G. S., and Sazanov, L. A. (2013) Crystal structure of the entire respiratory complex I. *Nature* **494**, 443-448

9. Zhu, J. P., Vinothkumar, K. R., and Hirst, J. (2016) Structure of mammalian respiratory complex I. *Nature* **536**, 354-358

10. Dröge, W. (2002) Free radicals in the physiological control of cell function. *Physiological reviews* **82**, 47-95

11. Schon, E. A., DiMauro, S., and Hirano, M. (2012) Human mitochondrial DNA: roles of inherited and somatic mutations. *Nature Reviews Genetics* **13**, 878-890

12. Cecchini, G. (2003) Function and structure of complex II of the respiratory chain. *Annual Review of Biochemistry* **72**, 77-109

13. Wikström, M., Sharma, V., Kaila, V. R., Hosler, J. P., and Hummer, G. (2015) New Perspectives on Proton Pumping in Cellular Respiration. *Chemical Reviews*. **115**, 2196-2221

14. Xia, D., Yu, C. A., Kim, H., Xia, J. Z., Kachurin, A. M., Zhang, L., Yu, L., and Deisenhofer, J. (1997) Crystal structure of the cytochrome bc1 complex from bovine heart mitochondria. *Science* **277**, 60-66

15. Mitchell, P. (1976) Possible molecular mechanisms of the protonmotive function of cytochrome systems. *Journal of theoretical biology* **62**, 327-367

16. Crofts, A. R. (2004) The cytochrome bc 1 complex: function in the context of structure. *Annu. Rev. Physiol.* **66**, 689-733

17. Warburg, O. (1924) Über den stoffwechsel der carcinomzelle. *Naturwissenschaften* **12**, 1131-1137

18. Wikstrom, M. K. (1977) Proton pump coupled to cytochrome *c* oxidase in

mitochondria. *Nature* **266**, 271-273

19. Wikström, M. (1984) Two protons are pumped from the mitochondrial matrix per electron transferred between NADH and ubiquinone. *FEBS letters* **169**, 300-304

20. Hinkle, P. C., Kumar, M. A., Resetar, A., and Harris, D. L. (1991) Mechanistic stoichiometry of mitochondrial oxidative phosphorylation. *Biochemistry* **30**, 3576-3582

21. Mogi, T., Saiki, K., and Anraku, Y. (1994) Biosynthesis and functional role of haem O and haem A. *Mol Microbiol* **14**, 391-398

22. Bareth, B., Dennerlein, S., Mick, D. U., Nikolov, M., Urlaub, H., and Rehling, P. (2013) The Heme a Synthase Cox15 Associates with Cytochrome *c* Oxidase Assembly Intermediates during Cox1 Maturation. *Mol Cell Biol* **33**, 4128-4137

23. García-Horsman, J. A., Barquera, B., Rumbley, J., Ma, J., and Gennis, R. B. (1994) The superfamily of heme-copper respiratory oxidases. *Journal of Bacteriology* **176**, 5587-5600

24. Hemp, J., and Gennis, R. B. (2008) Diversity of the heme–copper superfamily in Archaea: insights from genomics and structural modeling. in *Bioenergetics*, Springer. pp 1-31

25. Pereira, M. M., Sousa, F. L., Veríssimo, A. F., and Teixeira, M. (2008) Looking for the minimum common denominator in haem–copper oxygen reductases: Towards a unified catalytic mechanism. *Biochimica et Biophysica Acta (BBA)-Bioenergetics* **1777**, 929-934

26. Pereira, M. M., Santana, M., and Teixeira, M. (2001) A novel scenario for the evolution of haem–copper oxygen reductases. *Biochimica et Biophysica Acta (BBA)-Bioenergetics* **1505**, 185-208

27. Matsumoto, D., and Juang, L. (2012) *Culture and psychology*, Cengage Learning

28. Konstantinov, A. A., Siletsky, S., Mitchell, D., Kaulen, A., and Gennis, R. B. (1997) The roles of the two proton input channels in cytochrome c oxidase from Rhodobacter sphaeroides probed by the effects of site-directed mutations on time-resolved electrogenic intraprotein proton transfer. *Proceedings of the National Academy of Sciences* **94**, 9085-9090

29. Pereira, M. M., Sousa, F. L., Teixeira, M., Nyquist, R. M., and Heberle, J. (2006) A tyrosine residue deprotonates during oxygen reduction by the caa3 reductase from Rhodothermus marinus. *FEBS letters* **580**, 1350-1354

30. Michel, H., and Deisenhofer, J. (1988) Relevance of the photosynthetic reaction center from purple bacteria to the structure of photosystem II. *Biochemistry* **27**, 1-7

31. Dürr, K. L., Koepke, J., Hellwig, P., Müller, H., Angerer, H., Peng, G., Olkhova, E., Richter, O.-M. H., Ludwig, B., and Michel, H. (2008) A D-Pathway Mutation Decouples the Paracoccusdenitrificans Cytochrome c Oxidase by Altering the Side-Chain Orientation of a Distant Conserved Glutamate. *Journal of molecular biology* **384**, 865-877

32. Pereira, M. M., Santana, M., Soares, C. M., Mendes, J., Carita, J. N., Fernandes,

A. S., Saraste, M., Carrondo, M. A., and Teixeira, M. (1999) The caa3 terminal oxidase of the thermohalophilic bacterium Rhodothermus marinus: a HiPIP:oxygen oxidoreductase lacking the key glutamate of the D-channel. *Biochim Biophys Acta* **1413**, 1-13

33. Brzezinski, P., and Gennis, R. B. (2008) Cytochrome c oxidase: exciting progress and remaining mysteries. *J Bioenerg Biomembr* **40**, 521-531

34. von Ballmoos, C., Gennis, R. B., Ädelroth, P., and Brzezinski, P. (2011) Kinetic design of the respiratory oxidases. *Proceedings of the National Academy of Sciences* **108**, 11057-11062

35. Kannt, A., Soulimane, T., Buse, G., Becker, A., Bamberg, E., and Michel, H. (1998) Electrical current generation and proton pumping catalyzed by the ba3-type cytochrome c oxidase from Thermus thermophilus. *Febs Lett* **434**, 17-22

36. Giuffre, A., Stubauer, G., Sarti, P., Brunori, M., Zumft, W. G., Buse, G., and Soulimane, T. (1999) The heme-copper oxidases of Thermus thermophilus catalyze the reduction of nitric oxide: evolutionary implications. *Proceedings of the National Academy of Sciences* **96**, 14718-14723

37. Buschmann, S., Warkentin, E., Xie, H., Langer, J. D., Ermler, U., and Michel, H. (2010) The structure of cbb3 cytochrome oxidase provides insights into proton pumping. *Science* **329**, 327-330

38. Rauhamäki, V., Bloch, D. A., and Wikström, M. (2012) Proton translocation stoichiometry of proton translocation by cytochrome cbb_3. *Proceedings of the National Academy of Sciences* **109**, 7286-7291

39. Iwata, S., Ostermeier, C., Ludwig, B., and Michel, H. (1995) Structure at 2.8 A resolution of cytochrome c oxidase from Paracoccus denitrificans. *Nature* **376**, 660-668

40. Tsukihara, T., Aoyama, H., Yamashita, E., Tomizaki, T., Yamaguchi, H., Shinzawa-Itoh, K., Nakashima, R., Yaono, R., and Yoshikawa, S. (1995) Structures of metal sites of oxidized bovine heart cytochrome c oxidase at 2.8 A. *Science* **269**, 1069-1074

41. Tsukihara, T., Aoyama, H., Yamashita, E., Tomizaki, T., Yamaguchi, H., Shinzawa-Itoh, K., Nakashima, R., Yaono, R., and Yoshikawa, S. (1996) The Whole Structure of the 13-Subunit Oxidized Cytochrome c Oxidase at 2.8 Å. *Science* **272**, 1136-1144

42. Ostermeier, C., Harrenga, A., Ermler, U., and Michel, H. (1997) Structure at 2.7 Å resolution of the Paracoccus denitrificans two-subunit cytochrome c oxidase complexed with an antibody FV fragment. *Proceedings of the National Academy of Sciences* **94**, 10547-10553

43. Yoshikawa, S., Shinzawa-Itoh, K., Nakashima, R., Yaono, R., Yamashita, E., Inoue, N., Yao, M., Fei, M. J., Libeu, C. P., and Mizushima, T. (1998) Redox-coupled crystal structural changes in bovine heart cytochrome c oxidase. *Science* **280**, 1723-1729

44. Tsukihara, T., Shimokata, K., Katayama, Y., Shimada, H., Muramoto, K., Aoyama, H., Mochizuki, M., Shinzawa-Itoh, K., Yamashita, E., and Yao, M. (2003) The low-spin heme of cytochrome c oxidase as the driving element of

the proton-pumping process. *Proceedings of the National Academy of Sciences* **100**, 15304-15309

45. Florens, L., Schmidt, B., McCracken, J., and Ferguson-Miller, S. (2001) Fast deuterium access to the buried magnesium/manganese site in cytochrome c oxidase. *Biochemistry* **40**, 7491-7497

46. Pfitzner, U., Kirichenko, A., Konstantinov, A. A., Mertens, M., Wittershagen, A., Kolbesen, B. O., Steffens, G. C., Harrenga, A., Michel, H., and Ludwig, B. (1999) Mutations in the Ca 2+ binding site of the Paracoccus denitrificans cytochrome c oxidase. *FEBS letters* **456**, 365-369

47. Witt, I., Witt, H., Di Fiore, D., Rögner, M., Hinrichs, W., Saenger, W., Granzin, J., Betzel, C., and Dauter, Z. (1988) X-Ray Characterization of Single Crystals of the Reaction Center I of Water Splitting Photosynthesis. *Berichte der Bunsengesellschaft für physikalische Chemie* **92**, 1503-1506

48. Maneg, O., Malatesta, F., Ludwig, B., and Drosou, V. (2004) Interaction of cytochrome c with cytochrome oxidase: two different docking scenarios. *Biochimica et Biophysica Acta (BBA)-Bioenergetics* **1655**, 274-281

49. Hosler, J. P. (2004) The influence of subunit III of cytochrome c oxidase on the D pathway, the proton exit pathway and mechanism-based inactivation in subunit I. *Biochim Biophys Acta* **1655**, 332-339

50. Witt, H., and Ludwig, B. (1997) Isolation, analysis, and deletion of the gene coding for subunit IV of cytochrome c oxidase in Paracoccus denitrificans. *Journal of Biological Chemistry* **272**, 5514-5517

51. Lyons, J. A., Aragão, D., Slattery, O., Pisliakov, A. V., Soulimane, T., and Caffrey, M. (2012) Structural insights into electron transfer in caa3-type cytochrome oxidase. *Nature* **487**, 514-518

52. Lyons, J. A., Aragao, D., Slattery, O., Pisliakov, A. V., Soulimane, T., and Caffrey, M. (2012) Structural insights into electron transfer in caa(3)-type cytochrome oxidase. *Nature* **487**, 514-518

53. Soulimane, T., Buse, G., Bourenkov, G. P., Bartunik, H. D., Huber, R., and Than, M. E. (2000) Structure and mechanism of the aberrant ba3-cytochrome c oxidase from Thermus thermophilus. *The EMBO journal* **19**, 1766-1776

54. Tiefenbrunn, T., Liu, W., Chen, Y., Katritch, V., Stout, C. D., Fee, J. A., and Cherezov, V. (2011) High Resolution Structure of the ba3 Cytochrome c Oxidase from Thermus thermophilus in a Lipidic Environment. *Plos One* **6.** e22348

55. Sone, N., Koyanagi, S., and Sakamoto, J. (2000) Energy-yielding properties of SoxB-type cytochrome bo3 terminal oxidase: analyses involving Bacillus stearothermophilus K1041 and its mutant strains. *Journal of biochemistry* **127**, 551-557

56. Varotsis, C. A., and Babcock, G. T. (1995) Photolytic activity of early intermediates in dioxygen activation and reduction by cytochrome oxidase. *Journal of the American Chemical Society* **117**, 11260-11269

57. Ducluzeau, A.-L., Ouchane, S., and Nitschke, W. (2008) The cbb3 oxidases are an ancient innovation of the domain bacteria. *Molecular biology and evolution*

25, 1158-1166

58. Hemp, J., Han, H., Roh, J. H., Kaplan, S., Martinez, T. J., and Gennis, R. B. (2007) Comparative genomics and site-directed mutagenesis support the existence of only one input channel for protons in the C-family (cbb 3 oxidase) of heme-copper oxygen reductases. *Biochemistry* **46**, 9963-9972

59. Hino, T., Matsumoto, Y., Nagano, S., Sugimoto, H., Fukumori, Y., Murata, T., Iwata, S., and Shiro, Y. (2010) Structural basis of biological N2O generation by bacterial nitric oxide reductase. *Science* **330**, 1666-1670

60. Salomonsson, L., Reimann, J., Tosha, T., Krause, N., Gonska, N., Shiro, Y., and Ädelroth, P. (2012) Proton transfer in the quinol-dependent nitric oxide reductase from Geobacillus stearothermophilus during reduction of oxygen. *Biochimica et Biophysica Acta (BBA)-Bioenergetics* **1817**, 1914-1920

61. Wikstrom, M., Krab, K., and Saraste, M. (1981) Proton-translocating cytochrome complexes. *Annual review of biochemistry* **50**, 623-655

62. Wikström, M. (1989) Identification of the electron transfers in cytochrome oxidase that are coupled to proton-pumping. *Nature* **338**, 776-778

63. Mitchell, R., and Rich, P. R. (1994) Proton uptake by cytochrome c oxidase on reduction and on ligand binding. *Biochimica et Biophysica Acta (BBA)-Bioenergetics* **1186**, 19-26

64. Michel, H. (1999) Cytochrome c oxidase: Catalytic cycle and mechanisms of proton pumping-A discussion. *Biochemistry* **38**, 15129-15140

65. Rousseau, D. L., and Han, S. (2002) Time-resolved resonance Raman spectroscopy of intermediates in cytochrome oxidase. *Methods in enzymology* **354**, 351-368

66. Proshlyakov, D. A., Pressler, M. A., and Babcock, G. T. (1998) Dioxygen activation and bond cleavage by mixed-valence cytochrome c oxidase. *Proceedings of the National Academy of Sciences* **95**, 8020-8025

67. MacMillan, F., Kannt, A., Behr, J., Prisner, T., and Michel, H. (1999) Direct evidence for a tyrosine radical in the reaction of cytochrome c oxidase with hydrogen peroxide. *Biochemistry* **38**, 9179-9184

68. Wikström, M., and Verkhovsky, M. I. (2007) Mechanism and energetics of proton translocation by the respiratory heme-copper oxidases. *Biochimica et Biophysica Acta (BBA)-Bioenergetics* **1767**, 1200-1214

69. Antalis, T. M., and Palmer, G. (1982) Kinetic characterization of the interaction between cytochrome oxidase and cytochrome c. *Journal of Biological Chemistry* **257**, 6194-6206

70. Richter, O.-M. H., and Ludwig, B. (2009) Electron transfer and energy transduction in the terminal part of the respiratory chain—lessons from bacterial model systems. *Biochimica et Biophysica Acta (BBA)-Bioenergetics* **1787**, 626-634

71. Hill, B. C. (1993) The sequence of electron carriers in the reaction of cytochromec oxidase with oxygen. *Journal of bioenergetics and biomembranes* **25**, 115-120

72. Verkhovsky, M. I., Jasaitis, A., and Wikström, M. (2001) Ultrafast haem–haem

electron transfer in cytochrome c oxidase. *Biochimica et Biophysica Acta (BBA)-Bioenergetics* **1506**, 143-146

73. Oliveberg, M., and Malmstroem, B. G. (1991) Internal electron transfer in cytochrome c oxidase: evidence for a rapid equilibrium between cytochrome a and the bimetallic site. *Biochemistry* **30**, 7053-7057

74. Belevich, I., Bloch, D. A., Belevich, N., Wikström, M., and Verkhovsky, M. I. (2007) Exploring the proton pump mechanism of cytochrome c oxidase in real time. *Proceedings of the National Academy of Sciences* **104**, 2685-2690

75. Backgren, C., Hummer, G., Wikström, M., and Puustinen, A. (2000) Proton translocation by cytochrome c oxidase can take place without the conserved glutamic acid in subunit I. *Biochemistry* **39**, 7863-7867

76. Pfitzner, U., Odenwald, A., Ostermann, T., Weingard, L., Ludwig, B., and Richter, O.-M. H. (1998) Cytochrome c oxidase (heme aa 3) from Paracoccus denitrificans: analysis of mutations in putative proton channels of subunit I. *Journal of bioenergetics and biomembranes* **30**, 89-97

77. Pfitzner, U., Hoffmeier, K., Harrenga, A., Kannt, A., Michel, H., Bamberg, E., Richter, O.-M., and Ludwig, B. (2000) Tracing the D-pathway in reconstituted site-directed mutants of cytochrome c oxidase from Paracoccus denitrificans. *Biochemistry* **39**, 6756-6762

78. Wikström, M., Verkhovsky, M. I., and Hummer, G. (2003) Water-gated mechanism of proton translocation by cytochrome c oxidase. *Biochimica et Biophysica Acta (BBA)-Bioenergetics* **1604**, 61-65

79. Siletsky, S. A., Han, D., Brand, S., Morgan, J. E., Fabian, M., Geren, L., Millett, F., Durham, B., Konstantinov, A. A., and Gennis, R. B. (2006) Single-electron photoreduction of the P M intermediate of cytochrome c oxidase. *Biochimica et Biophysica Acta (BBA)-Bioenergetics* **1757**, 1122-1132

80. Koepke, J., Olkhova, E., Angerer, H., Müller, H., Peng, G., and Michel, H. (2009) High resolution crystal structure of Paracoccus denitrificans cytochrome c oxidase: new insights into the active site and the proton transfer pathways. *Biochimica et Biophysica Acta (BBA)-Bioenergetics* **1787**, 635-645

81. Ruitenberg, M., Kannt, A., Bamberg, E., Ludwig, B., Michel, H., and Fendler, K. (2000) Single-electron reduction of the oxidized state is coupled to proton uptake via the K pathway in Paracoccus denitrificans cytochrome c oxidase. *Proceedings of the National Academy of Sciences* **97**, 4632-4636

82. Yoshikawa, S., Muramoto, K., Shinzawa-Itoh, K., Aoyama, H., Tsukihara, T., Shimokata, K., Katayama, Y., and Shimada, H. (2006) Proton pumping mechanism of bovine heart cytochrome c oxidase. *Biochimica et Biophysica Acta (BBA)-Bioenergetics* **1757**, 1110-1116

83. Lee, H.-m., Das, T. K., Rousseau, D. L., Mills, D., Ferguson-Miller, S., and Gennis, R. B. (2000) Mutations in the putative H-channel in the cytochrome c oxidase from Rhodobacter sphaeroides show that this channel is not important for proton conduction but reveal modulation of the properties of heme a. *Biochemistry* **39**, 2989-2996

84. Yang, X. H., and Trumpower, B. L. (1986) Purification of a 3-Subunit

Ubiquinol-Cytochrome-C Oxidoreductase Complex from Paracoccus-Denitrificans. *J Biol Chem* **261**, 2282-2289

85. Berry, E. A., Huang, L. S., Saechao, L. K., Pon, N. G., Valkova-Valchanova, M., and Daldal, F. (2004) X-ray structure of Rhodobacter capsulatus cytochrome bc(1): comparison with its mitochondrial and chloroplast counterparts. *Photosynth Res* **81**, 251-275

86. Hunte, C., Koepke, J., Lange, C., Rossmanith, T., and Michel, H. (2000) Structure at 2.3 angstrom resolution of the cytochrome bc(1) complex from the yeast Saccharomyces cerevisiae co-crystallized with an antibody Fv fragment. *Structure* **8**, 669-684

87. Zhang, Z. L., Huang, L. S., Shulmeister, V. M., Chi, Y. I., Kim, K. K., Hung, L. W., Crofts, A. R., Berry, E. A., and Kim, S. H. (1998) Electron transfer by domain movement in cytochrome bc(1). *Nature* **392**, 677-684

88. Xia, D., Esser, L., Tang, W. K., Zhou, F., Zhou, Y. H., Yu, L. D., and Yu, C. A. (2013) Structural analysis of cytochrome bc(1) complexes: Implications to the mechanism of function. *Bba-Bioenergetics* **1827**, 1278-1294

89. Trumpower, B. L. (1990) The Protonmotive Q-Cycle - Energy Transduction by Coupling of Proton Translocation to Electron-Transfer by the Cytochrome-Bc1 Complex. *J Biol Chem* **265**, 11409-11412

90. Iwata, S., Lee, J. W., Okada, K., Lee, J. K., Iwata, M., Rasmussen, B., Link, T. A., Ramaswamy, S., and Jap, B. K. (1998) Complete structure of the 11-subunit bovine mitochondrial cytochrome bc1 complex. *Science* **281**, 64-71

91. Zhang, Z., Huang, L., Shulmeister, V. M., Chi, Y. I., Kim, K. K., Hung, L. W., Crofts, A. R., Berry, E. A., and Kim, S. H. (1998) Electron transfer by domain movement in cytochrome bc1. *Nature* **392**, 677-684

92. Kim, H., Xia, D., Yu, C.-A., Xia, J.-Z., Kachurin, A. M., Zhang, L., Yu, L., and Deisenhofer, J. (1998) Inhibitor binding changes domain mobility in the iron–sulfur protein of the mitochondrial cytochrome bc_1 complex from bovine heart. *Proceedings of the National Academy of Sciences* **95**, 8026-8033

93. Muller, F. L., Lustgarten, M. S., Jang, Y., Richardson, A., and Van Remmen, H. (2007) Trends in oxidative aging theories. *Free Radical Biology and Medicine* **43**, 477-503

94. Green, D. R., and Reed, J. C. (1998) Mitochondria and apoptosis. *Science* **281**, 1309-1312

95. Hatefi, Y., Haavik, A., Fowler, L., and Griffiths, D. E. (1962) Studies on the electron transfer system XLII. Reconstition of the electron transfer system. *J Biol Chem* **237**, 2661-2669

96. Tzagoloff, A., and MacLennan, D. H. (1965) Studies of the electron-transfer system LXIV. Role of phospholipid in cytochrome oxidase. *Biochimica et Biophysica Acta (BBA)-Enzymology and Biological Oxidation* **99**, 476-485

97. Esser, L., Elberry, M., Zhou, F., Yu, C. A., Yu, L., and Xia, D. (2008) Inhibitor-complexed structures of the cytochrome bc(1) from the photosynthetic bacterium Rhodobacter sphaeroides. *J Biol Chem* **283**, 2846-2857

98. Kleinschroth, T., Castellani, M., Trinh, C. H., Morgner, N., Brutschy, B.,

Ludwig, B., and Hunte, C. (2011) X-ray structure of the dimeric cytochrome bc1 complex from the soil bacterium Paracoccus denitrificans at 2.7-Å resolution. *Biochimica et Biophysica Acta (BBA)-Bioenergetics* **1807**, 1606-1615

99. Wu, M., Gu, J. K., Guo, R. Y., Huang, Y. S., and Yang, M. J. (2016) Structure of Mammalian Respiratory Supercomplex I1III2IV1. *Cell* **167**, 1598-+

100. Wiseman, B., Nitharwal, R. G., Fedotovskaya, O., Schafer, J., Guo, H., Kuang, Q., Benlekbir, S., Sjostrand, D., Adelroth, P., Rubinstein, J. L., Brzezinski, P., and Hogbom, M. (2018) Structure of a functional obligate complex III2IV2 respiratory supercomplex from Mycobacterium smegmatis. *Nat Struct Mol Biol* **25**, 1128-1136

101. Rathore, S., Berndtsson, J., Marin-Buera, L., Conrad, J., Carroni, M., Brzezinski, P., and Ott, M. (2019) Cryo-EM structure of the yeast respiratory supercomplex. *Nat Struct Mol Biol* **26**, 50-57

102. Soriano, G. M., Ponamarev, M. V., Carrell, C. J., Xia, D., Smith, J. L., and Cramer, W. A. (1999) Comparison of the cytochrome bc1 complex with the anticipated structure of the cytochrome b6f complex: Le plus ca change le plus c'est la meme chose. *J Bioenerg Biomembr* **31**, 201-213

103. Nett, J. H., Hunte, C., and Trumpower, B. L. (2000) Changes to the length of the flexible linker region of the Rieske protein impair the interaction of ubiquinol with the cytochrome bc(1) complex (vol 267, pg 5777, 2000). *Eur J Biochem* **267**, 7266-7266

104. Tian, H., White, S., Yu, L., and Yu, C.-A. (1999) Evidence for the Head Domain Movement of the Rieske Iron-Sulfur Protein in Electron Transfer Reaction of the Cytochromebc 1 Complex. *J Biol Chem* **274**, 7146-7152

105. Li, Y., De Vries, S., Leonard, K., and Weiss, H. (1981) Topography of the iron—sulphur subunit in mitochondrial ubiquinol: cytochrome c reductase. *Febs Lett* **135**, 277-280

106. Wikstrom, M. K., and Berden, J. A. (1972) Oxidoreduction of cytochrome b in the presence of antimycin. *Biochim Biophys Acta* **283**, 403-420

107. Erecinska, M., Chance, B., Wilson, D. F., and Dutton, P. L. (1972) Aerobic reduction of cytochrome b 566 in pigeon-heart mitochondria (succinate-cytochrome C1 reductase-stopped-flow kinetics). *Proc Natl Acad Sci U S A* **69**, 50-54

108. Brand, M. D., Reynafarje, B., and Lehninger, A. (1976) Re-evaluation of the H+/site ratio of mitochondrial electron transport with the oxygen pulse technique. *J Biol Chem* **251**, 5670-5679

109. Trumpower, B. L., and Edwards, C. A. (1979) Purification of a reconstitutively active iron-sulfur protein (oxidation factor) from succinate . cytochrome c reductase complex of bovine heart mitochondria. *J Biol Chem* **254**, 8697-8706

110. Yang, X. H., and Trumpower, B. L. (1988) Protonmotive Q cycle pathway of electron transfer and energy transduction in the three-subunit ubiquinol-cytochrome c oxidoreductase complex of Paracoccus denitrificans. *J Biol Chem* **263**, 11962-11970

111. Schutz, M., Schoepp-Cothenet, B., Lojou, E., Woodstra, M., Lexa, D., Tron, P., Dolla, A., Durand, M. C., Stetter, K. O., and Baymann, F. (2003) The naphthoquinol oxidizing cytochrome bc(1) complex of the hyperthermophilic knallgasbacterium Aquifex aeolicus: Properties and phylogenetic relationships. *Biochemistry-Us* **42**, 10800-10808

112. Wallace, C. J., and Proudfoot, A. E. (1987) On the relationship between oxidation-reduction potential and biological activity in cytochrome c analogues. Results from four novel two-fragment complexes. *Biochem J* **245**, 773-779

113. Hederstedt, L., Lewin, A., and Throne-Holst, M. (2005) Heme A synthase enzyme functions dissected by mutagenesis of Bacillus subtilis CtaA. *J Bacteriol* **187**, 8361-8369

114. Kim, E., Chufan, E. E., Kamaraj, K., and Karlin, K. D. (2004) Synthetic models for heme-copper oxidases. *Chem Rev* **104**, 1077-1133

115. Kim, H. J., Khalimonchuk, O., Smith, P. M., and Winge, D. R. (2012) Structure, function, and assembly of heme centers in mitochondrial respiratory complexes. *Bba-Mol Cell Res* **1823**, 1604-1616

116. Sousa, F. L., Alves, R. J., Ribeiro, M. A., Pereira-Leal, J. B., Teixeira, M., and Pereira, M. M. (2012) The superfamily of heme-copper oxygen reductases: Types and evolutionary considerations. *Bba-Bioenergetics* **1817**, 629-637

117. Puustinen, A., and Wikstrom, M. (1991) The Heme Groups of Cytochrome-O from Escherichia-Coli. *P Natl Acad Sci USA* **88**, 6122-6126

118. Glerum, D. M., and Tzagoloff, A. (1994) Isolation of a Human Cdna for Heme a-Farnesyltransferase by Functional Complementation of a Yeast Cox10 Mutant. *P Natl Acad Sci USA* **91**, 8452-8456

119. Brown, K. R., Allan, B. A., Do, P., and Hegg, E. L. (2002) Identification of novel hemes generated by heme A synthase: Evidence for two successive monooxygenase reactions. *Biochemistry-Us* **41**, 10906-10913

120. Brown, K. R., Brown, B. M., Hoagland, E., Mayne, C. L., and Hegg, E. L. (2004) Heme A synthase does not incorporate molecular oxygen into the formyl group of heme A. *Biochemistry-Us* **43**, 8616-8624

121. Lewin, A., and Hederstedt, L. (2016) Heme A synthase in bacteria depends on one pair of cysteinyls for activity. *Bba-Bioenergetics* **1857**, 160-168

122. Lewin, A., and Hederstedt, L. (2008) Promoted evolution of a shortened variant of heme A synthase in the membrane of Bacillus subtilis. *Febs Lett* **582**, 1330-1334

123. Svensson, B., Andersson, K. K., and Hederstedt, L. (1996) Low-spin heme A in the heme A biosynthetic protein CtaA from Bacillus subtilis. *Eur J Biochem* **238**, 287-295

124. Mogi, T. (2009) Probing Structure of Heme A Synthase from Bacillus subtilis by Site-Directed Mutagenesis. *J Biochem-Tokyo* **145**, 625-633

125. Lewin, A., and Hederstedt, L. (2006) Compact archaeal variant of heme A synthase. *Febs Lett* **580**, 5351-5356

126. Swenson, S., Cannon, A., Harris, N. J., Taylor, N. G., Fox, J. L., and Khalimonchuk, O. (2016) Analysis of Oligomerization Properties of Heme a

Synthase Provides Insights into Its Function in Eukaryotes. *J Biol Chem* **291**, 10411-10425

127. Antonicka, H., Mattman, A., Carlson, C. G., Glerum, D. M., Hoffbuhr, K. C., Leary, S. C., Kennaway, N. G., and Shoubridge, E. A. (2003) Mutations in COX15 produce a defect in the mitochondrial heme biosynthetic pathway, causing early-onset fatal hypertrophic cardiomyopathy. *Am J Hum Genet* **72**, 101-114

128. Bugiani, M., Tiranti, V., Farina, L., Uziel, G., and Zeviani, M. (2005) Novel mutations in COX15 in a long surviving Leigh syndrome patient with cytochrome c oxidase deficiency. *J Med Genet* **42**, e28

129. Oquendo, C. E., Antonicka, H., Shoubridge, E. A., Reardon, W., and Brown, G. K. (2004) Functional and genetic studies demonstrate that mutation in the COX15 gene can cause Leigh syndrome. *J Med Genet* **41**, 540-544

130. Alfadhel, M., Lillquist, Y. P., Waters, P. J., Sinclair, G., Struys, E., McFadden, D., Hendson, G., Hyams, L., Shoffner, J., and Vallance, H. D. (2011) Infantile Cardioencephalopathy due to a COX15 Gene Defect: Report and Review. *Am J Med Genet A* **155a**, 840-844

131. Hederstedt, L. (2012) Heme A biosynthesis. *BBA-Bioenergetics* **1817**, 920-927

132. Niwa, S., Takeda, K., Kosugi, M., Tsutsumi, E., Mogi, T., and Miki, K. (2018) Crystal structure of heme A synthase from Bacillus subtilis. *Proc Natl Acad Sci U S A* **115**, 11953-11957

133. Huber, R., and Eder, W. (2006) Aquificales. in *The Prokaryotes*, Springer. pp 925-938

134. Guiral, M., Tron, P., Aubert, C., Gloter, A., Iobbi-Nivol, C., and Giudici-Orticoni, M.-T. (2005) A membrane-bound multienzyme, hydrogen-oxidizing, and sulfur-reducing complex from the hyperthermophilic bacterium Aquifex aeolicus. *Journal of Biological Chemistry* **280**, 42004-42015

135. Deckert, G., Warren, P. V., Gaasterland, T., Young, W. G., Lenox, A. L., Graham, D. E., Overbeek, R., Snead, M. A., Keller, M., and Aujay, M. (1998) The complete genome of the hyperthermophilic bacterium Aquifex aeolicus. *Nature* **392**, 353-358

136. Uzarraga, R., Auria, R., Davidson, S., Navarro, D., and Combet-Blanc, Y. (2011) New cultural approaches for microaerophilic hyperthermophiles. *Current microbiology* **62**, 346-350

137. Pandelia, M.-E., Fourmond, V., Tron-Infossi, P., Lojou, E., Bertrand, P., Léger, C., Giudici-Orticoni, M.-T., and Lubitz, W. (2010) Membrane-bound hydrogenase I from the hyperthermophilic bacterium Aquifex aeolicus: enzyme activation, redox intermediates and oxygen tolerance. *Journal of the American Chemical Society* **132**, 6991-7004

138. Baymann, F., Tron, P., Schoepp-Cothenet, B., Aubert, C., Bianco, P., Stetter, K.-O., Nitschke, W., and Schütz, M. (2001) Cytochromes c 555 from the hyperthermophilic bacterium Aquifex aeolicus (VF5). 1. Characterization of two highly homologous, soluble and membranous, cytochromes c 555. *Biochemistry* **40**, 13681-13689

139. Peng, G., Fritzsch, G., Zickermann, V., Schägger, H., Mentele, R., Lottspeich, F., Bostina, M., Radermacher, M., Huber, R., and Stetter, K. O. (2003) Isolation, characterization and electron microscopic single particle analysis of the NADH: ubiquinone oxidoreductase (complex I) from the hyperthermophilic eubacterium Aquifex aeolicus. *Biochemistry* **42**, 3032-3039

140. Marcia, M., Ermler, U., Peng, G., and Michel, H. (2009) The structure of Aquifex aeolicus sulfide: quinone oxidoreductase, a basis to understand sulfide detoxification and respiration. *Proceedings of the National Academy of Sciences* **106**, 9625-9630

141. Schütz, M., Schoepp-Cothenet, B., Lojou, E., Woodstra, M., Lexa, D., Tron, P., Dolla, A., Durand, M.-C., Stetter, K. O., and Baymann, F. (2003) The naphthoquinol oxidizing cytochrome bc 1 complex of the hyperthermophilic knallgasbacterium Aquifex aeolicus: properties and phylogenetic relationships. *Biochemistry* **42**, 10800-10808

142. Gao, Y., Meyer, B., Sokolova, L., Zwicker, K., Karas, M., Brutschy, B., Peng, G., and Michel, H. (2012) Heme-copper terminal oxidase using both cytochrome c and ubiquinol as electron donors. *Proc Natl Acad Sci U S A* **109**, 3275-3280

143. Peng, G., Bostina, M., Radermacher, M., Rais, I., Karas, M., and Michel, H. (2006) Biochemical and electron microscopic characterization of the F 1 F 0 ATP synthase from the hyperthermophilic eubacterium Aquifex aeolicus. *FEBS letters* **580**, 5934-5940

144. Infossi, P., Lojou, E., Chauvin, J. P., Herbette, G., Brugna, M., and Giudici-Orticoni, M. T. (2010) Aquifex aeolicus membrane hydrogenase for hydrogen biooxidation: Role of lipids and physiological partners in enzyme stability and activity. *Int J Hydrogen Energ* **35**, 10778-10789

145. Pandelia, M. E., Fourmond, V., Tron-Infossi, P., Lojou, E., Bertrand, P., Leger, C., Giudici-Orticoni, M. T., and Lubitz, W. (2010) Membrane-Bound Hydrogenase I from the Hyperthermophilic Bacterium Aquifex aeolicus: Enzyme Activation, Redox Intermediates and Oxygen Tolerance. *J Am Chem Soc* **132**, 6991-7004

146. Guiral, M., Tron, P., Aubert, C., Gloter, A., Iobbi-Nivol, C., and Giudici-Orticoni, M. T. (2005) A membrane-bound multienzyme, hydrogen-oxidizing, and sulfur-reducing complex from the hyperthermophilic bacterium Aquifex aeolicus. *J Biol Chem* **280**, 42004-42015

147. Marcia, M., Ermler, U., Peng, G. H., and Michel, H. (2009) The structure of Aquifex aeolicus sulfide:quinone oxidoreductase, a basis to understand sulfide detoxification and respiration. *P Natl Acad Sci USA* **106**, 9625-9630

148. Scheide, D., Huber, R., and Friedrich, T. (2002) The proton-pumping NADH : ubiquinone oxidoreductase (complex 1) of Aquifex aeolicus. *Febs Lett* **512**, 80-84

149. Gao, Y., Meyer, B., Sokolova, L., Zwicker, K., Karas, M., Brutschy, B., Peng, G. H., and Michel, H. (2012) Heme-copper terminal oxidase using both cytochrome c and ubiquinol as electron donors. *P Natl Acad Sci USA* **109**, 3275-

3280

150. Guiral, M., Prunetti, L., Lignon, S., Lebrun, R., Moinier, D., and Giudici-Orticoni, M.-T. r. s. (2009) New insights into the respiratory chains of the chemolithoautotrophic and hyperthermophilic bacterium Aquifex aeolicus. *Journal of proteome research* **8**, 1717-1730

151. Prunetti, L., Infossi, P., Brugna, M., Ebel, C., Giudici-Orticoni, M.-T., and Guiral, M. (2010) New functional sulfide oxidase-oxygen reductase supercomplex in the membrane of the hyperthermophilic bacterium Aquifex aeolicus. *Journal of Biological Chemistry* **285**, 41815-41826

152. Urbani, A., Gemeinhardt, S., Warne, A., and Saraste, M. (2001) Properties of the detergent solubilised cytochrome c oxidase (cytochrome cbb(3)) purified from Pseudomonas stutzeri. *Febs Lett* **508**, 29-35

153. Scheres, S. H. (2012) RELION: implementation of a Bayesian approach to cryo-EM structure determination. *J Struct Biol* **180**, 519-530

154. Kimanius, D., Forsberg, B. O., Scheres, S. H. W., and Lindahl, E. (2016) Accelerated cryo-EM structure determination with parallelisation using GPUs in RELION-2. *Elife* **5**

155. Tang, G., Peng, L., Baldwin, P. R., Mann, D. S., Jiang, W., Rees, I., and Ludtke, S. J. (2007) EMAN2: An extensible image processing suite for electron microscopy. *J Struct Biol* **157**, 38-46

156. Kucukelbir, A., Sigworth, F. J., and Tagare, H. D. (2014) Quantifying the local resolution of cryo-EM density maps. *Nat Methods* **11**, 63-65

157. Li, C., Wen, A., Shen, B., Lu, J., Huang, Y., and Chang, Y. (2011) FastCloning: a highly simplified, purification-free, sequence- and ligation-independent PCR cloning method. *BMC Biotechnol* **11**, 92

158. Hanahan, D. (1983) Studies on Transformation of Escherichia-Coli with Plasmids. *J Mol Biol* **166**, 557-580

159. Choi, K. H., Kumar, A., and Schweizer, H. P. (2006) A 10-min method for preparation of highly electrocompetent Pseudomonas aeruginosa cells: Application for DNA fragment transfer between chromosomes and plasmid transformation. *J Microbiol Meth* **64**, 391-397

160. Huber, R., and Eder, W. (2006) Aquificales. in *The Prokaryotes: Volume 7: Proteobacteria: Delta, Epsilon Subclass* (Dworkin, M., Falkow, S., Rosenberg, E., Schleifer, K.-H., and Stackebrandt, E. eds.), Springer New York, New York, NY. pp 925-938

161. Eder, W., and Huber, R. (2002) New isolates and physiological properties of the Aquificales and description of Thermocrinis albus sp. nov. *Extremophiles* **6**, 309-318

162. Peng, G., Fritzsch, G., Zickermann, V., Schagger, H., Mentele, R., Lottspeich, F., Bostina, M., Radermacher, M., Huber, R., Stetter, K. O., and Michel, H. (2003) Isolation, characterization and electron microscopic single particle analysis of the NADH:ubiquinone oxidoreductase (complex I) from the hyperthermophilic eubacterium Aquifex aeolicus. *Biochemistry-Us* **42**, 3032-3039

163. Smith, P. K., Krohn, R. I., Hermanson, G. T., Mallia, A. K., Gartner, F. H., Provenzano, M. D., Fujimoto, E. K., Goeke, N. M., Olson, B. J., and Klenk, D. C. (1985) Measurement of Protein Using Bicinchoninic Acid. *Anal Biochem* **150**, 76-85

164. Schagger, H., and Vonjagow, G. (1991) Blue Native Electrophoresis for Isolation of Membrane-Protein Complexes in Enzymatically Active Form. *Anal Biochem* **199**, 223-231

165. Guikema, J. A., and Sherman, L. A. (1981) Electrophoretic Profiles of Cyanobacterial Membrane Polypeptides Showing Heme-Dependent Peroxidase-Activity. *Biochim Biophys Acta* **637**, 189-201

166. Thomas, P. E., Ryan, D., and Levin, W. (1976) An improved staining procedure for the detection of the peroxidase activity of cytochrome P-450 on sodium dodecyl sulfate polyacrylamide gels. *Anal Biochem* **75**, 168-176

167. Strop, P., and Brunger, A. T. (2005) Refractive index-based determination of detergent concentration and its application to the study of membrane proteins. *Protein Sci* **14**, 2207-2211

168. Liu, X., Yin, Y., Wu, J., and Liu, Z. (2014) Structure and mechanism of an intramembrane liponucleotide synthetase central for phospholipid biosynthesis. *Nat Commun* **5**, 4244

169. Morgner, N., Kleinschroth, T., Barth, H. D., Ludwig, B., and Brutschy, B. (2007) A novel approach to analyze membrane proteins by laser mass spectrometry: from protein subunits to the integral complex. *J Am Soc Mass Spectrom* **18**, 1429-1438

170. Mastronarde, D. N. (2005) Automated electron microscope tomography using robust prediction of specimen movements. *J Struct Biol* **152**, 36-51

171. Zheng, S. Q., Palovcak, E., Armache, J. P., Verba, K. A., Cheng, Y. F., and Agard, D. A. (2017) MotionCor2: anisotropic correction of beam-induced motion for improved cryo-electron microscopy. *Nat Methods* **14**, 331-332

172. Rohou, A., and Grigorieff, N. (2015) CTFFIND4: Fast and accurate defocus estimation from electron micrographs. *J Struct Biol* **192**, 216-221

173. Emsley, P., and Cowtan, K. (2004) Coot: model-building tools for molecular graphics. *Acta Crystallogr D Biol Crystallogr* **60**, 2126-2132

174. Adams, P. D., Afonine, P. V., Bunkoczi, G., Chen, V. B., Davis, I. W., Echols, N., Headd, J. J., Hung, L. W., Kapral, G. J., Grosse-Kunstleve, R. W., McCoy, A. J., Moriarty, N. W., Oeffner, R., Read, R. J., Richardson, D. C., Richardson, J. S., Terwilliger, T. C., and Zwart, P. H. (2010) PHENIX: a comprehensive Python-based system for macromolecular structure solution. *Acta Crystallogr D Biol Crystallogr* **66**, 213-221

175. Wenz, T., Covian, R., Hellwig, P., MacMillan, F., Meunier, B., Trumpower, B. L., and Hunte, C. (2007) Mutational analysis of cytochrome b at the ubiquinol oxidation site of yeast complex III. *J Biol Chem* **282**, 3977-3988

176. Zickermann, I., Anemuller, S., Richter, O. M., Tautu, O. S., Link, T. A., and Ludwig, B. (1996) Biochemical and spectroscopic properties of the four-subunit quinol oxidase (cytochrome ba3) from Paracoccus denitrificans. *Biochim*

Biophys Acta **1277**, 93-102

177. Ouchane, S., Agalidis, I., and Astier, C. (2002) Natural resistance to inhibitors of the ubiquinol cytochrome c oxidoreductase of Rubrivivax gelatinosus: Sequence and functional analysis of the cytochrome bc(1) complex. *J Bacteriol* **184**, 3815-3822

178. Hartley, A. M., Lukoyanova, N., Zhang, Y., Cabrera-Orefice, A., Arnold, S., Meunier, B., Pinotsis, N., and Marechal, A. (2019) Structure of yeast cytochrome c oxidase in a supercomplex with cytochrome bc1. *Nat Struct Mol Biol* **26**, 78-83

179. Letts, J. A., Fiedorczuk, K., and Sazanov, L. A. (2016) The architecture of respiratory supercomplexes. *Nature* **537**, 644-648

180. Prunetti, L., Infossi, P., Brugna, M., Ebel, C., Giudici-Orticoni, M. T., and Guiral, M. (2010) New Functional Sulfide Oxidase-Oxygen Reductase Supercomplex in the Membrane of the Hyperthermophilic Bacterium Aquifex aeolicus. *J Biol Chem* **285**, 41815-41826

181. Guiral, M., Prunetti, L., Lignon, S., Lebrun, R., Moinier, D., and Giudici-Orticoni, M. T. (2009) New Insights into the Respiratory Chains of the Chemolithoautotrophic and Hyperthermophilic Bacterium Aquifex aeolicus. *J Proteome Res* **8**, 1717-1730

182. Aubert, C., Guerlesquin, F., Bianco, P., Leroy, G., Tron, P., Stetter, K. O., and Bruschi, M. (2001) Cytochromes c555 from the hyperthermophilic bacterium Aquifex aeolicus. 2. Heterologous production of soluble cytochrome c555s and investigation of the role of methionine residues. *Biochemistry-Us* **40**, 13690-13698

183. Baymann, F., Tron, P., Schoepp-Cothenet, B., Aubert, C., Bianco, P., Stetter, K. O., Nitschke, W., and Schutz, M. (2001) Cytochromes c555 from the hyperthermophilic bacterium Aquifex aeolicus (VF5). 1. Characterization of two highly homologous, soluble and membranous, cytochromes c555. *Biochemistry-Us* **40**, 13681-13689

184. Obuchi, M., Kawahara, K., Motooka, D., Nakamura, S., Yamanaka, M., Takeda, T., Uchiyama, S., Kobayashi, Y., Ohkubo, T., and Sambongi, Y. (2009) Hyperstability and crystal structure of cytochrome c(555) from hyperthermophilic Aquifex aeolicus. *Acta Crystallogr D Biol Crystallogr* **65**, 804-813

185. Arslan, E., Schulz, H., Zufferey, R., Kunzler, P., and Thony-Meyer, L. (1998) Overproduction of the Bradyrhizobium japonicum c-type cytochrome subunits of the cbb3 oxidase in Escherichia coli. *Biochem Biophys Res Commun* **251**, 744-747

186. Iwata, S., Ostermeier, C., Ludwig, B., and Michel, H. (1995) Structure at 2.8-Angstrom Resolution of Cytochrome-C-Oxidase from Paracoccus-Denitrificans. *Nature* **376**, 660-669

187. Witt, H., Malatesta, F., Nicoletti, F., Brunori, M., and Ludwig, B. (1998) Cytochrome-c-binding site on cytochrome oxidase in Paracoccus denitrificans. *Eur J Biochem* **251**, 367-373

188. Witt, H., Malatesta, F., Nicoletti, F., Brunori, M., and Ludwig, B. (1998) Tryptophan 121 of subunit II is the electron entry site to cytochrome-c oxidase in Paracoccus denitrificans - Involvement of a hydrophobic patch in the docking reaction. *J Biol Chem* **273**, 5132-5136

189. Lubben, M., Kolmerer, B., and Saraste, M. (1992) An archaebacterial terminal oxidase combines core structures of two mitochondrial respiratory complexes. *Embo J* **11**, 805-812

190. Chang, H. Y., Hemp, J., Chen, Y., Fee, J. A., and Gennis, R. B. (2009) The cytochrome ba3 oxygen reductase from Thermus thermophilus uses a single input channel for proton delivery to the active site and for proton pumping. *Proc Natl Acad Sci U S A* **106**, 16169-16173

191. Gennis, R. B. (1998) Multiple proton-conducting pathways in cytochrome oxidase and a proposed role for the active-site tyrosine. *Bba-Bioenergetics* **1365**, 241-248

192. von Ballmoos, C., Gonska, N., Lachmann, P., Gennis, R. B., Adelroth, P., and Brzezinski, P. (2015) Mutation of a single residue in the ba3 oxidase specifically impairs protonation of the pump site. *Proc Natl Acad Sci U S A* **112**, 3397-3402

193. Pfitzner, U., Hoffmeier, K., Harrenga, A., Kannt, A., Michel, H., Bamberg, E., Richter, O. M., and Ludwig, B. (2000) Tracing the D-pathway in reconstituted site-directed mutants of cytochrome c oxidase from Paracoccus denitrificans. *Biochemistry-Us* **39**, 6756-6762

194. Qian, J., Shi, W. J., Pressler, M., Hoganson, C., Mills, D., Babcock, G. T., and FergusonMiller, S. (1997) Aspartate-407 in Rhodobacter sphaeroides cytochrome c oxidase is not required for proton pumping or manganese binding. *Biochemistry-US* **36**, 2539-2543

195. Thomas, J. W., Puustinen, A., Alben, J. O., Gennis, R. B., and Wikstrom, M. (1993) Substitution of asparagine for aspartate-135 in subunit I of the cytochrome bo ubiquinol oxidase of Escherichia coli eliminates proton-pumping activity. *Biochemistry-Us* **32**, 10923-10928

196. Riistama, S., Puustinen, A., GarciaHorsman, A., Iwata, S., Michel, H., and Wikstrom, M. (1996) Channelling of dioxygen into the respiratory enzyme. *Bba-Bioenergetics* **1275**, 1-4

197. Luna, V. M., Chen, Y., Fee, J. A., and Stout, C. D. (2008) Crystallographic studies of Xe and Kr binding within the large internal cavity of cytochrome ba(3) from Thermus thermophilus: Structural analysis and role of oxygen transport channels in the heme-Cu oxidases. *Biochemistry-Us* **47**, 4657-4665

198. Kaila, V. R. I., Verkhovsky, M. I., Hummer, G., and Wikstrom, M. (2008) Glutamic acid 242 is a valve in the proton pump of cytochrome c oxidase. *P Natl Acad Sci USA* **105**, 6255-6259

199. Shinzawa-Itoh, K., Aoyama, H., Muramoto, K., Terada, H., Kurauchi, T., Tadehara, Y., Yamasaki, A., Sugimura, T., Kurono, S., Tsujimoto, K., Mizushima, T., Yamashita, E., Tsukihara, T., and Yoshikawa, S. (2007) Structures and physiological roles of 13 integral lipids of bovine heart cytochrome c oxidase. *Embo J* **26**, 1713-1725

200. Yoshikawa, S., Shinzawa-Itoh, K., Nakashima, R., Yaono, R., Yamashita, E., Inoue, N., Yao, M., Fei, M. J., Libeu, C. P., Mizushima, T., Yamaguchi, H., Tomizaki, T., and Tsukihara, T. (1998) Redox-coupled crystal structural changes in bovine heart cytochrome c oxidase. *Science* **280**, 1723-1729

201. Esser, L., Zhou, F., Zhou, Y., Xiao, Y., Tang, W.-k., Yu, C.-A., Qin, Z., and Xia, D. (2016) Hydrogen bonding to the substrate is not required for Rieske iron-sulfur protein docking to the quinol oxidation site of complex III. *J Biol Chem* **291**, 25019-25031

202. Kleinschroth, T., Castellani, M., Trinh, C. H., Morgner, N., Brutschy, B., Ludwig, B., and Hunte, C. (2011) X-ray structure of the dimeric cytochrome bc(1) complex from the soil bacterium Paracoccus denitrificans at 2.7-A resolution. *Biochim Biophys Acta* **1807**, 1606-1615

203. Schutz, M., Schoepp-Cothenet, B., Lojou, E., Woodstra, M., Lexa, D., Tron, P., Dolla, A., Durand, M. C., Stetter, K. O., and Baymann, F. (2003) The naphthoquinol oxidizing cytochrome bc1 complex of the hyperthermophilic knallgasbacterium Aquifex aeolicus: properties and phylogenetic relationships. *Biochemistry-Us* **42**, 10800-10808

204. Degliesposti, M., Devries, S., Crimi, M., Ghelli, A., Patarnello, T., and Meyer, A. (1993) Mitochondrial Cytochrome-B - Evolution and Structure of the Protein. *Biochim Biophys Acta* **1143**, 243-271

205. Morgner, N., Kleinschroth, T., Barth, H. D., Ludwig, B., and Brutschy, B. (2007) A novel approach to analyze membrane proteins by laser mass spectrometry: From protein subunits to the integral complex. *J Am Soc Mass Spectr* **18**, 1429-1438

206. Svensson, B., and Hederstedt, L. (1994) Bacillus-Subtilis-Ctaa Is a Heme-Containing Membrane-Protein Involved in Heme-a Biosynthesis. *J Bacteriol* **176**, 6663-6671

207. Niwa, S., Takeda, K., Kosugi, M., Tsutsumi, E., Mogi, T., and Miki, K. (2018) Crystal structure of heme A synthase from Bacillus subtilis. *P Natl Acad Sci USA* **115**, 11953-11957

208. Taylor, N. G., Swenson, S., Harris, N. J., Germany, E. M., Fox, J. L., and Khalimonchuk, O. (2017) The Assembly Factor Pet117 Couples Heme a Synthase Activity to Cytochrome Oxidase Assembly. *J Biol Chem* **292**, 1815-1825

209. Khalimonchuk, O., Kim, H., Watts, T., Perez-Martinez, X., and Winge, D. R. (2012) Oligomerization of Heme o Synthase in Cytochrome Oxidase Biogenesis Is Mediated by Cytochrome Oxidase Assembly Factor Coa2. *J Biol Chem* **287**, 26715-26726

210. Bertero, M. G., Rothery, R. A., Palak, M., Hou, C., Lim, D., Blasco, F., Weiner, J. H., and Strynadka, N. C. J. (2003) Insights into the respiratory electron transfer pathway from the structure of nitrate reductase A. *Nat Struct Biol* **10**, 681-687

211. Hanson, M. A., Cherezov, V., Griffith, M. T., Roth, C. B., Jaakola, V. P., Chien, E. Y. T., Velasquez, J., Kuhn, P., and Stevens, R. C. (2008) A specific cholesterol

binding site is established by the 2.8 angstrom structure of the human beta(2)-adrenergic receptor. *Structure* **16**, 897-905

212. Murata, Y., Iwasaki, H., Sasaki, M., Inaba, K., and Okamura, Y. (2005) Phosphoinositide phosphatase activity coupled to an intrinsic voltage sensor. *Nature* **435**, 1239-1243

213. Nury, H., Dahout-Gonzalez, C., Trezeguet, V., Lauquin, G., Brandolin, G., and Pebay-Peyroula, E. (2005) Structural basis for lipid-mediated interactions between mitochondrial ADP/ATP carrier monomers. *Febs Lett* **579**, 6031-6036

214. Ball, W. B., Neff, J. K., and Gohil, V. M. (2018) The role of nonbilayer phospholipids in mitochondrial structure and function. *Febs Lett* **592**, 1273-1290

215. Martens, C., Shekhar, M., Borysik, A. J., Lau, A. M., Reading, E., Tajkhorshid, E., Booth, P. J., and Politis, A. (2018) Direct protein-lipid interactions shape the conformational landscape of secondary transporters. *Nat Commun* **9**, 4151

216. Contreras, F. X., Ernst, A. M., Wieland, F., and Brugger, B. (2011) Specificity of Intramembrane Protein-Lipid Interactions. *Csh Perspect Biol* **3**, a004705

217. Perez-Gordones, M. C., Lugo, M. R., Winkler, M., Cervino, V., and Benaim, G. (2009) Diacylglycerol regulates the plasma membrane calcium pump from human erythrocytes by direct interaction. *Arch Biochem Biophys* **489**, 55-61

218. Eroglu, C., Brugger, B., Wieland, F., and Sinning, L. (2003) Glutamate-binding affinity of Drosophila metabotropic glutamate receptor is modulated by association with lipid rafts. *P Natl Acad Sci USA* **100**, 10219-10224

219. Gimpl, G., and Fahrenholz, F. (2002) Cholesterol as stabilizer of the oxytocin receptor. *Bba-Biomembranes* **1564**, 384-392

220. Brugna-Guiral, M., Tron, P., Nitschke, W., Stetter, K. O., Burlat, B., Guigliarelli, B., Bruschi, M., and Giudici-Orticoni, M. T. (2003) [NiFe] hydrogenases from the hyperthermophilic bacterium Aquifex aeolicus: properties, function, and phylogenetics. *Extremophiles* **7**, 145-157

221. Ludwig, B., and Schatz, G. (1980) A two-subunit cytochrome c oxidase (cytochrome aa3) from Paracoccus dentrificans. *Proc Natl Acad Sci U S A* **77**, 196-200

222. Hendler, R. W., Pardhasaradhi, K., Reynafarje, B., and Ludwig, B. (1991) Comparison of energy-transducing capabilities of the two- and three-subunit cytochromes aa3 from Paracoccus denitrificans and the 13-subunit beef heart enzyme. *Biophys J* **60**, 415-423

223. Hill, B. C. (1994) Modeling the Sequence of Electron-Transfer Reactions in the Single Turnover of Reduced, Mammalian Cytochrome-C-Oxidase with Oxygen. *J Biol Chem* **269**, 2419-2425

224. Michel, H., Behr, J., Harrenga, A., and Kannt, A. (1998) Cytochrome C oxidase: Structure and spectroscopy. *Annu Rev Bioph Biom* **27**, 329-356

225. Moser, C. C., Keske, J. M., Warncke, K., Farid, R. S., and Dutton, P. L. (1992) Nature of Biological Electron-Transfer. *Nature* **355**, 796-802

226. Leferink, N. G. H., Pudney, C. R., Brenner, S., Heyes, D. J., Eady, R. R., Hasnain, S. S., Hay, S., Rigby, S. E. J., and Scrutton, N. S. (2012) Gating

mechanisms for biological electron transfer: Integrating structure with biophysics reveals the nature of redox control in cytochrome P450 reductase and copper-dependent nitrite reductase. *Febs Lett* **586**, 578-584

227. Yoshikawa, S., Shinzawa-Itoh, K., and Tsukihara, T. (1998) Crystal structure of bovine heart cytochrome c oxidase at 2.8 angstrom resolution. *J Bioenerg Biomembr* **30**, 7-14

228. Chang, H. Y., Choi, S. K., Vakkasoglu, A. S., Chen, Y., Hemp, J., Fee, J. A., and Gennis, R. B. (2012) Exploring the proton pump and exit pathway for pumped protons in cytochrome ba(3) from Thermus thermophilus. *P Natl Acad Sci USA* **109**, 5259-5264

229. Pfitzner, U., Odenwald, A., Ostermann, T., Weingard, L., Ludwig, B., and Richter, O. M. H. (1998) Cytochrome c oxidase (Heme aa(3)) from Paracoccus denitrificans: Analysis of mutations in putative proton channels of subunit I. *J Bioenerg Biomembr* **30**, 89-97

230. Lu, J. X., and Gunner, M. R. (2014) Characterizing the proton loading site in cytochrome c oxidase. *P Natl Acad Sci USA* **111**, 12414-12419

231. Svensson-Ek, M., Abramson, J., Larsson, G., Tornroth, S., Brzezinski, P., and Iwata, S. (2002) The X-ray crystal structures of wild-type and EQ(I-286) mutant cytochrome c oxidases from Rhodobacter sphaeroides. *J Mol Biol* **321**, 329-339

232. Lee, B. (1993) Estimation of the maximum change in stability of globular proteins upon mutation of a hydrophobic residue to another of smaller size. *Protein Sci* **2**, 733-738

233. Sedlak, E., and Robinson, N. C. (2015) Destabilization of the Quaternary Structure of Bovine Heart Cytochrome c Oxidase upon Removal of Tightly Bound Cardiolipin. *Biochemistry-Us* **54**, 5569-5577

234. Arnarez, C., Marrink, S. J., and Periole, X. (2013) Identification of cardiolipin binding sites on cytochrome c oxidase at the entrance of proton channels (vol 3, 1263, 2013). *Sci Rep-Uk* **3**

235. Liko, I., Degiacomi, M. T., Mohammed, S., Yoshikawa, S., Schmidt, C., and Robinson, C. V. (2016) Dimer interface of bovine cytochrome c oxidase is influenced by local posttranslational modifications and lipid binding. *P Natl Acad Sci USA* **113**, 8230-8235

236. Musatov, A., and Robinson, N. C. (2014) Bound cardiolipin is essential for cytochrome c oxidase proton translocation. *Biochimie* **105**, 159-164

237. Giustini, M., Castelli, F., Husu, I., Giomini, M., Mallardi, A., and Palazzo, G. (2005) Influence of cardiolipin on the functionality of the Q(A) site of the photosynthetic bacterial reaction center (vol 109B, pg 21193, 2005). *J Phys Chem B* **109**, 23108-23108

238. Nagy, L., Milano, F., Dorogi, M., Agostiano, A., Laczko, G., Szebenyi, K., Varo, G., Trotta, M., and Maroti, P. (2004) Protein/lipid interaction in the bacterial photosynthetic reaction center: phosphatidylcholine and phosphatidylglycerol modify the free energy levels of the quinones. *Biochemistry-US* **43**, 12913-12923

239. Schutz, M., Brugna, M., Lebrun, E., Baymann, F., Huber, R., Stetter, K. O.,

Hauska, G., Toci, R., Lemesle-Meunier, D., Tron, P., Schmidt, C., and Nitschke, W. (2000) Early evolution of cytochrome bc complexes. *J Mol Biol* **300**, 663-675

240. Nett, J. H., Hunte, C., and Trumpower, B. L. (2000) Changes to the length of the flexible linker region of the Rieske protein impair the interaction of ubiquinol with the cytochrome bc1 complex. *Eur J Biochem* **267**, 5777-5782

241. Tian, H., White, S., Yu, L., and Yu, C. A. (1999) Evidence for the head domain movement of the Rieske iron-sulfur protein in electron transfer reaction of the cytochrome bc(1) complex. *J Biol Chem* **274**, 7146-7152

242. ThonyMeyer, L., and Kunzler, P. (1997) Translocation to the periplasm and signal sequence cleavage of preapocytochrome c depend on sec and lep, but not on the ccm gene products. *Eur J Biochem* **246**, 794-799

243. Gerhus, E., Steinrucke, P., and Ludwig, B. (1990) Paracoccus-Denitrificans Cytochrome-C1 Gene Replacement Mutants. *J Bacteriol* **172**, 2392-2400

244. Thonymeyer, L., James, P., and Hennecke, H. (1991) From One Gene to 2 Proteins - the Biogenesis of Cytochrome-B and Cytochrome-C1 in Bradyrhizobium-Japonicum. *P Natl Acad Sci USA* **88**, 5001-5005

245. Hannappel, A., Bundschuh, F. A., and Ludwig, B. (2011) Characterization of heme-binding properties of Paracoccus denitrificans Surf1 proteins. *Febs J* **278**, 1769-1778

246. Schneider, S., Sharp, K. H., Barker, P. D., and Paoli, M. (2006) An induced fit conformational change underlies the binding mechanism of the heme transport proteobacteria-protein HemS. *J Biol Chem* **281**, 32606-32610

247. Cornish-Bowden, A. J., and Koshland, D. E., Jr. (1971) The quaternary structure of proteins composed of identical subunits. *J Biol Chem* **246**, 3092-3102

248. Goodsell, D. S., and Olson, A. J. (2000) Structural symmetry and protein function. *Annu Rev Bioph Biom* **29**, 105-153

249. Miller, S., Lesk, A. M., Janin, J., and Chothia, C. (1987) The Accessible Surface-Area and Stability of Oligomeric Proteins. *Nature* **328**, 834-836

250. Schuller, D. J., Wilks, A., Ortiz de Montellano, P. R., and Poulos, T. L. (1999) Crystal structure of human heme oxygenase-1. *Nat Struct Biol* **6**, 860-867

251. Palsdottir, H., Lojero, C. G., Trumpower, B. L., and Hunte, C. (2003) Structure of the yeast cytochrome bc1 complex with a hydroxyquinone anion Qo site inhibitor bound. *J Biol Chem* **278**, 31303-31311
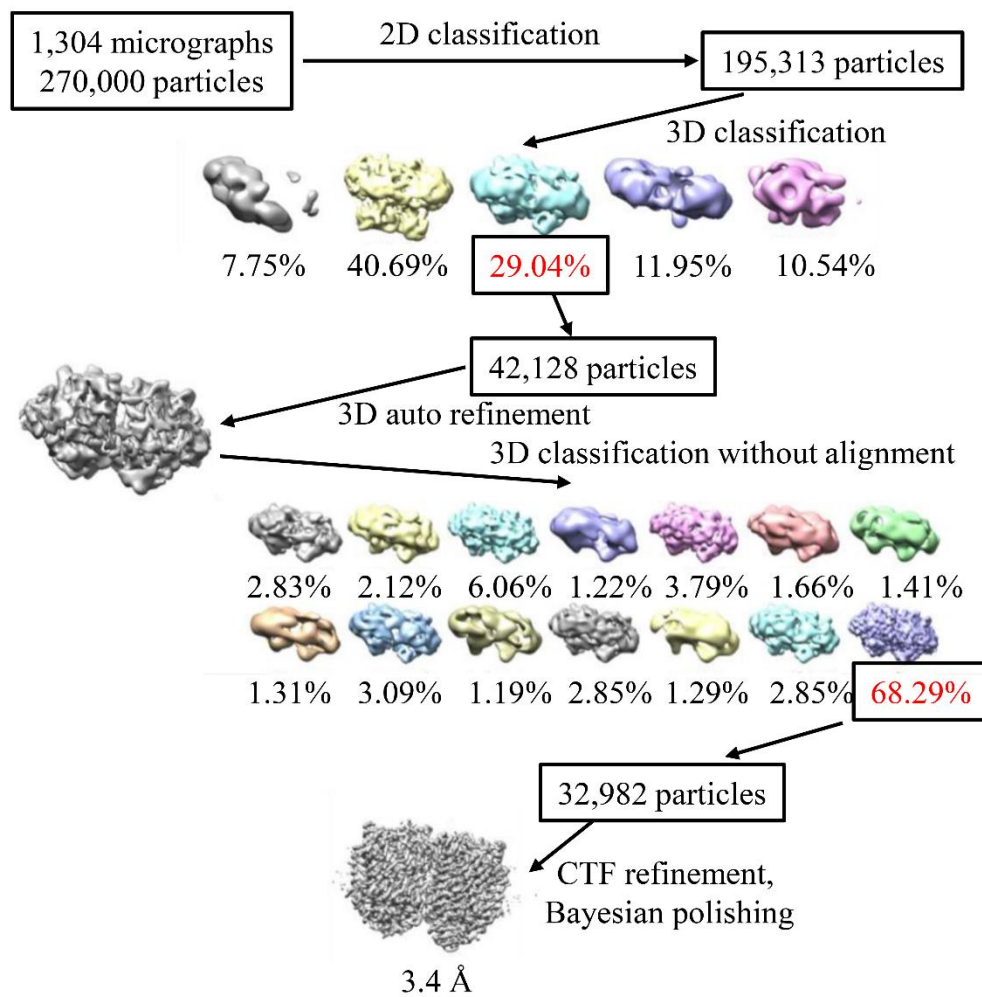
Appendix

Cytochrome *c* oxidase

Figure A1: A flowchart for cryo-EM data processing. The final average resolution for the AaC*c*O is estimated to be 3.4 Å.
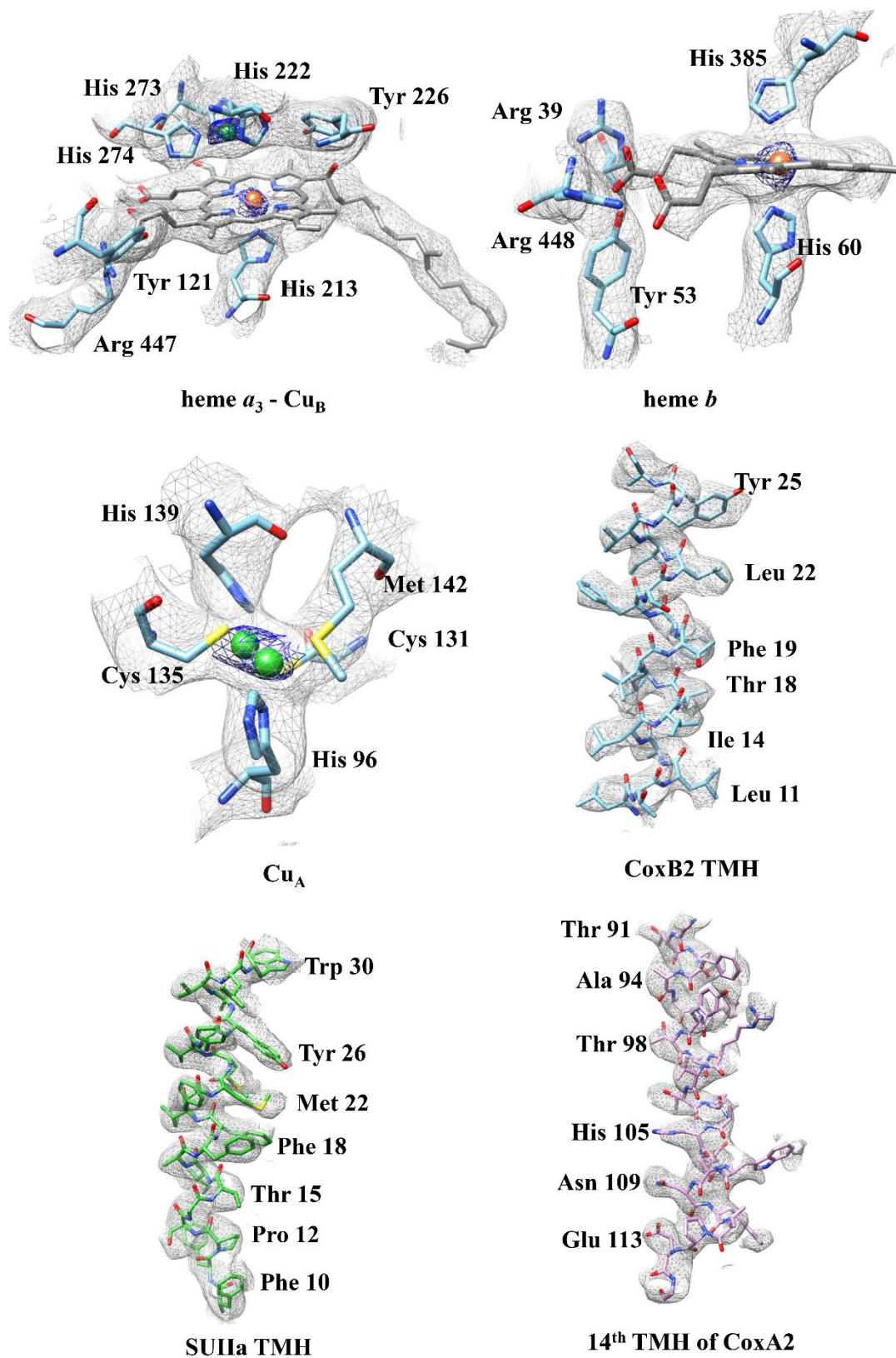
Figure A2: Representative cryo-EM densities of the proteins and ligands of the AaC*c*O
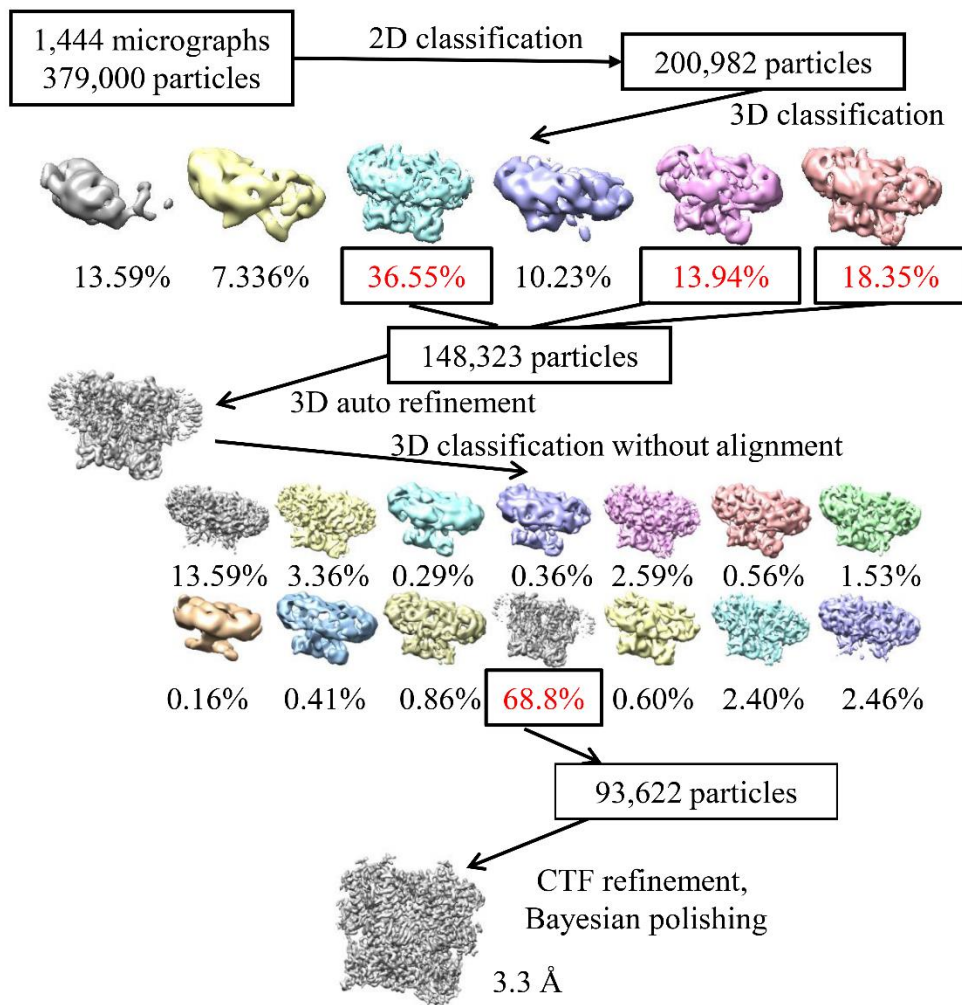
Cytochrome *bc*$_1$ complex

Figure A3: A flowchart for cryo-EM data processing. The final average resolution for the Aa*bc*$_1$ is estimated to be 3.3 Å.
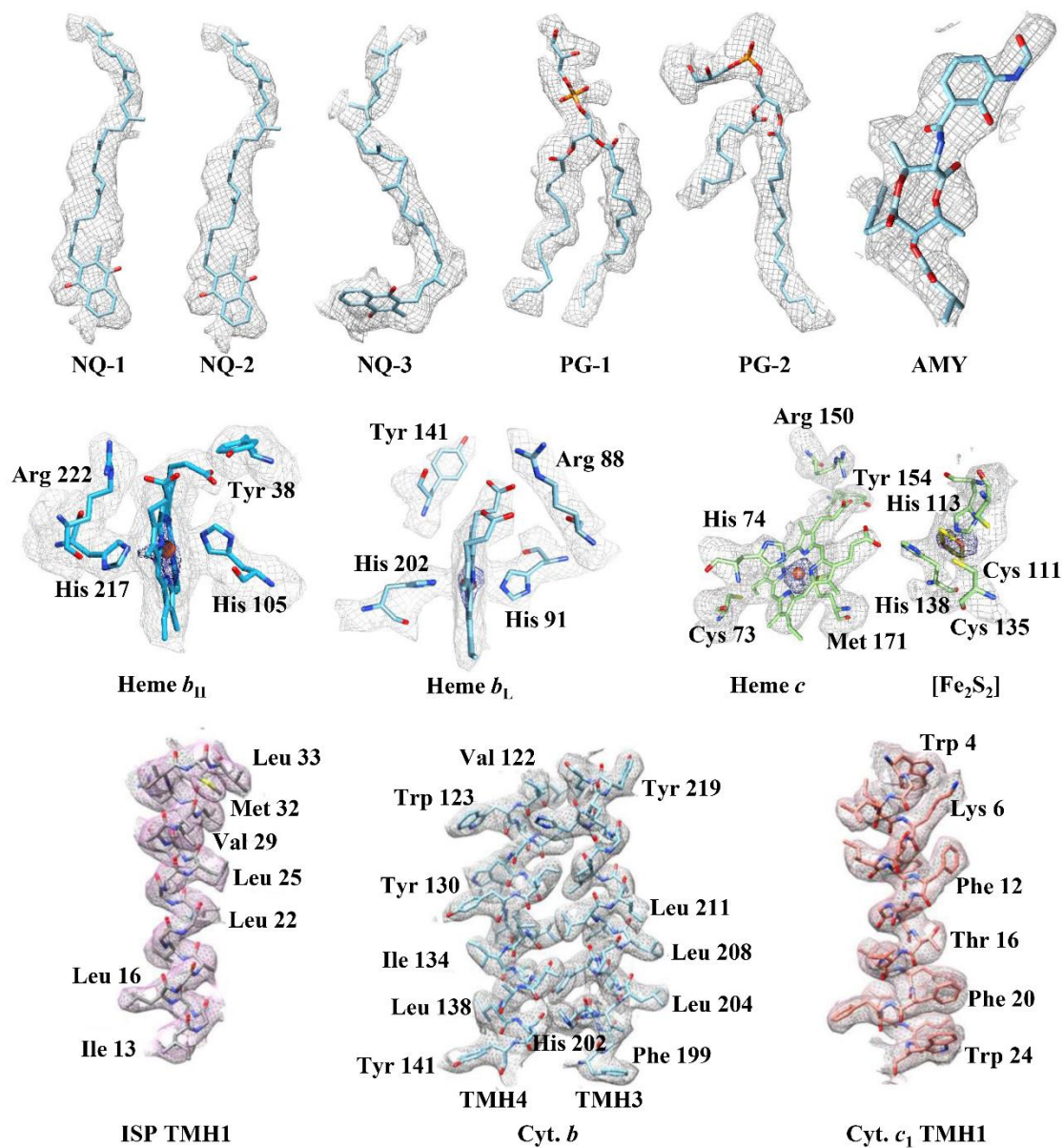
Figure A4: Representative cryo-EM densities of the proteins and ligands of the Aabc_1

Full wwPDB/EMDataBank EM Map/Model Validation Report (i)

Aug 15, 2019 – 10:31 AM JST

PDB ID	:	6KLS
EMDB ID:	:	EMD-0716
Title	:	Hyperthermophilic respiratory Complex III
Deposited on	:	2019-07-30
Resolution	:	3.30 Å(reported)

This is a Full wwPDB/EMDataBank EM Map/Model Validation Report.

This report is produced by the wwPDB biocuration pipeline after annotation of the structure.

We welcome your comments at *validation@mail.wwpdb.org*
A user guide is available at
https://www.wwpdb.org/validation/2017/EMValidationReportHelp
with specific help available everywhere you see the (i) symbol.

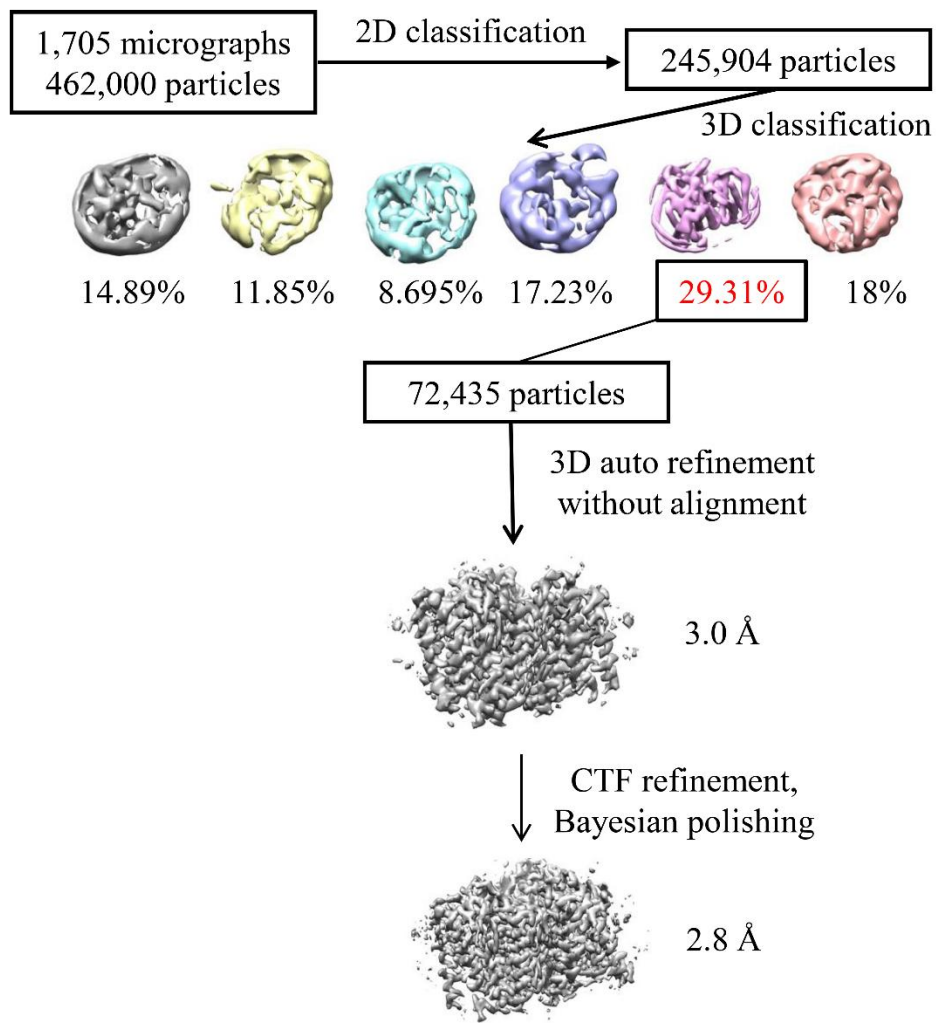|		
MolProbity	:	4.02b-467
Mogul	:	1.8.0 (224370), CSD as540be (2019)
Percentile statistics	:	20171227.v01 (using entries in the PDB archive December 27th 2017)
Ideal geometry (proteins)	:	Engh & Huber (2001)
Ideal geometry (DNA, RNA)	:	Parkinson et. al. (1996)
Validation Pipeline (wwPDB-VP)	:	2.4

Heme A synthase

Figure A5: A flowchart for cryo-EM data processing. The final average resolution for the Aa*bc*$_1$ is estimated to be 3.3 Å

Acknowledgements

Firstly, I would like to express my gratitude to my supervisor Prof. Hartmut Michel for accepting and supervising me as a graduate student in his laboratories. I am grateful for his constructive suggestions, critical decisions, and economic as well as scientific support in the project.

Secondly, I would like to thank my university supervisor Prof. Dr. Klaas Martinus Pos for taking the responsibility of internal supervision and insightful discussions.

Besides my advisors, I would like to thank my thesis committee member.

I thank Dr. Guohong Peng for her initial supervision and constant support in the projects.

I also would like to thank Dr. Hao Xie for his supervision and availability for discussion. I truly appreciate his proofreading of my thesis and my manuscripts.

Many thanks to Dr. Chunli Zhang form Shanghai Jiao Tong University for fruitful discussions.

In the department of Prof. Hartmut Michel at the Max Planck Institute of Biophysics, Dr. Julian Langer, Imke Wuellenweber, Martin Eisinger and Jakob Meier-Credo for performing the HPLC/MS and MALDI-TOF MS analysis. Cornelia Muenke prepared all the modified in-house vectors. Barbra Rathmann helped me to set up multiple plates. Sincere thanks to all current and previous members of the Molecular Membrane Biology Department, Max Planck Institute of Biophysics, Frankfurt for the nice working atmosphere, the scientific discussion and the kind technical assistance.

My work has been supported by the Max Planck Society and the Center of Excellence (Macromolecular Complexes) Frankfurt.

My sincere acknowledgements are extended to my collaborators who contributed to the successful of my projects.

Prof. Nina Morgner and Janosch Martin from Institute of Physical and Theoretical Chemistry, Goethe University for performing the LILBID-MS and fruitful discussions.

Prof. Fei Sun, Shuangbo Zhang, Guoliang Zhu and Dr. Yu Zhu from National

Acknowledgements

Curriculum Vitae

Name	Hui Zeng
Address	Neuenhainer Str. 30, 60326, Frankfurt am Main, Germany
Date of birth	July 8th 1988
Place of birth	Hubei, P.R. CHINA

Education

2014-present	Ph.D. candidate Max Planck Institute of Biophysics, Frankfurt am Main, Germany Department of Molecular Membrane Biology Internal supervisor: Prof. Dr. Klaas Martinus Pos External supervisor: Prof. Dr. Hartmut Michel Dissertation: Structural and functional characterization of cytochrome c oxidase, cytochrome bc_1 complex and heme A synthase from *A. aeolicus*
2011-2014	M.S.E Bioengineering Key Laboratory of Algal Biology, Institute of Hydrobiology, Chinese Academy of Sciences, Wuhan, China Supervisor: Prof. Kaiyao Huang Thesis: Identification the flagellar defects in *Chlamydomonas reinhardtii* and characterization of a long flagellar mutant lf6
2007-2011	B.S Aquaculture Science Huazhong Agricultural University, Wuhan, China Supervisor: Prof Li Li Thesis: Antioxidant response in liver of the Phyto planktivorous bighead carp (Aris ichthys Nobilis) intraperitoneally-injected with extracted microcystins.
9/2008-7/2009	B.S Pharmaceutical Science Wuhan University, Wuhan, China

Conferences

June, 2019	Bioenergetics Gordon Research Conference: Structure, Mechanism, and Theory, New Hampshire, USA.
August, 2018	EBEC, Budapest, Hungary.